



CRANFIELD UNIVERSITY

SCHOOL OF MECHANICAL ENGINEERING

Department of Turbomachinery and Engineering Mechanics

PhD THESIS

Academic Year 1996-1997

Michael Lee Dockney

**Fabrication of Wavelength Division Multiplexed
in-Fibre Bragg Grating Arrays for Structural
Monitoring Applications**

Supervisor: Ralph P Tatam

April 1997

This thesis is submitted in partial fulfilment of the requirements for the degree
of Doctor of Philosophy

ProQuest Number: 10820906

All rights reserved

INFORMATION TO ALL USERS

The quality of this reproduction is dependent upon the quality of the copy submitted.

In the unlikely event that the author did not send a complete manuscript and there are missing pages, these will be noted. Also, if material had to be removed, a note will indicate the deletion.



ProQuest 10820906

Published by ProQuest LLC (2018). Copyright of the Dissertation is held by Cranfield University.

All rights reserved.

This work is protected against unauthorized copying under Title 17, United States Code
Microform Edition © ProQuest LLC.

ProQuest LLC.
789 East Eisenhower Parkway
P.O. Box 1346
Ann Arbor, MI 48106 – 1346



Abstract

Wavelength division multiplexed arrays of in-fibre Bragg gratings (IFBGs) are fabricated in hydrogen loaded optical fibres. The IFBG arrays are embedded into a carbon fibre composite test beam for the purpose of quantitative dc strain sensing.

A near-field phase mask writing technique is compared to a conventional mirror interferometer and a novel phase mask based interferometer writing scheme. The combination of a wavelength tuneable UV source and a phase mask based interferometer offers, either a large spectral coverage of 51nm, or a laser limited Bragg wavelength accuracy of 0.03nm in the 800nm spectral region. The characteristics of gratings fabricated using these schemes are discussed.

The axial strain sensitivity of optical fibre is investigated in a preliminary experiment. A three point bend test is then used to compare the theoretical strain applied to a carbon fibre test beam with measurements made by electrical strain gauges and embedded IFBG sensors over the range $\pm 3400\mu\text{strain}$. A residual tensile strain results from embedding and is generally measured to be $>2000\mu\text{strain}$. The majority of IFBG sensors appear well bonded to the surrounding host material and, with one exception, the strain responses of uncoated IFBG sensors deviate from the theoretically predicted values by $\leq 4.3\%$. A buffer coat around the sensor reduces the strain response by $\sim 4\%$ but does not affect its linearity or reproducibility.

A spliced IFBG pair is used to separate strain and temperature measureands. A transfer matrix for the scheme is experimentally determined that has a calculated condition number of 23. The technique is compared to other reported methods of strain and temperature separation. Also, a demodulation scheme for IFBG sensors based on a volume holographic filter formed in photorefractive BaTiO_3 is reported. The filter has a strain measurement range of $2500\mu\text{strain}$, with a minimum detectable strain of $4\mu\text{strain}/\sqrt{\text{Hz}}$.

Acknowledgements

There are a number of people I would like to thank for their help during the course of my PhD.

Firstly, my supervisor Ralph Tatam for all his enthusiasm and technical input. I am especially grateful for his support during the writing of this thesis. Also, the various members of the optical sensors group at Cranfield, who have assisted me at one time or other with various aspects of the work. In particular, Steve James, who has helped me out on more than the odd occasion, and Steve Staines for making all those bits and pieces that I needed yesterday.

My industrial supervisor Pete Foote has always made me feel welcome when I have visited British Aerospace and has been an invaluable source of information. I am also indebted to his colleague Ian Read who was my co-worker whilst at BAe.

Finally, I'd like to thank my wife Yvonne for her love and support.

This project was funded by an EPSRC (CASE) award in association with British Aerospace, Sowerby Research Centre.

Contents

1	Introduction	1
1.1	Smart materials and structures	1
1.2	Optical fibre sensors for smart structures	2
1.2.1	Optical fibre sensors suitable for structural monitoring	3
1.2.2	The Bragg grating sensor	4
1.3	Thesis summary	5
	References	7
2	Overview of Bragg grating technology	9
2.1	Propagation of light within optical fibres and interaction with gratings	9
2.1.1	Cylindrical step-index optical fibre waveguides	9
2.1.2	Coupled-mode model of Bragg grating reflection in singlemode fibres	13
2.2	Photosensitivity in germanosilicate optical fibres and associated grating characteristics	17
2.2.1	Photosensitivity in germanosilicate fibres	18
2.2.2	Grating spectral characteristics and thermal stability	27
2.3	Externally written gratings	32
2.3.1	Interferometer writing schemes	32
2.3.2	Phase mask techniques	36
2.3.3	Other external fabrication techniques	39
2.3.4	UV laser sources for grating fabrication	40
2.4	Grating applications	42
2.5	Related photoinduced mode coupling devices	47
	References	50

3	Fabrication of Bragg grating arrays	62
3.1	Tuneable UV laser source for grating fabrication	62
3.1.1	Description of tuneable UV laser system	62
3.1.2	Laser beam profiling system	68
3.2	Grating writing schemes	70
3.2.1	Hydrogen loading of optical fibres	70
3.2.2	Scanning monochromator with white light source	72
3.2.3	Near-field phase mask	75
3.2.4	Two-beam mirror interferometer	78
3.2.5	Two-beam mirror interferometer with a phase mask beamsplitter	84
3.3	Grating characteristics	93
3.3.1	Writing conditions used to fabricate WDM grating arrays using the two-beam mirror interferometer.	94
3.3.2	Grating spectral characteristics	99
3.3.3	Bragg wavelength shift and optical fibre absorption band associated with hydrogen loading	105
	References	109
4	Embedded Bragg grating strain sensors in carbon fibre composite	111
4.1	Theoretical strain and temperature sensitivity of gratings	111
4.2	Experimental determination of grating strain sensitivity	114
4.2.1	Automated scanning monochromator with an ELED source	115
4.2.2	Determination of the axial strain gauge factor	117
4.3	Strain sensitivity of gratings embedded in a carbon fibre composite beam	127
4.3.1	Sensor-host structural integrity issues	127
4.3.2	Fabrication of the carbon fibre test beam	129

4.3.3 Measurement of residual strain due to embedding	133
4.3.4 Three-point bend test	139
4.3.5 Bragg grating and electrical strain gauge monitoring system	141
4.3.6 Three-point bend test results for carbon fibre test beam	145
References	150
 5 Measurement of strain independent of temperature	 152
5.1 Techniques for strain and temperature separation	152
5.2 Simultaneous determination of strain and temperature	153
5.2.1 Inverse matrix solution of simultaneous linear equations	153
5.2.2 Error sensitivity	155
5.3 Spliced grating pair technique	156
5.3.1 Theory	156
5.3.2 Experimental determination of the transfer matrix	159
References	165
 6 Volume holographic demodulation of Bragg grating sensors	 167
6.1 Interrogation and demultiplexing techniques for WDM grating arrays	167
6.2 Volume holographic demodulation scheme	168
6.3 Interrogation of a Bragg grating using a volume hologram written into BaTiO ₃	173
References	178

7	Conclusions and future developments	180
7.1	Bragg grating fabrication schemes	180
7.2	Embedded Bragg grating strain sensors in carbon fibre composite	182
7.3	Simultaneous strain and temperature measurement	184
7.4	Volume holographic demodulation scheme	185
	Appendix A: Laser beam calculations performed using the Spiricon LBA-100A	187
	Appendix B: Optical fibre parameters	189
	Appendix C: Two-beam mirror interferometer with a phase mask beamsplitter: sensitivity of the out-of-plane geometry to writing wavelength	192
	Appendix D: Carbon fibre composite test beam experimental data	194
	Publications arising from this study	205

Chapter 1

Introduction

1.1 Smart materials and structures

In the future, the civil engineering and aerospace industries could be revolutionised by ‘Smart Materials and Structures’, a new field of engineering that has emerged over the last decade (e.g. *The Engineer*, 1992; Wadley, 1996). This field encompasses a variety of structural and material technologies, that are at different stages of development. A necessary first step in the evolution of smart materials is the development of structures that have an integrated sensory capability, rather like a nervous system in biological systems. These integrated sensors could be used to continuously monitor such fundamental structural parameters as: strain, vibration, temperature and integrity. In more advanced systems, this sensory information could be used to control some physical property of a structure, (e.g., stiffness shape, position and orientation), and these have been termed ‘adaptive structures’ (Wada *et al*, 1990). Ultimately, it may be possible to develop adaptive smart structures that are capable of learning, and these have been termed ‘intelligent structures’ (Measures, 1992).

The use of smart material technology may be particularly useful in accelerating the acceptance of advanced composite materials for structural engineering. Although composite materials have many attractive properties, (e.g.,

high strength to weight ratio, tailored stiffness, ease of moulding into complex shapes, thermal expansion properties, and resistance to fatigue and corrosion), the material properties are anisotropic (Measures *et al*, 1989). The epoxy resin matrix is at least an order of magnitude weaker than the embedded fibres of carbon or Kevlar. Cracking parallel to the material fibres within a given ply and disbonding between successive plies, termed delamination, represents the major drawback of composite materials. Integrated sensors within composites could lead to greater confidence in the use of these materials and reduce overdesign. For instance, if the sensors could provide information about the composite during the manufacturing stage, they could be used to improve quality control.

The potential benefits that composite materials with integrated sensing may offer can be illustrated by an example from the aircraft industry. A new generation of carbon composite skinned aircraft is currently being developed (Foote and Read, 1995). Integrated sensors within composite panels would allow the load-history applied to aircraft structures to be logged. This could be used to increase maintenance efficiency, improve safety, and increase the operating lifetime of aircraft. The net benefit being reduced operating costs for the airlines.

Sensors for aircraft structural monitoring, would typically be required to measure strain near the surface of composite panels in the range $\pm 5\%$ over a temperature range of -50°C to 160°C (Foote and Read, 1995). The real time spatial resolution required, being of the order of 1cm (Measures, 1993).

1.2 Optical fibre sensors for smart structures

Embedded optical fibre sensors appear particularly suitable for integrated structural monitoring of composite materials, since they are: lightweight, immune to electromagnetic interference, resistant to corrosion and fatigue and are compatible with composite materials. Further, the optical fibre breaking strain is similar to that of carbon fibre composites at around 1% (Foote and Read, 1995). For aircraft structural monitoring the sensory information could be integrated into fly-by-light systems

currently under active investigation for the next generation of aircraft (e.g. Kandebo, 1993).

1.2.1 Optical fibre sensors suitable for structural monitoring

Optical fibre sensors can be classified as being distributed or localised. At first sight distributed sensors appear to offer an attractive solution, since they would permit the use of fewer sensors and make effective use of the whole length of the sensing fibre. For aircraft structural monitoring, time of flight measurements could be used to map the strain along the entire fibre length. However, at the present time distributed sensing is not practical or economic for monitoring the strain to the required spatial resolution (Measures, 1993). Localised fibre optic sensors determine the measure and over a specific segment of the optical fibre, and are similar in that way to conventional strain or temperature gauges. Information, about the state of the structure is impressed upon the transmitted light by a number of mechanisms. These include interactions that change the intensity, phase, frequency, polarisation, wavelength or modal distribution of the light propagating along the optical fibre.

For the example application, embedded strain sensors within composite aircraft structures, numerous types of optical fibre sensor have been demonstrated that are able to transduce strain. However, in order to assess their suitability for smart structures the criteria suggested by Turner *et al*, (1989) may serve as a useful guide. An ideal fibre optic strain sensor should be:

- (1) *intrinsic in nature for minimum perturbation and stability,*
- (2) *localised, so that it can operate remotely with insensitive leads,*
- (3) *able to respond only to the strain field and discern any change in direction,*
- (4) *well behaved with reproducible response,*
- (5) *all fibre for operational stability,*
- (6) *able to provide a linear response,*
- (7) *single optical fibre for minimum perturbation and common mode rejection,*
- (8) *single ended for ease of installation and connection,*
- (9) *sufficiently sensitive with adequate measurement range,*
- (10) *insensitive to phase interruption at the structural interface,*
- (11) *does not perturb the structure and is robust for installation,*
- (12) *interrupt immune and capable of absolute measurement,*

- (13) *amenable to multiplexing to form sensing networks within a structure,*
- (14) *easily manufactured and adaptable to mass production.*

Measures (1993) assessed all of the proposed optical fibre strain sensors according to these criteria, and found that only the polarimetric (Varnham *et al*, 1983; Kersey *et al*, 1984), two-mode (Kim *et al*, 1987; Murphy *et al*, 1989), Fabry-Pérot (Lee *et al*, 1989, Lesko *et al*, 1992) and in-fibre Bragg grating (Meltz *et al*, 1989; Morey *et al*, 1989), complied with criteria (1), (2), (4), (5), (7) and (10).

Of the remaining candidate strain sensors, the in-fibre Bragg grating (IFBG) is the only sensor type which spectrally encodes the measureand signal. The direct relationship between the Bragg wavelength and optical fibre strain gives the IFBG sensor an important advantage over other sensor types – the ability to make absolute strain measurements. Unlike other sensors, this makes the IFBG sensor immune to power interruption of the sensor demodulation system. Also, spectral encoding of the measureand makes IFBG sensors amenable to wavelength division multiplexing (WDM). This allows a much smaller physical separation between IFBGs compared to the alternative sensors, where only time division multiplexing can be used. For widespread use, an optical fibre sensor must be capable of being readily mass produced to keep the unit cost low. The fabrication of IFBGs during the optical fibre pulling process has been demonstrated (Dong *et al*, 1993; Askins *et al*, 1994), paving the way for mass production. Because of these advantages, the IFBG strain sensor is seen, at present, to be the leading candidate for aircraft structural monitoring (Foote and Read, 1995).

1.2.2 The Bragg grating sensor

An IFBG (Meltz *et al*, 1989) is a periodic perturbation of the core refractive index, which results from exposure to the intense optical field of an ultra-violet (UV) laser source at around 240nm. The induced intra-core phase grating acts as a narrowband reflection filter,

where the reflected wavelength λ_b satisfies the Bragg condition given by

$$\lambda_b = 2n_{eff}\Lambda \quad (1.1)$$

where n_{eff} is the effective mode index of the optical fibre and Λ is the grating period. All other wavelengths outside the narrow reflection band will be transmitted with only weak attenuation.

From equation 1.1 it can be seen that environmentally induced changes in either n_{eff} or Λ will result in a shift in the reflected Bragg wavelength. Morey *et al* (1989) showed that monitoring of the Bragg wavelength could be used to determine the strain or temperature experienced by an optical fibre. A schematic of an IFBG sensor system is shown in figure 1.1.

1.3 Thesis summary

The work reported in this thesis was funded through an Engineering and Physical Sciences Research Council Co-operative Award (CASE), in conjunction with the Sowerby Research Centre (Bristol) of British Aerospace Ltd.

The project focused on producing high quality WDM grating arrays, suitable for structural monitoring applications and to that end, several methods of fabricating WDM grating arrays were investigated. This included a novel method that combined a phase mask based interferometer and a tuneable UV source to provide high resolution control over the Bragg wavelength with high opto-mechanical stability. Further, to demonstrate a specific structural monitoring application, WDM grating arrays were embedded within an aerospace carbon fibre composite material for the purpose of quantitative dc strain measurement. Supplementary work was also conducted into the development of a new IFBG interrogation scheme suitable for use with WDM grating arrays, and a new technique for allowing simultaneous strain and temperature measurement using IFBG sensors was investigated.

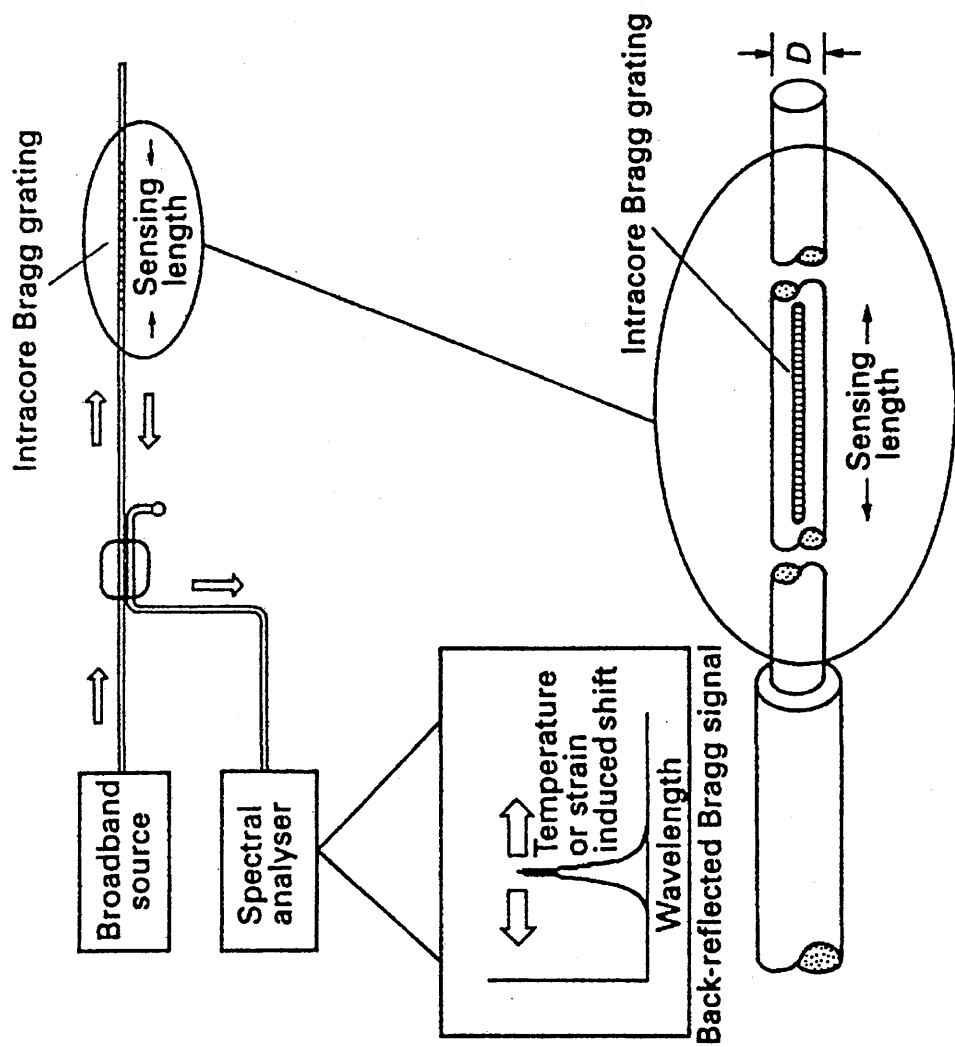


Figure 1.1 The in-fibre Bragg grating (IFBG) sensor. Also indicated is the back-reflected narrow band Bragg spectrum (reproduced from Measures, 1993).

References

- 'Smart moves in a material world', *The Engineer*, 16 April 1992.
- Askins, C.G., Putnam, M.A., Williams, G.M., and Friebele, E.J., 'Stepped wavelength optical fibre Bragg grating arrays fabricated in-line on a draw tower', *Opt. Lett.*, **19**, pp147-149 (1994).
- Foote, P.D., and Read, I.J., 'Optical Sensors for aerospace structural monitoring', *IEEE: Colloquium on Optical Techniques for Structural Monitoring*, Digest No: 1995/087, 28 April 1995.
- Kandebo., S.W., 'NASA, Navy to evaluate Fly by Light sensors in F/A-18', *Aviation Week and Space Technology*, pp55-56, 2nd August 1993.
- Kersey, A.D., Corke, M., and Jackson, D.A., 'Linearised remote sensing using a monomode fibre polarimetric sensor', *SPIE*, **514**, pp247-250 (1984).
- Kim, B.Y., Blake, J.N., Huang, S.Y., and Shaw, H.J., 'Use of highly elliptical core fibers for two-mode fibre devices', *Opt. Lett.*, **12**, pp729-731 (1987).
- Lee, C.E., Taylor, H.F., Markus, A.M., and Udd, E., 'Optical-fiber Fabry-Perot embedded sensor', *Opt. Lett.*, **14**, pp1225-1227 (1989).
- Lesko, J.J., Carman, G.P., Fogg, B.R., Miller III, W.V., Vengsarkar, A.M., Reifsnider, K.L., Claus, R.O., 'Embedded Fabry-Perot fiber optic strain sensors in the macromodel composites', *Opt. Eng.*, **31**, pp13-21 (1992).
- Measures, R.M., Glossop, N.D.W., Lymer, J., Leblanc, M., West, J., Dubois, S., Tsaw, T., and Tennyson, R.C., 'Structurally integrated fiber optic damage assessment system for composite materials', *Appl. Opt.*, **28**, pp2626-2633 (1989).
- Measures, R.M., 'Smart composite structures with embedded sensors', *Composites Eng.*, **2**, pp597-618 (1992).
- Measures, R.M., 'Fiber optic sensing for composite smart structures', *Composites Eng.*, **3**, pp715-750 (1993).
- Meltz, G., Morey, W.W., and Glen, W.H., 'Formation of Bragg gratings in optical fibers by a transverse holographic method', *Opt. Lett.*, **14**, pp823-825 (1989).

- Morey, W.W., Meltz, G., and Glenn, W.H., 'Fiber optic Bragg grating sensors', in *Proc. Fibre Optic and Laser Sensors VII*, Boston, pp98-107 (1989).
- Murphy, K.A., Gunther, M.F., Vengsarkar, A.M., and Claus, R.O., and Lewis, N.E., 'Embedded modal domain sensors using elliptical core optical fibers', *SPIE*, **1588**, pp134-144 (1989).
- Turner, R.D., Valis, T., Hogg, W.D., and Measures, R.M., 'Fiber optic strain sensors for smart structures', *J. Intell. Mater. Syst. Struct.*, **1**, pp26-49 (1989).
- Varnham, M.P., Barlow, A.J., Payne, D.N., and Okamoto, K., 'Polarimetric strain gauges using high birefringence fibres', *Electron. Lett.*, **19**, pp699-700 (1983).
- Wada, B.K., Fanson, J.L., and Crawley, E.F., 'Adaptive structures', *J. Intell. Mater. Syst. Struct.*, **1**, pp157-174 (1990).
- Wadley, H.N.G., 'Characteristics and Processing of Smart Materials', *AGARD SMP lecture series: Smart Structures and Materials: Implications for Military Aircraft of New Generation*, **LS-205** (1996).

Chapter 2

Overview of Bragg grating technology

2.1 Propagation of light within optical fibres and interaction with gratings

2.1.1 Cylindrical step-index optical fibre waveguides

A simple ray treatment of optical fibre waveguides, (e.g., Senior, 1992) describes how light propagates along an optical fibre by total internal reflection. Rays must have a sufficiently shallow angle of incidence to be guided by the fibre. A generally used parameter that relates the maximum acceptance angle θ_a to the refractive indices of the fibre core n_1 and cladding n_2 is the numerical aperture NA . The NA of a fibre is defined as

$$NA = n_0 \sin \theta_a = (n_1^2 - n_2^2)^{\frac{1}{2}} \quad (2.1)$$

where n_0 is the refractive index of the surrounding air.

The NA can also be expressed in terms of the relative refractive index difference Δ between the core and the cladding, which is defined as

$$\begin{aligned} \Delta &= \frac{n_1^2 - n_2^2}{2n_1^2} \\ \text{for } \Delta \ll 1 \quad &\approx \frac{n_1 - n_2}{n_1} \end{aligned} \quad (2.2)$$

Assuming $\Delta \ll 1$ the NA can be obtained from

$$NA \approx n_1 (2\Delta)^{\frac{1}{2}} \quad (2.3)$$

A detailed understanding of optical propagation within a fibre can only be attained using electromagnetic theory. It is necessary to solve Maxwell's equations subject to cylindrical boundary conditions. Since a complete treatment is beyond the scope of this thesis and can be found in a number of texts (e.g., Yariv, 1985), only a brief summary is presented below.

The scalar wave equation in cylindrical co-ordinates is given by

$$\nabla^2 \psi = \frac{\delta^2 \psi}{\delta r^2} + \frac{1}{r} \frac{\delta \psi}{\delta r} + \frac{1}{r^2} \frac{\delta^2 \psi}{\delta \phi^2} + \frac{\delta^2 \psi}{\delta z^2} = \epsilon \mu \frac{\delta^2 \psi}{\delta t^2} \quad (2.4)$$

where ψ represents each component of the electric field vector \mathbf{E} and magnetic intensity vector \mathbf{H} , ϵ is the dielectric permittivity and μ is the magnetic permeability of the medium. Solutions of the wave equation are separable and have the form

$$\psi = \psi_r(r) e^{i\nu\phi} e^{i(\omega t - \beta z)} \quad (2.5)$$

where ν is a positive integer, ω is the optical frequency and β is the component of the phase propagation constant in the z direction (along the fibre axis). Substituting the solutions given by equation 2.5 into equation 2.4 yields the Bessel differential equation

$$\frac{d^2 \psi_r(r)}{dr^2} + \frac{1}{r} \frac{d\psi_r(r)}{dr} \left(n_1^2 k^2 - \beta^2 - \frac{\nu^2}{r^2} \right) \psi_r(r) = 0 \quad (2.6)$$

where k is the vacuum phase propagation constant, which is related to the optical wavelength, λ , by $k = 2\pi/\lambda$. Equation 2.6 can be solved for regions inside and

outside the core and by applying boundary conditions the exact modes of the fibre may be determined.

The calculation of the exact modes of step-index optical fibres (the type of fibre used throughout this work) involves the manipulation of complex expressions. Fortunately the analysis can be simplified for most commercial fibres, where $\Delta \ll 1$, by using the ‘weakly-guiding’ approximation (Gloge, 1971). This assumes that the transverse x and y components of \mathbf{E} and \mathbf{H} dominate the longitudinal z components, and thus the solutions to the Bessel equation may be expressed in Cartesian form. Applying boundary conditions a set of linearly polarised (LP) transverse modes are obtained. These LP modes are comprised of a superposition of exact modes and are designated LP_{lm} where l and m are integers. The lowest order mode, LP_{01} , has no low frequency cut-off for wave propagation and so there is always at least one mode able to propagate within a fibre.

A useful quantity for characterising modal propagation within an optical fibre is the normalised frequency V , given by

$$V = ka(n_1^2 - n_2^2)^{\frac{1}{2}} \quad (2.7)$$

where a is the core radius. Further, using equation 2.1, V may be expressed in terms of the numerical aperture NA as follows

$$V = \frac{2\pi}{\lambda} a(NA) \quad (2.8)$$

The cut-off of frequency for a particular mode corresponds to a distinctive value of V . The condition for singlemode operation being

$$V \leq 2.405 \quad (2.9)$$

Now consider a nominally circular symmetric optical fibre supporting only the fundamental LP_{01} mode. The fibre will allow two nearly degenerate orthogonal polarisations to propagate (i.e., the orthogonal polarisations have almost identical propagation constants), with electric field polarisations denoted by E_x and E_y . In practice, any imperfections in the fibre symmetry, material anisotropy, or external perturbations will break the mode degeneracy. Thus the fibre will behave as a

birefringent medium and the orthogonal polarisations will have different propagation constants β_x and β_y . This will cause a variation in the resultant polarisation state along the length of the fibre. Given that the propagation constant of a mode β is related to the effective mode index n_{eff} by

$$\beta = \frac{2\pi n_{eff}}{\lambda} \quad (2.10)$$

The modal birefringence B_f for the fibre can be expressed as (Kaminow, 1981)

$$B_f = \frac{\lambda(\beta_x - \beta_y)}{2\pi} = n_x - n_y \quad (2.11)$$

The length of fibre over which the phase difference between the two orthogonal polarisations cycles through 2π is known as the beat length L_B where

$$L_B = \frac{2\pi}{\beta_x - \beta_y} = \frac{\lambda}{n_x - n_y} \quad (2.12)$$

One way of maintaining the polarisation state along the length of the fibre is to intentionally introduce a large birefringence into the fibre core. This creates two principal axes with very different propagation constants. Differences in the propagation constants due to intrinsic anomalies or external perturbations will be insignificant in comparison. Thus polarised light launched down one of these principal axes will retain its state of polarisation along the entire fibre length. This type of fibre is termed high birefringence (Hi-Bi). Typically a Hi-Bi fibre requires a B_f of $>10^{-5}$ (Senior, 1992).

Birefringence can be introduced by several methods. Some fibre types utilise dumbbell or, more usually, elliptical cores to break the circular symmetry. Alternatively stress birefringence can be induced by using an elliptical cladding or by introducing stress elements into the cladding either side of the core. A review of the various types of polarisation maintaining fibres, including Hi-Bi fibres can be found in Noda *et al* (1986).

In this work both singlemode and Hi-Bi (elliptical core) optical fibres were utilised for IFBG fabrication, details of which can be found in chapter 3.

2.1.2 Coupled-mode model of Bragg grating reflection in singlemode fibres

Coupled-mode theory (Yariv and Yeh, 1984) has successfully been applied to modelling the reflection filter characteristics of IFBGs (Lam and Garside, 1981; Meltz *et al*, 1989). In this model the periodic refractive index variation of an IFBG is considered as a weak perturbation that couples the normal modes of an optical fibre. Specifically, coupling a forward propagating mode into a backward propagating mode. This is valid approach since the refractive index perturbations are generally small, typically of the order of 10^{-4} (see section 2.2.1).

Consider an optical fibre supporting only the LP_{01} mode. Light propagating in the forward (+z) and backward (-z) directions can be described by the fields c^+ and c^- respectively, defined as

$$\begin{aligned} c^+(z,t) &= C^+ e^{i(\omega t - \beta z)} \\ c^-(z,t) &= C^- e^{i(\omega t + \beta z)} \end{aligned} \quad (2.13)$$

where C^+ and C^- are the field amplitudes, which are constant in an unperturbed fibre. Along the length of an IFBG, however, power is exchanged between the c^+ and c^- fields. Thus, C^+ and C^- are no longer constant but will depend on z .

Assuming a linear relationship between the intensity of the illuminating fringe pattern and the induced change in core refractive index, an ideal IFBG of constant amplitude and period will have a refractive index profile $n(z)$ which can be expressed as

$$n(z) = n_a + \Delta n \cos\left(\frac{2\pi}{\Lambda} z\right) \quad (2.14)$$

where n_a is the average core refractive index over the grating length and Λ is the grating period.

The variation in the field amplitudes due to the refractive index perturbation can be described by the coupled-mode equation (Yariv and Yeh, 1984)

$$\begin{aligned}\frac{d}{dz}C^+(z) &= -i\kappa C^-(z)e^{i\Delta\beta z} \\ \frac{d}{dz}C^-(z) &= i\kappa C^+(z)e^{-i\Delta\beta z}\end{aligned}\tag{2.15}$$

where $\Delta\beta$ is the phase mismatch constant given by

$$\Delta\beta = 2\beta - \frac{2\pi}{\Lambda}\tag{2.16}$$

and κ is the coupling coefficient defined as

$$\kappa = \frac{\pi\Delta n\eta(V)}{\lambda}\tag{2.17}$$

$\eta(V)$ is the fraction of the integrated fundamental mode intensity contained in the fibre core, and is function of the normalised frequency V . For singlemode operation $\eta(V)$ can be taken to be ~ 0.8 (Ungar, 1990).

To obtain an expression for the reflectivity of an IFBG, equation 2.15 is solved subject to the boundary conditions

$$\begin{aligned}C^+(0) &= 1 \\ C^-(L) &= 0\end{aligned}\tag{2.18}$$

where L is the grating length, and it is assumed that the light is incident on the grating at $z=0$. The solution of equation 2.15 is then given by (Yariv and Yeh, 1984)

$$\begin{aligned}C^+(z) &= e^{i(\Delta\beta/2)z} \frac{s \cosh s(L-z) + i(\Delta\beta/2) \sinh s(L-z)}{s \cosh sL + i(\Delta\beta/2) \sinh sL} \\ C^-(z) &= e^{-i(\Delta\beta/2)z} \frac{-\kappa \sinh s(L-z)}{s \cosh sL + i(\Delta\beta/2) \sinh sL}\end{aligned}\tag{2.19}$$

where $s = \left[\kappa^2 - (\Delta\beta/2)^2 \right]^{1/2}$.

The reflectivity of the IFBG is defined as

$$R = \left| \frac{C^-(0)}{C^+(0)} \right|^2\tag{2.20}$$

which, from equation 2.20, can be expressed as

$$R = \frac{\kappa^2 \sinh^2 sL}{s^2 \cosh^2 sL + (\Delta\beta/2)^2 \sinh^2 sL} \quad (2.21)$$

The maximum reflectivity occurs at the phase matched condition $\Delta\beta=0$, where equation 2.21 becomes

$$R_{\max} = \tanh^2 \kappa L \quad (2.22)$$

Figure 2.1 shows the variation of IFBG reflectivity as a function of wavelength, calculated using equation 2.21, for a grating with $\lambda_b=830\text{nm}$, $L=2.5\text{mm}$, $\Delta n=1.6 \times 10^{-4}$, and $n_{\text{eff}}=1.46$ (Senior, 1992). The reflectivity at the Bragg wavelength, R_{\max} , being 70%. It can be seen from figure 2.1 that the IFBG reflection spectrum consists of a main peak with a sharp cut-off and a series of sidebands.

The full bandwidth of the IFBG, which is defined as the wavelength separation between the first zeros of the reflection spectrum, can be obtained from

$$B_w = \frac{\lambda_b^2}{\pi n_{\text{eff}} L} \left[(\kappa_b L)^2 + \pi^2 \right]^{1/2} \quad (2.23)$$

where κ_b is the coupling coefficient at λ_b . In the case of the example shown in figure 2.1, $B_w = 0.2\text{nm}$.

It should be remembered that the foregoing analysis is based upon a grating with a uniform refractive index perturbation. In reality the index perturbation will usually vary along the grating length, often having a Gaussian envelope in accordance with the writing laser's beam profile. Huang *et al* (1994) have used coupled-mode theory to model non-uniform IFBGs, including those with Gaussian distributions. Gaussian distributions have the effect of suppressing the IFBG reflection sidebands, this suppression generally being referred to as 'apodisation' (e.g. Albert *et al*, 1995(a)). For WDM sensor arrays, apodisation of the IFBG spectrum is desirable, since sidebands increase the wavelength spacing required to prevent inter-grating interference.

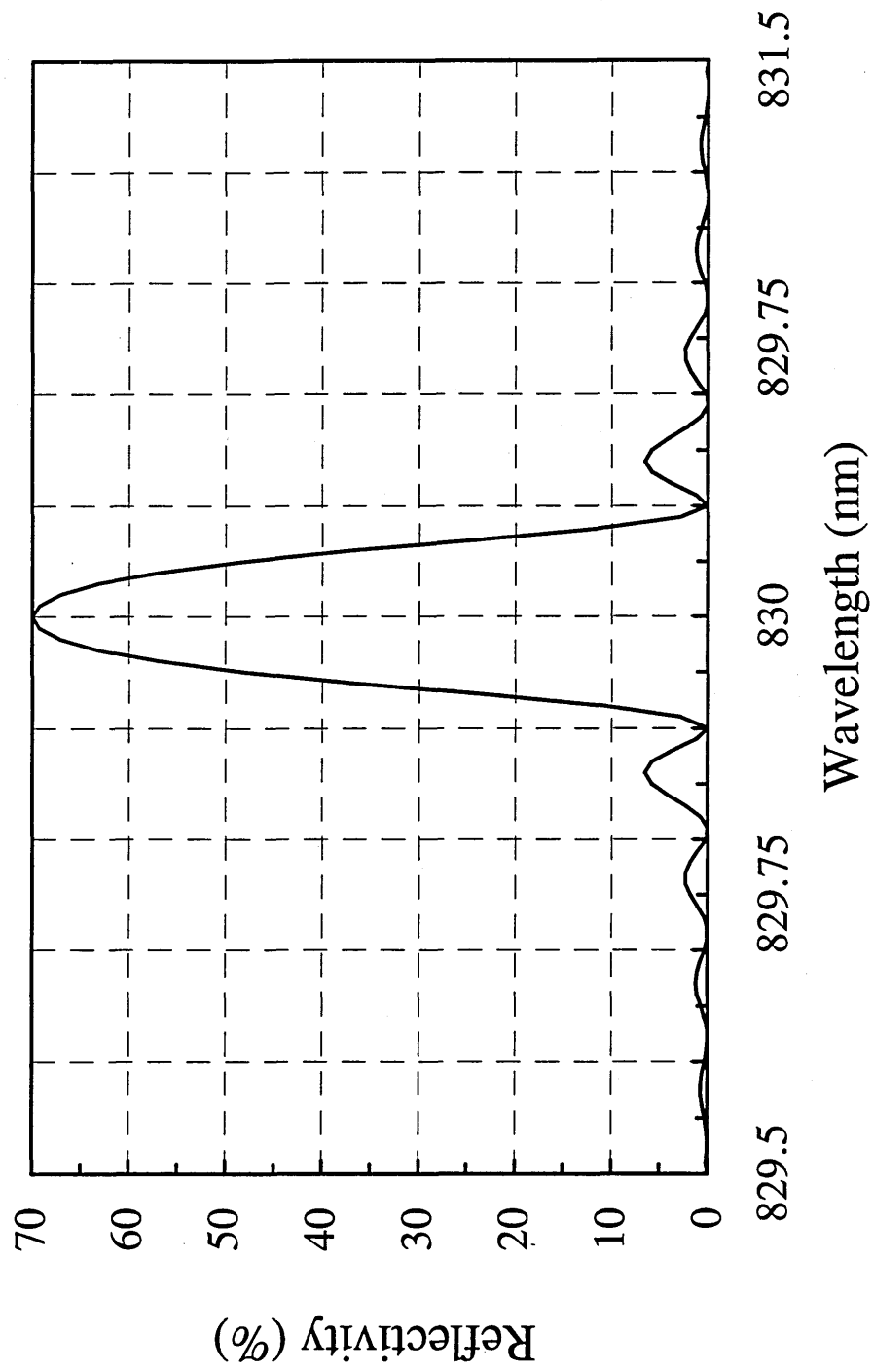


Figure 2.1 The reflectivity of an IFBG calculated using coupled-mode theory ($\lambda_p=830\text{nm}$, $L=2.5\text{mm}$, $\Delta n=1.6\times 10^{-4}$, $n_{eff}=1.46$).

Finally, it should be noted that, although only the Bragg reflection of the fundamental mode has been considered in this section, gratings can also be written into multimode fibres (Meltz *et al*, 1989). In fibres where there are a several modes propagating the phase matching conditions will be satisfied at a different wavelength for each mode. Thus the reflection spectrum from an IFBG will show a number of wavelength spaced Bragg reflection peaks, each corresponding to a different mode of the fibre. Indeed Meltz *et al*, (1989) suggested that IFBGs could be used to separate the fundamental mode from higher order modes. Similarly, in Hi-Bi singlemode fibre, the refractive index difference between the two principal axes will result in the component of light in each polarisation axis having a slightly different Bragg reflection wavelength (Meltz *et al*, 1989; Morey *et al*, 1989). If the fibre birefringence is known, the wavelength separation of the two Bragg reflections can easily be calculated using equation 1.1. Morey *et al* (1989) demonstrated this effect in Andrew Corp. elliptical core fibre (A fibre type that is utilised in section 3.3.5). It was shown that for an IFBG written around 820nm, the Bragg wavelengths of the principal polarisation axes were separated by 0.11nm.

2.2 Photosensitivity in germanosilicate optical fibres and associated grating characteristics

Photosensitivity in germanosilicate optical fibres was first demonstrated by Hill *et al* (1978). It was found that a single frequency argon-ion laser (operating at 488nm or 514nm) could be used to write an IFBG into the core of a singlemode fibre. The launched light interfered with back-reflected light from the distal end of the fibre to form a standing wave pattern. This induced a refractive index perturbation within the fibre core that was related to the local electric field amplitude and thus a periodic grating was formed. The main disadvantage with this method of fabricating IFBGs was that gratings could only be written that reflected at the writing wavelength, which was limited to the blue-green spectral region. This meant that IFBGs could not be

written that would reflect in the low loss telecommunications windows. Also, the grating was written along the entire fibre length and could not be localised to a specific region. As a consequence of these limitations, the field attracted little attention. However, a breakthrough came when Meltz *et al* (1989) demonstrated that gratings could be fabricated by interfering two UV beams on the side of a fibre. This so called transverse holographic technique allowed the Bragg reflected wavelength to be varied by adjusting the angle between the writing beams (see section 2.3.1), which paved the way for fabricating gratings within the low loss telecommunications window at 1550nm (Kashyap *et al*, 1990). Since then there has been intense interest in IFBGs for telecommunication and sensor applications.

Photosensitivity has also been demonstrated in germania free optical fibres. It has been shown that glass fibres, some of which had non-silica cores, doped with europium (Hill *et al*, 1991(a)) and cerium (Broer *et al*, 1991; Dong *et al*, 1993(a); Taunay *et al*, 1994) are photosensitive to UV radiation. IFBGs have also been fabricated in chalcogenide glass fibres using the transverse holographic method and a 633nm helium-neon laser (Asobe *et al*, 1996). Nonetheless, it is gratings photoinduced in germanosilicate fibres that offer the most potential for telecommunication and sensor applications. The nature of the photosensitivity in these fibres and the characteristics of the induced IFBGs are now considered.

2.2.1 Photosensitivity in germanosilicate fibres

Although there have been a number of investigations into the nature of UV induced refractive index changes in germanosilicate fibres, many questions still remain concerning the underlying physical processes responsible for IFBG formation.

It has been known for some time that an absorption band at around 240nm is associated with an oxygen-vacancy defect (GeO defect) in germania doped silica (Yuen, 1982). Normally germanium is substituted into the silica glass tetrahedral matrix in the Ge^{+4} oxidation state, i.e., as GeO_2 . However, the Ge^{+2} state and its associated GeO oxide can be formed during the thermal cycling of preforms prepared

using the modified chemical vapour deposition process (Yuen, 1982). The GeO defect is characterised by a Ge atom that is bonded to 3 oxygen atoms and either a silicon or germanium atom as shown in figure 2.2(a). Meltz *et al* (1989) suggested that the starting point for the refractive index change was related to the bleaching of the GeO absorption band. Subsequently, direct evidence of GeO band bleaching by 240nm radiation has been provided (Williams *et al*, 1992; Atkins and Mizrahi, 1992). Figure 2.3 shows the absorption at 240nm both before and after an IFBG was written into a fibre. The bleaching of the 240nm band as a result of UV exposure is apparent, as is an increase in absorption at shorter wavelengths.

It has been demonstrated that a positive refractive index change is induced by UV radiation (Malo *et al*, 1990). This was achieved by irradiating a photosensitive fibre placed in one arm of a Mach-Zehnder interferometer. The resulting fringe shift gave a measure of the index change. Typically, the refractive index modulations for gratings of this type are in the range 10^{-5} - 10^{-4} (Meltz *et al*, 1989; Patrick and Gilbert, 1993), depending upon the total UV fluence applied and the germania content within the optical fibre core. Although an unusually large change in the effective mode index of an optical fibre of 1.8×10^{-3} has been reported by Fertain *et al* (1991). This is the largest refractive index change that has been achieved for this type of grating without any additional enhancement to the photosensitivity (see later discussion on hydrogen loading). The change in the effective mode index was deduced by monitoring the shift in the Bragg wavelength of a grating during fabrication. Indeed, a continuous increase in the Bragg wavelength (due to induced changes in n_{eff}) during inscription is characteristic of IFBG growth. In the case of Fertain *et al* (1991) the maximum Bragg wavelength shift measured was +1.5nm.

To date, there has been no systematic study of the wavelength dependence of GeO band bleaching, though Meltz *et al* (1989) provided evidence that IFBG fabrication is more efficient at 244nm than 257nm, and Kanellopoulos *et al* (1992) have demonstrated that the photosensitivity of germanosilicate fibres is still significant at 266nm.

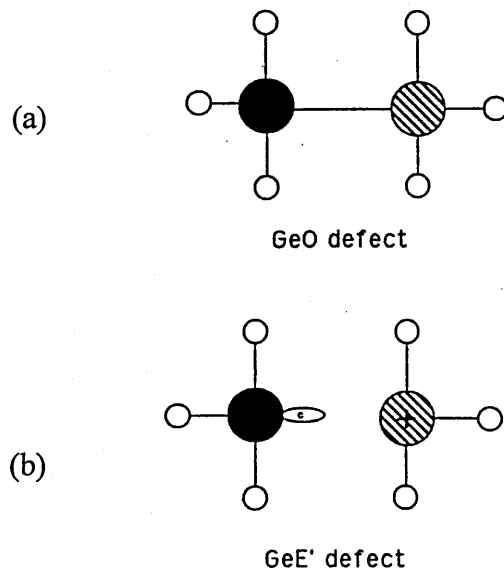


Figure 2.2 (a) GeO defect and (b) GeE' defect. Black filled circles, striped circles, and small open circles represent Ge, Ge or Si, and O atoms respectively (reproduced from Campbell and Kashyap, 1994).

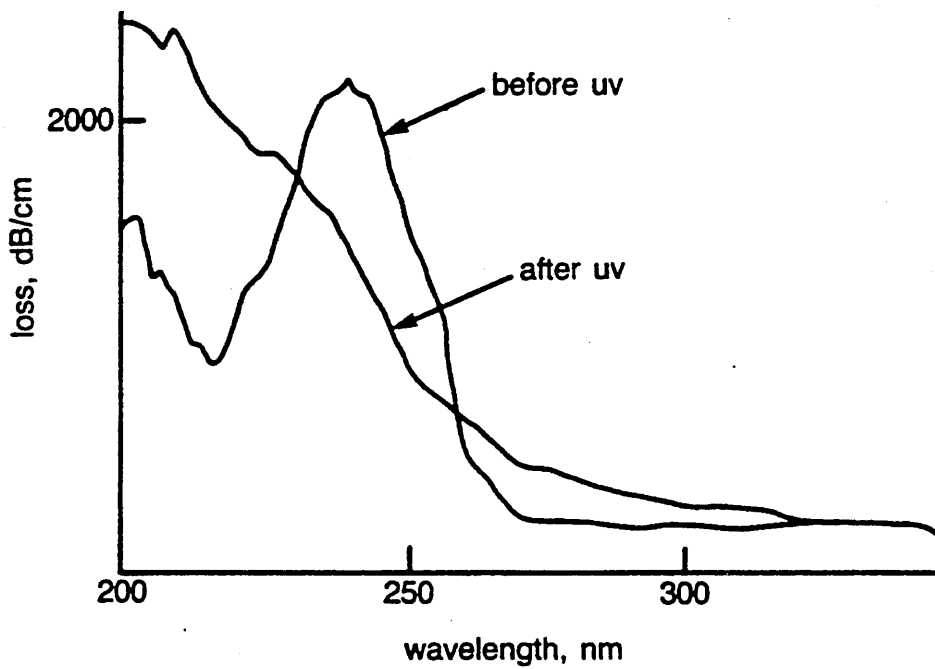


Figure 2.3 UV bleaching of the GeO absorption band (reproduced from Kashyap *et al*, 1993(a)).

Although a number of theories have been proposed to explain the UV induced refractive index change, currently only two mechanisms are widely supported that either separately or in combination could account for the observed index changes. Both mechanisms assume that bleaching of the GeO defect band is the precursor to the refractive index change and are outlined below.

Hand and Russell (1990) proposed that the refractive index changes could be related to photoinduced absorption changes using the Kramers-Kronig principle (Hutchings *et al*, 1992; Newell and Moloney, 1992). The principle is based upon the non-instantaneous response of matter to light, from which it can be shown that the refractive index n , is both frequency dependent and complex. A change in the absorption (imaginary part of n) in the UV part of the spectrum will subsequently lead to a change in the refractive index at longer wavelengths (real part of n). It was suggested that the breakage of Ge-Si bonds by 240nm light, through a one photon absorption (OPA) process, would lead to the creation of GeE' defects and a free electron. The GeE' defect consists of a Ge atom with a dangling bond and a Si⁺ ion, and is shown in figure 2.2(b). Electrons liberated by Ge-Si bond breakage eventually become trapped at other germania defect sites causing absorption bands (colour centres) to form in another part of the UV spectrum. Through the Kramers-Kronig relation, the bleaching of the 240nm absorption band would contribute a negative component to the index change and the photoinduced defects would contribute positive components. The overall index change being in a positive direction. Tsai *et al* (1992) have shown that GeE' centres can be photoinduced in germanosilicate optical fibres by 248nm radiation and a strong UV induced absorption band has been identified at 195nm that was thought responsible for the bulk of the refractive index change (Atkins *et al*, 1993(a)). More recently, Dong *et al* (1995) have managed to account for a refractive index change in the infrared of over 10^{-4} using the Kramers-Kronig relation with absorption changes from 165-300nm. Thermal erasure of an IFBG (see section 2.2.2) causes a partial recovery of the GeO defect band further indicating that changes in the absorption spectrum account for at least part of the refractive index change (Atkins and Mizrahi, 1992). The original gratings written by

Hill *et al* (1978) using argon-ion laser radiation can be explained by the same mechanism, if it is presupposed that two photon absorption (TPA) of 488nm photons is responsible for Ge-Si bond breakage (Lam and Garside, 1981; Hand and Russell, 1990).

However, the results obtained by Williams *et al* (1993(a)) challenged the notion that the Kramers-Kronig mechanism could solely explain the refractive index change. It was found that a boron co-doped fibre had a much greater photosensitive response than an otherwise similar germanosilicate fibre. Further, there was no evidence that the boron affected the 240nm absorption band or created any other UV absorption bands. Since it was known that a stress induced index change resulted from doping a silica fibre with boron (Camlibel *et al*, 1975), Williams *et al* (1993) postulated that the enhanced photosensitivity was due to a photoinduced stress relaxation effect initiated by the breaking of Ge-Si bonds.

Even prior to this, it had been hypothesised that a photoinduced refractive index change could be due to some form of modification of the glass matrix. Bernardin and Lawandy (1990) suggested that the breaking of Ge-Si bonds caused a structural rearrangement of the glass network which lead to a local volume compaction. Direct evidence that GeSiO₂ preforms undergo densification on UV exposure has been provided (Poumellec *et al*, 1995). However, it was calculated that the densification accounted for only 7% of the observed refractive index change. Sceats *et al* (1993) thought that volume compaction was less likely to occur in fibres than preforms, as any tendency for the core to compact will be opposed by an increase in stress arising from attachment to the cladding. An alternative model has been put forward by Wong *et al* (1992) that relates photoinduced stress-relief of the glass network to a refractive index change via the stress-optic effect. This was considered in more detail by Sceats *et al* (1993) who proposed that the breaking of Ge-Si bonds results in a local dilation of the lattice structure which, through a mechanism that has yet to be fully determined, leads to stress-relief of the surrounding network.

Patrick and Gilbert (1993) found that the dependence of the refractive index modulation on time and intensity did not agree with the predictions of a model based

on depletion of a defect population by a OPA process. Experiments conducted using continuous-wave (CW) source showed that the writing efficiency was dependent upon the UV intensity. Also, when comparing CW writing to previous experiments conducted by Mizrahi and Atkins (1992) that used a pulsed source and the same fibre type, it was found that a total fluence of over 42kJ was required to fabricate an 80% reflectance grating using CW irradiation compared with only 1kJ for pulsed irradiation. The greater efficiency of pulsed irradiation might indicate some form of multiphoton or thermally driven process that results in structural changes.

Further, it has been shown that for significantly long exposure times the refractive index change will saturate (Mizrahi and Atkins, 1992). At this point the fibre refractive index will no longer respond linearly to increasing UV fluence. A characteristic of saturated gratings is the emergence of second order diffraction (Xie *et al*, 1993(a)). This occurs as the refractive index profile evolves from being purely sinusoidal to more square wave in nature.

In addition to changes in refractive index, it has been shown that birefringence can be photoinduced in optical fibres. Parent *et al* (1985) first demonstrated birefringence induced by launched visible radiation, and subsequently it was shown that external UV exposure can also induce birefringence (Hill *et al*, 1991(b)). Bardal *et al* (1992) observed that birefringence changes could be induced by polarised 532nm light in both low-birefringence (Lo-Bi) and Hi-Bi fibres. In the case of Lo-Bi fibres the birefringence could be erased by launching orthogonally polarised light, whereas the birefringence change induced in Hi-Bi fibres could not be erased in his way. This difference may be explained if two other studies are taken into consideration. Firstly it has been shown that UV bleaching of the GeO band is anisotropic, and it has been proposed that this is due to preferential bleaching of GeO defects that have a dipole moment aligned with the UV polarisation (Poirier *et al*, 1993). Secondly, Wong *et al* (1992) have used the stress-relief model to account for photoinduced birefringence changes in Hi-Bi fibre. Thus the result from Lo-Bi obtained by Bardal *et al* (1992) may be explained purely in terms of photoinduced

absorption changes, whereas the birefringence changes induced into Hi-Bi fibre appear more likely to be dominated by a strain-relief mechanism.

The photosensitivity of germanosilicate fibres may be enhanced by ‘hydrogen loading’ (Lemaire *et al*, 1993). This is achieved by storing fibres under high pressure hydrogen gas (usually > 100 bar) for several days at room temperature. An alternative method is to locally heat a region of fibre with a hydrogen fuelled flame, and this is usually referred to as ‘flame brushing’ (Bilodeau *et al*, 1993). Using either method the peak refractive index change that can be photoinduced is an order of magnitude greater than in an untreated fibre. E.g., an index modulation of 1.75×10^{-3} was achieved in a flame brushed fibre by Bilodeau *et al* (1993), compared to 1.6×10^{-4} in an untreated fibre.

The photosensitivity is enhanced by creating additional GeO defects in addition to the Ge(OH)/Si(OH) groups that are formed (Atkins *et al*, 1993(b)). In the case of flame brushing the defect centres are generated by a purely thermal reaction. However, things are more complicated for room temperature, high pressure loading. After removal from a hydrogen atmosphere optical fibres do not exhibit any increase in the 240nm absorption band. It is thought that on exposure to UV radiation molecular hydrogen dissolved within the fibre core is driven to react with the germania in the glass by a combination of thermal and photolytic processing (Atkins *et al*, 1993(b)). Simultaneous UV bleaching of the newly created GeO centres leads to a permanent refractive index change.

Malo *et al* (1994) observed a shift over time in the Bragg wavelength of IFBGs written into fibres that had been hydrogen loaded using the high pressure technique. During the first 5h after fabrication the Bragg wavelength increased by ~0.6nm, following which it slowly decreased over the course of the next 14 days. Eventually ending up 0.16nm shorter than the initial Bragg wavelength. Malo *et al* (1994) explained this result by asserting that changes in the level of molecular hydrogen dissolved in the core were responsible for shifts in the effective mode index of the fibre and consequently the shifts in Bragg wavelength. On exposure to UV radiation the H₂ molecules dissociate throughout the fibre but in the in the cladding

the dissociated molecules would most likely recombine due to absence of reaction sites. On the other hand, the core would initially be depleted of H_2 after UV exposure due to reactions with the germania doped glass. Thus, the increase in the effective mode index of the fibre during the first few hours can be explained by diffusion of H_2 from the core to the cladding. In the longer term, however, diffusion to the surrounding atmosphere would gradually remove H_2 from the fibre. The small net reduction in the Bragg wavelength indicating that there was still some molecular hydrogen remaining in the core following UV irradiation.

It is apparent from the above discussion that the high pressure loading technique suffers from the disadvantage that fibres have to be exposed shortly after leaving the hydrogen atmosphere, since within a few days all of the hydrogen will have diffused out of the core. Both methods suffer from the creation of strong 1380nm absorption bands corresponding to the formation of Si(OH) (Lemaire *et al*, 1993), although this can be reduced by using deuterium in place of hydrogen (Kashyap *et al*, 1993(a)).

More recently photosensitivity to 193nm light has been demonstrated (Albert *et al*, 1994), questioning the importance of in-band bleaching at 240nm. Using 193nm irradiation, IFBGs have been fabricated with a refractive index modulation of more than 10^{-3} in fibres that had not been treated to enhance their photosensitivity. This was an order of magnitude greater than the index change induced by 248nm irradiation in the same fibre type (Malo *et al*, 1995(a)). Albert *et al*, (1995(b)) have shown that the growth rate of gratings written using a pulsed 193nm source is linearly proportional to the pulse energy density for fibres with a high germania concentration, but proportional to the square of the energy density for standard telecommunications fibres. Also, the saturated index change was greatest in the case of the standard telecommunications fibre. Albert *et al*, (1995(b)) proposed that both OPA and TPA processes could occur during 193nm irradiation and that the above results could be explained if the photoinduced changes proceeded as follows. In standard telecommunications fibres TPA occurs at the SiO_2 bandgap (10-12eV) liberating electrons from the valence to the conduction band which eventually become trapped

at other Ge defect centres. Larger absorption at 193nm in the highly doped fibre prevented enough photons being available for TPA, therefore the refractive index change proceeded via OPA in a similar way to 248nm exposure. The thermal stability of IFBGs appeared to be the same whether written at 193nm or 248nm, which implied that the gratings were essentially the same in nature (Albert *et al*, 1994).

The photosensitive mechanisms that have been described above all lead to the formation of the same type of grating, classed type I. In addition two other types of UV induced grating have been discovered. It has been demonstrated that a single UV laser pulse of sufficiently high energy can generate large refractive index changes through physical damage (Archambault *et al*, 1993). The resulting type II gratings are characterised by a surface relief pattern imprinted at the core-cladding interface on the UV exposed side, and a refractive index perturbation that does not extend uniformly across the fibre core (Archambault *et al*, 1993; Malo *et al*, 1993(a)). Archambault *et al* (1993) found that the transition from type I to type II gratings was marked by a sharp increase in the refractive index change. Doubling the pulse energy (from 20 to 40mJ) lead to a 1000 fold increase in refractive index change from 10^{-5} to 10^{-2} . Malo *et al* (1993(a)) found that the threshold energy density for type II formation was around 1Jcm^{-2} . Russell *et al* (1993) thought it likely that type II formation resulted from a two-stage TPA process. Firstly, high energy OPA absorption around 240nm excites electrons into the conduction band of silica where they seed the formation of a 'free' electron plasma. This would produce an abrupt surge in the UV absorption, resulting in physical damage.

Type II formation has also been demonstrated using 193nm laser pulses (Dyer *et al*, 1994). More recently type II gratings have been demonstrated in High-birefringence bow-tie fibres using a few shots of 240nm light with an energy density of only 0.06Jcm^{-2} (Hill *et al*, 1995). It is thought that the internal stress induced in the fibres by the bow-tie sectors is responsible for the much lower damage threshold.

The third type of IFBG that has been demonstrated is labelled type II-A (Xie *et al*, 1993(b); Niay *et al*, 1994). This is somewhat confusing since there is no evidence that it is related to the type II gratings previously discussed. It has been

known for some time that fringeless UV irradiation can be used to erase type I gratings and that following erasure a new IFBG can be fabricated at the same location (Fertain *et al* (1991). Also, that this writing and erasure cycle can be repeated several times. More recently Xie *et al* (1993(b)) found that if a type I grating was written in a fibre until it reached its maximum reflectivity continued exposure would eventually erase the IFBG. Surprisingly, it was discovered that after type I erasure further UV irradiation resulted in the growth of a new type II-A grating. Illumination by fringeless UV light also resulted in the erasure of a type I grating and type II-A formation. The saturated reflectivity of type II-A gratings was found to be higher than the initial type I gratings. An interesting feature of type I erasure and type II-A writing in elliptical core Hi-Bi fibres is that the grating reflectivity can be made highly polarisation sensitive (Niay *et al*, 1995). The greatest anisotropy was observed when the UV writing beam was linearly polarised along the slow axis. The mechanism by which type II-A growth occurs is unclear, but it is evident that a negative refractive index change is induced and it is thought that this occurs via a TPA process (Xie *et al*, 1993(b); Niay *et al*, 1994).

2.2.2 Grating spectral characteristics and thermal stability

It has been demonstrated that almost 100% reflectivity can be obtained from type I (Kashyap *et al*, 1995) and type II (Archambault *et al*, 1993) gratings. Also, from the work of Xie *et al* (1993(b)) there appears no reason why 100% reflectivity should not be achieved from type II-A gratings. The full width at half maximum (FWHM) bandwidths of type I gratings are generally $< 1\text{nm}$, and FWHM bandwidths as small as 0.01nm have been demonstrated using single pulse UV fabrication (Putnam *et al*, 1995). At the other extreme, if the IFBGs are written with a period that varies along the grating length, known as ‘chirped’ gratings, extremely large bandwidths can be obtained. Town *et al* (1995) have fabricated chirped gratings with FWHM bandwidths in excess of 140nm . Type II gratings, in comparison, generally have bandwidths of around 1nm or greater (e.g., Dong *et al*, 1993(b)).

The transmission spectra of strong type I gratings, where large refractive index modulations have been induced, are often accompanied by a pronounced short wavelength loss band. To illustrate this feature, figure 2.4 shows the transmission and loss spectrum of a strong ($\Delta n = 1.2 \times 10^{-3}$), 94% reflective grating (Limberger *et al*, 1993). The loss spectrum was obtained by subtracting the reflection spectrum from the transmission spectrum. This loss has been attributed to coupling of the back-reflected fundamental LP_{01} mode to cladding and radiation modes (Mizrahi and Sipe, 1993). In the case of type II gratings, the large and highly asymmetric refractive index profile results in particularly strong, short wavelength, radiation mode coupling on the UV exposed side of the IFBG (Archambault *et al*, 1993). A transmission and reflection spectrum obtained from a typical type II grating is shown in figure 2.5. Short wavelength loss bands will obviously be detrimental to the performance of WDM sensor arrays, and therefore should be minimised. Dong *et al* (1997) have proposed inserting a depressed cladding layer between the fibre core and the normal cladding. This will have the effect of reducing the cladding mode field strength over the core region, thereby suppressing core-cladding mode coupling.

It will also be noticed on figure 2.4 that there are some significant sideband features. This is also undesirable from the point of view of highly WDM grating arrays, as has been previously mentioned in section 2.1.2. Apodisation can be achieved using Gaussian (Albert *et al*, 1995(a)), or even more effectively, \cos^2 writing beam intensity profiles. Malo *et al* (1995(b)) have demonstrated a sideband suppression of more than 20dB using a \cos^2 writing beam profile.

There has been some confusion over the thermal stability of type I gratings. Initially, Meltz *et al* (1989) reported that IFBGs remained unaffected when heated to 500°C and held at that temperature for 18h. Later, Morey *et al* (1994) investigated the thermal stability of IFBGs over the range 370-650°C. In all cases an initial drop in the refractive index modulation was observed over the first 50-100h. At temperatures below 400°C the refractive index then stabilised and did not exhibit any significant further decay. Also, once preannealed to this temperature the IFBGs could subsequently be heated up to the annealing temperature without any further drop in

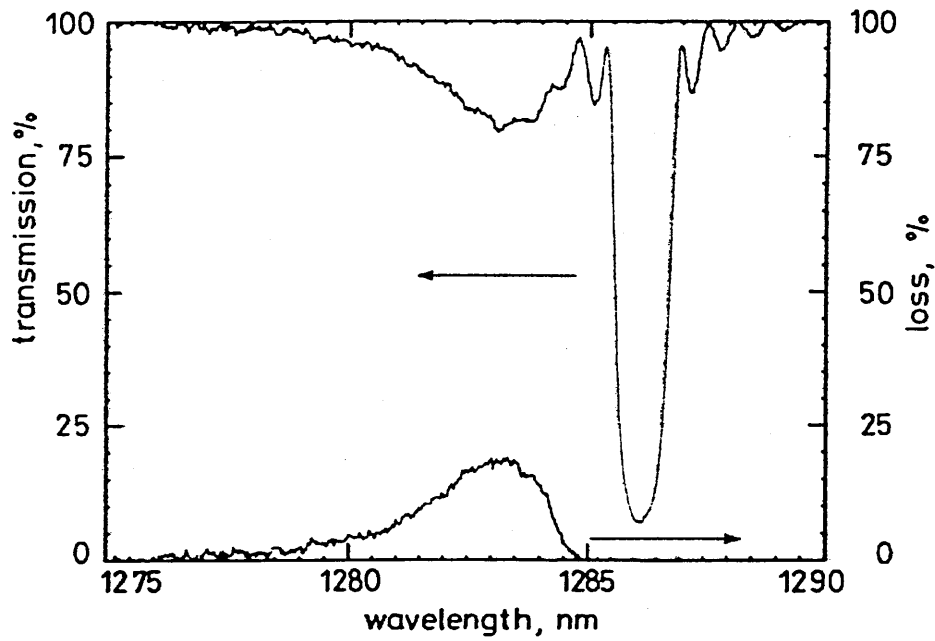


Figure 2.4 Transmission and loss spectrum of a type I grating written into a standard telecommunications fibre (reproduced from Linberger *et al*, 1993).

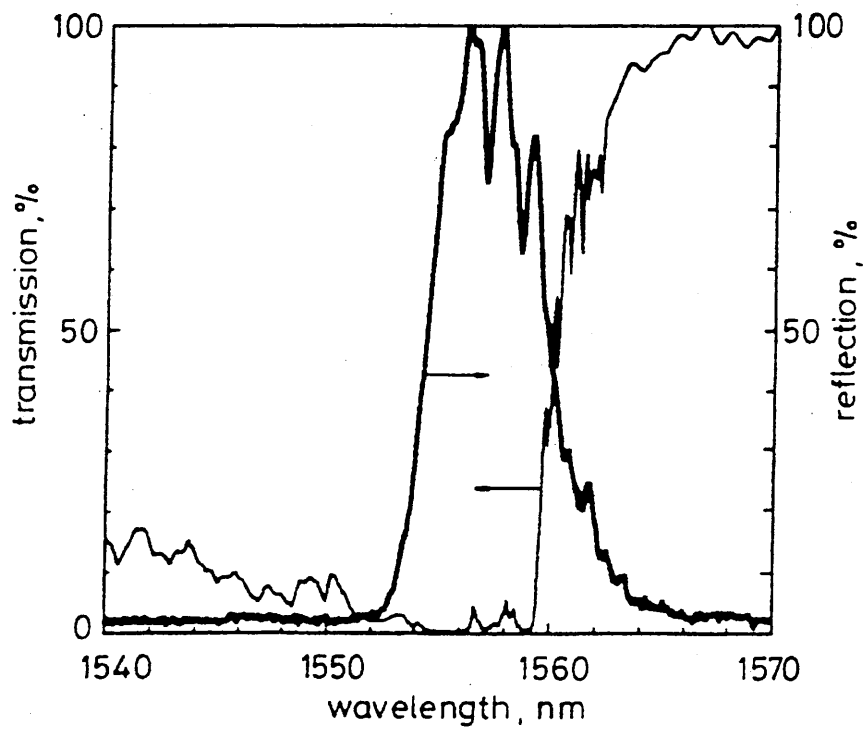


Figure 2.5 Transmission and reflection spectrum of a typical type II grating (reproduced from Archambault *et al*, 1993).

the UV induced refractive index. At temperatures approaching 650°C the photoinduced refractive index continued to decay after 100h, although at a slower rate. This result indicates that there are two components to the induced refractive index change. Morey *et al* (1994) speculated that the initial drop may be due to the annealing of colour centre traps with a low activation energy and that the more stable residual component was due, either to traps that had a much higher activation energy, or to some form of structural change. The ability to preanneal fibre gratings for operation at a particular temperature, had previously been reported by Williams *et al* (1993(b)). A theoretical extrapolation of the results from their study had indicated that gratings could be 'burnt in' for operation at 500°C and have an operational lifetime of greater than 10 years.

More recently, a detailed study has been conducted on IFBGs fabricated in both hydrogen loaded and unloaded germanosilicate fibre (Patrick *et al*, 1995). The gratings were written using both CW and pulsed sources. It was found that between room temperature and 350°C, gratings written into hydrogen loaded fibre showed significantly greater decay than similar gratings written into an unloaded fibre. The UV induced refractive index modulation in hydrogen loaded fibre was reduced by 40% after 10h at 176°C, whereas it was reduced by only 5% in unloaded fibre under the same conditions. The thermal stability of IFBGs was found to be independent of the type of source used to fabricate them, and the stability of gratings written into hydrogen loaded fibre did not depend on the magnitude of the initial refractive index modulation. It was observed that the majority of the index decay occurred over the first 10h, being particularly rapid during the first hour. Figure 2.6 shows the grating decay as a function of temperature for hydrogen loaded and unloaded fibres, written using both CW and pulsed UV sources. The IFBGs were annealed for 10h at each temperature prior to measurements being taken. It is unclear why gratings written into hydrogen loaded fibres should be less thermally stable than those written into unloaded fibre. Though Patrick *et al* (1995) thought that OH absorption centres were unlikely to be responsible, since they had a greater thermal stability than the IFBGs.

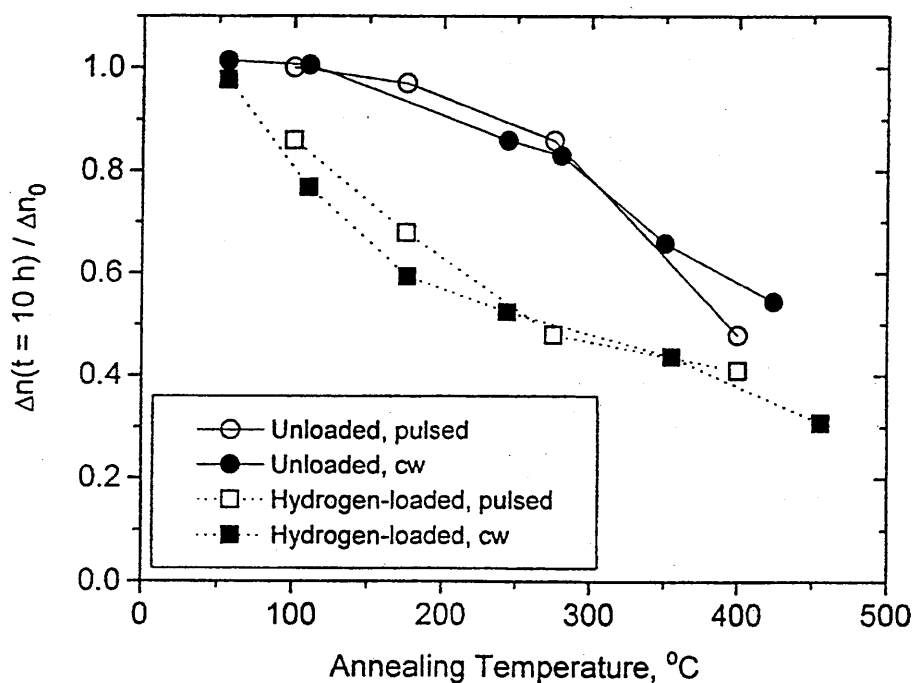


Figure 2.6 Normalised index modulation after 10 hours annealing as a function of annealing temperature (reproduced from Patrick *et al*, 1995).

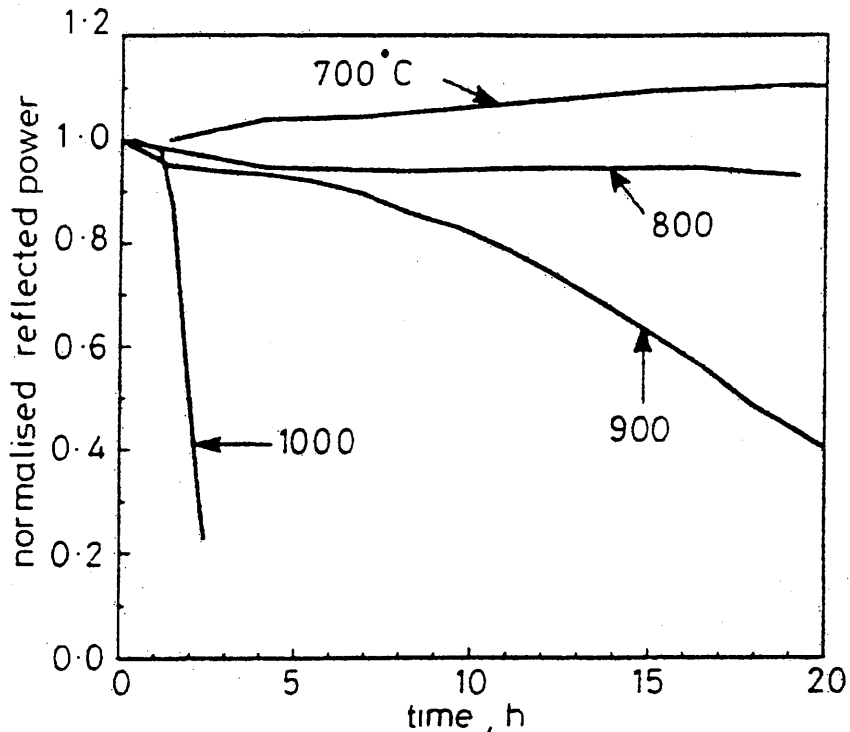


Figure 2.7 Temperature stability of type II gratings (reproduced from Archambault *et al*, 1993).

In comparison, type II gratings held at temperatures of 800°C for 24h showed no significant changes in grating characteristics (Archambault *et al*, 1993). At 900°C the gratings slowly started to decay, and at 1000°C IFBGs were nearly completely erased after 4h. The results of temperature stability tests conducted by Archambault *et al* (1993) on type II gratings are shown in figure 2.7.

It was found that the thermal stability of type II-A gratings lay somewhere between that of type I and type II gratings (Niay *et al*, 1994). Annealing started to occur at temperatures in the range 500-800°C, depending on the fibre type investigated.

2.3 Externally written gratings

2.3.1 Interferometer writing schemes

Transverse holographic writing using an external UV source (Meltz *et al*, 1989) is illustrated in figure 2.8. A two-beam interference pattern is formed on the side of an optical fibre, which has previously had its outer jacket removed at the site to be exposed. The interference pattern induces a refractive index perturbation with a periodicity equal to that of the fringe separation. The reflected Bragg wavelength λ_b being a function of the source writing wavelength λ_w and the half angle between the interfering beams θ_c , and is given by

$$\lambda_b = \frac{\lambda_w n_{eff}}{\sin \theta_c} \quad (2.24)$$

To obtain maximum fringe visibility the normal rules of interference apply (Hecht, 1987). In the case of this particular interferometer, the writing beams should be coherent, linearly polarised, of equal intensity, and the electric field vectors should be parallel. For $\theta_c > 0$ the latter condition can only be met when the writing beams are polarised orthogonal to the plane containing those beams, a point which is sometimes overlooked.

Meltz *et al* (1989) first demonstrated the transverse holographic technique using an amplitude splitting mirror interferometer, as shown in figure 2.9. The output from the UV source is divided into two beams by a beamsplitter, after which two steering mirrors redirect the beams so that they interfere at the fibre. Cylindrical lenses placed in each interferometer arm enable the interference pattern to be tightly focused to a narrow stripe at the fibre surface and thereby achieve the desired energy/power density. The interferometer can be used with low temporal coherence sources if the path lengths of each arm are carefully balanced. For sources with a poor spatial profiles, improved performance can be achieved if an additional mirror is placed in the path of the beam that is transmitted by the beamsplitter (Askins *et al*, 1992). The beams in both arms will then undergo the same number of reflections and will intersect having the same handedness. Thus interference will take place between parts of the beam with the same phase and intensity. Typically, the mirror interferometer method is used to fabricate gratings of several millimetres in length. The maximum grating length will ultimately be limited by the coherence length of the laser source.

WDM grating arrays can be readily fabricated using the mirror interferometer, since the Bragg wavelength can be controlled by varying the intersection half angle, θ_c , using the steering mirrors or by changing the writing wavelength. The sensitivity of the Bragg wavelength to small changes in writing wavelength simply being

$$\frac{d\lambda_b}{d\lambda_w} = \frac{\lambda_b}{\lambda_w} \quad (2.25)$$

One drawback of using a mirror interferometer is that, with the exception of single pulse writing (see below), a stable experimental set-up is required. For example, as little as 100nm change in one of the beam path lengths would be sufficient to wash out the interference fringes. Also, to be able to accurately set the Bragg wavelength precise control of θ_c and therefore the steering mirror angle is required (e.g., for an initial λ_b of 800nm and a λ_w of 244nm, changing θ_c by 0.5° would result in a shift in λ_b of ~ 14 nm).

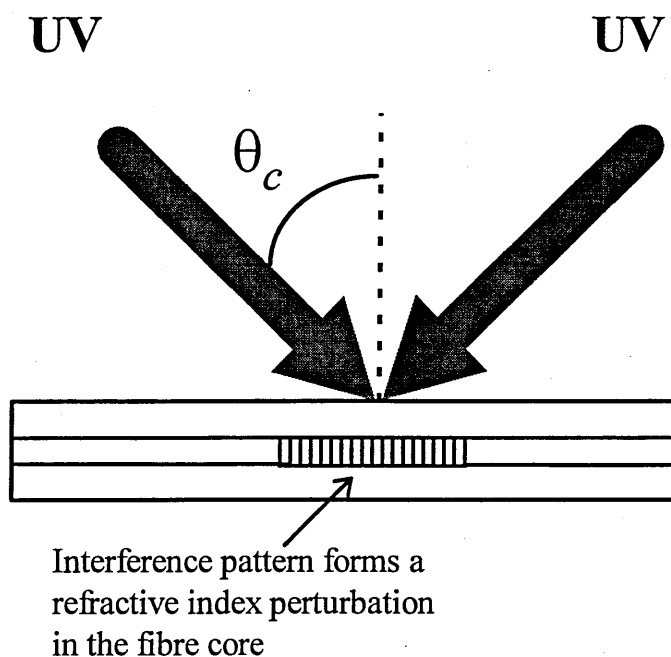


Figure 2.8 Transverse holographic writing. IFBGs written by interference of two UV beams incident at a half angle θ_c (Meltz *et al*, 1989).

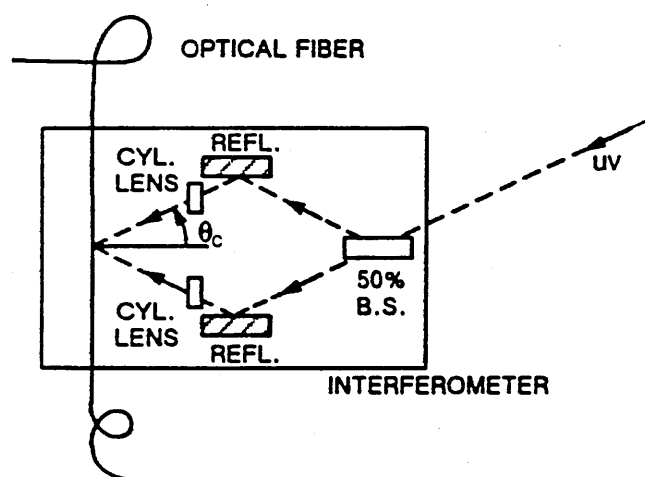


Figure 2.9 Mirror interferometer for transverse holographic writing (modified reproduction from Morey *et al*, 1989).

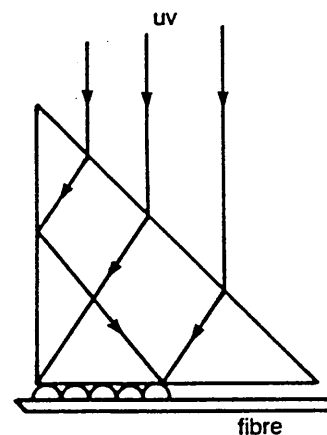


Figure 2.10 Prism interferometer for transverse holographic writing (reproduced from Kashyap *et al*, 1993).

As has already been mentioned in section 1.2.1, for IFBG technology to be widely employed gratings must be capable of mass production. This can be achieved by using single UV laser pulses to fabricate IFBGs in-line as the fibre is being pulled from a drawing tower (Dong *et al*, 1993(b); Askins *et al*, 1994). Using off-line fabrication a maximum of several gratings per hour can be written (Archambault *et al*, 1993), whereas for in-line writing the rate of production is ultimately only limited by the pulse repetition rate of the laser source and the maximum draw speed. In-line fabrication also has the advantage that IFBGs are written before the protective buffer coat is applied. In contrast off-line writing requires the local removal of the buffer coat, with a resultant degradation in the fibre strength.

The mirror interferometer is well suited to in-line fabrication, since none of the optical elements need to be in close contact with the fibre, and for single pulse writing the stability of the interferometer will not be an issue. Indeed Askins *et al* (1994) have demonstrated in-line fabrication of large WDM grating arrays using a mirror interferometer. The wavelength spacing between gratings was achieved by high resolution computer control of the steering mirror angles.

An alternative interferometer configuration is shown in figure 2.10 (Kashyap *et al*, 1990). In this writing scheme, the UV beam is directed through the hypotenuse face of a right-angle prism toward the apex in such a way that only half the beam is incident at the back face of the prism. The other half undergoes a reflection from the side face and is directed to interfere with the rest of the beam at the back face. A single cylindrical lens is used to bring the beam to a line focus at the fibre. The advantage of this configuration is that it is highly stable and can be used to fabricate IFBGs over long exposure times. Kashyap (1994) reported that IFBGs had been written with exposure times of over 8h using this interferometer. The technique suffers from the drawback that a source with reasonable temporal and spatial coherence is required, since there will be a path length imbalance between the two halves of the beam and, due to the reflection at the side face, the two halves will be of opposite handiness. Another disadvantage with the right angle prism reported by Kashyap *et al* (1990), is that it has to be placed in close proximity to the fibre so it is

unsuitable for on-line fabrication of IFBGs. Though this limitation may be overcome if a modified version of the interferometer, based upon a 'rooftop' prism, is utilised (Zhang *et al*, 1994). Finally, as with the mirror interferometer careful angular alignment is required to fabricate gratings with the desired Bragg wavelength.

2.3.2 Phase mask techniques

The fabrication of IFBGs using phase mask techniques has also been demonstrated (Hill *et al*, 1993; Anderson *et al*, 1993; Kashyap *et al*, 1993(a)). These phase masks are diffraction gratings which consist of a periodic surface-relief structure fabricated onto a UV grade fused-silica flat. The surface relief pattern approximates to a square wave in profile as shown in figure 2.11. The amplitude of the surface relief pattern is chosen so that the zero-order diffraction is nulled at the design wavelength and the power in the ± 1 orders are maximised. This is achieved by introducing a π phase modulation into the transmitted UV beam which leads to destructive interference of the undiffracted light. The amplitude of the surface-relief pattern d that is required to meet this condition can be obtained from (Hill *et al*, 1993)

$$d = \frac{\lambda_d}{4\pi(n_s - 1)} \quad (2.26)$$

where λ_d is the design wavelength for the phase mask, and n_s is the refractive index of fused-silica (commercially available Lasiris phase masks suppress the zero order to less than 5% and the ± 1 orders typically contain more than 35% of the diffracted light).

In the near-field phase mask technique (Hill *et al*, 1993; Anderson *et al*, 1993), shown in figure 2.11, the phase mask is placed in near contact with the optical fibre and an IFBG is written by interference of the first order beams. Again a cylindrical lens placed behind the phase mask is used to bring the writing beam to a sharp line focus on the fibre. The Bragg wavelength at which the grating is fabricated can easily be determined as follows. From the grating equation (Hecht, 1987), the half angle between the ± 1 orders θ_p is given by

$$\theta_p = \sin^{-1} \left(\frac{\lambda_w}{\Lambda_{pm}} \right) \quad (2.27)$$

where Λ_{pm} is the phase mask period. Given that θ_p is equivalent to θ_c in equation 2.24, substituting equation 2.27 into equation 2.24 reveals that λ_b is simply related to Λ_{pm} by

$$\lambda_b = n_{eff} \Lambda_{pm} \quad (2.28)$$

Thus the Bragg wavelength is independent of the source wavelength, which opens up the possibility of fabricating IFBGs with broadband sources.

The near-field phase technique relaxes both the temporal and spatial coherence requirements of the source and, since it is highly stable and is insensitive to translations in the writing beam, it is ideal for situations where consistent IFBG characteristics are required. Scanning the writing beam across the phase mask allows the creation of long gratings. Loh *et al* (1995) have fabricated 10cm long gratings using this method.

It is evident from equation 2.28 that in order to fabricate WDM grating arrays each IFBG would require its own phase mask. For large, highly multiplexed arrays this would be both impractical and expensive. Although limited tuning of a few nm can be achieved by: prestraining the fibre prior to exposure (Zhang *et al*, 1994), slowly scanning either the phase mask or the fibre (Cole *et al*, 1995), magnifying the phase mask periodicity using a lens (Prohaska *et al*, 1993) and tilting the phase mask relative to the fibre (Othonos and Lee, 1995). The latter two techniques require a source that has good spatial coherence, since there is some displacement between the fibre and the phase mask.

Another drawback with the near-field phase mask method is that, in common with the right angle prism interferometer, it is unsuitable for in-line writing due to the close proximity of the phase mask to the fibre. An alternative far-field phase mask technique has been demonstrated that removes this limitation and is illustrated in figure 2.12 (Kashyap *et al*, 1993(a)). In this configuration the ± 1 order beams are internally reflected within a rectangular prism before being recombined at the fibre.

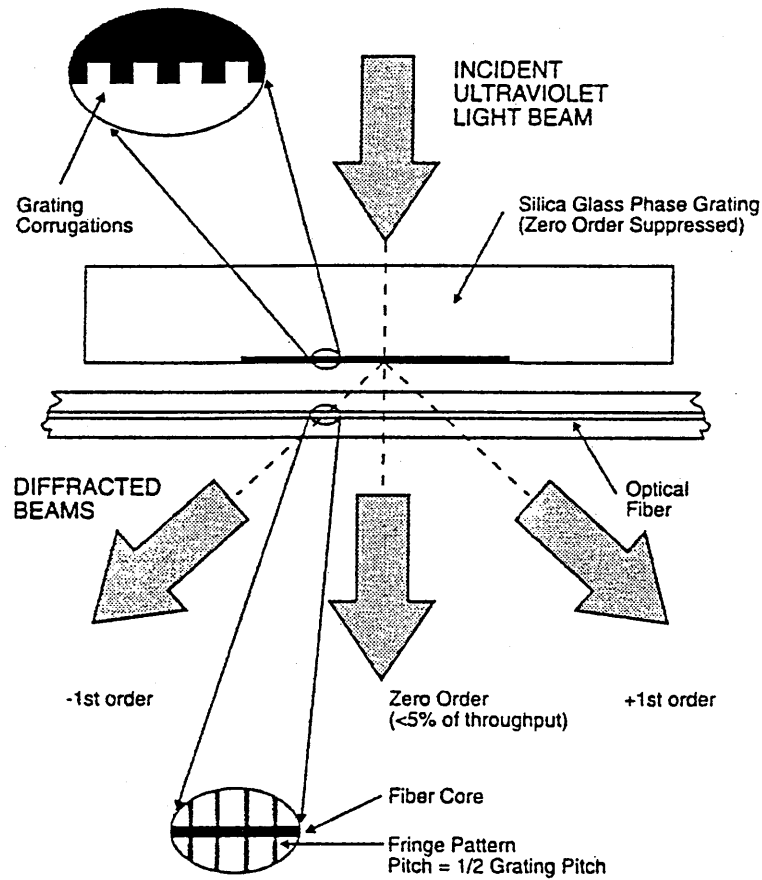


Figure 2.11 Near-field phase mask technique (reproduced from Hill *et al*, 1993).

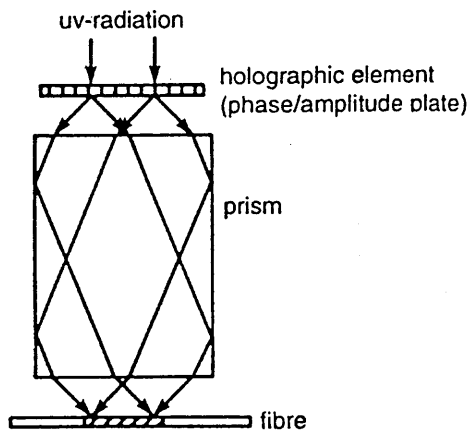


Figure 2.12 Far-field phase mask technique (reproduced from Kashyap *et al*, 1993(a)).

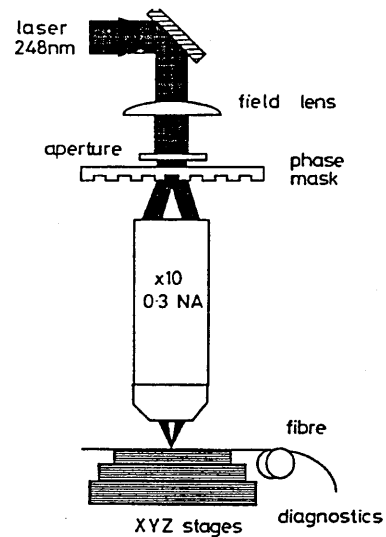


Figure 2.13 Image projection of a phase mask (reproduced from Rizvi *et al*, 1995).

This non-contact method also has the advantage that any residual zero-order transmission may be blocked, preventing any unwanted interference between the zero and first orders.

Any of the writing schemes discussed in this and the proceeding section can be used to fabricate all three grating types. Though care is required when fabricating type II gratings using the near-field phase mask or prism interferometer techniques, so as not to cause damage by focusing an unduly high energy density at the optical surface nearest the fibre.

2.3.3 Other external fabrication techniques

Although the majority of the gratings reported in the literature have been fabricated using one of the above methods, other external writing techniques have been demonstrated. An image projection system in combination with a transmission mask has been used to photoimprint gratings into optical fibres (Mihailov and Gower, 1994). Though due to the resolution limit of the system, it was not possible to write gratings with a sufficiently small period to obtain first-order Bragg reflection at telecommunications wavelengths. More recently Rizvi *et al* (1995) have demonstrated a more advanced system, in which the transmission mask was replaced by a phase mask, and this arrangement is shown in figure 2.13. Using this system it was possible to fabricate a type II grating with a first order Bragg reflection at 1530nm. The main advantage of the image projection technique being the reduction of the energy density at the phase mask and the consequent reduction in the risk of any radiation induced damage. However, as with the phase mask techniques discussed above, this writing scheme is limited to producing IFBGs with a fixed Bragg wavelength determined by the phase mask or transmission mask period.

A 'point-by-point' fabrication technique has been demonstrated by Malo *et al* (1993(b)). In this method the fibre is exposed to a beam of collimated light that has passed through a narrow slit. An IFBG is built up by indexing the fibre by small amounts using high resolution translation stages, after each step a small section of the

fibre is exposed. Although it was not possible to fabricate gratings with first-order Bragg reflections at 1550nm or less, strong second and third order Bragg reflections at these wavelengths have been achieved. The main advantage of the point-by-point method is its flexibility. The period of the grating is easily controlled and grating structures that have chirped periods or apodised profiles are possible. However, the technique was limited to inducing type II photosensitivity from single laser pulses in order to obtain sufficiently sharply defined features. Also, it is apparent that this scheme would not be suitable for in-line fabrication.

2.3.4 UV laser sources for grating fabrication

IFBGs are typically written using power densities of the order of 1Wcm^{-2} at around 240nm. To obtain such a power density over the several millimetre lengths typical for IFBGs necessitates the use of laser sources. Table 2.1 summarises the parameters of commercially available UV laser sources that have been shown to be suitable for grating fabrication. The three most popular types of laser being: pulsed tuneable dye laser systems (Meltz *et al*, 1989), line-narrowed excimer lasers (e.g., Archambault *et al*, 1993), and intra-cavity doubled argon-ion lasers (Kashyap *et al*, 1990). Solid state sources, such as frequency quadrupled neodymium lasers, are not commonly used, since their output wavelengths approach the long wavelength limit of the GeO defect band. Nonetheless, grating writing at 262nm (Armitage, 1993) and 266nm (e.g., Painchaud *et al*, 1995) using neodymium lasers has been demonstrated.

When assessing laser sources for IFBG fabrication the ultimate aim of in-line mass production should be born in mind. To date, only the line-narrowed KrF excimer laser has been used as a source for in-line writing (Dong *et al*, 1993(b)), although there is no reason to suppose that ArF excimer lasers and high power quadrupled Nd:YAG lasers would not also be suitable. Indeed, ArF excimer lasers would have the advantage of the enhanced photosensitivity demonstrated at 193nm (Albert *et al*, 1994). The main drawback of excimer lasers is their poor spatial coherence, although it has been shown that this can be substantially improved using

Laser type	Pulsed/CW	Wavelength (nm)	Average laser power/pulse energy*	Coherence length*	Comments
Excimer (KrF)	Pulsed	248	100mJ	~2.5cm (line-narrowed)	Generally poor spatial coherence, but this can be improved using phase conjugate optics
Excimer (ArF)	Pulsed	193	Estimated to be ~40mJ	~2.5cm (line-narrowed)	As KrF except benefits from enhanced photosensitivity at 193nm
Solid State (Nd:YAG)	Pulsed	266	35mJ	~ 1m (injection seeded)	Writing efficiency is lower at these wavelengths and therefore is not widely used
Pulsed tuneable dye	Pulsed	230-255	1mJ	~10cm	Only wavelength tuneable source in common use, but requires additional pump laser and low pulse energies make in-line writing impractical
Doubled Ar ⁺	CW	244/257	100mW	several metres	Excellent coherence, ideal for fabricating long gratings, but cannot be used for in-line writing

Table 2.1 Laser sources for IFBG fabrication

* The parameters are taken from the references quoted in the text, and are typical of the laser type. The exception being the solid state sources where, due to their comparatively rare use and large range of possible parameters, the quoted values are for an injection seeded Continuum (NY61-30) Nd:YAG laser with a fourth harmonic generation option. This laser was chosen because it's performance is fairly typical of that available from mid-range, laboratory, flashlamp pumped Nd:YAG lasers.

phase conjugate optics (Putnam *et al*, 1995). Frequency doubled argon-ion lasers, have excellent coherence properties, but they are limited to CW operation and can only be used for off-line fabrication.

Pulsed tuneable dye laser sources offer the ability to control the Bragg wavelength of an IFBG by varying the writing wavelength. Using equation 2.27 it can be easily shown that a laser with a 25nm tuneable range (as in the case of the laser used by Meltz *et al* (1989)) would allow the Bragg wavelength to be varied by greater than 80nm in the region of 800nm and by more than 150nm around 1550nm. This enables precise and broadband control over the Bragg wavelength without the requirement for high accuracy in setting the beam intersection angle, and so alignment is eased. Unfortunately the low pulse energies available from dye lasers makes in-line fabrication impractical. Nonetheless, for off-line, multi-pulse fabrication of WDM grating arrays in hydrogen loaded fibres, wavelength tuning of a pulsed dye laser provides an elegant way of controlling the Bragg wavelength.

To summarise, although the fabrication of in-line WDM gratings can be achieved using a KrF excimer laser in combination with an automated mirror interferometer (Askins *et al*, 1994), a pulsed tuneable laser with high spatial coherence, high pulse energy and large tuning range would make an ideal UV source.

2.4 Grating applications

The purpose of this section is to give an impression of the range of applications to which IFBG technology can be applied, but it is by no means a comprehensive review. Although in this thesis IFBGs are considered from the point of view of their application as strain and temperature sensors, it should be realised that gratings have a whole host of potential applications in the telecommunications industry.

IFBGs have been used as external cavities for semiconductor lasers. Morey *et al* (1990) demonstrated how a fibre containing a grating could be spliced onto a commercial AlGaAs diode laser. This provided narrow-line operation, and the laser

could be stepped from one laser mode to the next by strain or temperature tuning of the grating's Bragg wavelength. The IFBG may also be used as the cavity mirror itself, and narrow-line wavelength selectable lasers incorporating IFBG reflectors have been demonstrated (Bird *et al*, 1991). A simple schematic diagram of this latter type of laser source is shown in figure 2.14.

Rare-earth doped fibre lasers incorporating IFBG reflectors have been fabricated, providing a rugged, compact and tunable fibre laser source. The gratings can either be written into fibres spliced to the rare-earth doped fibre, or directly into the doped fibre itself. Kashyap *et al* (1990) first demonstrated the use of a single grating reflector in an erbium doped fibre. This was closely followed by the demonstration of a neodymium fibre laser with two IFBG reflectors (Ball *et al*, 1990), and this arrangement is shown in figure 2.15.

Dispersion in optical fibres may be compensated for by using a wavelength chirped IFBG (Ouellete, 1987), as shown in figure 2.16. This method induces a wavelength dependent propagation delay to compensate for dispersion with each wavelength in the incident optical pulse being reflected at a different point along the grating length.

If an IFBG is fabricated so that its grating planes are tilted with respect to the fibre axis normal, the waveguiding conditions of the fibre can be overcome and light will be coupled out of the side into radiation modes. Such blazed gratings can be used as wavelength selective taps (Meltz *et al*, 1990). Blazed gratings are written by inclining the UV writing beams relative to the fibre as shown in figure 2.17. These grating taps allow non-invasive monitoring of fibre networks and can also be used to couple light into fibres.

Bandpass filters for WDM optical systems can be fabricated by introducing a phase shift into the periodic structure of an IFBG (Agrawal *et al*, 1994). The phase shift introduces a narrow transmission window into the grating reflection spectrum. However, these are not true channel dropping filters as the stop-band is back-reflected. A band-pass filter based upon IFBGs that does not have this limitation was demonstrated by Morey (1991). This device consisted of two identical gratings

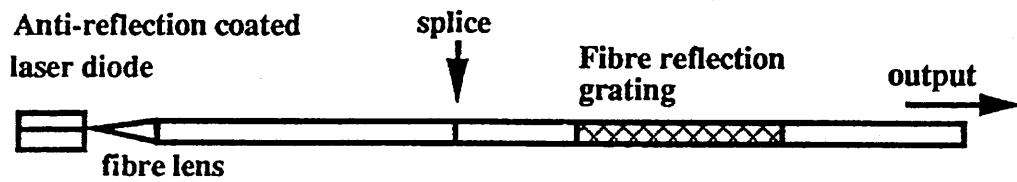


Figure 2.14 External fibre grating semiconductor laser (reproduced from Kashyap, 1994).

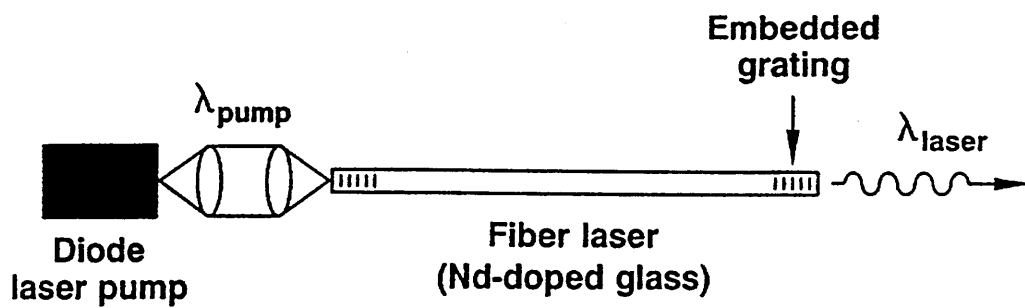


Figure 2.15 Neodymium fibre laser (reproduced from Ball and Morey, 1991).

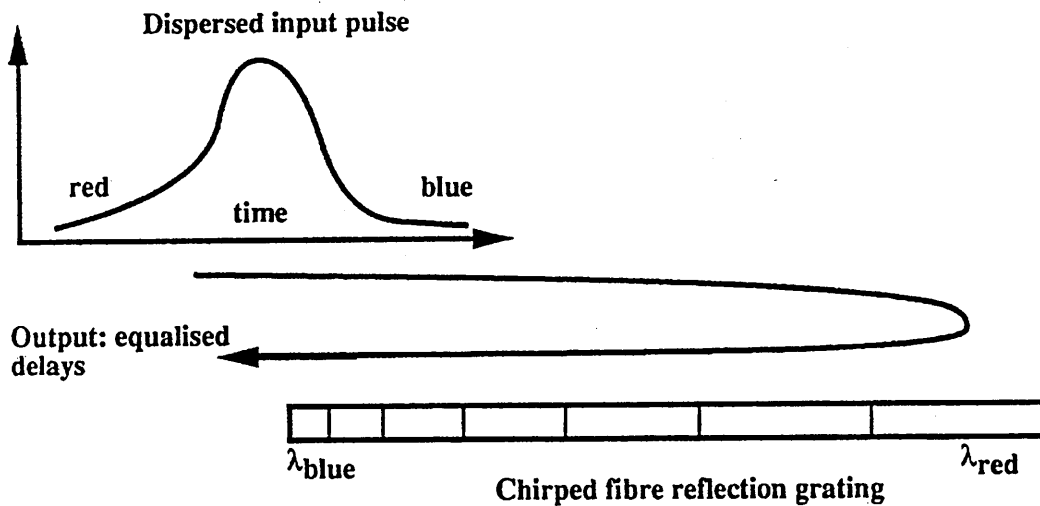


Figure 2.16 Chirped reflection for dispersion compensation (reproduced from Kashyap, 1994).

written into the two output arms of a 50:50 coupler, forming a Michelson interferometer. If the system is configured so that reflected light from the IFBGs arrives back at the coupler with a $\pi/2$ phase difference, then all the light in the narrow reflection band will be directed out of the second input port. In practice it is difficult to fabricate the gratings at the correct locations to obtain this precise phase relationship and the fibre based system is prone to environmental disturbances. To overcome these drawbacks, a more recent design utilised a planar waveguide Mach-Zehnder interferometer as shown in figure 2.18 (Kashyap *et al*, 1993(c)). The path lengths of the Mach-Zehnder could be precisely balanced by using a UV laser source to induce a local refractive index change in each arm of the interferometer.

As sensors, IFBGs can be used to transduce a range of other measurands in addition to temperature and strain. Vibration (Melle *et al*, 1992) and pressure sensing (Xu *et al*, 1993) have been demonstrated. Also strong a.c. magnetic fields have been measured by monitoring the effect that magnetically induced circular birefringence has on the grating reflection spectrum (Kersey and Marrone, 1994). However, this effect is weak and the technique is limited to strong magnetic fields, since it relies on the Faraday effect and the inherent Verdet constant of silica is small. Morey *et al* (1989) suggested that specialised fibre coatings could be used to convert measurands that cannot be directly measured into strain fields. Finally, pairs of gratings can be used to form Fabry-Pérot interferometers (Morey *et al*, 1989), which would allow higher resolution sensing, due to the narrow Fabry-Pérot passband.

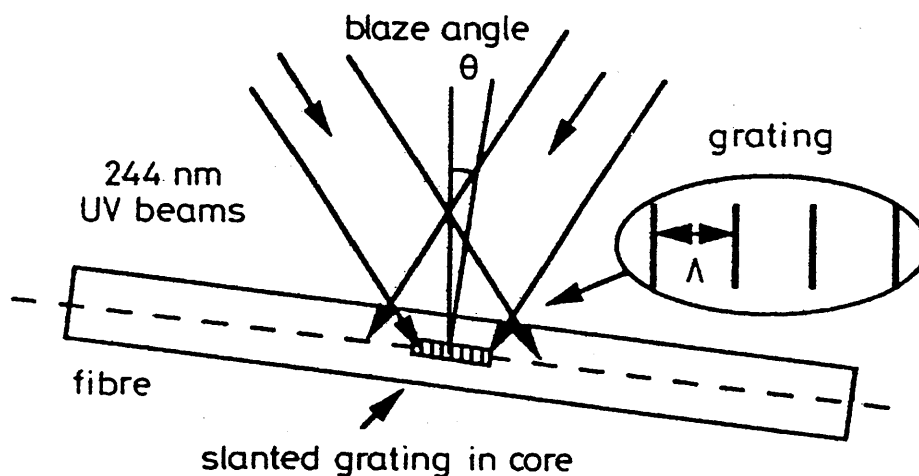


Figure 2.17 Schematic diagram of a tilted (blazed) grating writing scheme (reproduced from Kashyap *et al*, 1993(b)).

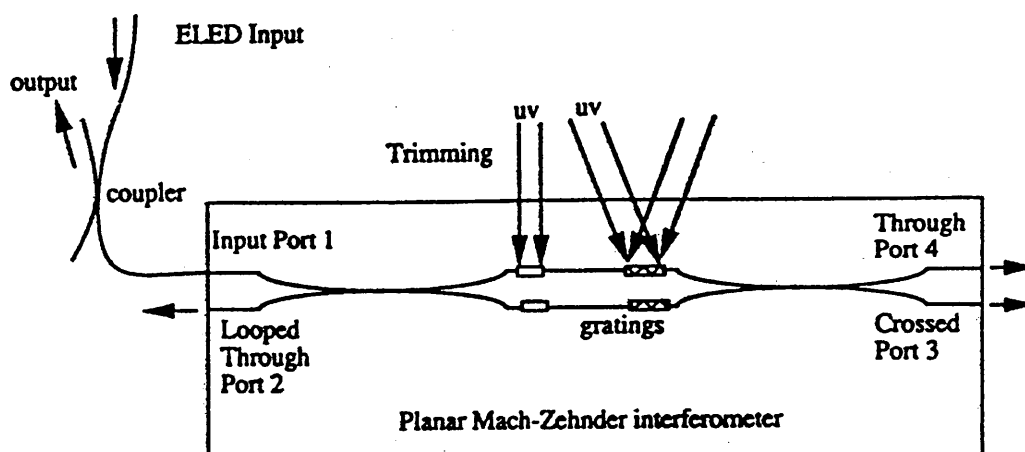


Figure 2.18 Experimental arrangement for the UV exposure of the arms of a Mach-Zehnder interferometer. The positions of the gratings and the trimming regions are shown (reproduced from Kashyap *et al*, 1993(c)).

2.5 Related photoinduced mode coupling devices

In addition to IFBGs, other closely related mode coupling devices can be photoinduced in germanosilicate optical fibres.

It has been shown that light propagating along one axis of a singlemode Hi-Bi fibre can be efficiently coupled to the orthogonal axis at a specific wavelength, if a periodic birefringence is introduced (Stolen *et al*, 1984). The coupling condition being met when the grating period is equal to the beat length of the fibre at the desired wavelength. Such polarisation mode couplers are often termed 'rocking filters', since the polarisation state is gently rocked to and fro as it passes through the periodic birefringent grating. As mentioned in section 2.2.1, birefringence can be photoinduced into germanosilicate fibres using either visible (Parent *et al*, 1985) or UV radiation (Hill *et al*, 1991(b)). Russell and Hand (1990) used an internal writing technique to fabricate rocking filters into elliptical core fibres, in which light from an argon-ion laser was launched at 45° to the fibre's principal axes. Though, as with IFBGs written using this method, the resonant wavelength of the filter is limited to the writing wavelength and the birefringent grating is written along the entire fibre length. These limitations can be overcome by using an external point-by-point writing technique, where a UV beam is incident on the fibre at 45° to the birefringent axes (Hill *et al*, 1991). The period of the birefringent grating can then be tailored to match the beat length of the fibre at the desired wavelength. Using the point-by-point method Kanellopoulos *et al* (1995) fabricated a 25cm rocking filter with a 3mm grating period (85 coupling points) in an elliptical core fibre. The filter had a peak coupling efficiency of 5% and a full-width bandwidth of 14nm centred around 798nm. Rocking filters can be used for strain and temperature sensing and, interestingly, although the strain sensitivity of a rocking filter's resonant wavelength is within an order of magnitude of an IFBG's its temperature sensitivity is two orders of magnitude greater (Kanellopoulos *et al*, 1993; Kanellopoulos *et al*, 1995).

Efficient two-mode couplers have been fabricated that offer wavelength selective coupling of the fundamental LP_{01} mode to LP_{11} (or LP_{02}) modes. If light

from an argon-ion laser is launched into an elliptical core fibre that is bimodal at that wavelength, spatial mode beating leads to the formation of a two-lobe pattern, as shown in figure 2.19 (Park and Kim, 1989). Given a sufficiently high laser intensity, a refractive index perturbation with the same periodicity as the modal beat length will be induced. Again an external UV point-by-point technique may be used to fabricate a localised grating that has a coupling wavelength independent of the writing wavelength (Hill, *et al*, 1990). For LP₀₁ to LP₁₁ mode coupling the grating has to be written at a blaze angle, so that the transverse refractive index variation approximates to the alternating two-lobe intensity pattern produced by spatial mode beating. If the correct blaze angle is not set sufficiently accurately the coupling efficiency will be poor. Hill *et al* (1990) fabricated a two-mode coupler using the point-by-point method, which demonstrated a complex spectral response over a 100nm bandwidth, centred around 835nm. Internal and external writing techniques have also been used to create LP₀₁ to LP₀₂ mode couplers, which have the advantage of a simpler, more highly selective spectral response (Bilodeau *et al*, 1991). The use of two-mode couplers for strain and temperature sensing applications has been demonstrated, in which the measurands are transduced by monitoring the far-field intensity changes in the two-lobe pattern (e.g., Vensarkar *et al*, 1991; Vensarkar *et al*, 1994).

Recently a new type of photosensitive device has been reported, the long-period in-fibre grating (LPG) (Vensarkar *et al*, 1996). These act as band rejection filters, in which light propagating in the fundamental mode is coupled to forward propagating cladding modes at phase matched wavelengths. To achieve phase matching a grating period of several hundred microns is required. The gratings were fabricated by external UV exposure through an amplitude mask, and using this method Vensarkar *et al* (1996) have demonstrated a 2.5cm long LPG with a maximum loss of 32dB at 1550nm and a 22nm FWHM. The temperature sensitivity and strain sensitivity of these devices depends heavily on the fibre type, but are generally within an order of magnitude of IFBGs (Vensarkar *et al*, 1996; Patrick *et al*, 1996).

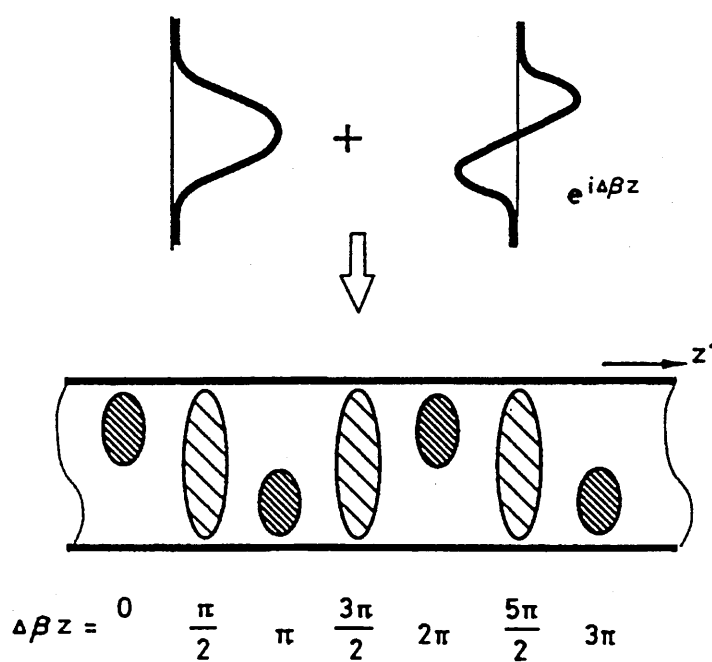


Figure 2.19 Two-lobe pattern formed by spatial mode beating of the $\overline{\text{LP}}_{01}$ and LP_{11} modes (reproduced from Park and Kim, 1989).

One limitation all the above devices share, when compared to IFBGs, is that, since in each case coupling takes place between forward propagating modes, they cannot by themselves be used in sensor applications where optical access is restricted to a single fibre end.

References

- Agrawal, G.P., and Radic, S., 'Phase-shifted fiber Bragg gratings and their application for wavelength demultiplexing', *IEEE Photon. Technol. Lett.*, **6**, pp995-997 (1994).
- Albert, J., Malo, B., Bilodeau, F., Johnson, D.C., Hill, K.O., Hibino, Y., and Kawachi, M., 'Photosensitivity in Ge-doped silica optical waveguides and fibers with 193nm light from an ArF excimer laser', *Opt. Lett.*, **19**, pp387-389 (1994).
- Albert, J., Hill, K.O., Malo, B., Thériault, S., Bilodeau, F., Johnson, D.C., and Erickson, L.E. (a), 'Apodisation of the spectral response of fibre Bragg gratings using a phase mask with variable diffraction efficiency', *Electron. Lett.*, **31**, pp222-223 (1995).
- Albert, J., Malo, B., Hill, K.O., Bilodeau, F., Johnson, D.C., and Thériault S. (b), 'Comparison of one-photon and two-photon effects in the photosensitivity of germanium-doped silica optical fibers exposed to intense ArF excimer pulses', *Appl. Phys. Lett.*, **67**, pp3529-3531 (1995).
- Anderson, D.Z., Mizrahi, V., Erdogan, T., and White, A.E., 'Production of in-fibre gratings using a diffractive optical element', *Electron. Lett.*, **29**, pp566-568 (1993).
- Archambault, J.-L., Reekie, L., and Russell, P.St.J., '100% reflectivity Bragg reflectors produced in optical fibres by single excimer laser pulses', *Electron. Lett.*, **29**, pp453-454 (1993).

- Armitage, J.R., 'Fibre Bragg grating reflectors written at 262nm using a frequency quadrupled diode-pumped Nd^{3+} :YLF laser', *Electron. Lett.*, **29**, pp1181-1183 (1993).
- Askins, C.G., Tsai, T.-E., Williams, G.M., Putnam, M.A., Bashkansky, and Friebele, E.J., 'Fibre Bragg reflectors prepared by a single excimer pulse', *Opt. Lett.*, **17**, pp833-835 (1992).
- Askins, C.G., Putnam, M.A., Williams, G.M., and Friebele, E.J., 'Stepped-wavelength optical-fiber Bragg grating arrays fabricated in line on a draw tower', *Opt. Lett.*, **19**, pp147-149 (1994).
- Asobe, M., Ohara, T., Yokohama, I., and Kaino, T., 'Fabrication of Bragg grating in chalcogenide glass fibre using the transverse holographic method', *Electron. Lett.*, **32**, pp1611-1613 (1996).
- Atkins, R.M., and Mizrahi, V., 'Observation of changes in UV absorption bands of singlemode germanosilicate core optical fibres on writing and thermally erasing refractive index gratings', *Electron. Lett.*, **28**, pp1743-1744 (1992).
- Atkins, R.M., Mizrahi, V., and Erdogan, T. (a), '248nm induced vacuum UV spectral changes in optical fibre preform cores: support for a colour centre model of photosensitivity', *Electron. Lett.*, **29**, pp385-387 (1993).
- Atkins, R.M., Lemaire, P.J., Erdogan, T., and Mizrahi, V. (b), 'Mechanisms of enhanced UV photosensitivity via hydrogen loading in germanosilicate glasses', *Electron. Lett.*, **29**, pp1234-1235 (1993).
- Ball, G.A., Morey, W.W., and Waters, J.P., ' Nd^{3+} fibre laser utilising intra-core Bragg reflectors', *Electron. Lett.*, **26**, pp1829-1830 (1990).
- Ball, G.A., and Morey, W.W., 'Efficient integrated Nd^{3+} fiber laser', *IEEE Photon. Technol. Lett.*, **3**, pp1077-1078 (1991).
- Bardal, S., Kamal, A., and Russell, P.St.J., 'Photoinduced birefringence in optical fibers: a comparative study of low-birefringence and high-birefringence fibers', *Opt. Lett.*, **17**, pp411-413 (1992).
- Bernardin, J.P., and Lawandy, N.M., 'Dynamics of the formation of Bragg gratings in germanosilicate optical fibers', *Opt. Commun.*, **79**, pp194-199 (1990).

- Bilodeau, F., Hill, K.O., Malo, B., Johnson, D.C., Skinner, I.M., 'Efficient, narrowband $LP_{01} \leftrightarrow LP_{02}$ mode convertors fabricated in photosensitive fibre: spectral response', *Electron. Lett.*, **27**, pp682-684 (1991).
- Bilodeau, F., Malo, B., Albert, J., Johnson, D.C., Hill, K.O., Hibino, Y., Abe, M., and Kawachi, M., 'Photosensitisation of optical fiber and silica-on-silicon/silica waveguides', *Opt. Lett.*, **18**, pp953-955 (1993).
- Bird, D.M., Armitage, J.R., Kashyap, R., Fatah, R.M.A., Cameron, K.H., 'Narrow line semiconductor laser using fibre grating', *Electron. Lett.*, **27**, pp1115-1116 (1991).
- Broer, M.M., Cone, R.L., and Simpson J.R., 'Ultraviolet-induced distributed-feedback gratings in Ce^{3+} -doped silica optical fibers', *Opt. Lett.*, **16**, pp1391-1393 (1991).
- Cambell, R.J., and Kashyap, R., 'The properties and applications of photosensitive germanosilicate fibre', *International J. of Optoelectronics*, **9**, pp33-57 (1993).
- Camlibel, I., Pinnow, D.A., and Darby, F.W., 'Optical ageing characteristics of borosilicate clad fused silica core fiber optical waveguides', *Appl. Phys. Lett.*, **26**, pp185-187 (1975).
- Cole, M.J., Loh, W.H., Laming, R.I., Zervas, M.N., and Barcelos, S., 'Moving fibre/phase mask-scanning beam technique for enhanced flexibility in producing fibre gratings with uniform phase mask', *Electron. Lett.*, **31**, pp1488-1490 (1995).
- Dong, L., Archambault, J.-L., Reekie, L., Russell, P.St.J., and Payne, D.N. (a), 'Bragg gratings in Ce^{3+} -doped fibers written by a single excimer pulse', *Opt. Lett.*, **18**, pp861-863 (1993).
- Dong, L., Archambault, J.-L., Reekie, L., Russell, P.St.J., and Payne, D.N. (b), 'Single pulse Bragg gratings written during fibre drawing', *Electron. Lett.*, **29**, pp1577-1578 (1993).
- Dong, L., Archambault, L., Reekie, L., Russell, P.St.J., and Payne, D.N., 'Photoinduced absorption change in germanosilicate preforms: evidence for the color-center model of photosensitivity', *Appl. Opt.*, **34**, pp3436-3440 (1995).

- Dong, L., Reekie, L., Cruz, J.L., Caplen, J.E., de Sandro, J.P., and Payne, D.N., 'Optical fibers with depressed claddings for suppression of coupling into cladding modes in fiber Bragg gratings', *IEEE Photon. Technol. Lett.*, **9**, pp64-66 (1997).
- Dyer, P.E., Farley, R.J., Giedl, R., Byron, K.C., and Reid, D., 'High reflectivity fibre gratings produced by incubated damage using a 193nm ArF laser', *Electron. Lett.*, **30**, pp860-862 (1994).
- Fertein, E., Legoubin, S., Douay, M., Canon, S., Bernage, P., Niay, P., 'Shifts in resonance wavelengths of Bragg gratings during writing or bleaching experiments by UV illumination within germanosilicate optical fibre', *Electron. Lett.*, **27**, pp1838-1839 (1991).
- Gloge, D., 'Weakly guiding fibres', *Appl. Opt.*, **10**, pp2252-2258 (1971).
- Hand, D.P., and Russell, P.St.J., 'Photoinduced refractive-index changes in germanosilicate fibers', *Opt. Lett.*, **15**, pp102-104 (1990).
- Hecht, E., 'Optics', Addison-Wesley Publishing Company, Inc. (1987).
- Hill, K.O., Fujii, Y., Johnson, D.C., and Kawasaki, B.S., 'Photosensitivity in optical fiber waveguides: Application to reflection filter fabrication', *Appl. Phys. Lett.*, **32**, pp647-649 (1978).
- Hill, K.O., Malo, B., Vineberg, K.A., Bilodeau, F., Johnson, D.C., and Skinner, I., 'Efficient mode conversion in telecommunications fibre using externally written gratings', *Electron. Lett.*, **26**, pp1270-1272 (1990).
- Hill, K.O., Malo, B., Bilodeau, F., Johnson, D.C., Morse, T.F., Kilian, A., Reinhart, L., and Kyunghwan, Oh (a), 'Photosensitivity in $\text{Eu}^{2+}:\text{Al}_2\text{O}_3$ -doped-core fibre: preliminary results and application to mode convertors', in *Proc. Optical Fibre Communication Conference, OFC'91*, pp14-17, February 1991.
- Hill, K.O., Bilodeau, F., Malo, B., Johnson, D.C. (b), 'Birefringent photosensitivity in monomode optical fibre: application to external writing of rocking filters', *Electron. Lett.*, **27**, pp1548-1550 (1991).

- Hill, K.O., Malo, B., Bilodeau, F., Johnson, D.C., and Albert, J., 'Bragg gratings fabricated in monomode photosensitive optical fiber by UV exposure through a phase mask', *Appl. Phys. Lett.*, **62**, pp1035-1037 (1993).
- Hill, P.C., Atkins, G.R., Canning, J., Cox, G.C., and Sceats, M.G., 'Writing and visualization of low-threshold type II Bragg gratings in stressed optical fibers', *Appl. Opt.*, **33**, pp7689-7694 (1995).
- Huang, S., Ohn, M.M., LeBlanc, M., Lee, R., Measures, R.M., 'Fiber optic intra-grating distributed strain sensor', in *Proc. Distributed and Multiplexed Fiber Optic Sensors IV*, San Diego, California, (1994).
- Hutchings, D.C., Sheik-Bahae, M., Hagan, D.J., and Van Stryland E.W., 'Kramers-Kronig relations in nonlinear optics' , *Opt. Quant. Electron.*, **24**, pp1-30 (1992).
- Kaminow, I.P., 'Polarisation in optical fibres', *IEEE J. Quantum Electron.*, **17**, pp15-22 (1981).
- Kanellopoulos, S.E., Handerek, V.A., and Rogers, A.J., 'Photoinduced polarisation couplers in elliptical core optical fibres written using 532 and 266 nm sources', *Electron. Lett.*, **28**, pp1558-1560 (1992).
- Kanellopoulos, S.E., Handerek, V.A., and Rogers, A.J., 'Compact Mach-Zehnder fiber interferometer incorporating photoinduced gratings in elliptical-core fibers', *Opt. Lett.*, **18**, pp1013-1015 (1993).
- Kanellopoulos, S.E., Handerek, V.A., and Rogers A.J., 'Simultaneous strain and temperature sensing with photogenerated in-fiber gratings', *Opt. Lett.*, **20**, pp333-335 (1995).
- Kashyap, R., Armitage, J.R., and Wyatt, R., 'All-fibre narrow reflection gratings at 1500nm', *Electron. Lett.*, **26**, pp730-731 (1990).
- Kashyap, R., Armitage, J.R., Campbell, R.J., Williams, D.L., Maxwell, G.D., Ainslie, B.J., and Millar, C.A. (a), 'Light-sensitive optical fibres and planar waveguides', *BT Technol. J.*, **11**, pp150-160 (1993).

- Kashyap, R., Wyatt, R., and Campbell, R.J. (b), 'Wideband gain flattened erbium fibre amplifier using a photosensitive fibre blazed grating', *Electron. Lett.*, **29**, pp154-155 (1993).
- Kashyap, R., Maxwell, G.D., Ainslie, B.J. (c), 'Laser-trimmed four-port bandpass filter fabricated in single-mode photosensitive Ge-doped planar waveguide', *IEEE Photon. Technol. Lett.*, **5**, pp191-194 (1993).
- Kashyap, R., 'Photosensitive optical fibers: devices and applications', *Optical Fiber Technol.*, **1**, pp17-34 (1994).
- Kashyap, R., McKee, P.F., Armes, D.J., Shabeer, M., and Cotter, D., 'Measurement of ultra-steep edge, high rejection fibre Bragg grating filters', *Electron. Lett.*, **31**, pp1282-1283 (1995).
- Kersey, A.D., and Marrone, M.J., 'Fiber Bragg grating high-magnetic-field probe', in *Proc. 10th Optical Fibers Sensors Conference, OFS-10*, Glasgow, pp53-56, Oct 11-13 1994.
- Lam, D.K.W., and Garside, B.K., 'Characterisation of single-mode optical fiber filters', *Appl. Opt.*, **20**, pp440-445 (1981).
- Lemaire, P.J., Atkins, R.M., Mizrahi, V., and Reed, W.A., 'High pressure H₂ loading as a technique for achieving ultrahigh UV photosensitivity and thermal sensitivity in GeO₂ doped optical fibres', *Electron. Lett.*, **29**, pp1191-1193 (1993).
- Limberger, H.G., Fonjallaz, P.Y., and Salathé, R.P., 'Spectral characterisation of photoinduced high efficient Bragg gratings in standard telecommunications fibres', *Electron. Lett.*, **29**, pp47-49 (1993).
- Loh, W., Cole, M.J., Zervas, M.N., and Lamming, R.I., 'Compensation of imperfect phase mask with moving fibre-scanning beam technique for production of fibre gratings', *Electron. Lett.*, **31**, pp1483-1485 (1995).
- Malo, B., Vineberg, K.A., Bilodeau, F., Albert, J., Johnson, D.C., and Hill, K.O., 'Ultraviolet light photosensitivity in Ge-doped silica fibers: wavelength dependence of the light induced index change', *Opt. Lett.*, **15**, pp953-955 (1990).

- Malo, B., Johnson, D.C., Bilodeau, F., Albert, J., and Hill, K.O. (a), 'Single-excimer-pulse writing of fiber gratings by use of a zero-order nulled phase mask: grating spectral response and visualization of index perturbations', *Opt. Lett.*, **18**, pp1277-1279 (1993).
- Malo, B., Hill, K.O., Bilodeau, F., Johnson, D.C., and Albert, J. (b), 'Point-by-point fabrication of micro-Bragg gratings in photosensitive fibre using single excimer pulse refractive index modification techniques', *Electron. Lett.*, **29**, pp1668-1669 (1993).
- Malo, B., Albert, J., Hill, K.O., Bilodeau, F., and Johnson, D.C., 'Effective index drift from molecular hydrogen diffusion in hydrogen-loaded optical fibres and its effect on Bragg grating fabrication', *Electron. Lett.*, **30**, pp442-443 (1994).
- Malo, B., Albert, J., Hill, K.O., Bilodeau, F., Johnson, D.C., and Thériault S. (a), 'Enhanced photosensitivity in lightly doped standard telecommunications fibre exposed to high fluence ArF excimer laser light', *Electron. Lett.*, **31**, pp879-880 (1995).
- Malo, B., Thériault, S., Johnson, D.C., Bilodeau, F., Albert, J., and Hill, K.O. (b), 'Apodised in-fibre Bragg reflectors photoimprinted using a phase mask', *Electron. Lett.*, **31**, pp223-225 (1995).
- Melle, S.M., Liu, K., and Measures, R.M., 'A passive wavelength demodulation system for guided-wave Bragg grating sensors', *IEEE Photon. Technol. Lett.*, **4**, pp516-518 (1993).
- Meltz, G., Morey, W.W., and Glen, W.H., 'Formation of Bragg gratings in optical fibers by a transverse holographic method', *Opt. Lett.*, **14**, pp823-825 (1989).
- Meltz, G., Morey, W.W., and Glenn, W.H., 'In-fiber Bragg grating tap', in *Proc. Optical Fiber Communication Conference, OFC'90*, p24 (1990).
- Mihailov, S.M., and Gower, M.C., 'Recording of efficient high-order Bragg reflectors in optical fibres by mask projection and single pulse exposure with an excimer laser', *Electron. Lett.*, **30**, pp707-709 (1994).

- Mizrahi, V., and Atkins, R.M., 'Constant fluorescence during phase grating formation and defect band bleaching in optical fibres under 5.1eV laser exposure', *Electron. Lett.*, **28**, pp2210-2211 (1992).
- Mizrahi, V., and Sipe, J.E., 'Optical properties of photosensitive fiber phase gratings', *J. Lightwave Technol.*, **11**, pp1513-1517 (1993).
- Morey, W.W., Meltz, G., and Glenn, W.H., 'Fiber optic Bragg grating sensors', in *Proc. Fibre Optic and Laser Sensors VII*, Boston, pp98-107 (1989).
- Morey, W.W., Meltz, G., and Ferrar, C.M., 'Tunable narrowband external-cavity diode laser with an embedded fiber grating reflector', *LEOS Summer Topical Digest: New semiconductor laser devices and applications*, Monterey, California, August 1-3 1990.
- Morey, W.W., 'Tunable narrow-line bandpass filter using fiber gratings', in *Proc. Optical Fiber Communication Conference, OFC'91*, San Diego, California, pp96-98 (1991).
- Morey, W.W., and Meltz, G., 'High temperature capabilities and limitations of fiber grating sensors', in *Proc. 10th Optical Fibers Sensors Conference, OFS-10*, Glasgow, pp234-237 (1994).
- Newell, A.C., Moloney, J.V., 'Nonlinear Optics', Addison-Wesley Publishing Company (1992).
- Niay, P., Bernage, P., Legoubin, S., Douay, M., Xie, W.X., Bayon, J.F., Georges, T., Monerie, M., and Poumellec, B., 'Behaviour of spectral transmission of Bragg gratings written in germania-doped fibres: writing and erasing experiments using pulsed or cw uv exposure', *Opt. Commun.*, **113**, pp176-192 (1994).
- Niay, P., Bernage, P., Taunay, T., Douay, M., Delavaque, E., Boj, S., and Poumellec, B., 'Polarization selectivity of gratings written in Hi-Bi fibers by the external method', *IEEE Photon. Technol. Lett.*, **7**, pp391-393 (1995).
- Noda, J., Okamoto, K., and Sasaki, Y., 'Polarization-maintaining fibers and their applications', *J. Lightwave Technol.*, **4**, pp1071-1089 (1986).
- Othonos, A., and Lee, X., 'Novel and improved methods of writing Bragg gratings with phase masks', *IEEE Photon. Technol. Lett.*, **7**, pp1183-1185 (1995).

- Ouellette, F., 'Dispersion cancellation using linearly chirped Bragg grating filters in optical waveguides', *Opt. Lett.*, **12**, pp847-849 (1987).
- Painchaud, Y., Chandonnet, A., and Lauzon, J., 'Chirped fibre gratings produced by tilting the fibre', *Electron. Lett.*, **31**, pp171-172 (1995).
- Parent, M., Bures, J., Lacroix, S., and Lapiere, J., 'Propriétés de polarization de réflecteurs de Bragg induits par photosensibilité dans les fibres optiques monomodes', *Appl. Opt.*, **24**, pp354-357 (1985).
- Park, H.G., and Kim, B.Y., 'Intermodal coupler using permanently photoinduced grating in two-mode optical fibre', *Electron. Lett.*, **25**, pp797-799 (1989).
- Patrick, H., and Gilbert, S.L., 'Growth of Bragg gratings produced by continuous-wave ultraviolet light in optical fiber', *Opt. Lett.*, **18**, pp1484-1486 (1993).
- Patrick, H., Gilbert, S.L., Lidgard, A., and Gallagher, M.D., 'Annealing of Bragg gratings in hydrogen-loaded optical fiber', *J. Appl. Phys.*, **78**, pp2940-2945 (1995).
- Patrick, H.J., Williams, G.M., Kersey, A.D., Pedrazzani, J.R., and Vengsarkar, A.M., 'Hybrid fiber Bragg grating/long period fiber grating sensor for strain/temperature discrimination', *IEEE Photon. Technol. Lett.*, **8**, pp1223-1225 (1996).
- Poirier, M., Thibault, S., Lauzan, J., and Ouellette, F., 'Dynamic and orientational behaviour of UV-induced luminescence bleaching in Ge-doped silica optical fiber', *Opt. Lett.*, **18**, pp870-872 (1993).
- Poumellec, B., Riant, I., Niay, P., Bernage, P., and Bayon J.F., 'UV induced densification during Bragg grating inscription in Ge:SiO₂ preforms: interferometric microscopy investigations', *Opt. Mater.*, **4**, pp404-409 (1995).
- Prohaska, J.D., Snitzer, E., Rishton, S., and Boegli, V., 'Magnification of mask fabricated fibre Bragg gratings', *Electron. Lett.*, **29**, pp1614-1615 (1993).
- Putnam, M.A., Askins, C.G., Williams, G.M., Friebele, E.J., Baskansky, M., and Reintjes, J., 'Single pulse fabrication of fibre Bragg gratings using a phase-conjugated KrF excimer laser', *Electron. Lett.*, **31**, pp885-886 (1995).

- Rizvi, N.H., Gower, M.C., Goodall, F.C., Arthur, G., and Herman, P., 'Excimer laser writing of submicrometre period fibre Bragg gratings using phase-shifting mask projection', *Electron. Lett.*, **31**, pp901-902 (1995).
- Russell, P.St.J., Archambault, J.-L., and Reekie, L., 'Fibre gratings', *Physics World*, pp41-46, October 1993.
- Russell, P.St.J., Hand, D.P., 'Rocking filter formation in photosensitive high birefringence optical fibres', *Electron. Lett.*, **26**, pp1846-1848 (1990).
- Sceats, M.G., Atkins, G.R., and Poole, S.B., 'Photolytic index changes in optical fibres', *Annu. Rev. Mater. Sci.*, **23**, 125-57 (1993).
- Senior, J.M., 'Optical fiber communications: Principles and Practice', Prentice Hall, New York, USA (1992).
- Stolen, R.H., Ashkin, A., Pleibel, W., and Dziedzic, J.M., 'In-line fiber-polarization-rocking rotator and filter', *Opt. Lett.*, **9**, pp300-303 (1984).
- Taunay, T., Niay, P., Bernage, P., Xie, E.X., Poignant, H., Boj, S., Delevaque, E., and Monerie, M., 'Ultraviolet-induced permanent Bragg gratings in cerium-doped ZBLAN glasses or optical fibers', *Opt. Lett.*, **19**, pp1269-1271 (1994).
- Town, G.E., Sugden, K., Williams, J.A.R., Bennion, I., and Poole, S.B., 'Wide-band Fabry-Pérot-like filters in optical fiber', *IEEE Photon. Technol. Lett.*, **7**, pp78-80 (1995).
- Tsai, T.E., Askins, C.G., and Friebele, E.J., 'Photoinduced grating and intensity dependence of defect generation in Ge-doped silica optical fiber', *Appl. Phys. Lett.*, **61**, pp390-392 (1992).
- Ungar, S., 'Fibre Optics: theory and applications', John Wiley and Sons, Inc., New York, USA (1990).
- Vengsarkar, A.M., Greene, J.A., and Murphy, K.A., 'Photoinduced refractive-index changes in two-mode elliptical core fibers: sensing applications', *Opt. Lett.*, **16**, pp1541-1543 (1991).
- Vengsarkar, A.M., Michie, W.C., Jankovic, L., Culshaw, B., and Claus, R.O., 'Fiber-optic dual-technique sensor for simultaneous measurement of strain and temperature', *J. Lightwave Technol.*, **12**, pp170-177 (1994).

- Vengsarkar, A.M., Lemaire P.J., Judkins, B.J., Bhatia, V., Erdogan, T., and Sipe., J.E., 'Long-period fiber gratings as band-rejection filters', *J. Lightwave Technol.*, **14**, pp58-65 (1996).
- Williams, D.L., Davey, S.T., Kashyap, R., Armitage., J.R., and Ainslie, B.J., 'Direct observation of UV induced bleaching of 240nm absorption band in photosensitive germanosilicate glass fibres', *Electron. Lett.*, **28**, pp369-371 (1992).
- Williams, D.L., Ainslie, B.J., Armitage, J.R., Kashyap, R., and Campbell, R. (a), 'Enhanced UV photosensitivity in boron codoped germanosilicate fibres', *Electron. Lett.*, **29**, pp45-47 (1993).
- Williams, D.L., Ainslie, B.J., Kashyap, R., Sherlock, G., Smith, R.P., and Collins, J.V. (b), 'Temperature stable 1.3 μ m laser with Bragg fibre grating external cavity for access networks', in *Proc. European Conference on Optical Communications, ECOC'93 vol-2*, p209 (1993).
- Wong, D., Poole, S.B., and Sceats, M.G., 'Stress-birefringence reduction in elliptical-core fibers under ultraviolet irradiation', *Opt. Lett.*, **17**, pp1773-1775 (1992).
- Xie, W.X., Douay, M., Bernage, P., Niay., P. (a), 'Second order diffraction efficiency of Bragg gratings written within germanosilicate fibres', *Opt. Commun.*, **101**, pp85-91 (1993).
- Xie, W.X., Niay, P., Bernage, P., Douay, M., Bayon, J.F., Georges, T., Monerie, M., and Poumellec, B. (b), 'Experimental evidence of two types of photorefractive effects occurring during photoinscription of Bragg gratings within germanosilicate fibres', *Opt. Commun.*, **104**, pp185-195 (1993).
- Xu, M.G., Reekie, L., Chow, Y.T., and Dakin, J.P., 'Optical in-fibre grating high pressure sensor', *Electron. Lett.*, **29**, pp398-399 (1993).
- Yariv, A., Yeh, P., 'Optical waves in crystals', John Wiley and Sons, Inc., New York, USA (1984).
- Yariv, A., 'Optical Electronics', Holt-Saunders International Editions, New York, USA (1985).

- Yuen, M.J., 'Ultraviolet absorption studies of germanium silicate glasses', *Appl. Opt.*, **21**, pp136-140 (1982).
- Zhang, Q., Brown, D.A., Reinhart, L., Morse, T.F., Wang, J.Q., and Xiao, G., 'Tuning Bragg wavelength by writing gratings on prestrained fibers', *IEEE Photon. Technol. Lett.*, **6**, pp839-84 (1994).

Chapter 3

Fabrication of Bragg grating arrays

3.1 Tuneable UV laser source for grating fabrication

At the start of the project some time was spent selecting a suitable laser source for writing IFBGs. The selection was strongly influenced by the requirements anticipated for the primary application of creating sensor networks for structural monitoring. Such sensor networks may readily be constructed from serial arrays of WDM gratings. In order to fabricate grating arrays the ability to step the Bragg wavelength in a controlled manner is required. In section 2.3.1 it was shown that a tuneable UV laser source would allow the control of the Bragg wavelength by varying the writing wavelength in accordance with equation 2.24. The flexibility offered by this method of controlling the Bragg wavelength was the primary reason for specifying a tuneable UV laser.

3.1.1 Description of the tuneable UV laser system

The laser system was selected against certain criteria: laser power, tuning range and coherence; wavelength accuracy and repeatability; the ease and safety of use and maintenance. Table 3.1 outlines these selection criteria in more detail, with the parameters of the tuneable dye system used by Morey *et al* (1989) taken as

Selection criteria	Frequency doubled, Nd:YAG pumped dye laser system specifications
Laser Power (40mW*)	2.6mJ per pulse at 244nm ≡ 65mW @ 25Hz
Spatial coherence	Least squares fit to Gaussian profile of UV beam measured to be ~7.6 or better (see section 4.1.2)
Temporal coherence (10cm coherence length*)	7cm coherence length
Tunable range in the UV (230nm to 255nm*)	236nm to 256nm stable range 240nm to 250nm
Output polarisation state	Horizontally polarised >98%
Absolute wavelength accuracy in the UV	±0.02nm
Wavelength resettability	±0.0008nm
Ease and safety of use and maintenance	Solid state pump source, DCM dye less toxic than other UV dyes, dye lifetime >1 month

* Benchmark parameters from Morey *et al* (1989)

Table 3.1 Selection criteria for the UV laser system and, for comparison, the frequency doubled, Nd:YAG pumped dye laser system specifications.

benchmarks. Also, to justify the substantial capital expenditure required for such a system (~£100,000), the laser had to satisfy the requirements of a number of other projects unrelated to the fabrication of IFBGs.

Using the selection criteria a pulsed, frequency doubled Nd:YAG pumped dye laser was chosen. A schematic diagram and a photograph of the laser system are shown in figures 3.1 and 3.2 respectively. To satisfy the requirements of unrelated applications, Continuum supplied a custom Nd:YAG source, consisting of two separate NY61 lasers mounted on a single optical breadboard. An NY61 being a flashlamp pumped Nd:YAG oscillator and single-pass amplifier, actively Q-switched using a Pockels cell. An injection seeder is used to line-narrow the Nd:YAG system, its output being divided between the two NY61s. The maximum pulse repetition frequency of each NY61 is 25Hz; frame rate operation primarily being a requirement for other applications, but was also seen to be useful for on-line monitoring of grating spectra during writing. Specifically, allowing the synchronisation of the laser to a CCD camera based detection system with a 25Hz frame rate. Such a spectral monitoring system was not used during the project, but one has subsequently been developed. The outputs from the two NY61s are combined at a polarising beam splitter, before passing co-linearly through a temperature stabilised second harmonic generator. Each NY61 delivers a maximum pulse energy of 550mJ at the fundamental wavelength of 1064nm, and up to 265mJ at 532nm from the harmonic generator when injection seeded. Injection seeding improves the spatial and temporal coherence of the Nd:YAG beam, thereby increasing the conversion efficiency of the harmonic generator. Unconverted 1064nm radiation is separated out from the 532nm beam using a dichroic beamsplitter.

The frequency doubled Nd:YAG output is used to pump a Continuum ND60 pulsed dye laser. Either of the NY61 lasers can be used to pump the dye laser. Simultaneous pumping using both the NY61 lasers was not used, mainly due to the difficulties encountered in aligning both of the pump beams to be sufficiently co-linear. The dye laser contains DCM dye and is tuneable from 607nm to 676nm, with a peak response around 640nm. A Continuum UVX3 wavelength extension package

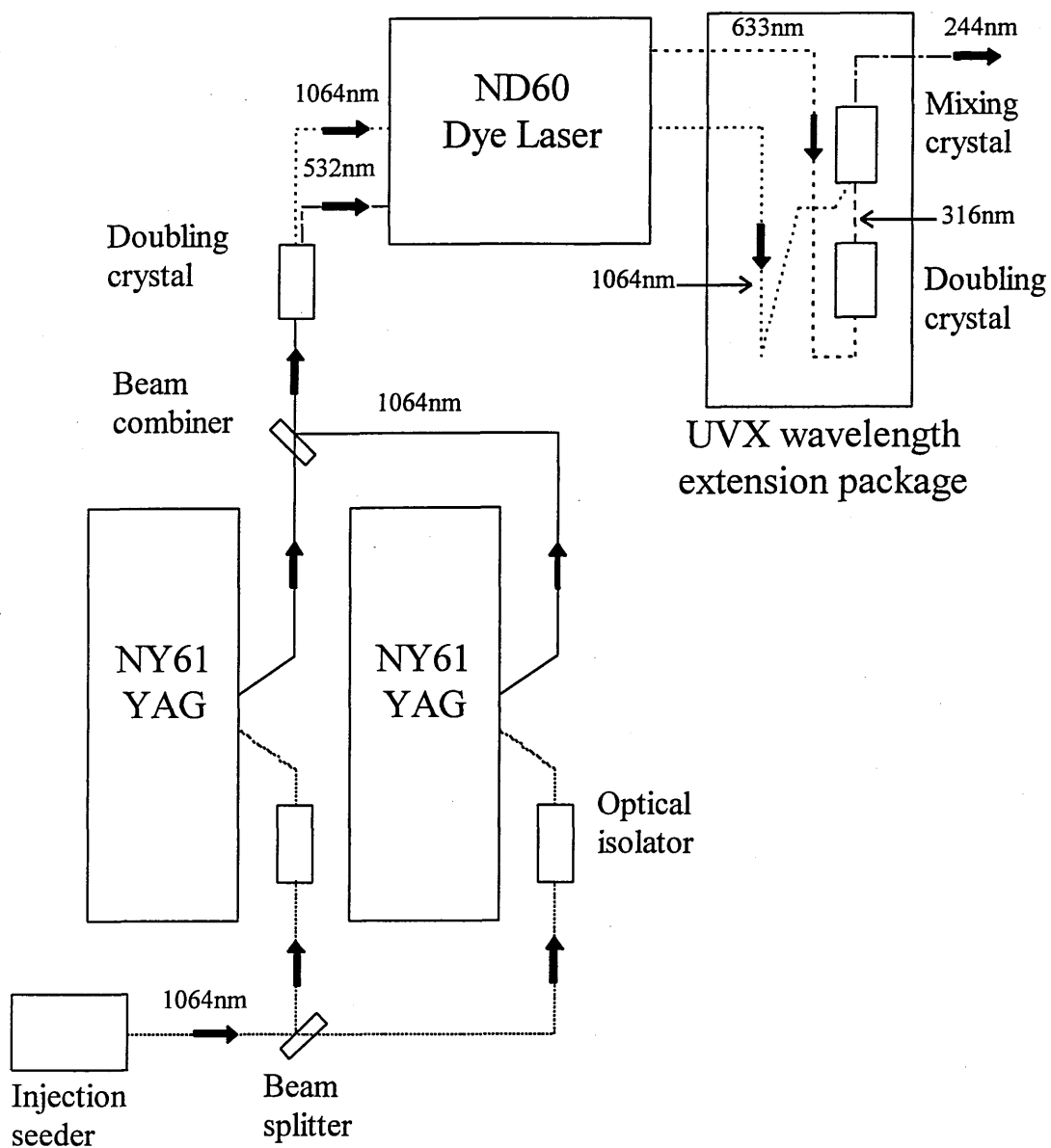


Figure 3.1 Schematic diagram of the frequency doubled, Nd:YAG pumped dye laser system

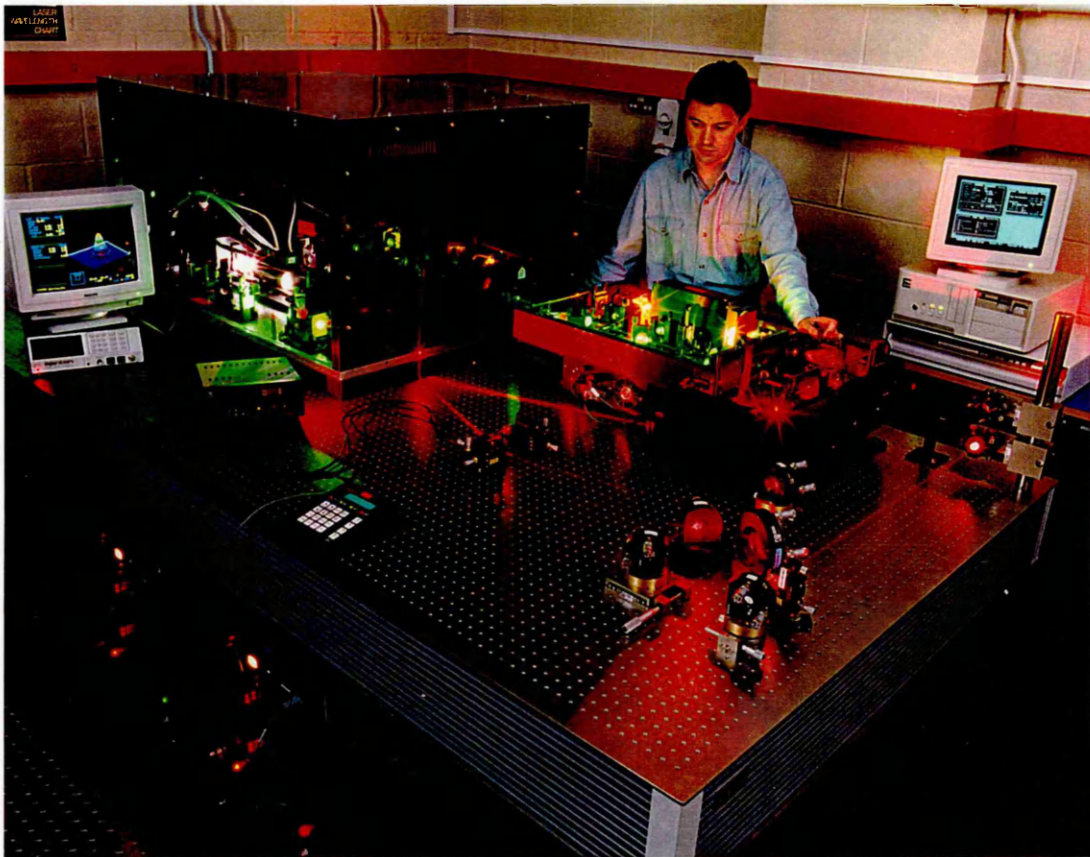


Figure 3.2 Photograph showing the frequency doubled, Nd:YAG pumped dye laser system (and author).

firstly frequency doubles the dye output to around 320nm. Then the doubled dye beam is sum frequency mixed with residual Nd:YAG fundamental that has passed through the dye laser via a mirror delay line. A delay line is necessary so that the doubled dye and the residual 1064nm laser pulses will arrive at the mixing crystal simultaneously. The final UV output is tuneable from 236nm to 256nm. and is horizontally polarised to >98%. Improvements to the Nd:YAG coherence properties provided by injection seeding also have benefits for the UV beam quality. Line-narrowing of the Nd:YAG minimised degradation of the laser system's temporal coherence during the final sum frequency mixing stage. The UV output had a specified coherence length of approximately 7cm. Also, the improved spatial coherence of the Nd:YAG fundamental was translated into increased conversion efficiency at the mixing crystal along with a higher quality UV output. When injection seeded, the maximum pulse energy in the UV was 2.6mJ at 244nm, corresponding to an average power of 65mW for a 25Hz pulse repetition rate.

Due to its complexity, the laser system required regular re-alignment and some time to fully warm up. The Nd:YAG system took approximately 30 minutes to attain maximum stability. A further 15 minutes were required to obtain the optimum UV performance, during which time the frequency doubling and sum frequency mixing crystals within the wavelength extension package had to be frequently adjusted. In addition, each time the dye laser wavelength was adjusted, it took approximately 10 minutes for the UV output to fully stabilise. Although the UV output was tuneable from 236nm to 256nm, satisfactory power stability could only be achieved between 240nm and 250nm. For completeness, the appropriate laser system specifications are listed alongside the selection criteria in table 3.1.

An alternative configuration considered, was to pump the dye laser with the 355nm third harmonic of Nd:YAG instead of 532nm. The dye output could then be frequency doubled directly to the 240nm range. However, this would have meant using one of the more carcinogenic coumarin dyes, which typically have a lifetime of a few days compared to greater than one month for DCM.

3.1.2 Laser beam profiling system

To gauge the spatial quality of the UV beam, intensity profiles were obtained using a commercial beam profiling system. The laser output was viewed using a Pulnix TM6-CN CCD camera connected to a Spiricon LBA-100A laser beam analyser (LBA). Figure 3.3 shows the optical arrangement used for beam-profiling the laser. The UV output was directed onto a borosilicate glass slide, the fluorescence from which was viewed by the CCD camera through a zoom lens. The CCD was an interlaced interline transfer type (0.5-inch CCIR, with 752 x 582 pixels and 8.6 μ m x 8.3 μ m cell size). A composite video signal from the camera was fed to the LBA, which digitised the signal to eight bits of resolution and laser beam profiles were captured as frames of 120 x 120 pixels. The zoom lens was spatially calibrated by viewing a grid pattern of known dimensions placed at the surface of the borosilicate glass slide. A laser beam of a known average power was used to calibrate the system for power and energy.

The UV beam was generally elliptical in shape and the dimensions varied with beam quality. The most circular profiles being associated with the best beam quality. Figure 3.4 shows a three-dimensional wire-frame representation of a captured beam profile. The intensity profile was taken at a distance of 1.45m from the UV output (laser wavelength 244nm, pulse energy 1.8mJ). For this example, the widths of the major and minor beam axes were measured to be 3.2mm and 2.5mm respectively. The method used to calculate beam widths is described in appendix A.

To give an indication of the beam quality, a two dimensional least squares fit to a Gaussian profile was performed on the captured data using a LBA algorithm. A second algorithm was used to correlate the Gaussian fit with the data. This gave a relative value for how well the data matched the Gaussian profile. The better the correlation, the closer to one the result becomes. However, the result is relative not absolute. A result of 0.8 represents a better correlation than 0.7, but it does not indicate by how much. The equations used to fit the data and obtain the correlation of fit are also given in appendix A. For the beam profile shown in figure 3.4 the

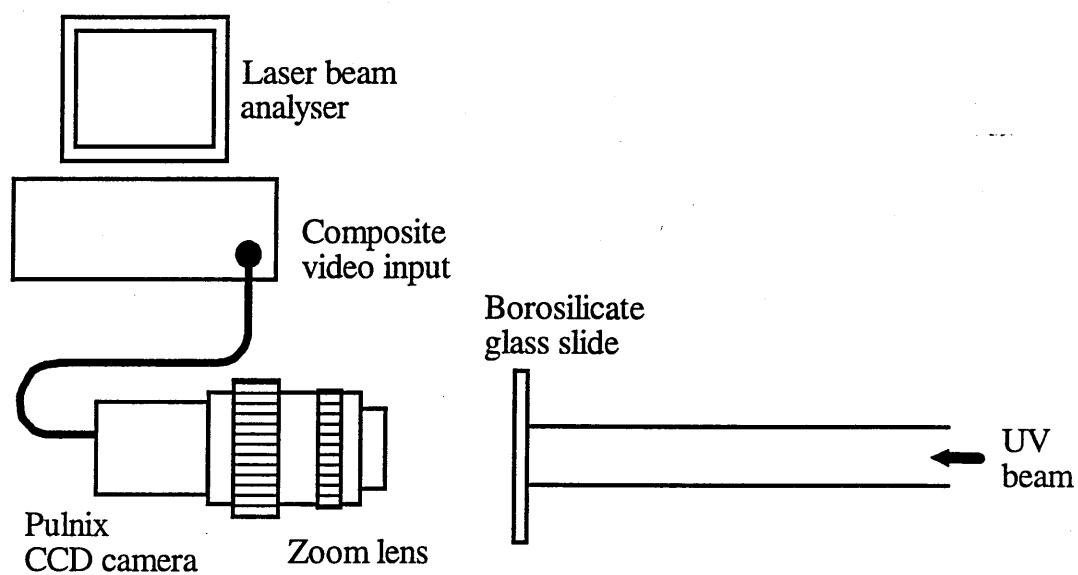


Figure 3.3 Experimental arrangement for viewing the laser beam profile

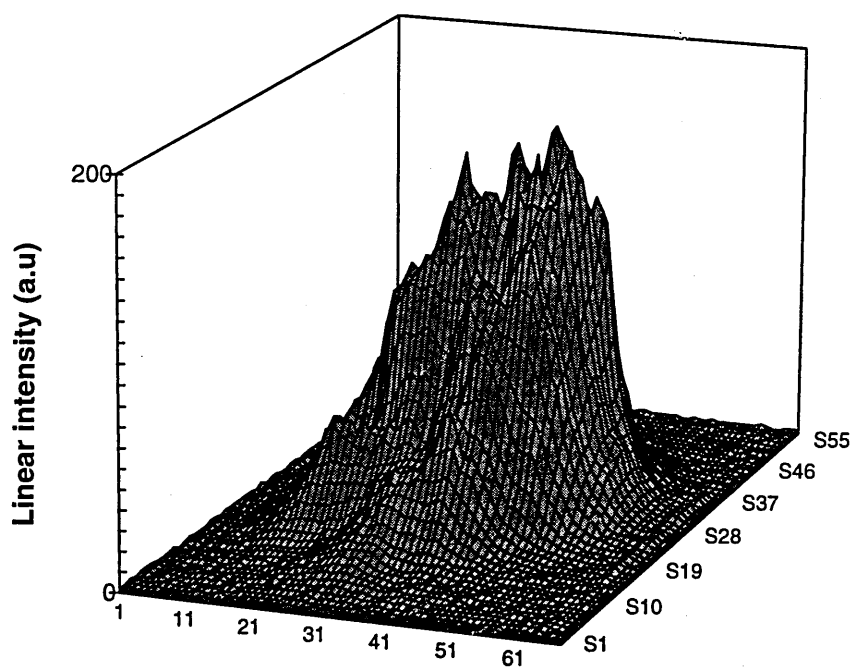


Figure 3.4 Three-dimensional wire-frame representation of a typical laser beam profile.

correlation was calculated to be 0.76. This example was chosen because it was typical of the laser quality used for grating fabrication, although significantly higher beam quality could be obtained with careful alignment of the system.

3.2 Grating writing schemes

A number of writing schemes were investigated from the view point of creating WDM grating arrays. All the techniques make use of hydrogen loaded optical fibres, so firstly a brief description of the experimental rig used to hydrogen load the fibres is given below. The parameters of all the optical fibres used in the experimental work can be found in appendix B. To obtain spectral profiles of gratings after fabrication, a spectrometer system based upon a commercial monochromator was developed and details of this system are also included.

3.2.1 Hydrogen loading of optical fibres

As has previously been discussed in section 2.1.1, the photosensitivity of standard germanosilicate telecommunications fibres can be significantly enhanced by room temperature, high pressure hydrogen loading (Lemaire *et al*, 1993). Since we did not have access to special fibres with high germania concentrations or co-dopants, but had a ready supply of more standard fibres, hydrogen loading was seen as an attractive method for ensuring that the fibres had sufficient photosensitivity to allow grating fabrication.

Therefore, a simple rig for hydrogen loading was constructed, a schematic diagram of which is shown in figure 3.5. A general research grade (~98% pure) hydrogen gas cylinder was used to pressurise a stainless steel tube. The tube contained a steel rod around which lengths of fibre were helically wrapped. The fibres were taped down at either end of the rod to prevent them becoming unwound during handling. The steel rod was loaded and unloaded via a screw cap termination at one end of the tube. Gas tap valves were placed at each end of the tube. Gas tap 1 was

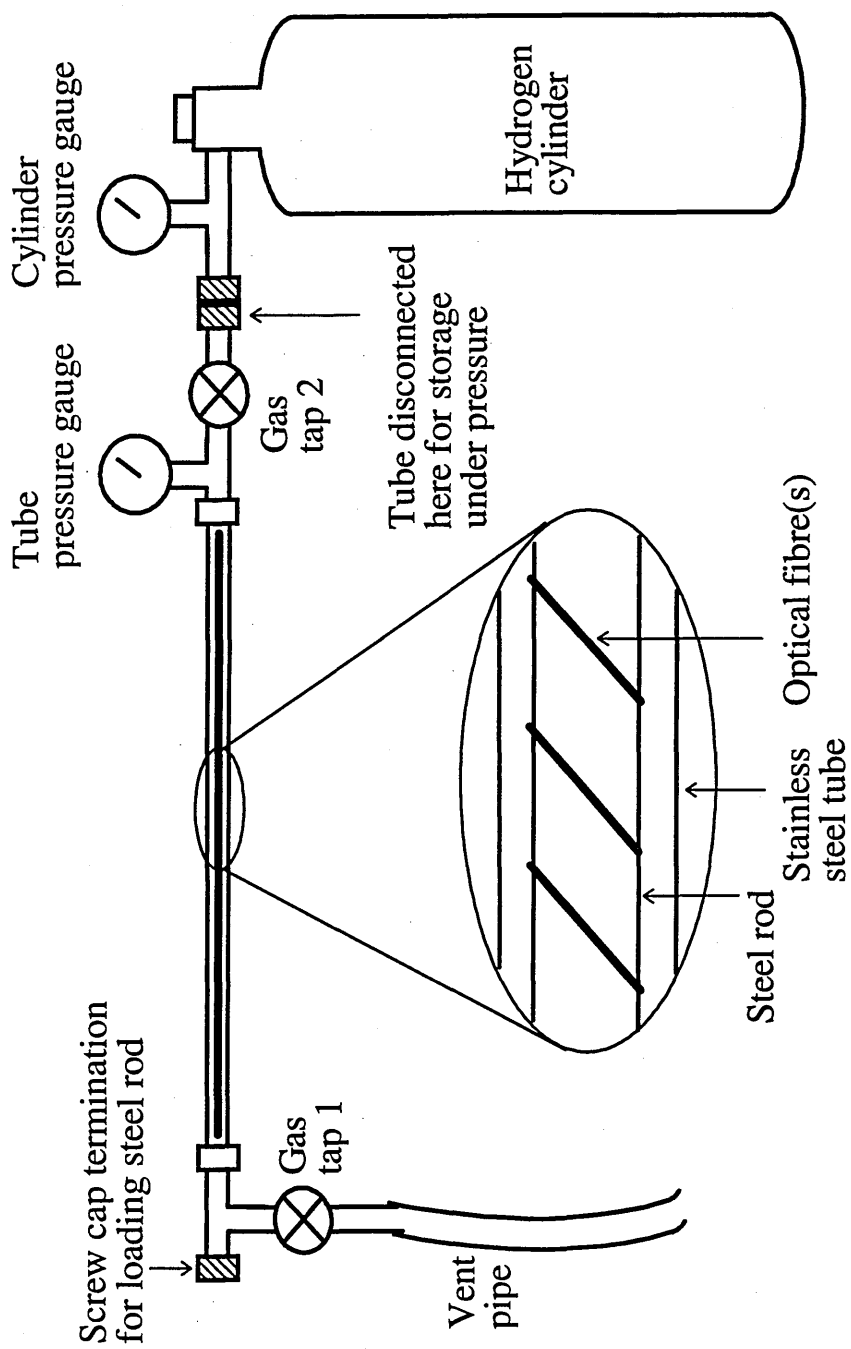


Figure 3.5 Schematic diagram of the assembly used to hydrogen load optical fibres.

opened slightly to allow hydrogen purging and to vent off the hydrogen when access to the fibres was required. It could also be used to reduce the tube pressure below that of the gas cylinder. Once pressurised, gas tap 2 was closed and the tube disconnected from the gas cylinder for safe storage. A pressure gauge on the tube allowed the hydrogen pressure to be monitored during storage.

Using this method up to ten, 2m lengths of fibre were simultaneously hydrogen loaded on a routine basis. A new gas cylinder typically had a pressure of around 220 bar and lasted for greater than 20 tube fills, before its pressure dropped below 150 bar, which was the minimum gas pressure used. Fibres were soaked for greater than 2 days at gas cylinder pressure.

3.2.2 Scanning monochromator with white light source

The majority of the grating spectral profiles were obtained using a wavelength scanned monochromator with a white light source, illustrated in figure 3.6. The white light source was a Bentham IL1 illuminator, 100W quartz halogen lamp, which had a randomly polarised output. The spectral profile of the quartz lamp is shown in figure 3.7. The lamp was imaged onto the entrance slit of a Bentham M300HR monochromator. Two separate monochromators were used. The first had an 1800 lines per mm grating, with a resolution limit of 0.05nm, and an upper operating wavelength of 950nm. The second had a 900 lines per mm grating, with a resolution limit of 0.1nm, and an upper operating wavelength of 1900nm. Narrowband light emerging from the exit slit of the monochromator was launched into one input arm of a 50:50 singlemode coupler. The optical fibre containing the IFBG(s) was mechanically spliced to one output arm of this coupler. Using this arrangement, a photodetector can either be placed at the far end of the fibre containing the IFBG(s) to obtain a transmissive spectral profile, or at the end of the coupler's free input arm to obtain a reflective spectral profile. Depending upon the spectral region, either Si or InGaAs photodiodes were used as detectors. The silicon photodiodes were used for wavelengths up to 1000nm and the InGaAs detectors for longer wavelengths. Since

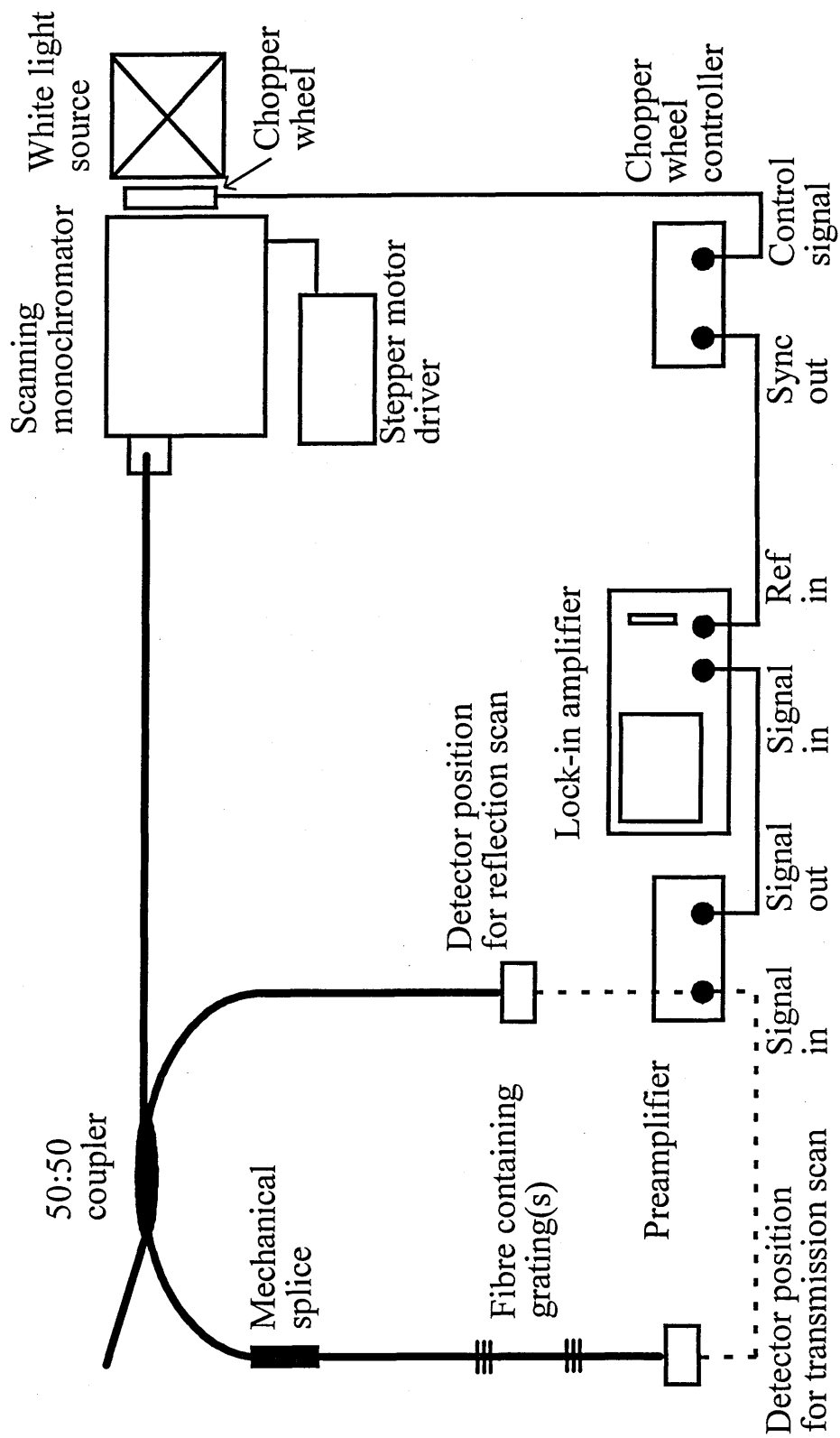


Figure 3.6 Experimental arrangement for grating characterisation system, consisting of a scanning monochromator and a white light source.

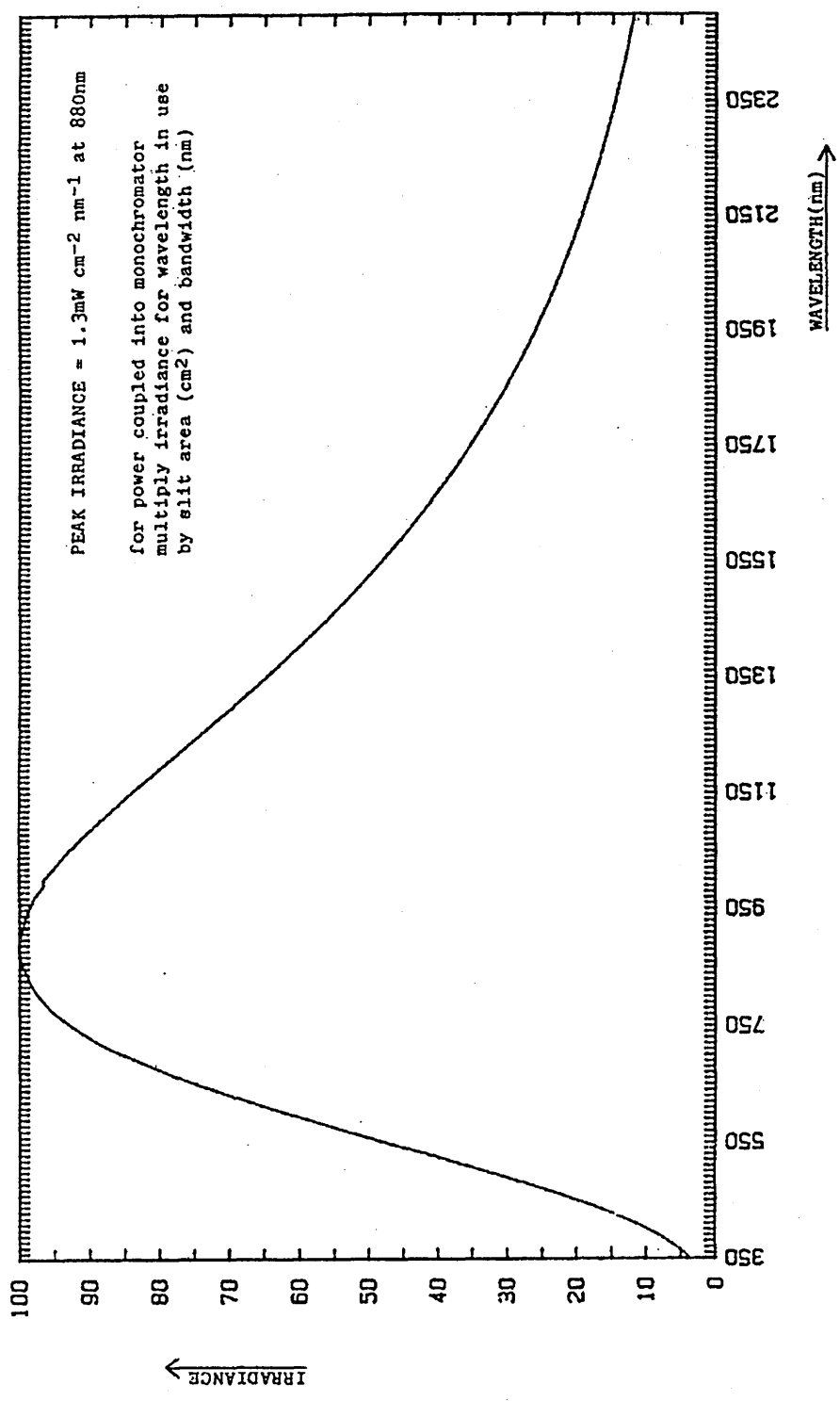


Figure 3.7 Spectral irradiance produced by the white light source at the plane of the monochromator.

the signal levels obtained using this method were very low (of the order of a few nanowatts of optical power at the photodetector), lock-in detection was used to improve the signal to noise ratio of the system. To modulate the detected signal, an optical chopper wheel was inserted between the white light source and the monochromator (133Hz modulation frequency). The synchronisation output from the chopper wheel driver was used as the reference input to a Stanford Research SR850 DSP lock-in amplifier. The photodetector signal was first amplified using a Stanford Research SR560 low noise preamplifier. The amplified output being used as the input signal for the lock-in amplifier.

The monochromator grating was scanned using a stepper motor, controlled by a Bentham SMD 3B/IEEE stepper motor driver. The stepper motor driver could be manually controlled from the front panel, in the range 1 to 400 steps per second. The step size was 0.01nm for the 1800 lines per mm grating and 0.02nm for the 900 lines per mm grating. When a grating spectral profile was all that was required, it was sufficient to simultaneously start the stepper motor driver and a lock-in amplifier trace using the front panel controls. The trace recorded on the lock-in amplifier was of the modulated component of the photodetector signal against time. Since the monochromator scan speed was known, the time base of the trace could easily be related to wavelength units. The recorded data was stored using the lock-in's built in disk drive.

3.2.3 Near-field phase mask technique

The first writing scheme to be investigated was the near-field phase mask technique (Anderson *et al*, 1993 and Hill *et al*, 1993). This was chosen as the initial fabrication method, because it was very simple to set-up and did not require as stable an experimental arrangement as the interferometric techniques.

A Lasiris phase mask (25.4mm diameter and 0.896 μ m periodicity), which fabricated gratings with a 1300nm Bragg wavelength, was positioned in near contact to the fibre surface as shown in figure 2.11. A phase mask for this Bragg wavelength

was only chosen because it represented the most affordable option available at that time. For the design wavelength of 248nm, the diffraction efficiencies of the \pm first orders were maximised to 35% and the zero order nulled to less than 3%. A periscope, which comprised of two dielectric coated mirrors, served to rotate the output polarisation state of the laser from horizontal to vertical. This was necessary to obtain a laser polarisation state that was orthogonal to the plane containing the diffracted beams. A requirement for maximum fringe visibility that has been mentioned in section 2.3.1 To ensure a sufficient energy density at the fibre surface, a cylindrical lens was used to focus the light through the phase mask onto the fibre. Its focal length measured to be 88cm at 248nm. To confirm that the fringe pattern was striking the fibre at precisely the right height, a piece of white card was placed close behind the fibre. When the laser struck the fibre a fluorescent diffraction pattern was observed on the card. A symmetrical diffraction pattern above and below the fibre indicated that the laser was at the correct height.

As an example, figure 3.8 shows a reflection spectrum of a 3.4mm long IFBG written using the phase mask technique. The spectrum was obtained using the monochromator with 900 lines per mm grating and white light source. The grating was written in an OF Deeside (1300nm) fibre that had been hydrogen loaded for 7 days at 215 bar. During writing, the average laser power was 7.3mW (8.33Hz repetition rate) and the total exposure time was 25 minutes. The grating had a measured Bragg wavelength of 1302.8nm and a 1.8nm FWHM. The FWHM measurement being considerably broadened by the monochromator resolution, which was set to 0.6nm. Using the transmission minima, the peak reflectivity was estimated to be approximately 60%. This is almost certainly an underestimate of the grating reflectivity, since the transmission minima will be flattened and reduced in depth by the coarse monochromator resolution. It will also be noticed that there are no sidebands evident on the reflection spectrum. This again is due to the limited monochromator resolution, which will prevent any sidebands being resolved, even without any apodisation of the IFBG spectrum, caused by the Gaussian laser beam profile, being taken into consideration. In fact, the limited resolution of the

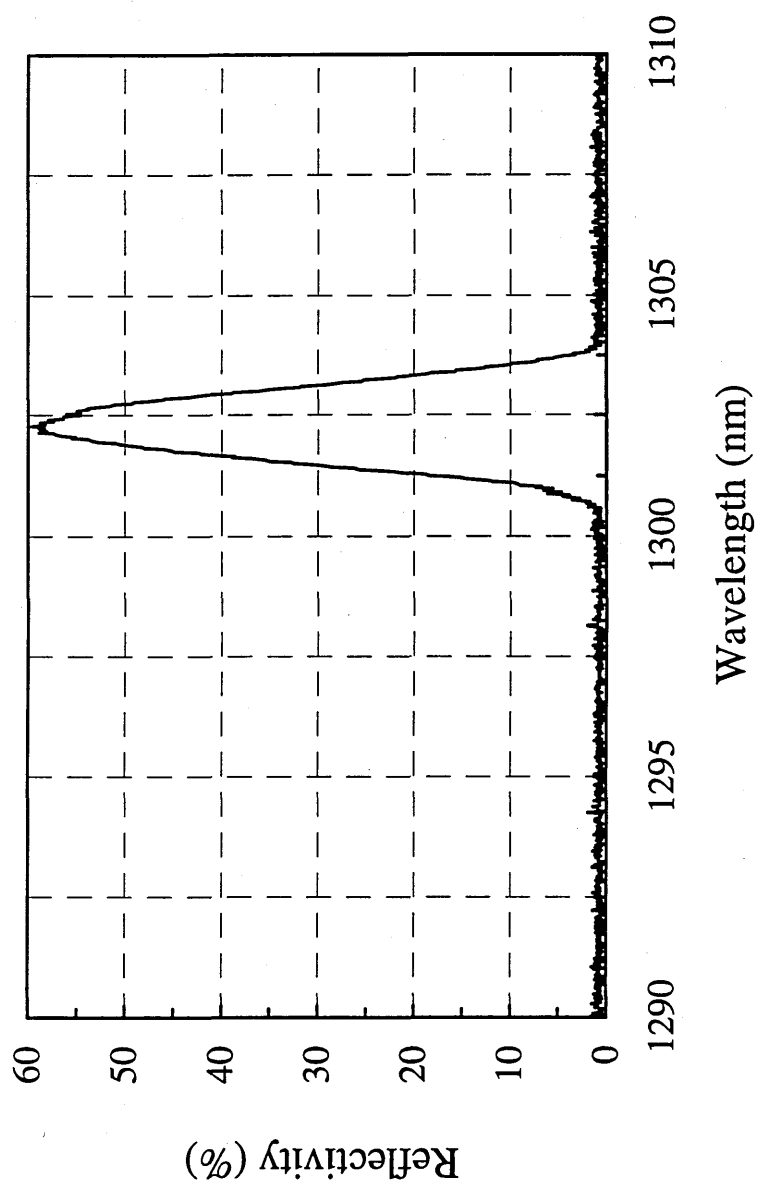


Figure 3.8 Monochromator scan showing the reflection spectrum of a grating written into OF Deeside (1300nm) fibre using the near-field phase mask method.

monochromator based spectrometer systems prevented the detection of sidebands throughout the experimental work. This is clearly demonstrated in section 3.3.2, in which a comparison is made between an experimental and a theoretically derived grating spectrum.

The long 25 minute exposure time used in this example served to illustrate the stability of the phase mask writing technique, and as has previously been discussed in section 2.3.2, this method is best suited to applications where large numbers of identical gratings are required. Since the Bragg wavelength is independent of writing wavelength, as shown by equation 2.28, the tuneable laser could not be used to control the Bragg wavelength. Therefore, to enable laser wavelength tuning, alternative writing techniques were investigated.

3.2.4 Two-beam mirror interferometer

The majority of the gratings were fabricated using an amplitude splitting mirror interferometer, similar to that first used by Meltz *et al* (1989). This method was chosen because it offered the most flexibility, allowing IFBGs to be written over a wide range of Bragg wavelengths by varying the angle of the interferometer mirrors. Once the interferometer had been set up for a particular spectral region, WDM grating arrays could be written by varying the UV source wavelength.

The laser system and the interferometer were mounted on an optical table which had air suspension. The table provided a rigid working surface and insulated the interferometer from floor vibrations, essential requirements for optimum interferometer stability, enabling multi-pulse exposure. Again the periscope was used to rotate the laser output polarisation state. A schematic diagram of the mirror interferometer is shown in figure 3.9. It consisted of a flat plate beamsplitter with a dielectric coating that, for the design wavelength of 248nm and at a 45° beam incidence, gave a 50:50 split ratio. The split ratio varied by less than $\pm 2.5\%$, in each arm, over the wavelength range 240nm-250nm. Aluminium mirrors, designed for low power UV operation (reflectivity 80-90%), were used to steer the beams through a

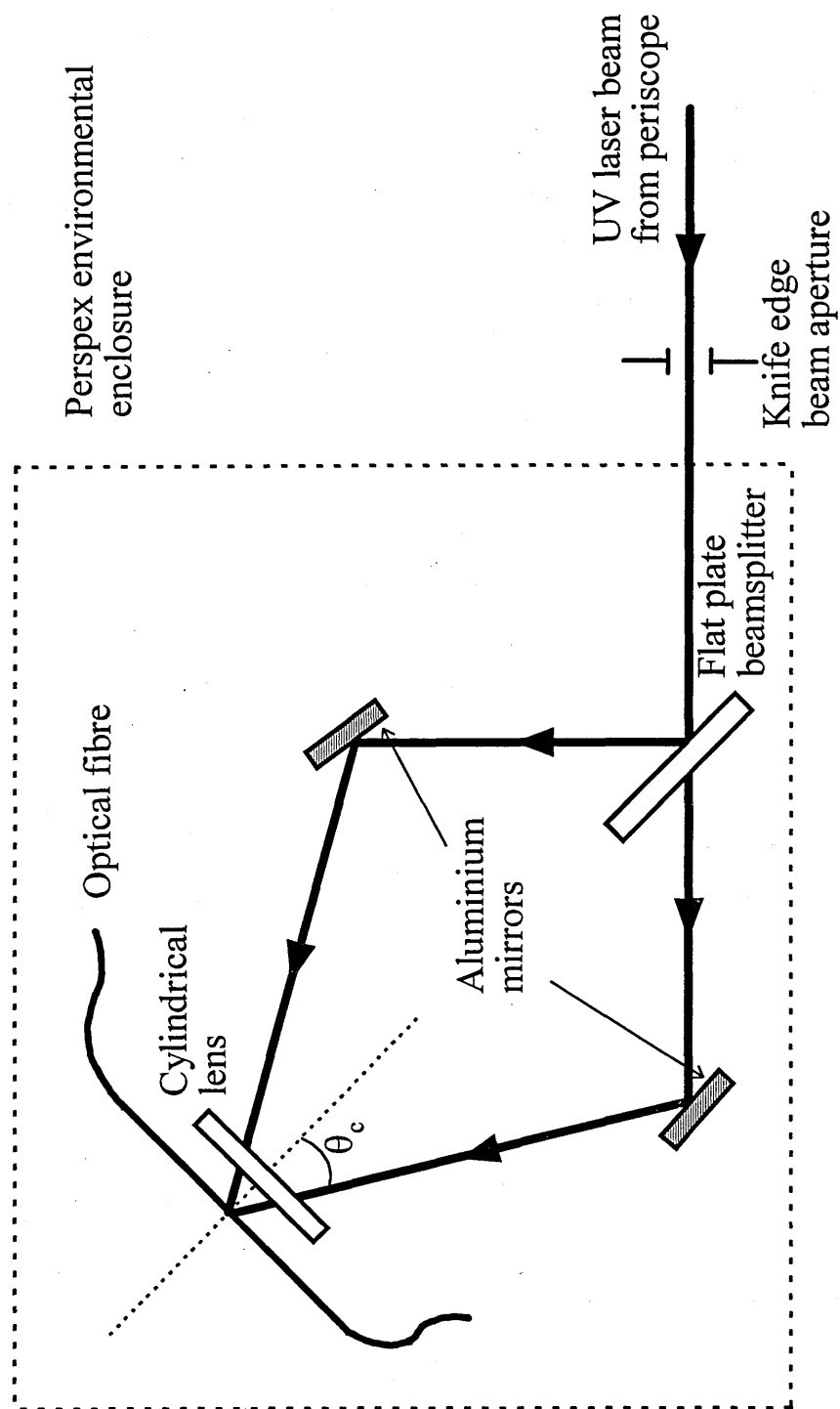


Figure 3.9 Experimental arrangement for fabricating gratings using a two-beam mirror interferometer.

plano-convex cylindrical lens before being interfered at the optical fibre, with a half angle of θ_c between the intersecting beams. It was found that the laser had sufficient spatial coherence, to enable gratings to be written without the need for an additional mirror to equalise the handedness of the beams in each arm of the interferometer (Askins *et al*, 1992). Mirrors made from dielectric coated substrates have damage thresholds several orders of magnitude greater than aluminium but were not used as their reflectivity is wavelength and angularly dependent. The cylindrical lens was 60mm long with a measured focal length of 46mm at 244nm. The position of the lens with respect to the fibre was varied to control the energy density at the fibre surface. Using a single lens placed before the fibre simplifies the alignment of the interferometer compared to using a lens in each arm, as with the interferometer of Meltz *et al* (1989) shown in figure 2.9. It also means that each of the interferometer arms are equally focused at the fibre surface, ensuring the best visibility fringes.

The interferometer was readily configured to have a path length imbalance of less than 1cm (c.f. laser coherence length of 7cm). To minimise losses the cylindrical lens and flat plate beamsplitter were made from UV grade synthetic fused silica. Even so, the total optical power loss through the interferometer was measured to be 32%. A perspex box placed over the optics served to reduce the disturbances caused by air currents within the laboratory.

The grating length was more precisely defined by inserting a knife edge, slit aperture into the UV beam. The aperture was placed before the beamsplitter rather than the alternative near-field position, almost in contact with the fibre. This reduced the risk of damaging the fibre and eased the alignment of the aperture, though diffraction effects degraded the edge definition. The slit width could be adjusted from fully closed to greater than the beam diameter.

To ensure that the two interfering beams fully overlapped at the fibre surface, a borosilicate glass slide, placed immediately below the fibre, allowed the fluorescence from the UV beams to be viewed. The cylindrical lens was lowered slightly to deflect the beams onto the glass slide.

The fabrication of grating arrays was made possible by a simple fibre mount that could be slid against a fixed back rail. This arrangement is illustrated in figure 3.10. To enable the physical spacing between adjacent gratings to be accurately controlled, stainless steel spacer blocks, precisely machined to known dimensions, could be inserted between the fibre holder and a fixed reference post. Using this fibre mount, grating arrays covering up to 20cm of fibre could be fabricated, with the spacing between adjacent gratings set to an accuracy that was estimated to be better than 100 microns.

To demonstrate laser wavelength tuning an array of five, 2.8mm long gratings were written into a Spectran (780nm) fibre that had been hydrogen loaded for five weeks at 180 bar. The average laser power during writing was ~30mW and the exposure time for individual gratings varied from 3 to 5 minutes. A transmission spectrum of the grating array is shown in figure 3.11. The spectrum was obtained using the monochromator with the 1800 lines per mm grating and white light source. The monochromator resolution being set to 0.35nm. The results are summarised in table 3.2, which compares the experimentally determined wavelength spacings to those determined theoretically using equation 2.25. Since the sensitivity of the Bragg wavelength to changes in writing wavelength, $d\lambda_b/d\lambda_w$, is a constant for a fixed intersection angle, $d\lambda_b/d\lambda_w$ can be calculated by substituting the measured Bragg wavelength and writing wavelength for any of the gratings into equation 2.25. Indeed all gratings yielded a consistent value for $d\lambda_b/d\lambda_w$ of 3.38 (i.e., a 1nm change in λ_w will lead to a 3.38nm change in λ_b).

As can be seen from table 3.2, the experimental results agreed with the theoretical values within the limits of experimental error. Although there was a large experimental error in the measured wavelength spacing, this was mainly due to the limited wavelength accuracy of the monochromator. The theoretical accuracy to which the Bragg wavelength can be set using laser wavelength tuning will be limited by the product of the laser systems wavelength accuracy and $d\lambda_b/d\lambda_w$. For example, a grating written around 800nm with a laser initially at 244nm gives a $d\lambda_b/d\lambda_w$ of 3.3,

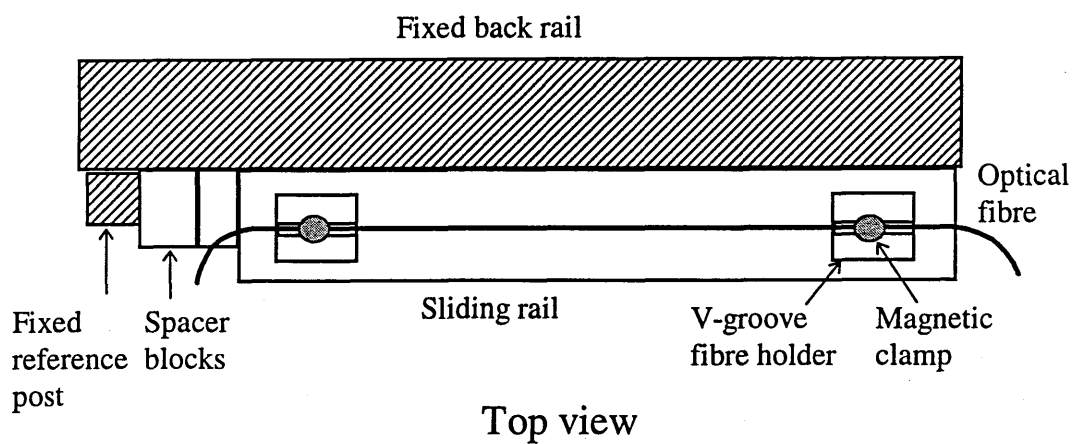


Figure 3.10 Fibre mount for fabrication of grating arrays.

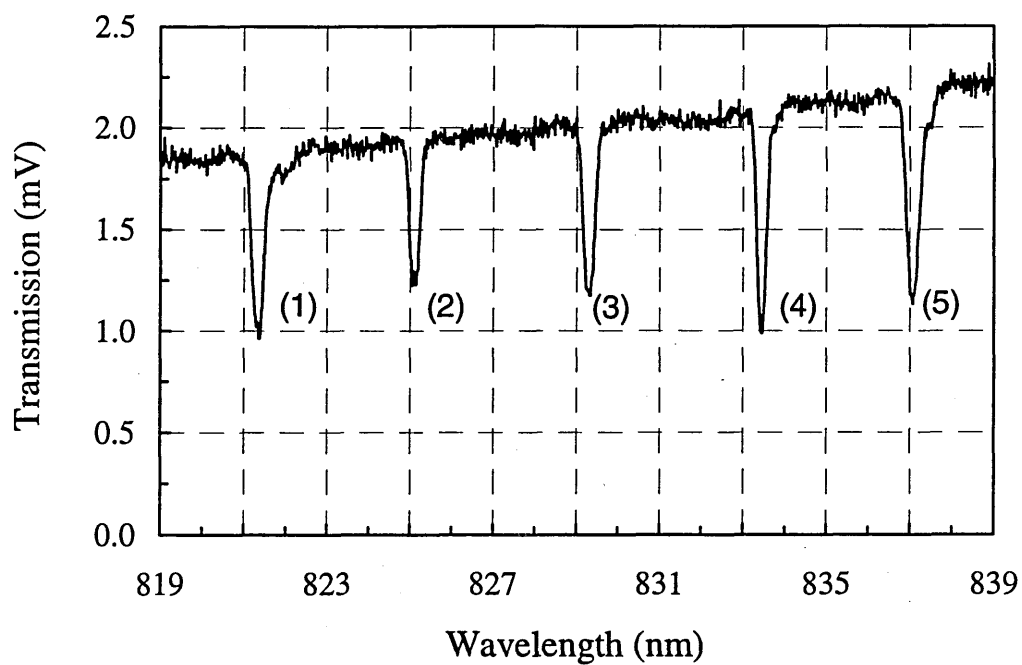


Figure 3.11 Monochromator scan showing the transmission spectrum of a grating array written into a Spectran (780nm) fibre using the two-beam mirror interferometer.

Grating		Bragg wavelength, λ_b (nm)	Writing wavelength, λ_w (nm)	Measured wavelength spacing, $\Delta\lambda_b$ (nm)	Theoretical wavelength spacing, $\Delta\lambda_b$ (nm)
1	2-1	821.4±0.2	243.10±0.02	3.6±0.5	4.1
2	3-2	825.0±0.2	244.30±0.02	4.3±0.5	4.1
3	4-3	829.3±0.2	245.50±0.02	4.2±0.5	4.1
4	5-4	833.5±0.2	246.70±0.02	3.6±0.5	4.1
5		837.1±0.2	247.90±0.02		

Table 3.2 Comparison of experimental and theoretical wavelength spacings for gratings written using a two-beam mirror interferometer.

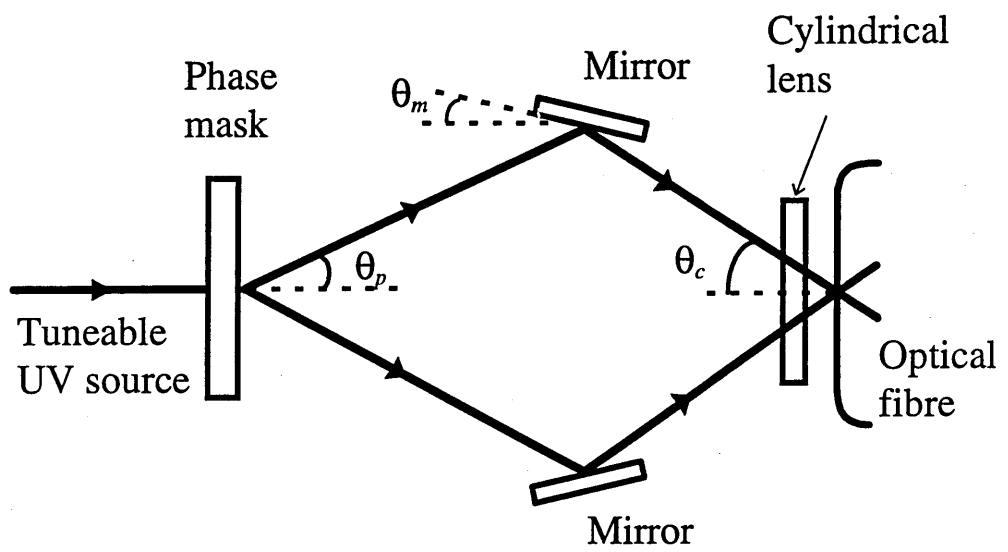
which means that the Bragg wavelength can be set to an accuracy of $\pm 0.07\text{nm}$ using the laser wavelength accuracy given in table 3.1 ($\pm 0.02\text{nm}$). Also for this example, the spectral coverage that can be obtained using the lasers stable tuning range (10nm) will be 33nm.

In practice, other factors, which have been discussed in section 2.2.1, will limit the wavelength accuracy. Firstly, the Bragg wavelength of the grating will gradually increase during fabrication, as a result of photoinduced changes in the effective mode index (Fertain *et al*, 1991). Therefore, it would not be possible to accurately set the absolute Bragg wavelengths or the relative spacing between gratings without in-line monitoring of either the IFBGs' reflectivity or, better still, the Bragg wavelengths. Secondly, for room temperature, hydrogen loaded fibres, shifts in the Bragg wavelengths of IFBGs would be observed over the first few weeks as the hydrogen diffused out of the fibre cores (Malo *et al*, 1994). This would further complicate the fabrication of IFBGs at specific Bragg wavelengths. This latter problem could be overcome if hydrogen flame brushing were used as an alternative method of enhancing the fibre photosensitivity (Bilodeau *et al*, 1993). Another solution would be to thermally anneal the sections of the fibre where the gratings were to be written following hydrogen loading (Lemaire *et al*, 1993). The fibre could then be left for several weeks until the remaining molecular hydrogen had diffused out of the core.

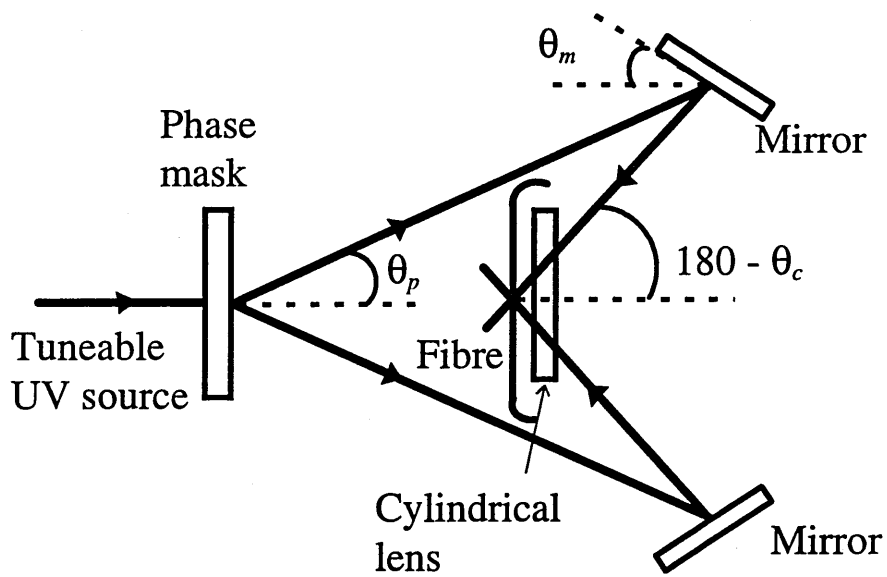
3.2.5 Two-beam mirror interferometer with a phase mask beamsplitter

A modified version of the preceding two-beam interferometer has been investigated. This extended the usefulness of laser source tuning to situations where, either greater spectral coverage was required than could normally be provided by laser wavelength tuning, or finer control of the Bragg wavelength was needed.

The normal beamsplitter in the interferometer described in section 3.2.4 was replaced by the Lasiris phase mask used in section 3.2.3. Two interferometer configurations were investigated and these are illustrated in figures 3.12(a) and (b).



(a)



(b)

Figure 3.12 Experimental geometries for fabricating gratings using an interferometer with a phase mask beamsplitter.

The first order beams generated by the phase mask were reflected by the two steering mirrors at an angle θ_m to the phase mask normal. Then as previously the beams were focused by the cylindrical lens onto the optical fibre. The interferometer geometry shown in figure 3.12(b) represents the case where θ_m is increased to the point where the beams are now back reflected towards the phase mask. In this geometry the beams had to be tilted slightly out of the plane to prevent the outgoing beams from the phase mask striking the fibre and cylindrical lens. For consistency θ_c is defined as the obtuse angle shown in figure 3.12(b). Both geometries have the advantage that the diffracted beams emerging from the phase mask are of the same handedness; therefore a third mirror is not required when working with poor spatial profile beams to compensate for any wave-front or intensity non-uniformities (Askins *et al*, 1992). As with the previous two-beam interferometer, a stable experimental set-up is required for multi-pulse exposure.

Considering the geometry of the interferometer, it can be shown that the half-angle between the intersecting beams at the fibre, θ_c is given by

$$\theta_c = \theta_p + 2\theta_m \quad (3.1)$$

where θ_p is the half angle between the diffracted first orders of the phase mask. Substituting into equation 2.24 the Bragg wavelength, λ_b , can be expressed as

$$\lambda_b = \frac{n_{eff}\lambda_w}{\sin(\theta_p + 2\theta_m)} \quad (3.2)$$

Using the expression for the phase mask angle, given in equation 2.27, equation 3.2 becomes

$$\lambda_b = \frac{n_{eff}\lambda_w}{\sin\left[\sin^{-1}\left(\frac{\lambda_w}{\Lambda_{pm}}\right) + 2\theta_m\right]} \quad (3.3)$$

When $\theta_m=0^\circ$ ($\theta_c=\theta_p$) the interferometer meets the condition for achromatic response and equation 3.3 reduces to equation 2.28. The interferometer is then essentially

equivalent to the far-field phase mask system described by Kashyap *et al* (1993). More generally when $\theta_m \neq 0$ this achromatic response no longer holds.

A plot of the Bragg wavelength against mirror angle for a laser wavelength of 244nm is shown by the solid line in figure 3.13. It can be seen that as θ_m increases from zero the Bragg wavelength decreases to a minimum at 365nm when the interfering beams are counter-propagating ($\theta_m=37^\circ$, $\theta_c=90^\circ$), a configuration that is not obtainable in practice. If the mirror angle is further increased, the geometry is changed to that shown in figure 3.12(b), and the Bragg wavelength now increases. Differentiating equation 3.2 with respect to λ_w , gives the sensitivity of λ_b to changes in λ_w , $d\lambda_b/d\lambda_w$, which can be shown to be

$$\frac{d\lambda_b}{d\lambda_w} = \frac{n_{eff}}{\sin \left[\sin^{-1} \left(\frac{\lambda_w}{\Lambda_{pm}} \right) + 2\theta_m \right]} \quad (3.4)$$

$$- \frac{n_{eff} \lambda_w \cos \left[\sin^{-1} \left(\frac{\lambda_w}{\Lambda_{pm}} \right) + 2\theta_m \right]}{\sin^2 \left[\sin^{-1} \left(\frac{\lambda_w}{\Lambda_{pm}} \right) + 2\theta_m \right] \cdot \left[\Lambda_{pm} \sqrt{1 - \frac{\lambda_w^2}{\Lambda_{pm}^2}} \right]}$$

A plot of $d\lambda_b/d\lambda_w$ against θ_m is shown by the dashed line in figure 3.13. This shows the sensitivity of the Bragg wavelength to changes in source wavelength is dependent upon the interferometer chosen. Using the example from the previous section of a grating written around 800nm with an initial writing wavelength of 244nm, for geometry 3.12(a) $d\lambda_b/d\lambda_w=1.4$ and for geometry 3.12(b) $d\lambda_b/d\lambda_w=5.1$ (c.f. $d\lambda_b/d\lambda_w=3.3$ for the interferometer in section 3.2.4).

The above analysis does not take into account the effects that tilting the writing beam out of the plane of the interferometer would have on the Bragg wavelength and sensitivity to source wavelength changes. Figure 3.14 defines the out-of-plane angles for geometry 3.12(b), from which it can be shown that the true half

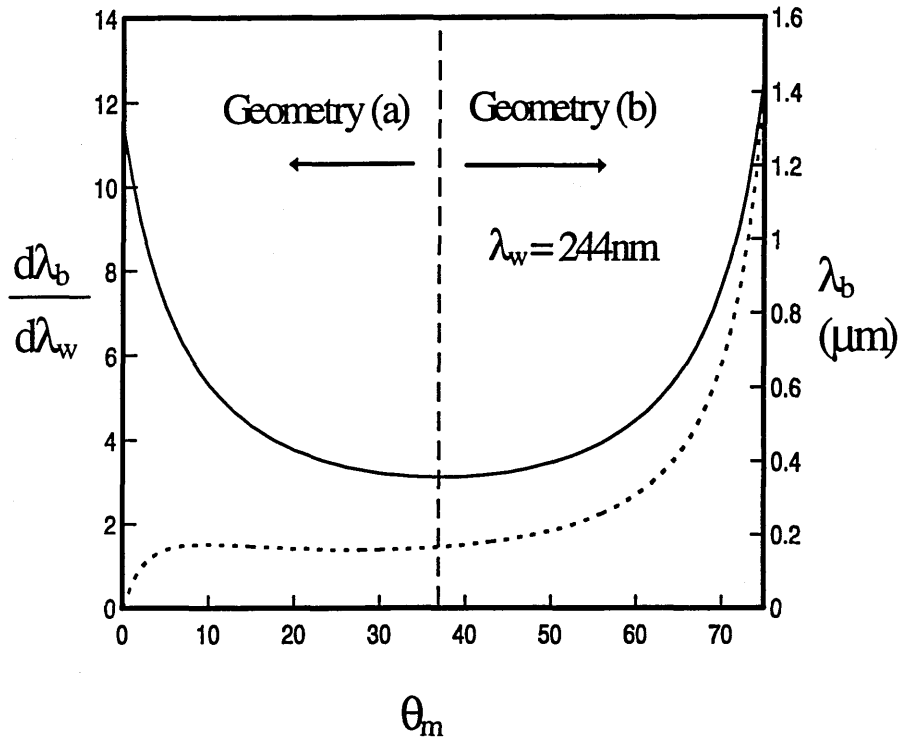


Figure 3.13 Graph showing the dependence of the Bragg wavelength λ_b , solid line, and the Bragg wavelength sensitivity $d\lambda_b/d\lambda_w$, dashed line, upon the mirror angle θ_m .

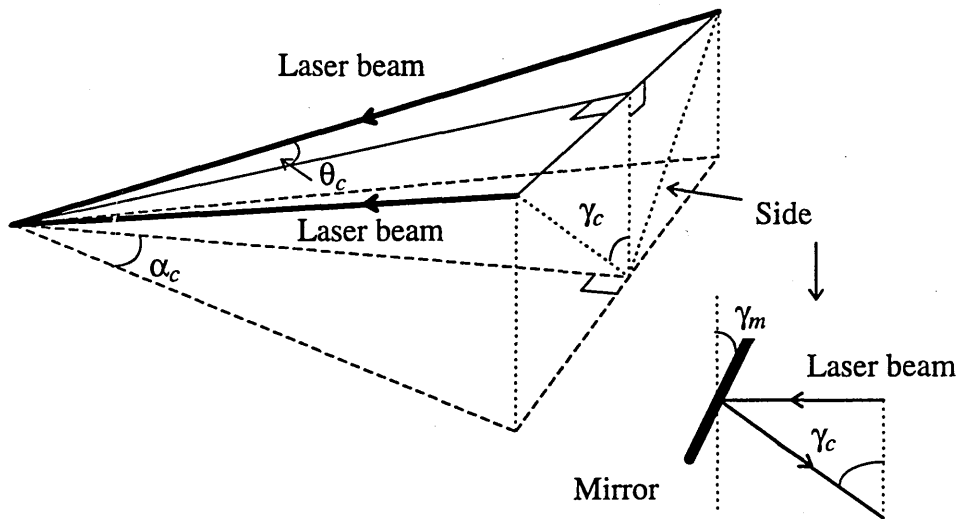


Figure 3.14 Out of plane tilting of writing beams in geometry 3.12(b).

angle between the intersecting beams, θ_c is related to the in-plane half angle, α_c and the out-of-plane half angle, γ_c by the expression

$$\frac{1}{\tan^2 \theta_c} = \frac{1}{\tan^2 \alpha_c} + \frac{1}{\tan^2 \gamma_c} \quad (3.5)$$

where in analogy to equation 3.1

$$\alpha_c = \theta_p + 2\theta_m \quad (3.6)$$

Also, γ_c is related to the out-of-plane mirror tilt angle, γ_m , by

$$\gamma_c = \frac{\pi}{2} - 2\gamma_m \quad (3.7)$$

Using equations 3.5 to 3.7 it can be shown that a modified form of equation 3.3, which takes into account the out-of-plane mirror tilt angle, γ_m , is given by

$$\lambda_b = \frac{n_{eff} \lambda_w}{\sin \left[\tan^{-1} \left[\sqrt{\frac{\tan^2 \left(\sin^{-1} \left(\frac{\lambda_w}{\Lambda_{pm}} \right) + 2\theta_m \right) \cdot \cot^2 2\gamma_m}{\tan^2 \left(\sin^{-1} \left(\frac{\lambda_w}{\Lambda_{pm}} \right) + 2\theta_m \right) + \cot^2 2\gamma_m}} \right] \right]} \quad (3.8)$$

Equation 3.8 reveals that for the out-of-plane mirror tilt angle, $\gamma_m=5^\circ$, used in geometry 3.12(b), the Bragg wavelength of a grating written around 800nm ($\lambda_w=244\text{nm}$) would be 2.4nm less than for a grating written with $\gamma_m=0^\circ$. To derive $d\lambda_b/d\lambda_w$ from equation 3.8, a mathematics computer software package was used. The derived expression for $d\lambda_b/d\lambda_w$ is lengthy and for succinctness it is not shown here, but is given in appendix C. Using this expression for $d\lambda_b/d\lambda_w$, it was calculated that there is a less than a 0.02 change in $d\lambda_b/d\lambda_w$ for a grating written at 800nm ($\lambda_w=244\text{nm}$) with $\gamma_m=5^\circ$ compared to an 800nm grating written with $\gamma_m=0^\circ$. Therefore, for gratings written around 800nm with geometry 3.12(b), equation 3.4 should provide a close approximation to $d\lambda_b/d\lambda_w$.

One drawback of the technique is that since θ_p , and consequently θ_c , are wavelength dependent, significant changes in λ_w require that the interferometer has to be translated with respect to the optical fibre to maintain the overlap of the two interfering beams. This is the same problem that is encountered when tuning the centre wavelength by varying the mirror angle. In order to compensate for changes in θ_p the distance of the phase mask from the turning mirrors was varied using a micrometer driven translation stage.

To demonstrate the operation of the system, gratings were written into Andrew Corp. E-series (820nm) fibre which had been hydrogen loaded for 3 days at 175bar. The fibres were exposed for up to 5 minutes with average writing powers of approximately 30mW. A series of gratings was written for each of the two geometries. For geometry 3.12(a) gratings were written at two different source wavelengths and for geometry 3.12(b) at four different source wavelengths. After exposure transmission spectra were obtained using the monochromator with a 900 lines per mm grating and the white light source (monochromator resolution 0.6nm). Transmission spectra for gratings written using geometries 3.12(a) and (b) are shown in figures 3.15(a) and (b) respectively. The strong wavelength dependence of the background transmission seen on these spectra were due to the use of a 50:50 coupler that had been designed for 1300/1550nm operation. Since the IFBGs were written into Hi-Bi fibres, light in each of the principal axis will be reflected at a slightly different Bragg wavelength, the wavelength separation being determined by the fibre birefringence (see section 2.2.2). For the gratings shown in figure 3.12, the Bragg wavelength separation of the polarisation states was calculated from equation 1.1 ($n_{eff} = 1.46$) and the fibre birefringence, and was found to be in the range 0.08-0.09nm (depending upon λ_b). As the monochromator resolution was 0.6nm, the individual Bragg reflection wavelengths for the two polarisation states could not be resolved.

Table 3.3 summarises the results, comparing the experimentally determined Bragg wavelength spacings to those calculated theoretically. As in section 3.2.4 this is done by calculating $d\lambda_b/d\lambda_w$ from the Bragg wavelength and writing wavelength for

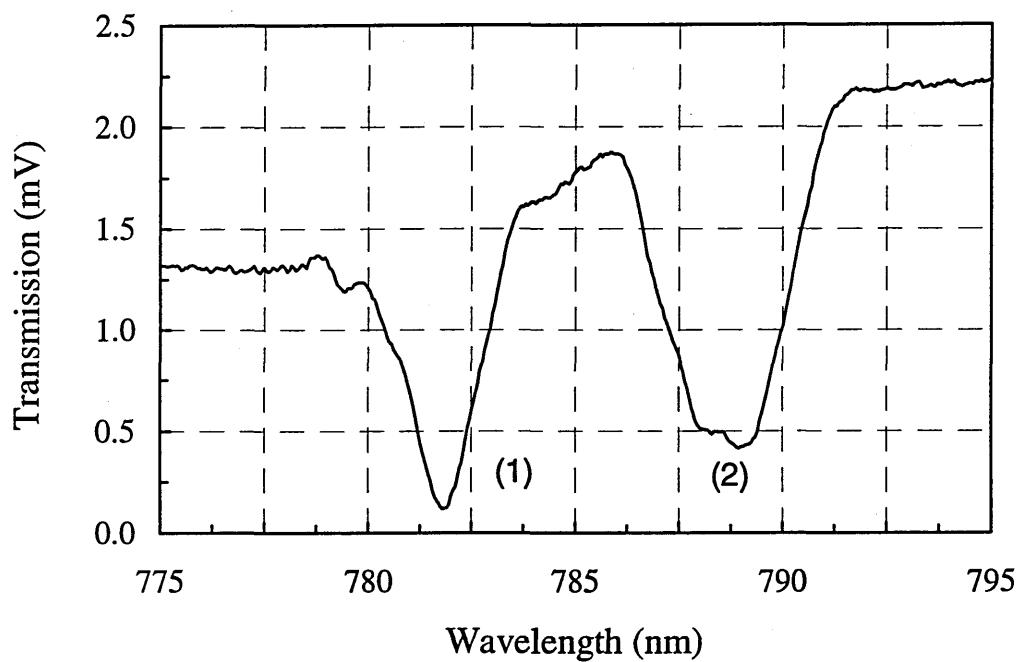


Figure 3.15(a) Monochromator scans showing transmission spectra of grating arrays written into Andrew Corp. E-series (820nm) fibre using geometry 3.12(a).

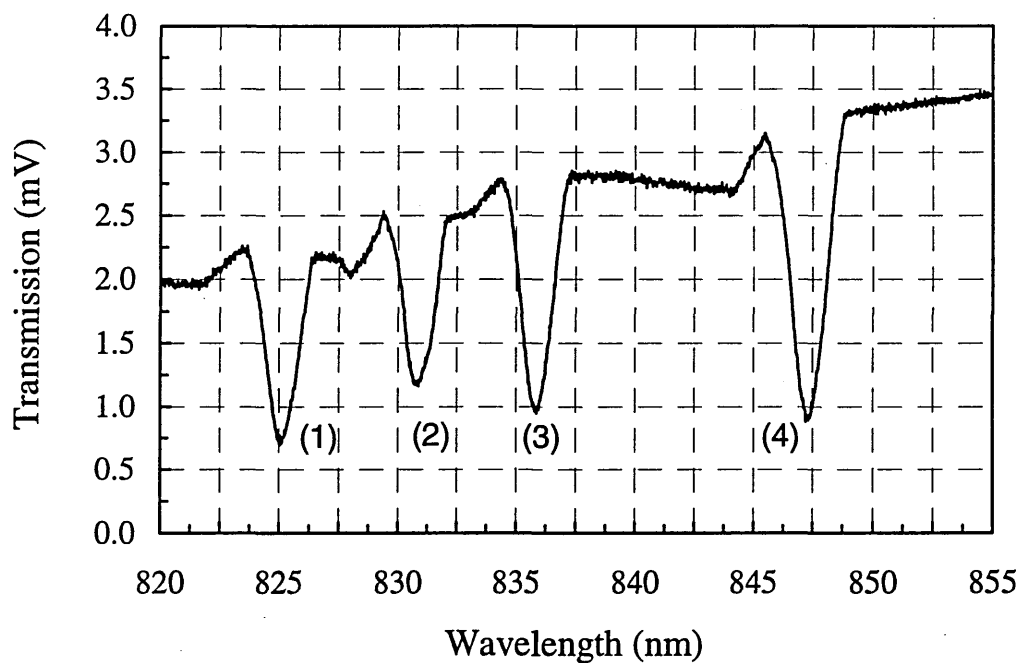


Figure 3.15(b) As figure (a) except gratings written using geometry 3.12(b).

Grating	Bragg wavelength, λ_b (nm)	Writing wavelength, λ_w (nm)	Measured wavelength spacing, $\Delta\lambda_b$ (nm)	Theoretical wavelength spacing, $\Delta\lambda_b$ (nm)
Geometry (a)				
1 2-1	825.0 \pm 0.2	240.00 \pm 0.02	5.9 \pm 0.6	5.5
2 3-2	830.9 \pm 0.2	241.00 \pm 0.02	5.0 \pm 0.6	5.5
3 4-3	835.9 \pm 0.2	242.00 \pm 0.02	11.4 \pm 0.6	11.1
4	847.3 \pm 0.2	244.00 \pm 0.02		
Geometry (b)				
1 2-1	781.8 \pm 0.2	240.00 \pm 0.02	7.2 \pm 0.5	7.0
2	789.0 \pm 0.2	245.00 \pm 0.02		

Table 3.3 Comparison of experimental and theoretical wavelength spacings for gratings written using a two-beam interferometer with a phase mask beamsplitter.

each grating. This time using equations 3.3 and 3.4 ($n_{eff}=1.46$). However, in this case $d\lambda_b/d\lambda_w$ slowly varies with λ_w , so to determine the theoretical wavelength spacing the average value of $d\lambda_b/d\lambda_w$ is calculated for adjacent grating pairs. As can be seen from table 3.3, the measured wavelength spacings agreed with the expected shifts, within the limits of experimental error.

The theoretical analysis and experimental work have demonstrated that the phase mask based interferometer has two distinct regimes of operation. Geometries 3.12(a) and (b) offer fine and coarse tuning of the Bragg wavelength respectively. This allows greater accuracy in determining the Bragg wavelength in the former case, and increased spectral coverage in the latter. Using the specifications of the laser system given in table 3.1: for the case of an 800nm grating with an initial writing wavelength of 244nm, geometry 3.12(a) has a Bragg wavelength accuracy of 0.03nm and geometry 3.12(b) has a spectral coverage of 51nm. (c.f. the 0.07nm Bragg wavelength accuracy and 33nm spectral coverage of the interferometer in section 3.2.4). These values, however are specific to the period of the phase mask used. By appropriate selection of the phase mask the Bragg wavelength accuracy or spectral coverage can be increased, so that the wavelength sensitivity of the system can be tailored to the required application. Of course, the practical limitations discussed in section 3.2.4 will also apply to the geometries shown in figure 3.12.

If in future, higher power, broadly tuneable sources become available for the UV, then the technique could be used for in-line writing of gratings in fibre being pulled from a drawing tower.

3.3 Grating characteristics

A systematic study of the dependence of grating formation on writing parameters was not undertaken. However, for the two-beam mirror interferometer writing technique, the range of conditions used for fabrication of WDM grating arrays

were established. Also in this section, the spectral characteristics of IFBGs fabricated using both the two-beam mirror interferometer and the near-field phase mask technique are summarised, as are effects associated with hydrogen loading.

3.3.1 Writing conditions used to fabricate WDM grating arrays using the two-beam mirror interferometer

In the preceding sections the average laser power used to fabricate IFBGs has been quoted. However, strictly speaking, it is the laser energy/power density incident on the optical fibre that is important, rather than the average laser power. For gratings written using the two-beam interferometer, the method used to fabricate the majority of WDM grating arrays, an assessment was made of the energy density per pulse incident on the optical fibre using the laser beam analyser (LBA) (see section 3.1.2). Figure 3.16 shows a three-dimensional, wire-frame representation of the focused beam intensity profile in the plane of the optical fibre for mirror interferometer writing. The intensity profile is of a laser beam with 28mW average power that has been apertured by a ~2mm wide knife edge slit before being focused at the fibre. The beam has dimensions of 2.8mm x 0.4mm (the beam widths being calculated using the method given in appendix A) and a peak energy density of 81mJcm^{-2} . As a result of passing through the aperture, the beam had an almost top hat intensity profile along the major axis, though diffraction at the aperture degraded the edge definition. Therefore, providing that the fibre core was aligned with the centre of the UV beam, the energy density would have been close to the quoted peak value along most of the exposed core length. The mirror interferometer was operated at the focus condition shown in figure 3.16 throughout the fabrication of WDM grating arrays. From the LBA measurements, it was estimated that the energy density per pulse incident on the fibre was in the range $70\text{-}145\text{mJcm}^{-2}$ corresponding to an average laser output power of 25-50mW.

As an aside. In a separate investigation, it was found that when IFBGs were written with tightly focused beams there was a risk of damaging the fibre, particularly

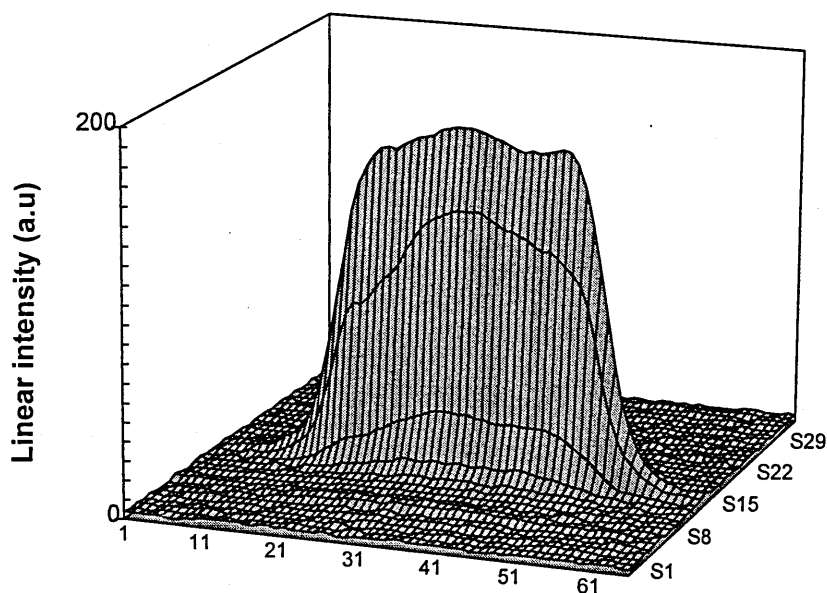


Figure 3.16 Three-dimensional wire-frame representation of a focussed laser beam profile in the plane of the optical fibre for the two-beam mirror interferometer.

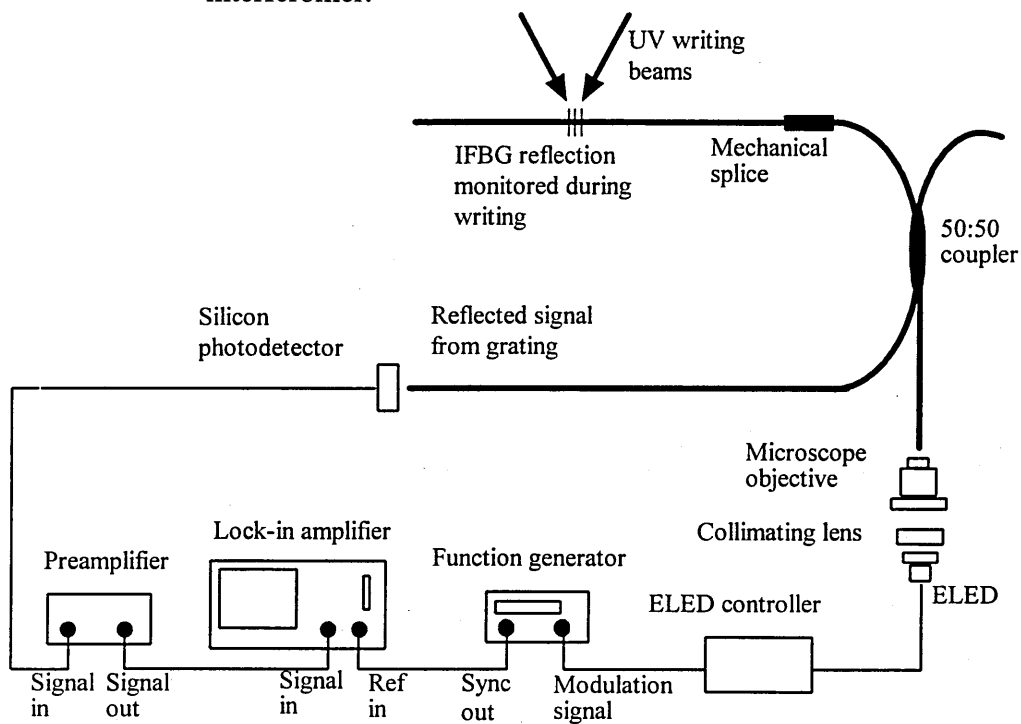


Figure 3.17 Experimental arrangement for monitoring the growth of an IFBG during fabrication.

for long exposure periods. For example, it was found that exposing a Spectran (780nm) fibre to a highly focused 35mW beam for 1 minute, sufficiently weakened the fibre so that it broke easily when handled. For these focus conditions, it proved difficult to establish a reliable figure for the energy density per pulse at the fibre, though there was no evidence of type II grating formation for which the energy density threshold is $\sim 1\text{Jcm}^{-2}$ (Malo *et al*, 1993). It was thought that the fibre was weakened by thermal damage, since when viewed under a microscope the fibre surface was visibly marked.

An assessment was made of how, during UV exposure, the Bragg reflection signal grew over time for typical gratings written into Spectran (780nm) fibre using the two-beam mirror interferometer. This was done by monitoring the component of a broadband ELED source that was reflected by the IFBG during writing. A diagram of the experimental configuration is shown in figure 3.17. The ELED (EG&G S86018E) had a 0.4mW power output, a 21nm FWHM and the peak wavelength was at 832nm. The ELED was launched into a 50:50 fibre coupler and approximately 1 μ W emerged from each of the fibre coupler output arms. A spectral scan of the ELED taken at an output of the 50:50 coupler is shown in figure 3.18 (monochromator with 1800 lines per mm grating, 0.35nm resolution). The reflected signal from the grating was monitored using a silicon photodiode and the same lock-in detection technique that was used as in section 3.2.2. However, instead of using a chopper wheel, the ELED was directly modulated by a square wave signal supplied by a Stanford Research DS345 function generator (133Hz modulation frequency). The TTL synchronisation signal from the function generator served as the reference frequency for the lock-in amplifier.

The experiment was performed at several different writing wavelengths in the range 240-250nm but any variation in the writing efficiency across this range was masked by the laser power instability. An example growth curve for an IFBG written into Spectran (780nm) fibre is shown in figure 3.19. The writing wavelength was 249nm and the grating was written over a 500s period. The peak pulse energy density at the fibre was measured to be 98mJcm^{-2} using the LBA. A transmission spectrum of

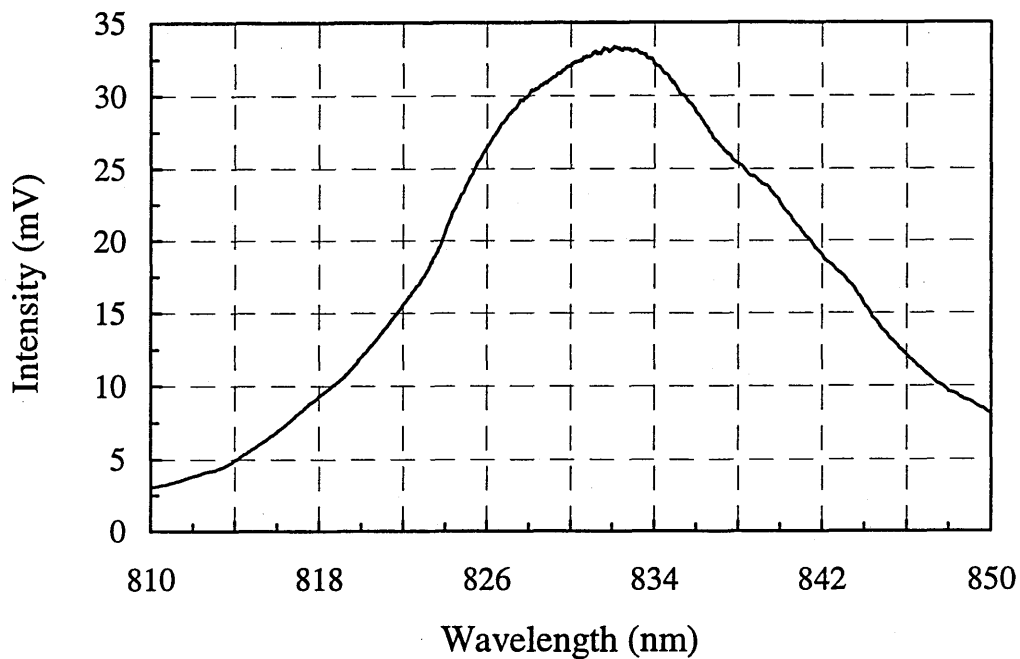


Figure 3.18 Monochromator scan showing the ELED spectral profile at the output of the 50:50 coupler.

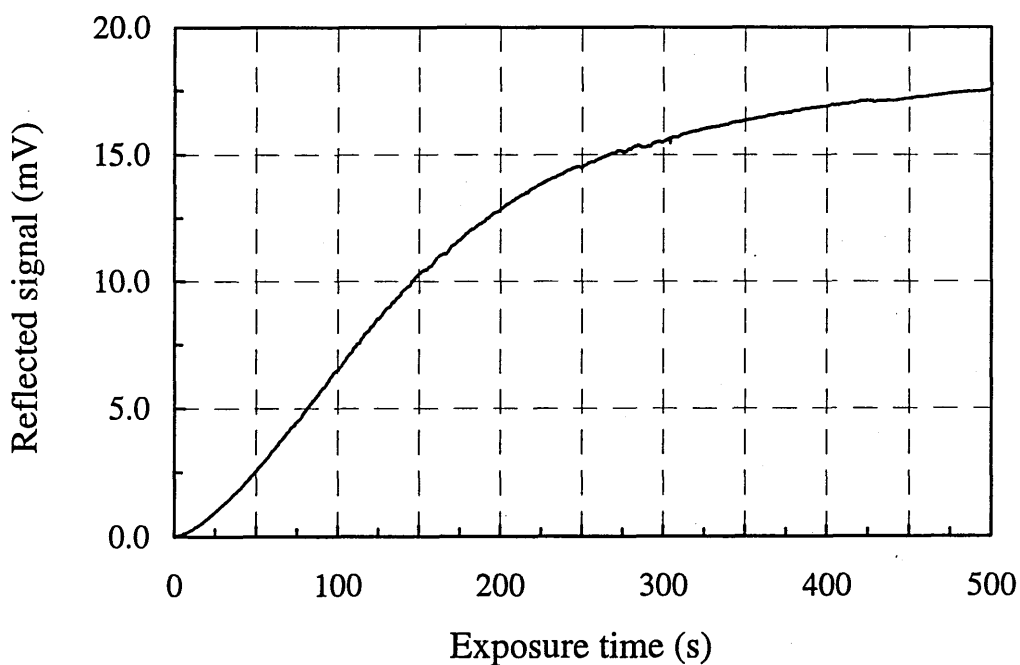


Figure 3.19 Growth of Bragg reflection during UV exposure for a grating written into Spectran (780nm) fibre using the two-beam mirror interferometer.

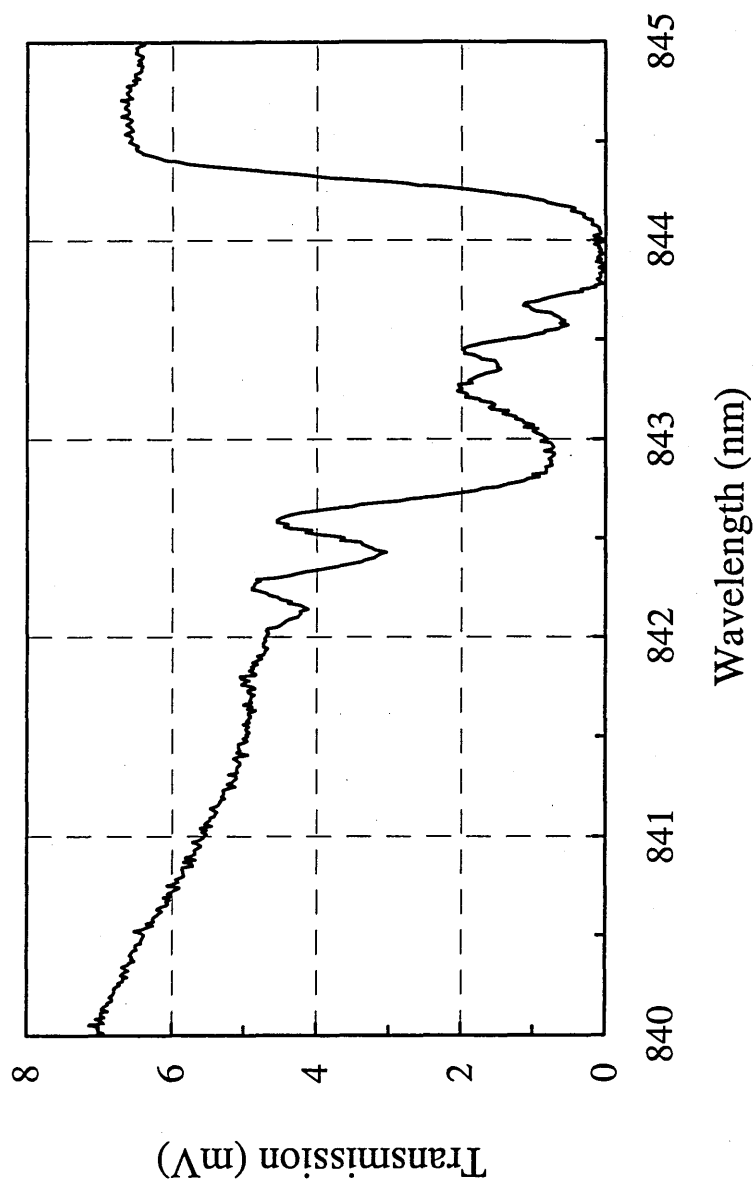


Figure 3.20 Monochromator scan showing the transmission spectrum of a saturated grating written into Spectran (780nm) fibre using the two-beam mirror interferometer.

the grating taken at the end of the exposure period (monochromator with the 1800 lines per mm grating, 0.35nm FWHM resolution) revealed that the IFBG had an almost 100% saturated reflectivity, as shown in figure 3.20. It can be seen from figure 3.20 that there is extended, structured transmission dropout on the short wavelength side of the grating and it was thought that these features were a result of the back-reflected fundamental mode being coupled into cladding and radiation modes (Mizrahi and Sipe, 1993). The short wavelength transmission dropout will be discussed further in the following section.

3.3.2 Grating spectral characteristics

As has already been mentioned in section 3.2.3, limited monochromator resolution prevented the observation of grating sideband features. To demonstrate this point, the reflection spectrum of a typical grating written into hydrogen loaded Spectran (780nm) fibre, using the two-beam mirror interferometer, is shown in figure 3.21. The spectrum was acquired using a 0.1nm resolution Monolight Optical Spectrum Analyser (at British Aerospace, Sowerby Research Centre). The experimental arrangement is described in more detail in section 4.3.3, where it is discussed in context with the rest of the experimental work performed at British Aerospace. It is only mentioned here because the IFBG spectra acquired using this system were the highest resolution obtained during the project. The reflectivity of the spectrum shown in figure 3.21 was estimated from the transmission minimum, measured at the time of fabrication using the monochromator system described in section 3.2.2 (1800 lines per mm grating, 0.35nm FWHM resolution). The writing parameters and the grating characteristics are listed in table 3.4. Coupled-mode theory was used to calculate the reflection spectrum of a uniform grating using the parameters listed in table 3.4 (see section 2.1.2). From the grating length, peak reflectivity and Bragg wavelength, the photoinduced refractive index modulation was calculated using equation 2.22. The calculated index modulation of 1.1×10^{-4} was in-line with previously reported values for gratings written into hydrogen loaded fibres

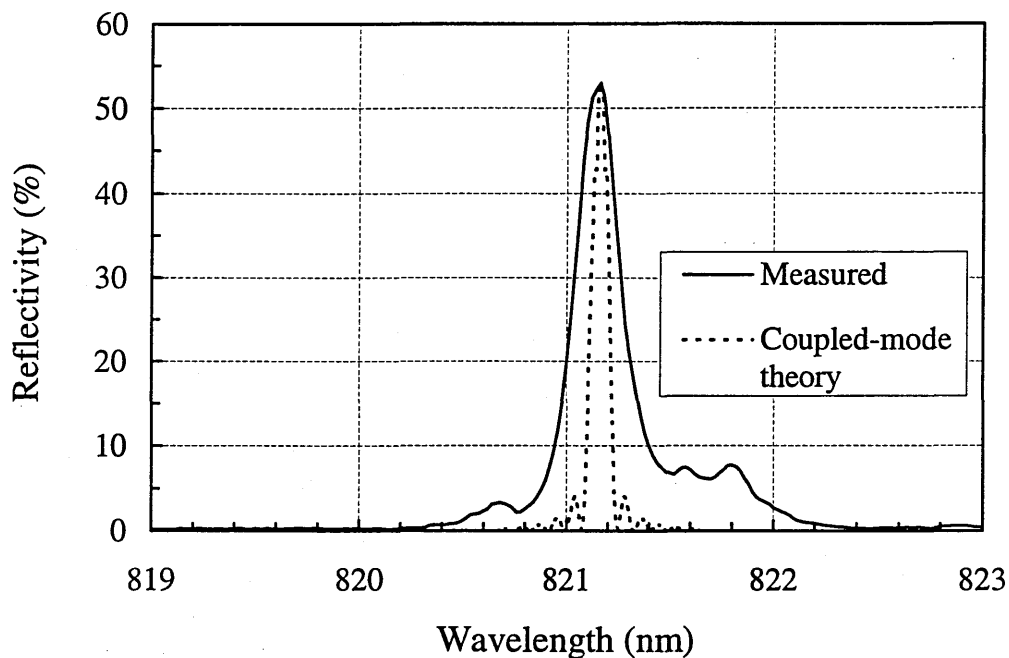


Figure 3.21 A spectrum analyser trace showing the reflection spectrum of an IFBG written into Spectran (780nm) fibre using the two-beam mirror interferometer. Also shown is a theoretical plot calculated from coupled-mode theory.

Fibre Type	Hydrogen loaded Spectran (780nm)
Average laser Power (mW)	32
Pulse energy density (mJcm^{-2})/ average power density (Wcm^{-2}) at fibre	93/2.3
Exposure time (s)	180
Grating length (mm)	2.8
Bragg wavelength, λ_b (nm)	821.2
Peak reflectivity (%)	53
Measured FWHM (nm) (monochromator resolution 0.1nm FWHM)	0.26
Refractive index modulation, Δn , calculated from coupled-mode theory	1.1×10^{-4}
Theoretical FWHM (nm)	0.11
Theoretical full bandwidth, B_w (nm)	0.17

Table 3.4 Comparison of the experimental and theoretical characteristics of the IFBG shown in figure 3.21.

with low germania dopant levels (Atkins *et al*, 1993). Using the calculated index modulation, a theoretical IFBG spectrum was obtained using equation 2.21 (assuming $n_{eff}=1.46$) and this is also shown in figure 3.21. From the theoretical plot, it can be clearly be seen that the predicted sidebands fall well within the main experimentally determined peak.

The structure surrounding the main experimental peak is now unaccounted for, but this can be explained as follows. Often the laser beam power fell during writing and it became necessary to readjust the non-linear crystals in the UVX3 wavelength extension unit. This caused a slight beam steer which could have resulted in the Bragg wavelength being shifted by a small amount during grating fabrication. Taking into consideration the monochromator bandwidth, the measured FWHM was still broader than would have been expected for a uniform grating. This could be due to any one of a number of reasons, such as: laser beam steer as previously mentioned, environmental perturbations to the interferometer, non-uniformities in the laser beam intensity profile, and the laser source having a less than perfect spatial coherence.

A full bandwidth value, B_w , was also calculated for the theoretical reflection spectrum using equation 2.23 and is given in table 3.4. Unfortunately, the side structure on the experimental spectrum made it impossible to obtain a meaningful measurement of B_w .

The full bandwidth was also calculated for gratings written around 1300nm using the near-field phase mask technique. For these gratings, the value of B_w predicted from coupled-mode theory was generally around 0.4nm (twice the B_w of the 820nm grating). Since the monochromator system used to acquire the grating spectra, written using the phase mask, had a resolution of only 0.6nm FWHM (6 times worse than the Monolight spectrum analyser), it is unsurprising that sidebands could not be seen on these spectra either.

On many of the IFBG transmission spectra, dropouts were seen on the short wavelength side of the gratings that were not represented in the reflection spectra. This short wavelength feature was particularly evident on strong gratings. To

illustrate this, figures 3.22(a) and (b) show respectively the transmission and reflection spectra acquired for a grating written into OF Deeside (1300nm) fibre using the near-field phase mask technique (monochromator with 900 lines per mm grating, 0.6nm resolution). The transmission spectrum was normalised by dividing through by the maximum transmitted signal recorded during the wavelength scan. As previously, the peak reflectivity was estimated from the transmission minimum. Mizrahi and Sipe (1993) proposed that this short wavelength loss was a result of the back-reflected fundamental mode being coupled into radiation modes. The radiation mode coupling being modulated by a, Fabry-Pérot like, resonant structure imposed by the cladding. For the majority of gratings fabricated in this work, usually only a single sideband loss was seen accompanying the main peak, as shown in figure 3.22(a). Hewlett *et al* (1995) demonstrated that the strength and distribution of cladding mode resonances are highly sensitive to the grating blaze angle. Further, that the transmission spectra of blazed gratings written into depressed-cladding fibre are characterised by a dominant single sideband loss. Therefore, it may be that preferential coupling into a single cladding mode, due to a slight grating tilt angle, is responsible for the type of spectrum shown in figure 3.22(a). Alternatively the sideband loss could be attributable to coupling into a leaky fibre mode, as has been observed in depressed cladding fibre by Morey *et al* (1994). However, this is merely conjecture, since the OF Deeside fibre did not have a depressed cladding and no further investigation has been performed to validate either theory. The saturated grating spectrum shown in figure 3.20 may be explained by multiple cladding mode resonances, which modulate a strong radiation mode loss.

An example of an IFBG with an extended radiation mode loss is shown in figure 3.23. This shows a transmission spectrum of an IFBG written into a non-hydrogen loaded Andrew Corp. D-series (1550nm) fibre using the near-field phase mask technique (monochromator with 900 lines per mm, 0.35nm resolution). Of all the fibres types investigated only the Andrew Corp. fibre was sufficiently photosensitive to allow gratings to be written without hydrogen loading. The enhanced photosensitivity was almost certainly due to the high germania dopant

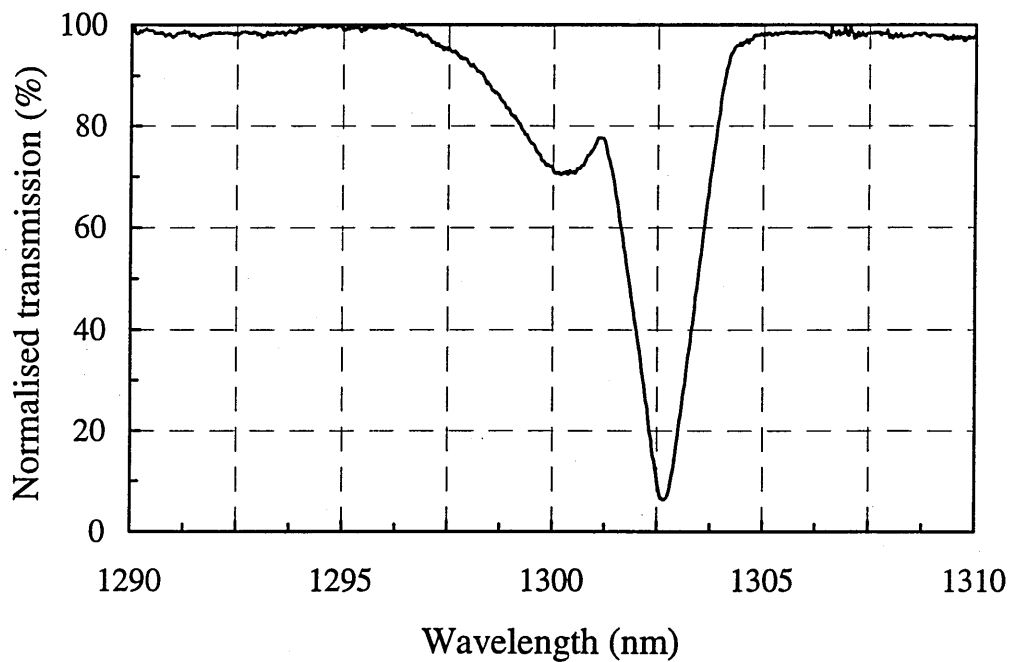


Figure 3.22(a) Monochromator scan showing a transmission spectrum of a grating written into OF Deeside (1300nm) fibre using the near-field phase mask method and accompanying short wavelength loss.

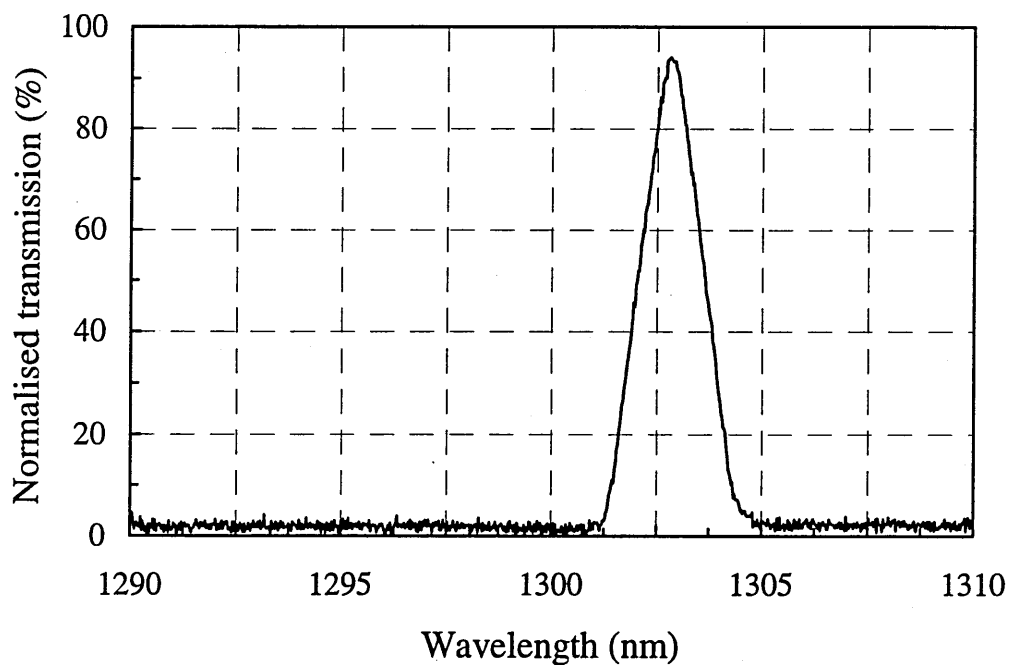


Figure 3.22(b) Monochromator scan showing the reflection spectrum of grating in (a).

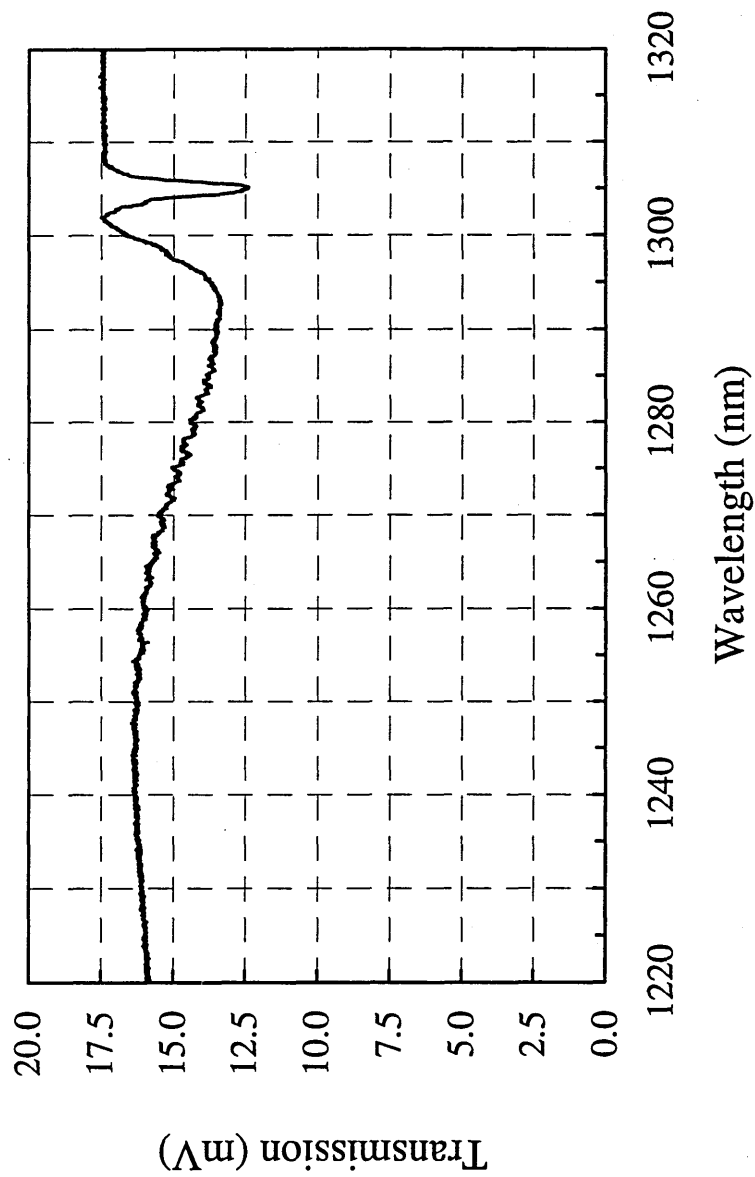


Figure 3.23 Monochromator scan showing the transmission spectrum of a grating written into Andrew Corp. D-series (1550nm) fibre using the near-field phase mask method and radiation mode loss.

concentration within the fibre core (18%). The grating was written using an average laser power of 25mW over a period of 350s, and had a peak reflectivity of ~30% (measured from the transmission minimum).

The short wavelength loss accompanying the grating was relatively strong and extended over 50nm. The ripple in the loss feature seemed to indicate the presence of cladding mode structure. Though it has to be said that the amplitude of the ripple is so slight, that one cannot discount it simply being due to noise on the spectrum. Unfortunately, the limited monochromator resolution prevented this from being clearly resolved. This was the only IFBG that exhibited such a smooth radiation mode loss, and it was unclear why this should be the case; although, it could be related to the cladding geometry of the D-series fibre.

Surprisingly, gratings could not be written into a similarly doped Andrew Corp. E-series (820nm) fibre using the two-beam mirror interferometer. This may have been due to the greater stability of the phase mask technique compared to the mirror interferometer.

Comparing optical fibre transmission spectra before and after UV exposure revealed no evidence of any significant broadband losses induced by IFBG fabrication, other than the short wavelength loss discussed above.

3.3.3 Bragg wavelength shift and optical fibre absorption band associated with hydrogen loading

After hydrogen loading, IFBGs could be readily fabricated in all the fibre types listed in appendix B. Gratings were normally written into fibres within a few hours of being taken out of the hydrogen tube, although IFBGs were written into fibres, with reduced efficiency, up to 24 hours after they had been removed from the hydrogen atmosphere.

An investigation into the effects of hydrogen loading on IFBGs written using the near-field phase mask technique, not only demonstrated that the Bragg wavelength of a grating shifted over time as the hydrogen diffused out of the fibre

core but, interestingly, revealed an absorption band around 1245nm that was associated with the presence of molecular hydrogen within the core.

Figures 3.24(a) and (b) show transmission spectra of an IFBG written into an OF Deeside (1300nm) fibre using the two-beam mirror interferometer (monochromator with 900 lines per mm grating, 0.6nm FWHM). The transmission spectra were normalised by dividing through by the maximum transmitted signal recorded during each wavelength scan. Figure 3.24(a) shows the spectrum of the IFBG acquired within 10 minutes of fabrication. In addition to the grating, a very strong transmission dropout around 1245nm can be seen that had a 9.3nm FWHM. On further investigation it was found that there was no evidence of this feature on the reflection spectrum, and it was not present on non-hydrogen loaded fibre. However, the 1245nm loss band was present on the transmission spectrum of a hydrogen loaded OF Deeside fibre that had not been UV irradiated. It was calculated that the initial loss shown in figure 3.24(a) was 1420dBkm^{-1} (23% loss over 0.8m). Over time, as the hydrogen diffused out of the core, the Bragg wavelength gradually reduced and the 1245nm absorption band diminished. Measurements taken of the Bragg wavelength and the absorption loss during the next 37 days are listed in table 3.5.

After 37 days no evidence of the 1245nm band could be seen and the Bragg wavelength of the grating had reduced by 1.3nm. The large shift in the Bragg wavelength, 1.3nm compared to the 0.16nm net shift seen by Malo *et al*, (1994) (see section 2.2.1), indicated that there was still a significant amount of hydrogen left within the fibre core after exposure. It can also be seen from table 3.5 that the reflectivity of the grating was not significantly affected by the diffusion of hydrogen out of the core. A transmission spectrum taken after 37 days is shown in figure 3.24(b). From section 2.2.1 it will be apparent that significant shifts in the Bragg wavelength can occur during the first few hours following the fabrication of an IFBG (Malo *et al*, 1994). Therefore, to obtain a more complete picture, any future study should include measurements taken within this period.

This 1245nm loss is almost certainly due to the H_2 first overtone absorption band that has previously been identified at 1240nm (Lemaire, 1991). The wavelength

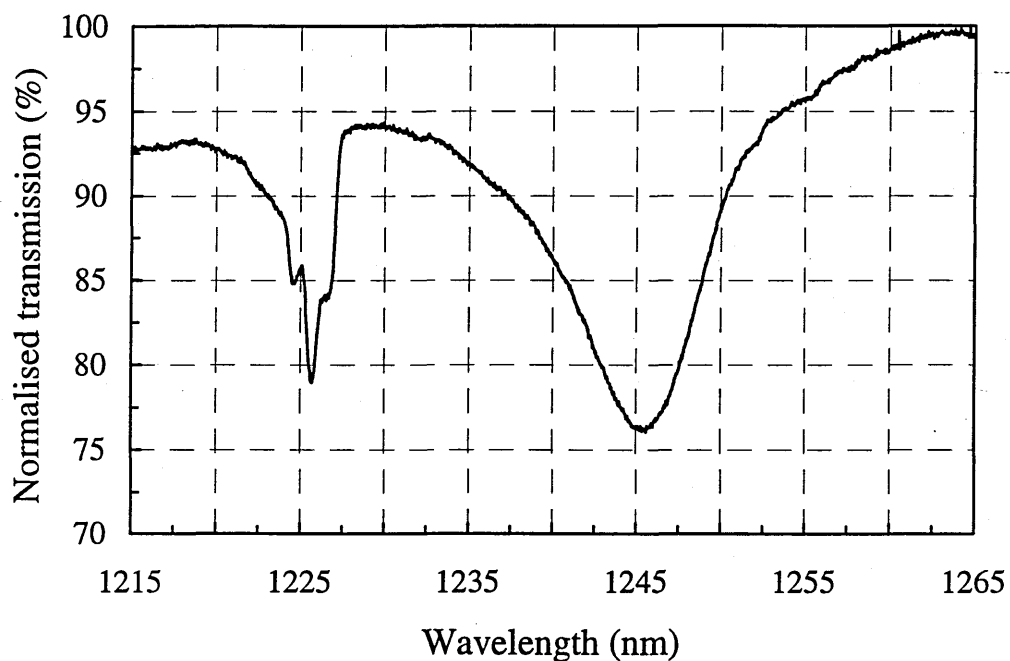


Figure 3.24(a) Monochromator scan showing a transmission spectrum of a grating written into OF Deeside (1300nm) fibre using the two-beam mirror interferometer method and a 1245nm absorption band. Spectrum taken approximately 10 minutes after grating fabrication.

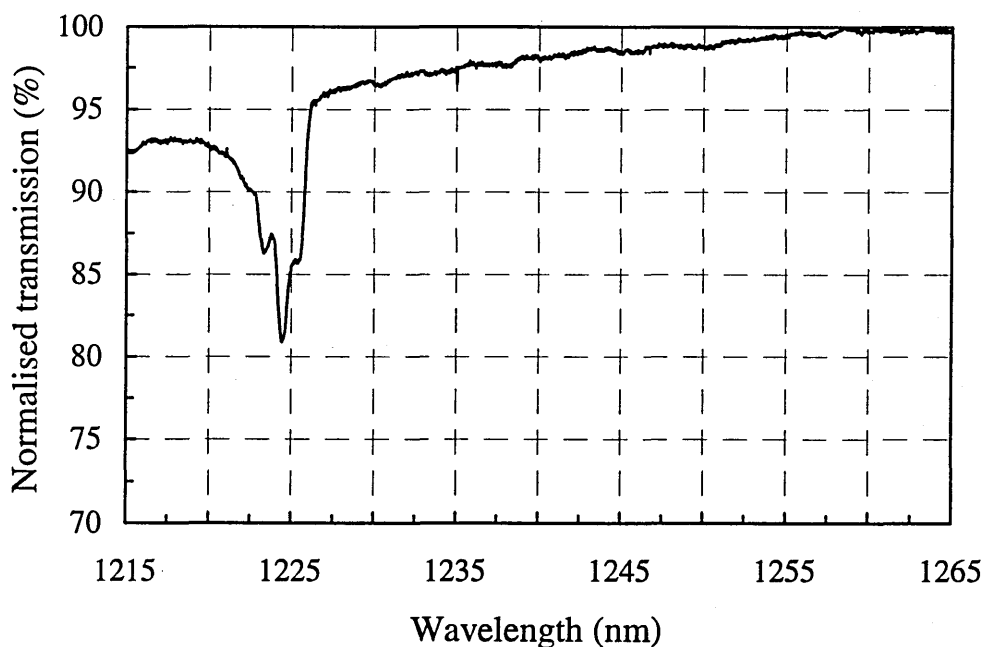


Figure 3.24(b) Monochromator scan showing a transmission spectrum of the grating in (a) 37 days after fabrication. No evidence of 1245nm absorption.

Time elapsed since fabrication	Bragg wavelength, λ_b (nm)	Estimate of peak grating reflectivity (%)	Absorption band, centre wavelength (nm)	Estimate of peak absorption loss (%)
10 minutes	1225.7 \pm 0.2	16	1245.4 \pm 0.2	23 (\equiv 1420dBkm ⁻¹)
3 days	1225.4 \pm 0.2	16	1244.9 \pm 0.2	14 (\equiv 820dBkm ⁻¹)
6 days	1224.8 \pm 0.2	16	1245.7 \pm 0.2	7 (\equiv 390dBkm ⁻¹)
37 days	1224.4 \pm 0.2	15	unmeasurable	unmeasurable

Table 3.5 Shift in the IFBG Bragg wavelength and reduction in the 1245nm absorption band over time. Grating written into an OF Deeside (1300nm) fibre using the two-beam mirror interferometer method.

difference implies that the monochromator (900 lines per mm grating) was miscalibrated in this spectral region. There was no evidence of an absorption band at 1380nm associated with Si(OH) formation (Lemaire *et al*, 1993). Indeed, no other loss bands were observed over the wavelength range 600-1600nm. The H₂ absorption band can be used to determine the concentration of molecular hydrogen within the fibre core; however this was not taken any further, since the monochromator that covered this spectral region was required for another project.

References

- Anderson, D.Z., Mizrahi, V., Erdogan, T., and White, A.E., 'Production of in-fibre gratings using a diffractive optical element', *Electron. Lett.*, **29**, pp566-568 (1993).
- Askins, C.G., Tsai, T.-E., Williams, G.M., Putnam, M.A., Bashkansky, M., and Friebele, E.J., 'Fibre Bragg reflectors prepared by a single excimer pulse', *Opt. Lett.*, **17**, pp833-835 (1992).
- Atkins, R.M., Lemaire, P.J., Erdogan, T., and Mizrahi, V. , 'Mechanisms of enhanced UV photosensitivity via hydrogen loading in germanosilicate glasses', *Electron. Lett.*, **29**, pp1234-1235 (1993).
- Bilodeau, F., Malo, B., Albert, J., Johnson, D.C., Hill, K.O., Hibino, Y., Abe, M., and Kawachi, M., 'Photosensitisation of optical fiber and silica-on-silicon/silica waveguides', *Opt. Lett.*, **18**, pp953-955 (1993).
- Fertein, E., Legoubin, S., Douay, M., Canon, S., Bernage, P., Niay, P., 'Shifts in resonance wavelengths of Bragg gratings during writing or bleaching experiments by UV illumination within germanosilicate optical fibre', *Electron. Lett.*, **27**, pp1838-1839 (1991).
- Hewlett, S.J., Love, J.D., Meltz, G., Bailey T.J., and Morey, W.W., 'Cladding-mode coupling in depressed-cladding fibre', *Electron. Lett.*, **31**, pp820-822 (1995).

- Hill, K.O., Malo, B., Bilodeau, F., Johnson, D.C., and Albert, J., 'Bragg gratings fabricated in monomode photosensitive optical fibre by UV exposure through a phase mask', *Appl. Phys. Lett.*, **62**, pp1035-1037 (1993).
- Kashyap, R., Armitage, J.R., Campbell, R.J., Williams, D.L., Maxwell, G.D., Ainslie, B.J., and Millar, C.A., 'Light-sensitive optical fibres and planar waveguides', *BT Technol. J.*, **11**, pp150-160 (1993).
- Lemaire, P.J., 'Reliability of optical fibers exposed to hydrogen: prediction of long-term loss increases', *Opt. Eng.*, **30**, pp780-789 (1991).
- Lemaire, P.J., Atkins, R.M., Mizrahi, V., and Reed, W.A., 'High pressure H₂ loading as a technique for achieving ultrahigh UV photosensitivity and thermal sensitivity in GeO₂ doped optical fibres', *Electron. Lett.*, **13**, pp1191-1192 (1993).
- Malo, B., Johnson, D.C., Bilodeau, F., Albert, J., and Hill, K.O., 'Single-excimer-pulse writing of fiber gratings by use of a zero-order nulled phase mask: grating spectral response and visualization of index perturbations', *Opt. Lett.*, **18**, pp1277-1279 (1993).
- Malo, B., Albert, J., Hill, K.O., Bilodeau, F., and Johnson, D.C., 'Effective index drift from molecular hydrogen diffusion in hydrogen-loaded optical fibres and its effect on Bragg grating fabrication', *Electron. Lett.*, **30**, pp442-443 (1994).
- Meltz, G., Morey, W.W., and Glen, W.H., 'Formation of Bragg gratings in optical fibers by a transverse holographic method', *Opt. Lett.*, **14**, pp823-825 (1989).
- Mizrahi, V., and Sipe, J.E., 'Optical properties of photosensitive fiber phase gratings', *J. Lightwave Technol.*, **11**, pp1513-1517 (1993).
- Morey, W.W., Meltz, G., and Glenn, W.H., 'Fiber optic Bragg grating sensors', in *Proc. Fibre Optic and Laser Sensors VII*, Boston, pp98-107 (1989).
- Morey, W.W., Meltz, G., Love, J.D., and Hewlett, S.J., 'Mode-coupling characteristics of UV-written Bragg gratings in depressed-cladding fibre', *Electron. Lett.*, **30**, pp730-732 (1994).

Chapter 4

Embedded Bragg grating strain sensors in carbon fibre composite

4.1 Theoretical strain and temperature sensitivity of gratings

A summary is presented below of the relationship between changes in the applied strain and Bragg wavelength shifts based upon the analysis by Measures (1992(a)).

From the Bragg condition given in equation 1.1 it can be seen that environmentally induced changes in either the effective core refractive index or the index modulation period will result in a shift in the reflected Bragg wavelength. A Taylor expansion of equation 1.1 allows the shift in Bragg wavelength, $\Delta\lambda_\alpha$, resulting from an applied strain field to be expressed as

$$\frac{\Delta\lambda_\alpha}{\lambda_{0,\alpha}} = \frac{1}{\Lambda_{0,\alpha}} \frac{\partial\Lambda_\alpha}{\partial\varepsilon_\gamma} \varepsilon_\gamma + \frac{1}{n_{0,\alpha}} \frac{\partial n_\alpha}{\partial\varepsilon_\gamma} \varepsilon_\gamma \quad (4.1)$$

where $\lambda_{0,\alpha}$ is the initial Bragg wavelength prior to the application of a strain field, for linearly polarised light in the α ($\alpha = 2,3$) directions; n_α and Λ_α are respectively the refractive index and index modulation period experienced by light polarised in the α directions ($n_{0,\alpha}$ and $\Lambda_{0,\alpha}$ being the initial values); and ε_γ ($\gamma = 1-6$) is the strain tensor,

comprising of 3 principal and 3 shear strain components. From the strain-optic effect, the fractional wavelength change due to the refractive index can be given by

$$\frac{1}{n_{0,\alpha}} \frac{\partial n_{\alpha}}{\partial \varepsilon_{\gamma}} \varepsilon_{\gamma} = -\frac{n_{0,\alpha}^2}{2} P_{\alpha\gamma} \varepsilon_{\gamma} \quad (4.2)$$

where $P_{\alpha\gamma}$ are the strain-optic coefficients. If, as always been assumed to date (e.g. Morey *et al*, 1989, Melle *et al*, 1993), the strain-induced change in the index modulation period is independent of the state of polarisation of the incident light and only dependent on axial strain, then

$$\frac{1}{\Lambda_{0,\alpha}} \frac{\partial \Lambda_{\alpha}}{\partial \varepsilon_{\gamma}} = 1 \quad (4.3)$$

Using the relationships given in equations 4.2 and 4.3 it can be shown that

$$\frac{\Delta \lambda_{\alpha}}{\lambda_{0,\alpha}} = \varepsilon_1 - \frac{n_{0,\alpha}^2}{2} \sum_{\gamma=1}^6 P_{\alpha\gamma} \varepsilon_{\gamma} \quad (4.4)$$

If a uniaxial longitudinal stress σ_x is applied to an isotropic, elastic optical fibre orientated along the x axis and we assume zero shear strain (Butter and Hocker, 1978), then

$$\varepsilon_{\gamma} = \begin{bmatrix} -\nu \varepsilon_1 \\ -\nu \varepsilon_1 \\ \varepsilon_1 \end{bmatrix} = \begin{bmatrix} -\nu \varepsilon_x \\ -\nu \varepsilon_x \\ \varepsilon_x \end{bmatrix} \quad (4.5)$$

where $\varepsilon_1 = \varepsilon_x = \sigma_x / E$ is the longitudinal strain, with E being Young's modulus; and $-\nu \varepsilon_x$ is the corresponding transverse strain, with ν being Poisson's ratio. Using the simplifications introduced by the Butter and Hocker (1978) model it can be shown that for a singlemode optical fibre

$$\frac{\Delta \lambda}{\lambda_0} = (1 - P_{eff}) \varepsilon_x \quad (4.6)$$

where P_{eff} is the effective strain-optic coefficient and is defined as

$$P_{eff} = \frac{n_{eff}^2}{2} [P_{12} - \nu(P_{11} + P_{12})] \quad (4.7)$$

with P_{11} and P_{12} being the only non-zero strain-optic coefficients for a homogeneous, isotropic optical fibre. From equation 4.6, a strain gauge factor S_B can be defined that relates the fractional Bragg wavelength shift to the applied strain, such that

$$\frac{\Delta\lambda}{\lambda_0} = S_B \varepsilon_x \quad (4.8)$$

where $S_B = (1 - P_{eff})$. Given that P_{eff} for germanosilicate glass is 0.22 (e.g. Morey *et al*, 1989 and Measures, 1992(a)), equation 4.8 gives a theoretical value for S_B of 0.78.

In addition to strain, temperature changes will also result in a Bragg wavelength shift. The fractional Bragg wavelength shift for a change in temperature ΔT being given by

$$\frac{\Delta\lambda}{\lambda_0} = (\rho + \xi) \Delta T \quad (4.9)$$

where ρ is the thermal expansion coefficient and ξ is the thermo-optic coefficient (Morey *et al*, 1989). The index change due to the thermo-optic effect being predominant. In a similar way to the strain gauge factor, a temperature gauge factor T_B can be defined, such that

$$\frac{\Delta\lambda}{\lambda_0} = T_B \Delta T \quad (4.10)$$

where $T_B = (\rho + \xi)$. The thermal coefficient values for germanosilicate optical fibres are $\rho = 0.55 \times 10^{-6}$ and $\xi = 8.3 \times 10^{-6}$ (Takahashi and Shibata, 1979). This gives a theoretical value for T_B of 8.85×10^{-6} .

The total fractional wavelength shift due to temperature and strain changes can therefore be expressed as

$$\frac{\Delta\lambda}{\lambda_0} = S_B \varepsilon_x + T_B \Delta T \quad (4.11)$$

From equation 4.11 it can be seen that, from a single measurement of the Bragg wavelength shift, it is impossible to differentiate between the effects of changes in strain and temperature. This imposes a significant limitation on the application of IFBGs to quasi-dc strain measurement. A number of techniques have

been reported to overcome this limitation and these are discussed in chapter 5, along with a new method for temperature and strain separation.

Referring back to the aircraft structural monitoring application discussed in section 1.1. Assuming that an IFBG sensor experiences $\pm 5\%$ strain over a temperature range of -50°C to 160°C . From equation 4.11, it can be seen that the maximum possible excursion of the Bragg wavelength for gratings written around 800nm, using the theoretical values of S_B and T_B given above, would be -3.5nm to +4.3nm. Thus, if WDM were to be used, adjacent IFBG sensors would have to be spaced by greater than 7.8nm to ensure there was no possibility of confusion.

4.2 Experimental determination of grating strain sensitivity

If accurate strain measurements are to be obtained from IFBG sensors, it is important that the strain gauge factor, S_B , be known as accurately as possible. Since the germanium dopant levels present in the cores of optical fibres vary between different types of fibre, and the values of the stain-optic coefficients are dependent upon germanium dopant levels (Namiyama, 1985), the true strain gauge factor can differ significantly from the theoretical value given in section 4.1. To ensure accurate strain measurements, the value of S_B should be experimentally determined for the particular type of optical fibre being deployed.

For the embedded strain sensor work, IFBGs were to be written into Spectran (780nm) singlemode fibre. The Spectran fibre was chosen for a number of reasons. Firstly, IFBGs could be readily fabricated in hydrogen loaded Spectran fibre, as has already been demonstrated in section 3.2.4. For compatibility with the detectors and broadband sources that were available for this work, Bragg wavelengths of 810nm to 840nm were desired. Also, a previous study conducted by British Aerospace (Foote, 1994; Foote and Read, 1995) demonstrated that germanosilicate fibres of similar diameter (125 μm cladding, 245 μm buffer coat) could be successfully embedded into

carbon fibre composites, and be used to monitor the structural strain of the host material. Finally, sufficient quantities of this fibre type were available.

Thus, an experimental determination was made of S_B for the Spectran fibre, using a simple strain rig and a modified version of the spectrometer system described in section 3.2.2.

4.2.1 Automated scanning monochromator with an ELED source

The manually operated, scanning monochromator system described in section 3.2.2 was found not to be sufficiently accurate or consistent for measuring shifts in Bragg wavelength that would result from an applied strain field. Errors arose in the measurement of wavelength due to small timing differences between the lock-in amplifier time base and the indicated monochromator scan speed.

For this reason, an automated version of the spectrometer was developed based upon the Bentham Monochromator with an 1800 lines per mm grating and an ELED source. The automated spectrometer system is illustrated in figure 4.1. A personal computer (PC) was used to control the monochromator scan and the acquisition of data. Both the lock-in amplifier and the stepper motor driver were connected to the PC via an IEEE/488 interface bus. Software was written for the PC, which sequentially instructed the lock-in amplifier to acquire a data point and then the stepper motor driver to advance the monochromator by a single step. As with the manually scanned system, a trace appeared on the lock-in amplifier which could be stored using the internal disk drive. The wavelength interval between successive data points was determined by the wavelength step size of the monochromator, which in this case was 0.01nm.

The data acquisition rate, of both the manual system previously described and the automated version, is limited by the time constant of the lock-in amplifier's low-pass filter. Longer time constants give a superior signal to noise performance, but at the cost of a reduced data acquisition rate. To obtain acceptable spectra from weak optical signals, such as those that occur when the monochromator slits are closed for

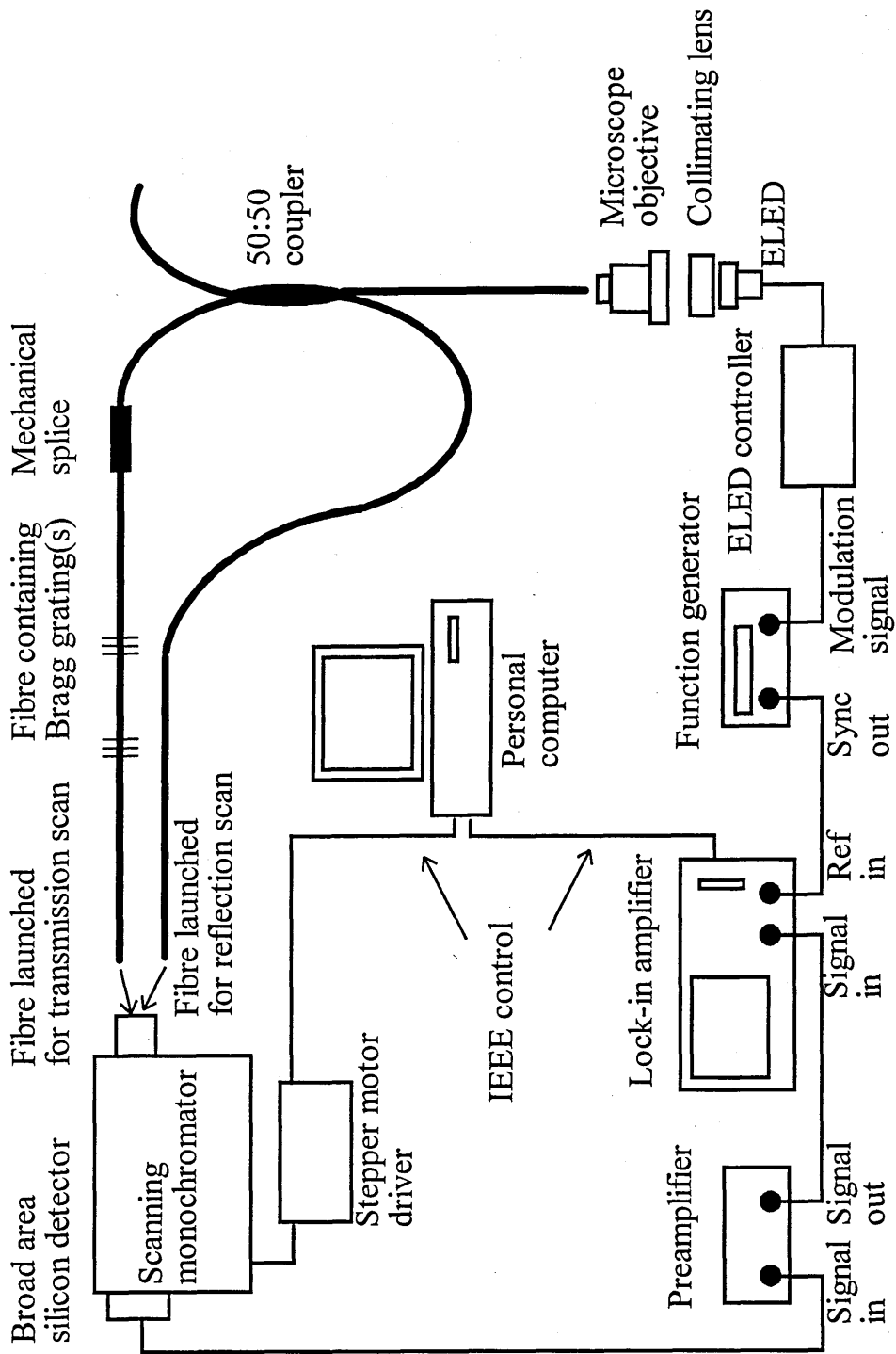


Figure 4.1 Experimental arrangement for the automated grating characterisation system, consisting of a computer controlled scanning monochromator and an ELED broadband source.

the highest resolution operation, time constants had to be used that often limited the data acquisition rate to less than 1 sample per second. Clearly this could not be achieved using manual scanning, since the front panel controls on the stepper driver allow a minimum step rate of 1 step per second. Therefore, automated control had the additional advantage of offering improved signal to noise performance.

The ELED described in section 3.3.1 was used in place of the quartz halogen lamp, because, although the white light system could be used over a large spectral range, the ELED provided a greater optical intensity over the wavelength region of interest. The higher intensity improved the signal to noise ratio of the system and allowed the Bragg wavelengths of gratings to be more accurately measured.

Compared to the previous system (section 3.2.2) the source and detector positions were reversed. A broad area (100 mm^2) silicon detector was placed at the exit slit of the monochromator and the ELED was launched directly into the fibre coupler, with approximately $1 \mu\text{W}$ of optical power emerging from each arm of the coupler. Also, instead of using a chopper wheel to modulate the source signal, the ELED was directly modulated by a square wave signal supplied by a Stanford Research DS345 function generator (133Hz modulation frequency). A TTL synchronisation signal from the function generator served as the reference frequency for the lock-in amplifier. The system could be configured to obtain either transmissive or reflective spectral profiles. The transmissive configuration gave the best signal to noise performance, since light only had to make one pass through the 50:50 coupler.

4.2.2 Determination of the axial strain gauge factor

The experimental arrangement used to apply axial strain to the optical fibre under test is shown in figure 4.2. The buffer coat was removed from the entire section of fibre under test, and the test section was fixed at both ends to V-groove mounts using superglue. One V-groove mount was held in a fixed position, the other mounted on a linear translation stage that was manually driven by a micrometer screw gauge. The fibre cladding was glued directly to the V-groove mounts, rather than the buffer

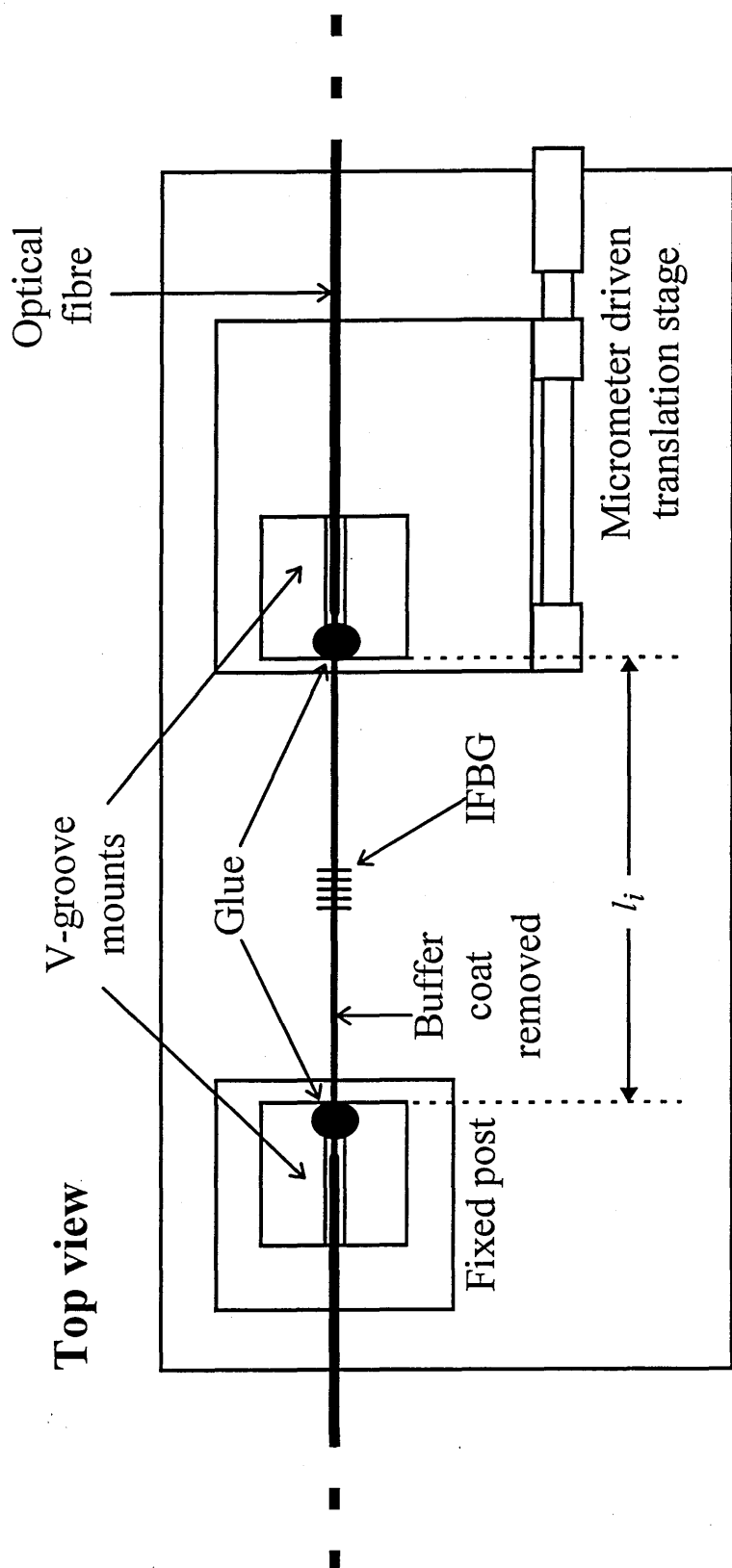


Figure 4.2 Experimental apparatus for applying strain to optical fibres.

coat, to reduce the chance of the fibre slipping under load at the glue points. Removing the buffer coat also ensured that the strain was transferred uniformly along the length of the fibre. The translation stage had a travel range of 50mm and the micrometer screw gauge could be set to an accuracy of $\pm 0.5\mu\text{m}$. The strain applied to the optical fibre ε_x by an extension of its length Δl simply being.

$$\varepsilon_x = \frac{\Delta l}{l_i} \quad (4.12)$$

where l_i is the initial length between glue points.

To begin with, the strain sensitivities of single IFBGs written into separate lengths of hydrogen loaded Spectran (780nm) fibre, using the two-beam mirror interferometer technique (see section 3.2.4), were investigated. Strain was applied to a fibre in $100\pm 5\mu\text{strain}$ increments, over a range of $0\text{--}3500\mu\text{strain}$. The Bragg wavelength of a grating being measured after each strain increment. Measurements were taken, both as the strain was being increased, and as it was being reduced back to zero. Any significant differences in the Bragg wavelength-strain relationships obtained from the increasing and decreasing strain measurements could indicate, either hysteresis in the translation stage, or creep of the fibre at the glue points. The initial length of a fibre section was $100\pm 0.5\text{mm}$. This uncertainty in the fibre length, resulted in a systematic error of $\pm 0.5\%$. The zero strain condition was taken to be the point at which the fibre just went taught and this could be repeatably set to an accuracy of $\pm 50\mu\text{strain}$. After straining the fibre, checking the position of the translation stage at zero applied strain, acted as a simple additional test for fibre creep.

Transmissive spectral profiles were taken to measure the variation of Bragg wavelength with applied strain. The monochromator resolution was set to 0.3nm , which allowed the transmission minimum to be located with a noise limited accuracy of $\pm 0.02\text{nm}$. For the best accuracy, the monochromator was always scanned in the direction of increasing wavelength. Measurement of the Bragg wavelength was made with respect to a reference grating, spliced directly in-line with the IFBG under test. Making relative measurements meant that there was no reliance on the monochromator resetting itself accurately to the same initial wavelength. Thus, the

maximum random error in the measurement of the relative wavelength spacing was $\pm 0.04\text{nm}$. Also, since the reference grating and the test gratings will have almost the same temperature sensitivity, the reference grating will compensate for any Bragg wavelength shifts due to changes in the ambient temperature. The maximum temperature change observed during an experiment was 3°C , which if uncompensated could lead to an error of $\pm 1\%$ in the calculated strain gauge factor. However, of much more concern is the systematic error introduced by the absolute wavelength accuracy of the system, $\pm 0.2\text{nm}$. More precisely, the manner in which the monochromator wavelength step size varies across the scan range will be critical in determining the accuracy of the strain gauge factors, as will be seen later.

The strain gauge factor, S_B , can be determined by plotting the Bragg wavelength against the applied strain. According to equation 4.8 a linear relationship should emerge, the gradient of the line being equal to $S_B\lambda_0$. The results obtained from two IFBGs written into separate Spectran fibres are plotted in figures 4.3(a) and (b). Figure 4.3(a) shows the results obtained from a grating with an unstrained Bragg wavelength λ_0 , of 828.4nm , with shifts in Bragg wavelength being measured relative to a reference grating at 822.6nm . Accordingly, figure 4.3(b) shows the results obtained from a grating with $\lambda_0=832.6\text{nm}$, with measurements made relative to a reference grating at 836.3nm . It can be seen from figure 4.3 that there was good agreement between measurements taken during increasing and decreasing strain, with no evidence of hysteresis in the translation stage or creep at the glue points. Also, after straining the fibre, the zero strain position remained unchanged, within the limits of experimental error, confirming that the fibres had remained fixed. Fitting the data plotted in figures 4.3(a) and (b) to straight lines (using a 'least squares' method) allowed values for S_B to be calculated from the gradients. Figures 4.3(a) and (b) yielded values for S_B of 0.805 ± 0.005 and 0.665 ± 0.006 respectively. The errors in S_B being determined from the standard errors in the gradients. It can clearly be seen that the two experimentally determined strain gauge factors differ substantially from each other and the theoretical value. Since the standard errors in the gradients are small, the

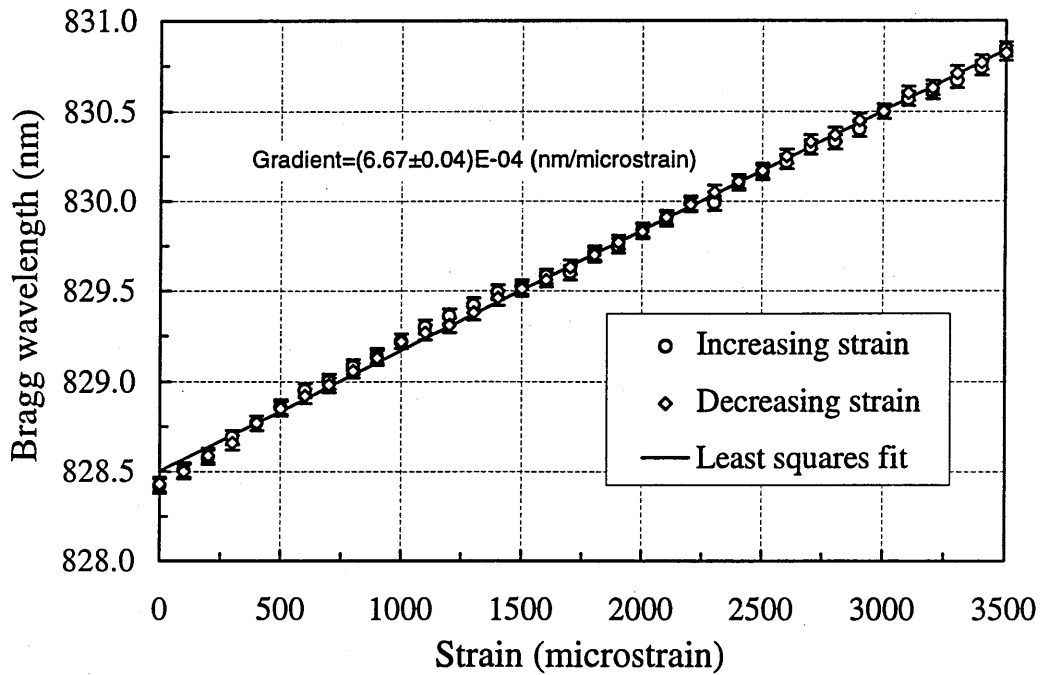


Figure 4.3(a) Bragg wavelength shift against applied strain for a grating with $\lambda_0=828.4\text{nm}$ written into Spectran (780nm) fibre.

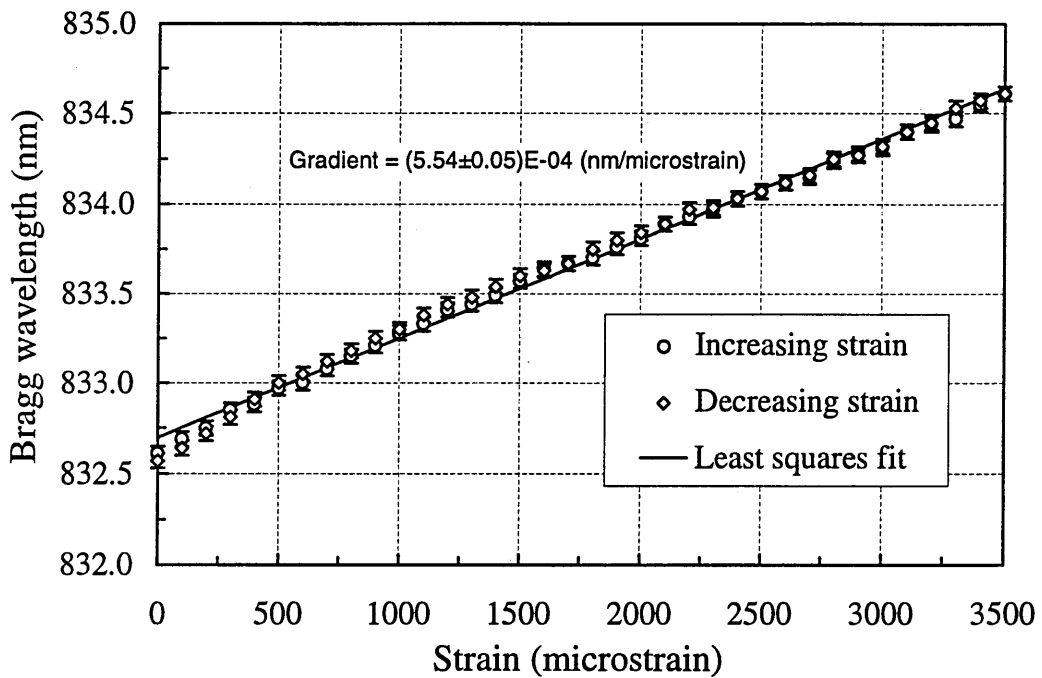


Figure 4.3(b) Bragg wavelength shift against applied strain for a grating with $\lambda_0=832.6\text{nm}$ written into Spectran (780nm) fibre.

most obvious cause of this difference is a wavelength dependent systematic error, which as has previously been speculated, results from the limited absolute wavelength accuracy of the monochromator. Therefore, some form of wavelength calibration of the monochromator was required if a meaningful value for S_B was to be obtained.

Since it was not possible within the time frame of the project, to obtain either a suitable spectral calibration of the monochromator, or investigate other Bragg wavelength measurement techniques, an alternative strategy was adopted. Discussions with the manufacturer had revealed that the errors were most likely to be due to the limited precision of the monochromators gearbox and would be periodic. It was hoped that if strain measurements could be taken over a sufficiently large spectral region the effects of this periodic error could be averaged out.

To this end, an array of five wavelength multiplexed IFBGs were written into a single length of hydrogen loaded Spectran fibre, using the two-beam mirror interferometer technique and laser source wavelength tuning (see section 3.2.4). The gratings were written with unstrained Bragg wavelengths in the range 821.1-836.7nm, and were nominally spaced by 4nm. A reference grating was written at 816.6nm. The fibre length between the fixed points was 150 ± 0.5 mm which gave a systematic strain error of $\pm 0.3\%$, and the zero strain point could be located to an accuracy of $\pm 30 \mu\text{strain}$. Strain was applied in increments of $133 \pm 3 \mu\text{m}$ and after each strain increment, the Bragg wavelength of each grating within the array was measured in turn.

Three separate sets of data were acquired from the array. Two from a 'low' strain region, with a range of $0-3467 \mu\text{strain}$. One data set being recorded for increasing strain, and the other for decreasing strain. As previously, any hysteresis between these data sets would indicate fibre creep at the glue points. Additionally a 'high' strain region of $2400-8533 \mu\text{strain}$ was investigated, but in this case measurements were only recorded for increasing strain.

The results from the array are presented in two ways. Firstly, in figure 4.4 the measured Bragg wavelength is plotted against applied strain. All of the acquired data is plotted, the results from individual IFBGs being numbered 1-5. In the regime where

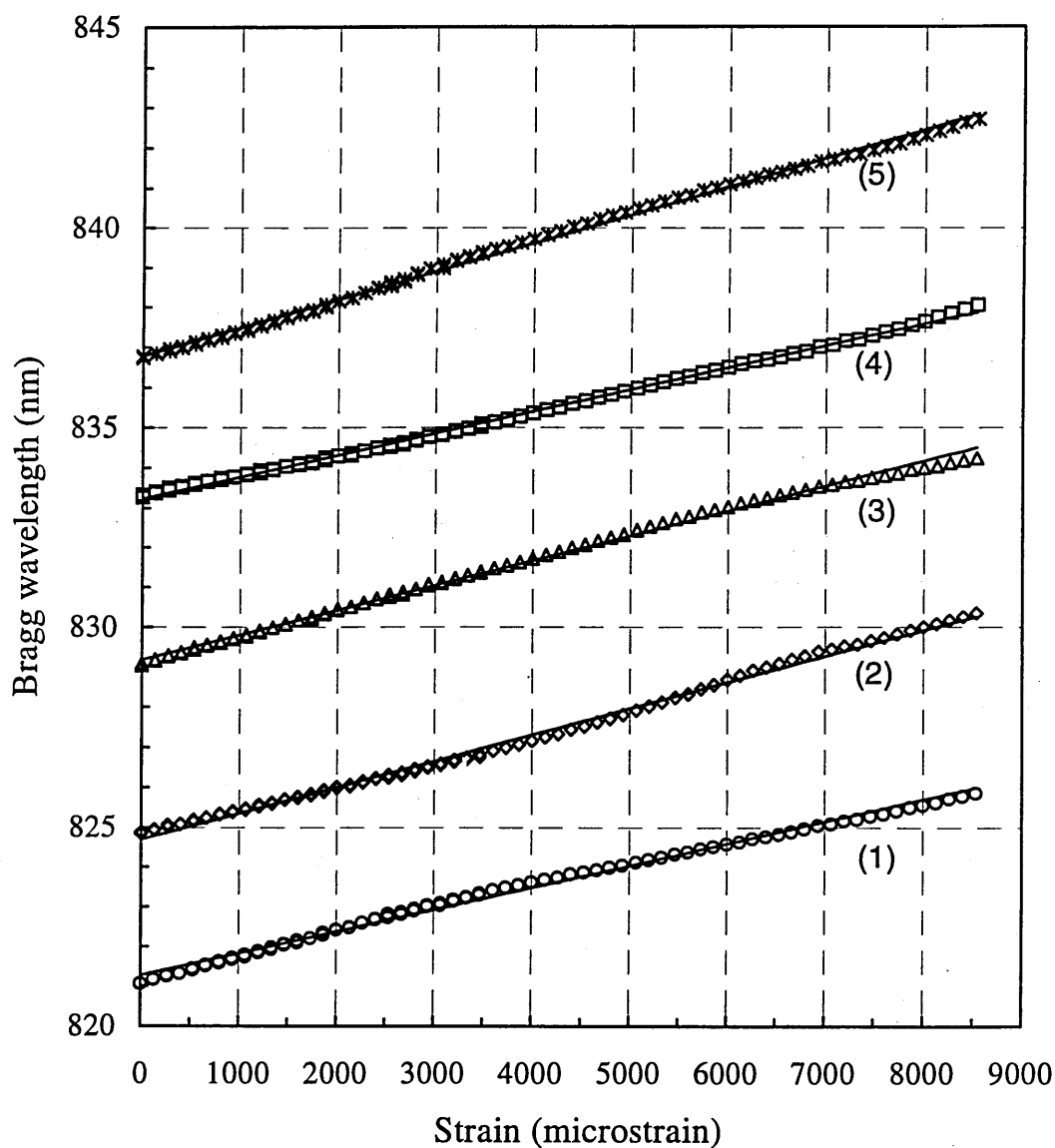


Figure 4.4 Bragg wavelength shift against applied strain for the five grating array written into Spectran (780nm) fibre.

Grating No	Gradient of straight line fit (nm/ μ strain)	Calculated S_B
1	5.53 ± 0.05	6.74 ± 0.06
2	6.52 ± 0.05	7.90 ± 0.06
3	6.25 ± 0.03	7.54 ± 0.04
4	5.44 ± 0.02	6.52 ± 0.02
5	7.10 ± 0.04	8.49 ± 0.05

Table 4.1 Values of S_B calculated from the data shown in figure 4.4. by applying a straight line fit to all the results obtained from an individual grating.

the low and high strain data sets overlapped, equivalent measurements of Bragg wavelength agreed within the limits of experimental error. This gave some confidence in the repeatability of the results. For the low strain regime, as with the previous fibres, there was no evidence of any translation stage hysteresis or creep of the optical fibre at the glue points. Also, after applying strain in both the low and high strain regimes, the zero strain condition remained unchanged, within the limits of experimental error, which confirmed that the fibre had remained fixed throughout the experiment. Since, the strain applied to each grating within the array is identical, the gradients of their associated Bragg wavelength-strain response should be almost the same, differing from each other by only by 0.6% (the fractional difference in initial Bragg wavelengths). As before, values of S_B could be calculated from the gradients of straight line fits to the data obtained from each of the IFBGs. The gradients of the line fits, and the associated values of S_B are shown in table 4.1 The differences between the results obtained from individual gratings, further substantiates the precept that the monochromator step size varies with wavelength.

Secondly, since the monochromator wavelength step size was thought to vary periodically, and S_B is directly related to the wavelength step size, a plot of S_B against the monochromator wavelength should vary with the same periodicity. Therefore, to verify that S_B did indeed vary periodically, the results were treated as follows. A sliding least squares fit to the data was performed, on the three data sets obtained from each IFBG. The sliding window was 10 data points wide; a data point representing the measured Bragg wavelength at a given strain, (λ_B, ϵ_x) . So for example, a line fit would be initially made to points 1-10 of a data set and then to points 2-11 and so on; this being repeated for each data set of every grating. The monochromator wavelength associated with the line fit, was taken to be the median Bragg wavelength within the window. Figure 4.5 shows a plot of S_B values, calculated from the gradients of the line fits, against monochromator wavelength for all results. The error in an S_B value being determined from the standard error in the gradient. Also, as S_B is plotted against the monochromator wavelength and not

absolute wavelength, the wavelength error is the random noise limited value of $\pm 0.04\text{nm}$ (c.f. absolute error $\pm 0.2\text{nm}$). As can be seen from figure 4.5, the variation of S_B with wavelength does seem to have a periodic structure, with features being repeated with a period of $\sim 10\text{nm}$. Using a window 10 data points wide, gave sufficient resolution to ensure that the major trends could be identified, but also limited the errors in S_B to $\pm 1-4\%$.

Using the data plotted in figure 4.5 an average value for S_B over one period was calculated. A simple mean of all the S_B values in one period could not be taken, since the concentration of plotted S_B values was greater in some wavelength regions than others and this would bias the final result. To evenly weight the results across one period, the wavelength region between 828.4nm and 838.6nm (i.e. one period), was divided into eighty 'bins' of equal wavelength. For each bin, the mean was found of all the S_B values lying within that bin, S_{bin} . Finally, the mean value of the strain gauge factor, $\overline{S_B}$ was determined by taking the average of all eighty S_{bin} values. Using eighty bins gave close to the best weighted spectrum possible, as using significantly more than eighty would have meant having some empty bins, which would have been counter productive. It was not possible to quote an error for $\overline{S_B}$ since a varying systematic error is being dealt with, rather than random measurement errors.

Using this method, a mean strain gauge factor of $\overline{S_B} = 0.76$ was calculated for Spectran (780nm) fibre, which was only 2.6% different from the theoretical value of 0.78 quoted in section 4.1.

Since it was appreciated that this was a far from ideal method of determining the strain gauge factor, it was decided that a second fibre type, Fibrecore SM800, would also be used for embedded sensing. British Aerospace had already determined the strain gauge factor of SM800 using a similar strain rig to the one detailed in this section, but in conjunction with a grating monitoring system that gave far more accurate Bragg wavelength measurements. The system was based on an in-line

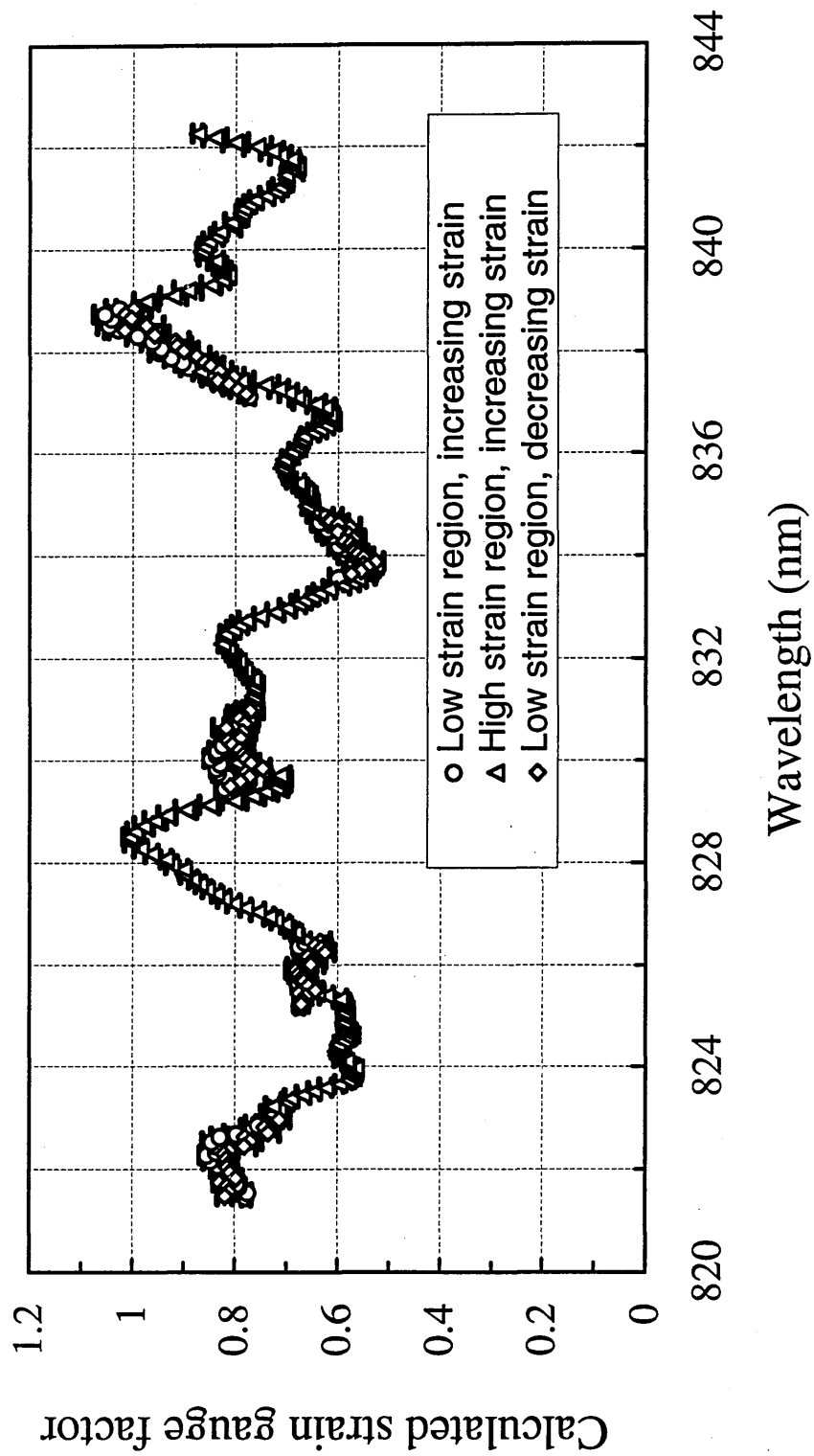


Figure 4.5 The calculated strain gauge factor, S_B , for Spectran (780nm) fibre as a function of monochromator wavelength, determined using the results obtained from the five grating array.

tuneable Fabry-Pérot filter and SLD broadband source, and is discussed in section 4.3.5. The mean strain gauge factor determined for SM800 using the British Aerospace system was $\overline{S_B} = 0.754 \pm 0.005$.

4.3 Strain sensitivity of gratings embedded in a carbon fibre composite test beam

The fabrication of the carbon fibre test beam and the three-point bend test discussed in the following sections were conducted at the British Aerospace, Sowerby Research Centre, in collaboration with Dr P.D. Foote and Dr I.J. Read of British Aerospace.

4.3.1 Sensor-host structural integrity issues

A number of structural integrity issues arise from embedding optical fibres into composite materials that have implications for the material properties and also the performance of IFBG sensors within the material.

If optical fibre sensors are to be successfully embedded into composite structures they should not adversely affect the tensile or compressive strength of the host material. Preliminary evidence indicates that optical fibres of 125 μ m in diameter and less cause minimal degradation of the host material properties (Blagojevic et al, 1989; Roberts and Davidson, 1992). In these trials the protective fibre buffer coat had been removed. If the buffer coat is left intact it will melt during the composite cure cycle and it has been suggested that this might lead to voids being created in the host material (Measures, 1992(b)). More recently, however, buffer coated optical fibres (125 μ m cladding/ 240 μ m buffer coat) have been successfully embedded into a carbon fibre composite. IFBG sensors written into the cores of these optical fibres exhibited a linear response to the host strain (Foote, 1994; Foote and Read 1995). Further, there is

evidence that these buffer coated fibres do not significantly reduce the tensile strength of carbon fibre composites, particularly if they are embedded parallel to the adjacent ply directions (*private communication*, Dr P.D. Foote, British Aerospace).

For fibres that are embedded at angle to adjacent ply directions, it is known that resin filled cavities will form around optical fibres. (e.g. Measures, 1993). These 'resin eyes' (so called because of their shape) lead to high stress concentrations at the host-optical fibre interface which may over a period of time cause debonding between the optical fibre and the host matrix. Optical fibres embedded parallel to the adjacent ply direction do not create resin eyes and therefore minimally disturb the host material. In this case, however, a resin-eye will form at the free end of an embedded optical fibre. There is evidence that the presence of an optical fibre coating may reduce the stress concentrations that can occur in the host material around the fibre, and thus reduce the chance of the fibre debonding. (Waite *et al*, 1988; Sirkis and Dasgupta, 1990). The same work also indicates that coatings do not appear to significantly reduce the strain sensitivity of the optical fibre sensors.

The theoretical calculation of the strain gauge factor S_B is based on the assumption of the Butter and Hocker (1978) model that there is no transverse strain coupled from the host to the optical fibre. However, Sirkis and Haslasch (1990) have shown that under transverse loading conditions significant errors may arise if the strain is predicted using this assumption. The errors in the model increasing as the optical fibre stiffness approaches that of the host material. The best strain predictions occur when the optical fibres are embedded parallel to the adjacent ply layers and the loading is in this ply direction. As has been suggested by Measures (1992(a)), fibre coatings could offer the additional advantage of reducing the transverse strain coupled from the host to an embedded fibre.

4.3.2 Fabrication of the carbon fibre test beam

The carbon fibre composite test beam was fabricated by British Aerospace from Ciba-Geigy 914 T300 prepreg (7 μ m diameter carbon fibres and 34% by weight epoxy resin). The carbon fibre composite is made up of a stack of individual plies. Each ply consisting of a matrix of parallel carbon fibres surrounded by an epoxy resin. The plies are stacked so that they are angled, with respect to each other, according to a particular sequence. The stacking sequence being critical to the overall tensile strength of the material. Finally, the composite is placed in an autoclave and the epoxy resin is cured at elevated temperature and pressure.

The stack sequence of the 914 T300 was (+45,-45,0,0,90,0,-45,+45,0,90,0) which was repeated with the +45 plies on the outer surfaces giving 22 plies in total. Four optical fibres, containing wavelength multiplexed IFBG arrays were placed between the adjacent 0,0 plies. The fibres were embedded running parallel to the ply direction (along the length of the beam) to prevent the formation of resin eyes, which might lead to debonding of the host from the optical fibres, and also to minimise transverse strain transfer from the host to the optical fibres. The carbon fibre stack sequence and location of the optical fibres within the composite are illustrated in figure 4.6.

The beam underwent the following cure cycle: heat from temperature to 120°C at 4°C/min, hold for 30 minutes, heat to 175°C at 4°C/min, hold for 60 minutes, cool to room temperature at 4°C/min. The autoclave pressure was 85-90 psi. Teflon sleeving was used to protect the optical fibres where they entered the composite beam from the autoclave environment. Once cured the material had a Young's modulus of 133GPa, which is a roughly median value for carbon fibre composite (cf. $E=70$ GPa for fused silica (Measures, 1993)). The final dimensions of the beam were 403mm x 23.5mm, with a thickness of 3.4 ± 0.1 mm. The optical fibres being embedded at a depth of 0.5mm below the beam surface.

Of the four IFBG arrays, two were written into hydrogen loaded Fibrecore SM800 and two into hydrogen loaded Spectran (780nm) singlemode fibres. Each

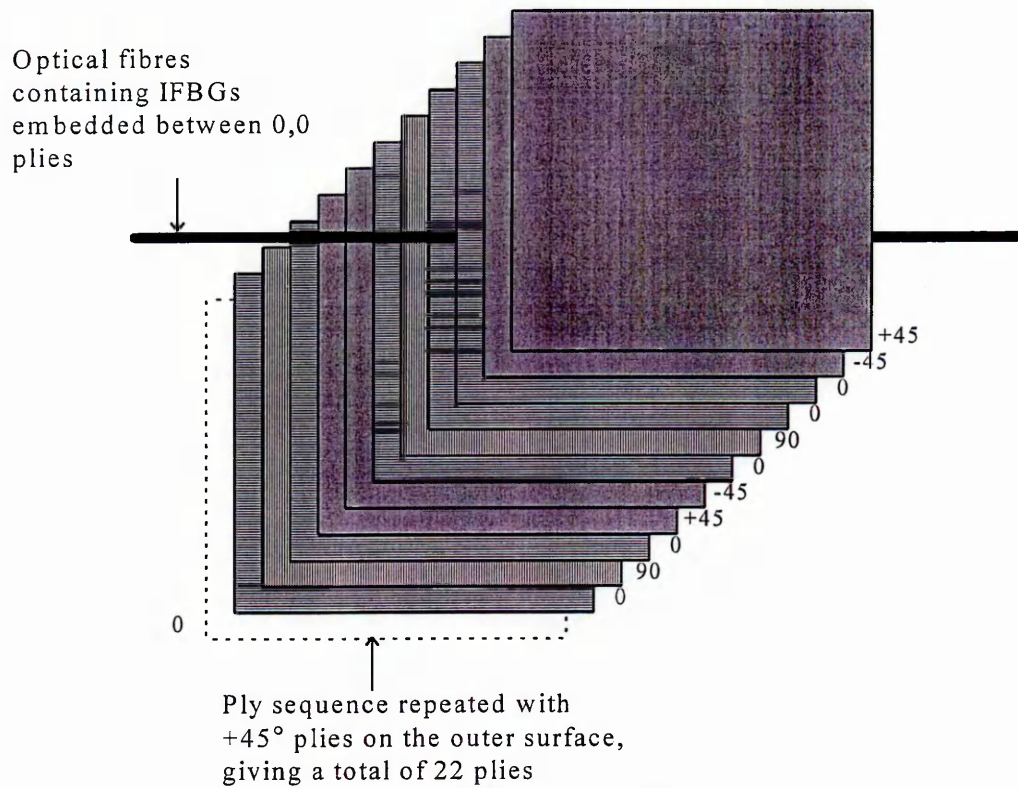


Figure 4.6 The stack sequence used for the carbon fibre composite (Ciba-Geigy 914 T300 prepreg) and ply depth of the embedded IFBG arrays.

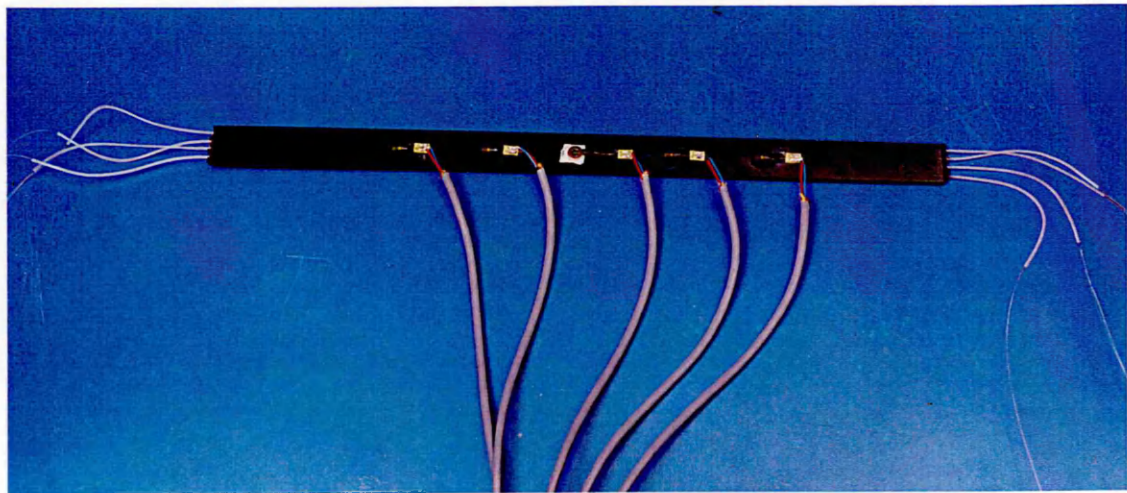


Figure 4.7 Photograph showing the carbon fibre composite test beam with embedded IFBG sensors and surface mounted electrical strain gauges.

optical fibre contained an array of five, 2.8mm long gratings, which were fabricated using the two-beam mirror interferometer technique and laser source wavelength tuning (see section 3.2.4). The gratings were written around 830nm with a nominal 4nm Bragg wavelength spacing. IFBGs were fabricated into SM800 fibres several weeks before they were embedded into the test beam, by which time all the hydrogen had fully diffused out from the fibre cores. However, gratings were only written into Spectran fibres three days before they were embedded, and therefore at the time of embedding, almost certainly still contained a certain amount of hydrogen within their cores. The optical fibre buffer coat was only removed from the small sections where gratings were written, these 'stripped' areas being <3.5cm in length. The entire buffer coat was not removed because otherwise the grating arrays would have been too fragile to handle, and because previous work had suggested that this might not necessarily cause any significant structural weakening or debonding problems (*private communication*, Dr P.D. Foote, British Aerospace). To investigate the effect of a coating on the performance of the IFBG sensors, one fibre of each type had a Desoto acrylate coating applied, using a Vytran RC-100 recoater, to the small sections of stripped fibre where the gratings had been written. The gratings in each array were separated by 50.0 ± 0.1 mm, the precise physical spacing being achieved using the fibre mount described in section 3.2.4. To enable the position of each grating within an array to be located, a datum point was marked on each fibre 130 ± 1 mm from the centre grating. Using this datum point the centre grating was located mid-way along the length of the test beam to an accuracy of $\leq \pm 3$ mm.

Five electrical, resistive foil strain gauges of 2mm length were bonded to the surface of the test beam. The surface had first been prepared by abrasion and solvent degreasing. The strain gauges were located along the length of the beam in the same way as the IFBG sensors, with a positional accuracy of ± 1 mm, relative to the centre of the test beam. A photograph of the carbon fibre test beam is shown in figure 4.7, while figure 4.8 illustrates the position of the IFBGs within the beam.

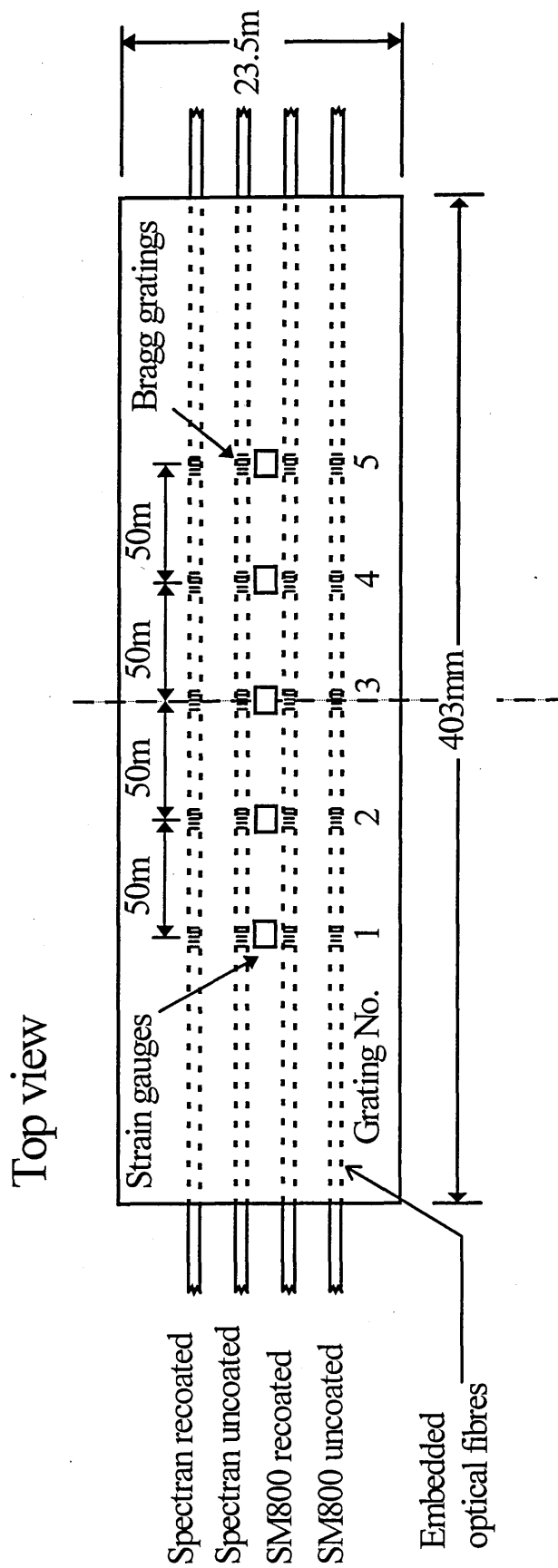


Figure 4.8 Location of the surface mounted, electrical strain gauges and the arrangement of the embedded IFBGs within the carbon fibre composite test beam.

4.3.3 Measurement of residual strain due to embedding

Dunphy *et al* (1990) measured a shift in the Bragg wavelength of gratings that had been embedded into a composite material. This was due to residual strain, presumably caused by a mismatch in the thermal properties of the optical fibre and the composite host. To confirm and quantify this effect, reflection spectra were taken of the four IFBG arrays, both before and after embedding. The spectra were recorded using a commercial spectrometer, a Monolight Optical Spectrum Analyser (model 6602). The spectrum analyser utilised a single diffraction grating, and had a 0.1nm resolution and a 0.1nm absolute wavelength accuracy. A built in helium neon laser allowed automatic calibration of the instrument. The grating arrays were illuminated by a high power pigtailed superluminescent diode (SLD) broadband source. The SLD (Superlum Ltd) had a near Gaussian spectrum centred on 818nm with a 20nm FWHM, and around 1.0mW of optical power was launched into fibre. A schematic diagram of the experimental arrangement used to obtain the grating spectra is shown in figure 4.9. The SLD output passed through a 50:50 coupler which was then mechanically spliced to one of the IFBG arrays. Reflection spectra were obtained, and to improve the signal to noise ratio, several hundred successive traces were averaged. The grating spectra were stored on the instruments internal disk drive. For a spectrum recorded in this way, the relative reflected peak heights were normalised by dividing through by the corresponding wavelength region of the SLD emission spectrum. Since the coupler split ratio was wavelength dependent, the recorded reflection spectra from the IFBGs would be twice convolved with the coupler's transfer function, once on transmission and once again on reflection. So that the normalisation procedure could account for the coupler's wavelength dependence, the SLD emission spectra was similarly twice convolved with the coupler's transfer function. To achieve this, the system was configured as in figure 4.9, except that the coupler output arm was removed from the mechanical splice and the Fresnel reflection spectrum from the free fibre end was recorded. The region of the convolved spectrum used to normalise the grating arrays is shown in figure 4.10. The normalised spectra, obtained prior to

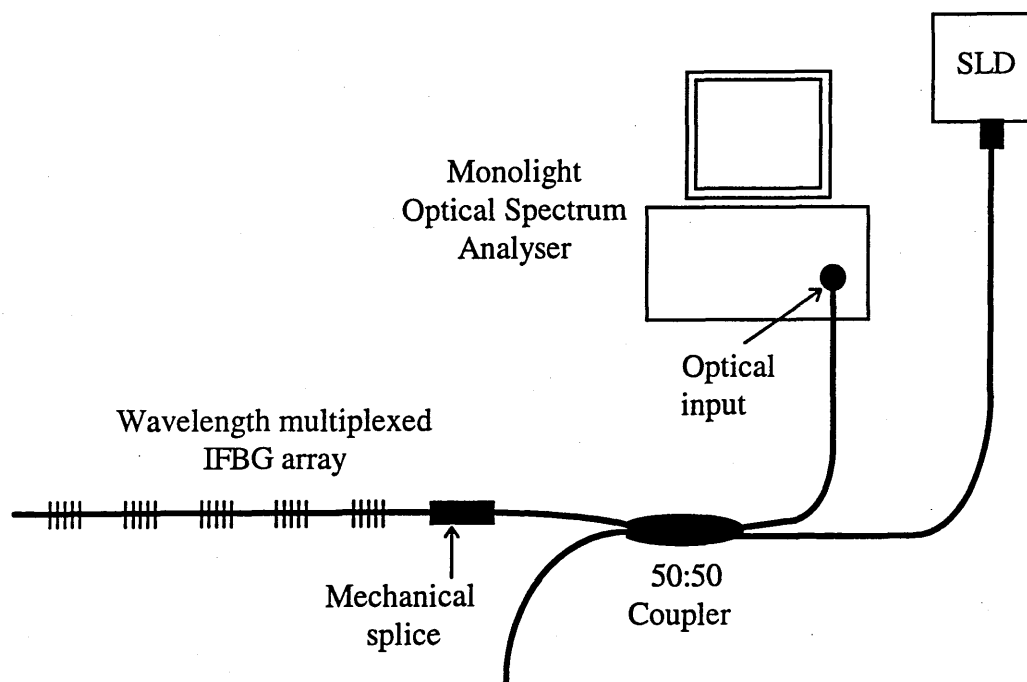


Figure 4.9 British Aerospace grating characterisation system, consisting of a Monolith Optical Spectrum Analyser and an SLD broadband source.

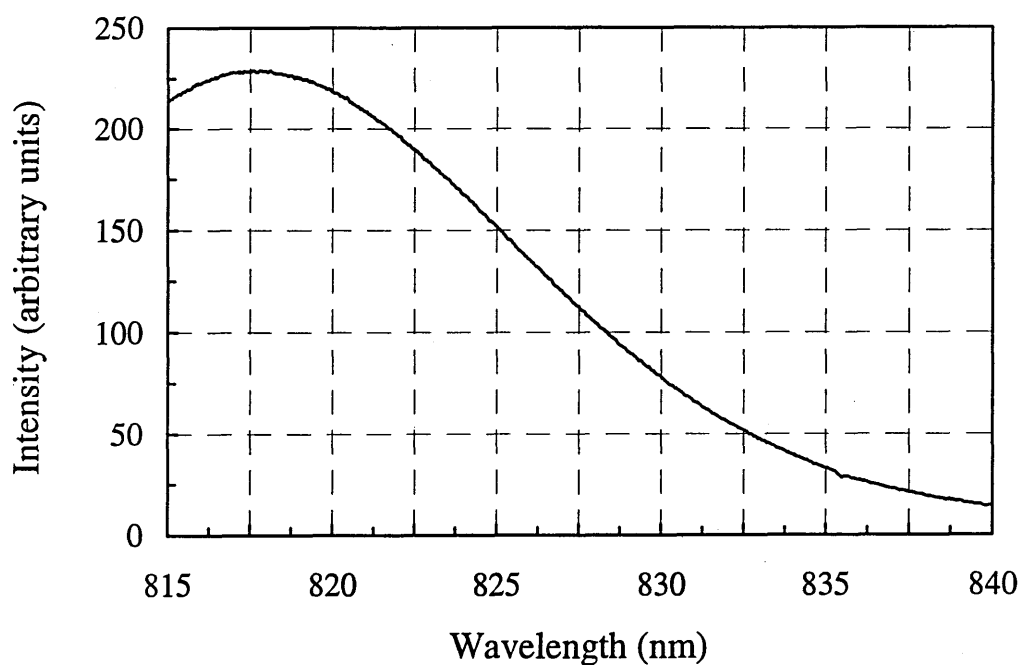


Figure 4.10 The region of the SLD source emission spectrum used to normalise the IFBG array reflection spectra.

embedding, from grating arrays written into Spectran (780nm) fibre are shown in figures 4.11(a) and (b). Figures 4.12(a) and (b) show similar spectra obtained from grating arrays written into Fibrecore SM800 fibre. The gratings are numbered according to their location within the composite, defined in figure 4.8. The reflectivity scale was not based on direct measurement, but rather was inferred from the maximum transmission dropout seen by a grating in an array. The transmission dropout was measured at the time of fabrication by the system described in section 3.2.2. Therefore, there could be significant errors in the absolute reflectivity values shown. However, these values are only intended to indicate the magnitude of the reflected signal. The gratings appeared to be of good quality, with the exception of grating 5 on the Spectran fibre, and had measured FWHM's of 0.3nm.

After embedding, the above measurements were repeated, and the corresponding reflection spectra are shown in figures 4.11(c) and (d), and figures 4.12(c) and (d). All of the gratings survived the cure process. The FWHM's were not significantly greater, and on average still measured 0.3nm. It will be noted that the relative peak heights of IFBGs within an array have changed between the pre-embedded and post-embedded reflection spectra. This implies that there has been some non-uniform reduction in reflectivity as a result of embedding, possibly due to a combination of thermal degradation during the cure process and stress concentrations around the optical fibres causing coupling to cladding modes. However, the cause and the magnitude of this reflection loss was not investigated any further.

As expected, shifts in grating Bragg wavelengths could be seen when comparing pre-embedded and post-embedded spectra. The shifts in Bragg wavelength measured for all gratings are listed in table 4.2. Also, the residual strain was calculated for all gratings written into SM800, using the quoted value of $\overline{S_B}$, and these values are also shown in table 4.2. The residual strain was not calculated for gratings written into Spectran fibre, since hydrogen would still have been present in the core when the initial wavelength measurements were made, and this would have almost certainly influenced the result. All, bar one, of the gratings appeared to be

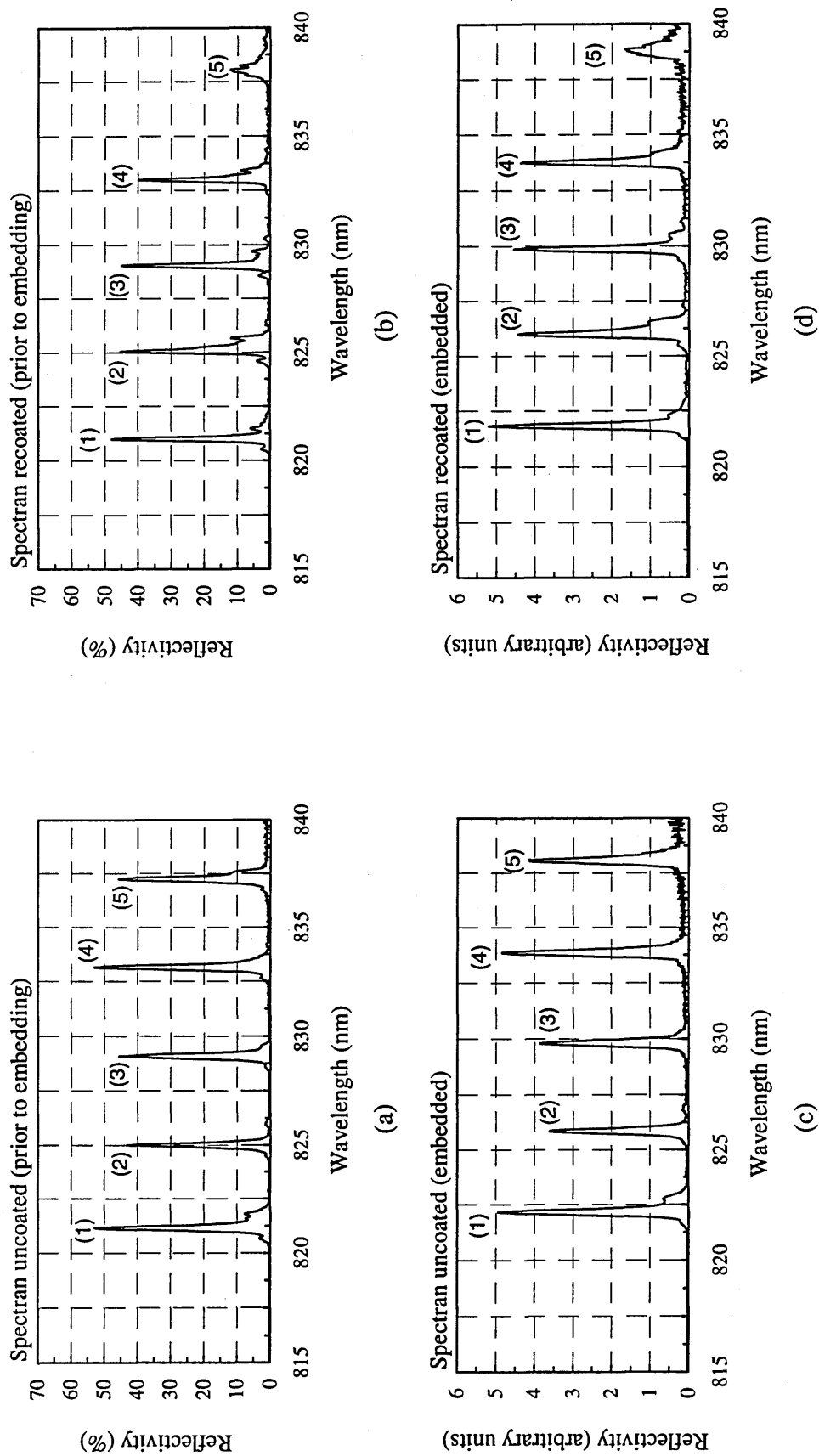


Figure 4.11 Spectrum analyser traces showing reflection spectra of grating arrays written into Spectran (780nm) singlemode fibre, taken: (a)-(b) prior to embedding and (c)-(d) after embedding in carbon fibre composite.

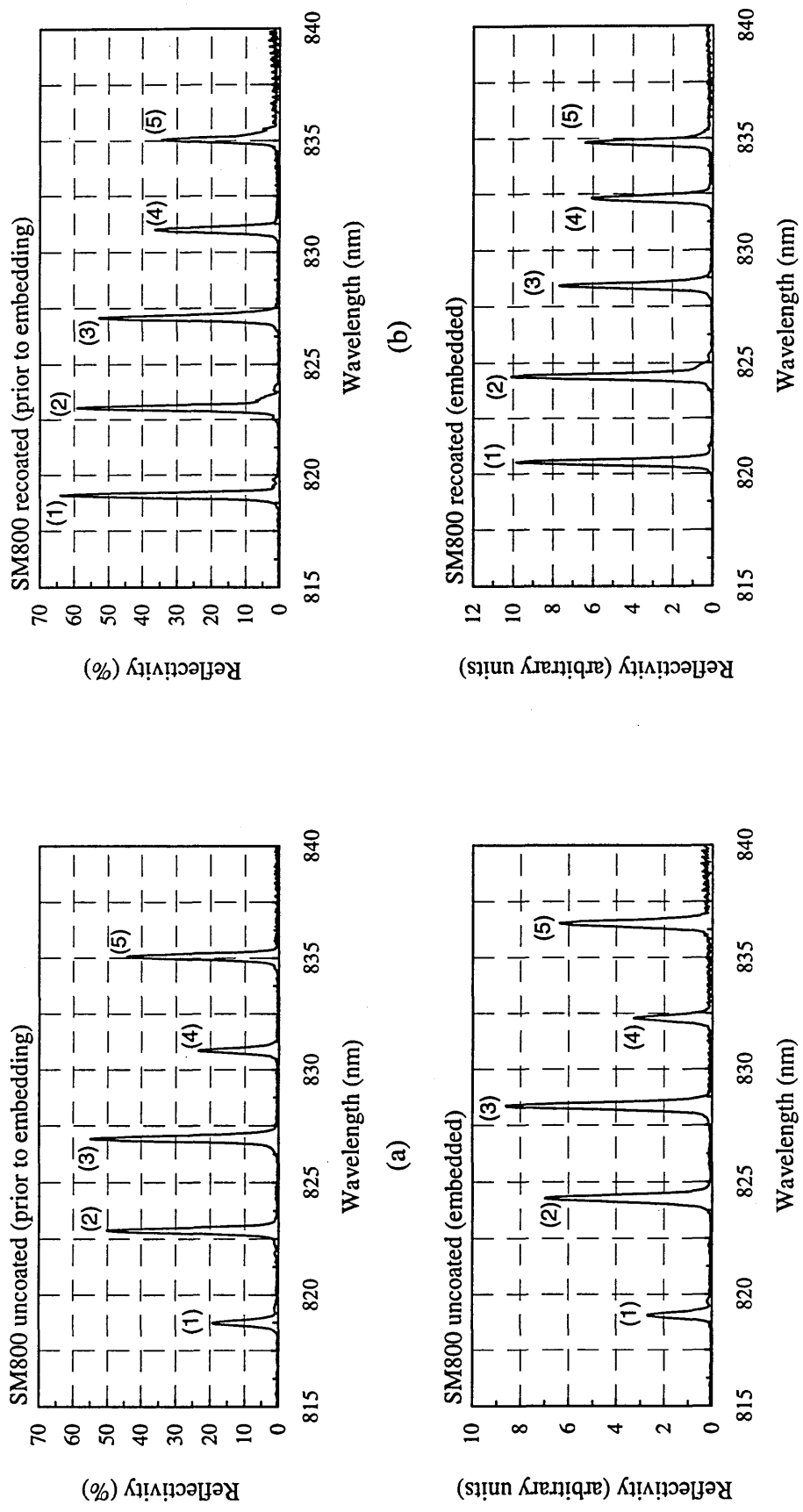


Figure 4.12 Spectrum analyser traces showing reflection spectra of grating arrays written into Fibrecore SM800, taken: (a)-(b) prior to embedding and (c)-(d) after embedding in carbon fibre composite.

Fibre type	Grating No.	Bragg wavelength prior to embedding λ_0 (nm)	Embedded Bragg wavelength λ_e (nm)	Bragg wavelength shift $\Delta\lambda = \lambda_e - \lambda_0$ (nm)	Residual strain $\epsilon_r = \Delta\lambda / S_B \lambda_0$ (μ strain)
Spectran (780nm) uncoated	1	821.16	822.16	1.00	-
	2	825.00	825.84	0.84	-
	3	829.08	829.80	0.72	-
	4	833.16	833.86	0.70	-
	5	837.24	838.02	0.78	-
Spectran (780nm) recoated	1	821.00	821.82	0.82	-
	2	825.04	826.00	0.96	-
	3	829.04	829.86	0.82	-
	4	833.00	833.74	0.74	-
	5	838.06	838.84	0.78	-
Fibrecore SM800 uncoated	1	818.74	819.06	0.32	518
	2	822.88	824.28	1.40	2256
	3	826.92	828.36	1.44	2277
	4	830.86	832.28	1.42	2267
	5	835.06	836.54	1.48	2351
Fibrecore SM800 recoated	1	819.10	820.52	1.42	2299
	2	823.04	824.40	1.36	2192
	3	827.08	828.44	1.36	2181
	4	831.00	832.32	1.32	2107
	5	835.06	834.80	-0.26	-413

Table 4.2 The residual strain induced Bragg wavelength shifts, for IFBGs embedded into the carbon fibre composite. (Note, the residual strain was not calculated for the Spectran fibre, since hydrogen diffusing from the core would almost certainly have affected the magnitude of the wavelength shift.)

under tensile strain as a result of the cure process, which was the opposite direction to that expected. It was assumed that the epoxy resin, which has a much greater thermal expansion coefficient than the optical fibres, would impart a compressive strain on the optical fibres as the composite material cooled. This positive strain result has yet to be adequately explained and will require further investigation.

It can be seen from table 4.2 that most of the fibre gratings, written into the same fibre type, experience a similar Bragg wavelength shift due to embedding. The two notable exceptions, grating 1 on the uncoated SM800 fibre and grating 5 on the recoated SM800 fibre, experienced much lower Bragg wavelength shifts. Grating 5 on the recoated SM800 fibre being the only IFBG that experienced a compressive strain. The lower residual strain could imply that the fibre in the region of the IFBG is poorly bonded to the host, and may not respond as predicted when strain is applied to the composite beam.

4.3.4 Three-point bend test

The experimental arrangement for the three-point bend test is shown in figure 4.13. If the simply supported test beam undergoes a central deflection D , the deflection $w(x)$ at a given point along its length is described by

$$w(x) = 4D \left(\frac{3x}{L} - \frac{x^3}{L^3} \right) \quad (4.12)$$

where x is the horizontal distance to the nearest support and L is the distance between supports.

The strain experienced by an axial fibre embedded within the composite is proportional to the curvature of the beam. The strain neutral axis of the test beam (axis with zero resultant strain due to deflection) is situated at mid-depth within the beam (in this case between plies 11 and 12). For an optical fibre embedded at a distance z from the strain neutral axis, the strain applied along the length of the fibre, ϵ_x , will be given by

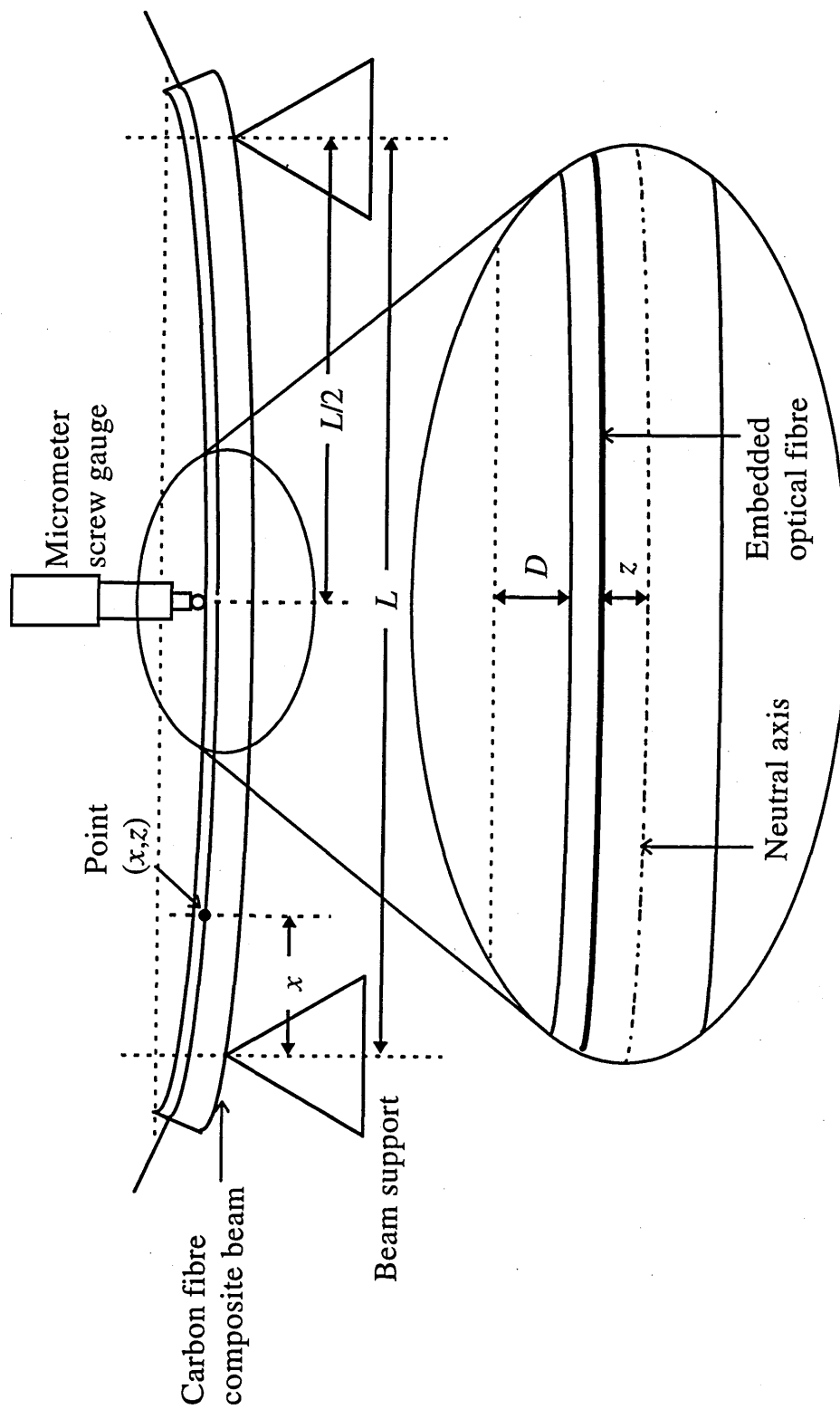


Figure 4.13 Schematic diagram showing the three-point bend test configuration.

$$\epsilon_x = -z \frac{\partial^2 w}{\partial x^2} \quad (4.13)$$

Substituting equation (4.12) into (4.13), ϵ_x can be expressed as

$$\epsilon_x = \frac{24Dxz}{L^3} \quad (4.14)$$

For the three point bend test the beam supports were separated by $384 \pm 1 \text{ mm}$ and the load was applied mid-way between the two supports using a micrometer screw gauge. The beam was deflected in $1 \text{ mm} \pm 0.05 \mu\text{m}$ steps with a total deflection range of $\pm 25 \text{ mm}$. Measurements were taken for both increasing and decreasing load. Differences between the two sets of measured data would indicate that the fibre had moved within the composite as a result of loading. To apply strain of the opposite sign the composite beam was simply inverted and the test repeated. Using this configuration a surface strain in the range $\pm 3400 \mu\text{strain}$ was applied to the centre of the test beam.

4.3.5 Bragg grating and electrical strain gauge monitoring system

The Bragg wavelength shifts induced by an applied strain were monitored using a system developed by British Aerospace. IFBG arrays were interrogated by a system based upon a piezo scanned, in-line Fabry-Pérot tuneable filter and a broadband high power SLD. Such a system has been previously reported (Kersey *et al*, 1993). However, this system differs from the system previously reported by Kersey *et al* (1993), in that it utilises a novel signal subtraction technique and can acquire data at a substantially higher rate (Read, 1997).

To locate the Bragg wavelength of a WDM grating array, the tuneable filter's passband is scanned, using a linear ramp, over the spectral region occupied by the IFBGs. However, uncertainties arise in the measurement of the Bragg wavelength due to amplitude noise. The solution adopted by Kersey *et al* (1993) was to apply an

additional dither signal to the linear ramp. Then by feeding the detected signal to a lock-in amplifier, referenced to the dither frequency, a differentiated spectrum was obtained from the lock-in. The zero crossing points on this spectrum corresponded to the Bragg wavelengths of the gratings in the array. A potential problem of the ramp and dither method is that it is relatively slow. The maximum dither frequency is determined by the tuning bandwidth of the Fabry-Pérot filter. The time-constant of the lock-in amplifier has to long compared with the period of the dither frequency and the time for a scan must be long compared to the lock-in amplifier time constant. Thus a Fabry-Pérot filter with a tuning bandwidth of a few kHz may only yield a data rate of a few Hz.

In contrast the solution adopted by British Aerospace, can yield data rates of up to 1kHz. The principle of operation is as follows. Two scans of the wavelength region of interest are taken, the wavelength scan of the second spectrum being offset by a small amount relative to the first. The second spectrum is then subtracted from the first, the resultant trace being shorter than the two spectral scans by an amount equal to the wavelength offset. Figure 4.14 shows the resultant differential trace obtained from the subtraction process. As with the differentiated spectrum obtained from the scan and dither technique, the zero crossing points correspond to the Bragg wavelengths of the gratings in the array. The size of the wavelength offset is crucial to the accuracy of the wavelength measurement. The optimum performance being obtained when the gradient of the zero crossing transition is maximised. Positive and negative thresholds levels were used to prevent noise spikes causing spurious Bragg wavelength measurements. To be accepted as a genuine Bragg wavelength measurement the differential trace has to cross the threshold levels on either side of the zero crossing point.

This signal subtraction process is more prone to noise than the ramp and dither method, but the maximum data acquisition rate is limited only by how fast the filter can be scanned without compromising the linearity of the ramp.

A schematic diagram of the experimental arrangement is shown in figure 4.15. The grating arrays were illuminated by the same type of high power SLD as described

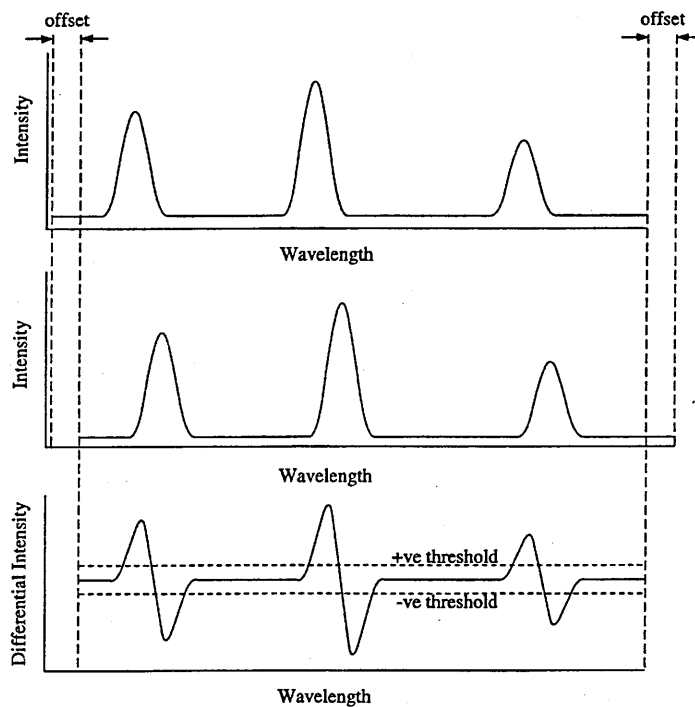


Figure 4.14 Production of a differential trace using the signal subtraction method (Read, 1997).

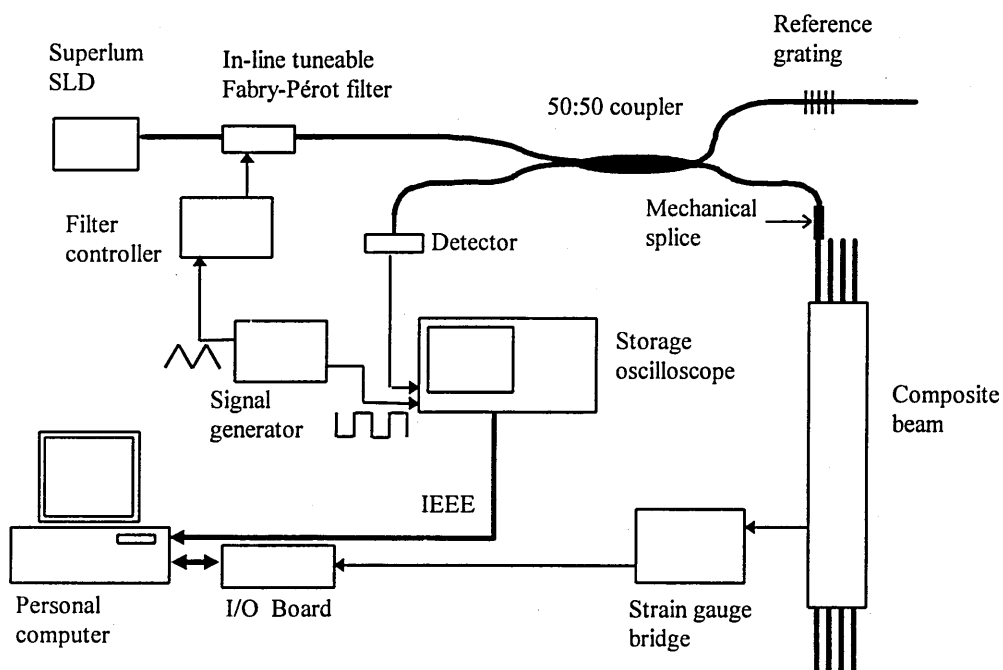


Figure 4.15 Experimental arrangement for the British Aerospace grating interrogation system based upon an in-line tuneable Fabry-Pérot filter and a broadband SLD source (Read, 1997).

in section 4.3.3, however, this time it had a peak wavelength around 835nm. The piezo driven, in-line Fabry-Pérot tuneable filter (Queensgate Instruments) had a passband with a 0.5nm FWHM, a free spectral range of 35nm and an operating wavelength range of 810nm to 870nm. The reflected signal from a IFBG array was measured using an avalanche photodiode. The Fabry-Pérot cavity was scanned at 50Hz using triangular waves from a signal generator. The photodiode output was recorded by a digital storage oscilloscope, synchronised to the Fabry-Pérot scan by the signal generator. Once a complete trace was acquired it was transferred via an IEEE/488 interface bus to a PC for signal processing. The wavelength offset and signal subtraction were performed in software, with the most recent spectral scan being subtracted from the previous one. The wavelength offset used for this work was 0.85nm. Since only the rising edge of the triangular wave was used, the data acquisition rate was the same as the 50Hz Fabry-Pérot scan frequency. Also in software, a sliding rectangular window which averaged over 0.04nm was used to filter out high frequency noise. Using this system, wavelength could be measured to an accuracy of approximately 6 parts per million. For gratings written around 800nm this corresponds to a strain measurement error of $\sim 10\mu\text{strain}$. Potentially even higher accuracy is attainable, since in this experiment the accuracy of the wavelength measurement was limited by the linearity of the Fabry-Pérot response, which could be calibrated for, and the linearity of the signal generator ramp. All of the Bragg wavelength measurements were made relative to a fixed fibre grating that provided a reference wavelength and could compensate for any ambient temperature changes.

Electrical strain gauge measurements were made by monitoring the voltage changes from a 1/4 bridge circuit, with a 5V supply, using a data acquisition card fitted to the PC. The bridge outputs were balanced to zero, for a zero beam deflection, using trimmer pots. The surface strain ϵ_s was calculated from the bridge output voltage V_b using

$$\epsilon_s = \frac{4V_b}{V_s k_b} \quad (4.15)$$

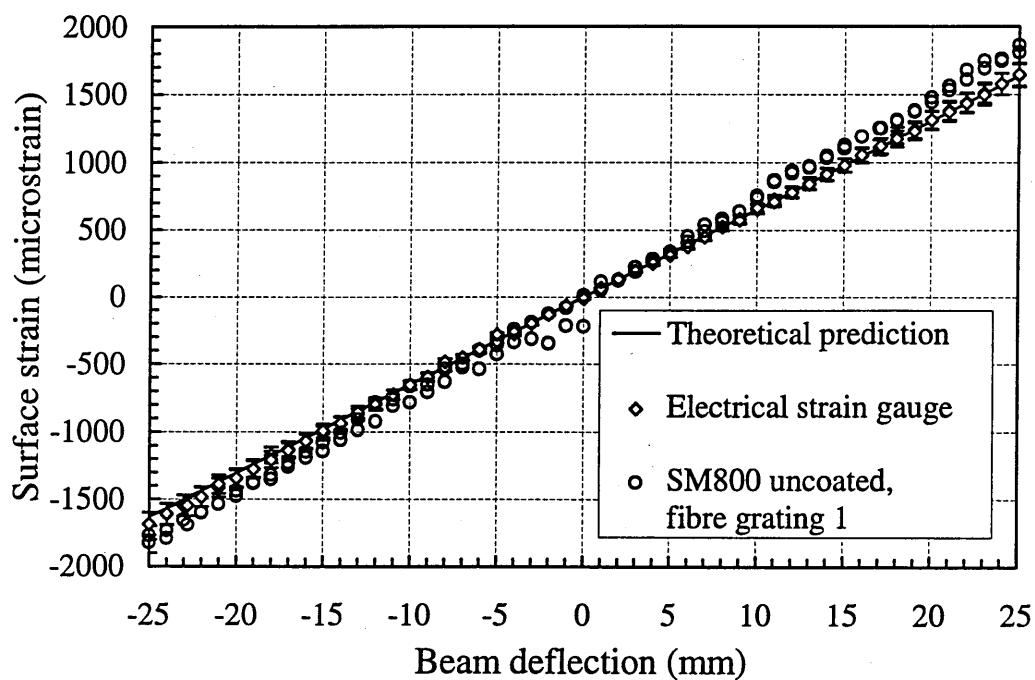
where V_s is the bridge supply voltage and k_b is the strain gauge calibration factor, quoted by the manufacturer to be $k_b=2.0$. The accuracy of the strain gauge measurements was estimated to be approximately 5%.

Since only a single IFBG array could be interrogated at any one time using the above monitoring system, a series of identical bend tests were conducted to obtain equivalent data sets from each of the four fibre grating arrays.

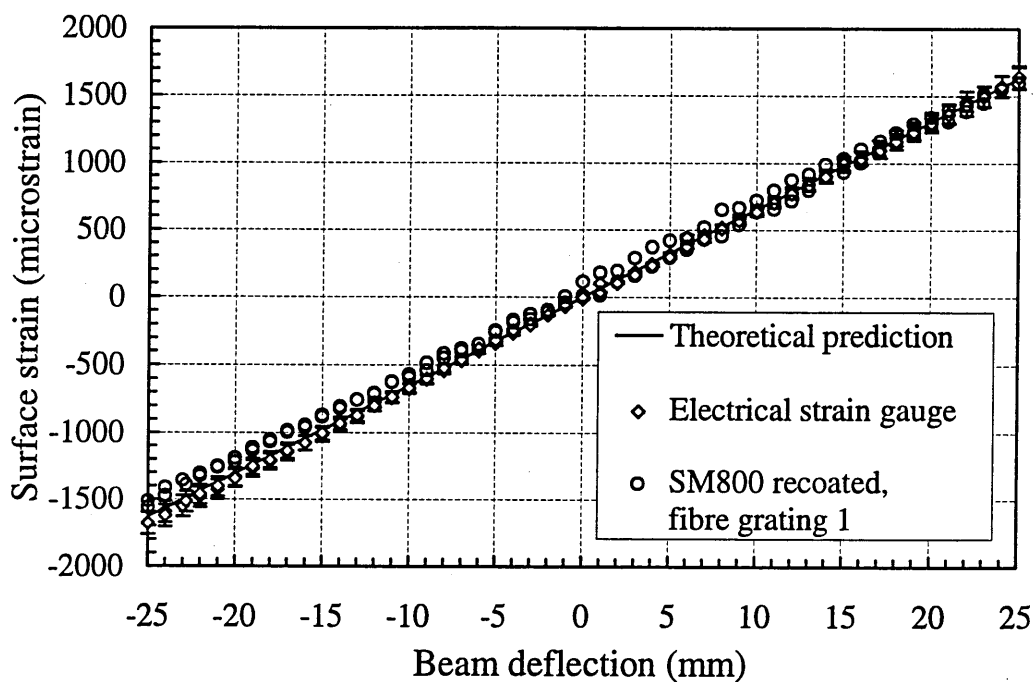
4.3.6 Three-point bend test results for carbon fibre test beam

To compare results from the three-point bend test, the theoretically and experimentally determined surface strain, ϵ_s , were plotted against the central beam deflection, D , which according to equation 4.14 should yield a linear relationship. To achieve this, the IFBG sensor measurements had to be scaled by the theoretical ratio of the surface strain to the strain at the depth of the embedded optical fibres (1.375). Then the experimental strain was calculated using the values of $\overline{S_B}$ for Spectran (780nm) and SM800 fibre given in section 4.2.2. A full set of graphs comparing the theoretical surface strain applied to the carbon fibre test beam, with the measurements made by the electrical strain gauges and the embedded IFBG arrays, are shown in appendix D. To serve as examples, the graphs generated using the measurements obtained from grating 1 of the uncoated and recoated SM800 fibres are reproduced in figures 4.16(a) and (b) respectively. These graphs were chosen as examples, since the results presented in figure 4.16(a) are particularly pertinent to much of the following discussion. In all the graphs, error bars are not shown on the grating strain measurements, since they were only of the order of $10\mu\text{strain}$. However, the errors on the electrical strain gauge measurements (5%) are shown.

In general there was good agreement between the measurements made by the IFBGs under increasing and decreasing load. Although differences did arise in the measurements made by several IFBGs that were outside of experimental error over a portion of the applied strain range. This indicated that there was little movement of



(a)



(b)

Figure 4.16 Theoretical strain, electrical strain gauge data, and IFBG data obtained from (a) grating 1 of the uncoated SM800 fibre and (b) grating 1 of the recoated SM800 fibre.

the embedded fibres within the composite due to loading, and the fibres were well bonded to the surrounding host matrix.

The gradients of straight line fits to the results plotted in appendix D, give the surface strain/deflection response, ϵ_s/D , of the test beam. Table 4.3 summarises the theoretically and experimentally determined ϵ_s/D characteristics of the beam. It can be seen from table 4.3, that the standard errors in the experimentally determined ϵ_s/D values were no greater than 0.5% for the embedded IFBGs. Also, the ϵ_s/D values determined from gratings written into uncoated Spectran fibres agreed with the theoretical values to $\leq 3.1\%$. Similarly for uncoated IFBGs in SM800, all but one ϵ_s/D value agreed with the theoretical prediction to $\leq 4.3\%$. The exception being grating 1 on the uncoated SM800 fibre which had an ϵ_s/D value 12.4% greater than the theoretical value.

On average the recoated IFBGs yielded ϵ_s/D values $\sim 4\%$ lower than the equivalent gratings written into uncoated fibres (excluding grating 1 on SM800 fibres). The ϵ_s/D response being up to 10.9% less than the theoretical prediction for gratings written into recoated Spectran fibre. For IFBGs in recoated SM800 the ϵ_s/D response was up to 7.0% less than the theoretical prediction.

For the surface mounted, electrical strain gauges, the standard errors in the ϵ_s/D values were no greater than 0.2%, and the ϵ_s/D values gave a slightly better fit to theory than the uncoated IFBGs. All electrical strain gauge measurements agreed with the theoretical value to $\leq 3.1\%$.

The results obtained from the uncoated fibre gratings appear particularly encouraging when the possible sources and magnitude of systematic errors are taken into consideration. The error due to the positional tolerance of the fibre gratings, $\pm 3\text{mm}$, would equate to $\pm 1.6\%$ for the centre gratings and up to $\pm 3.3\%$ for the outermost gratings. Also, the uncertainty in the thickness of the beam could lead to an error of $\pm 3\%$ between the experimental results and the theoretical prediction. Finally,

Fibre type	Grating No.	Theoretical ϵ_s/D ($\mu\text{strain/mm}$)	Electrical strain gauge ϵ_s/D ($\mu\text{strain/mm}$)	Bragg grating ϵ_s/D ($\mu\text{strain/mm}$)
Spectran (780nm) uncoated	1	65.3	65.6 \pm 0.1	63.3 \pm 0.2
	2	100.8	101.7 \pm 0.2	101.5 \pm 0.2
	3	136.3	138.4 \pm 0.2	137.1 \pm 0.3
	4	100.8	100.9 \pm 0.1	98.7 \pm 0.3
	5	65.3	64.5 \pm 0.1	64.6 \pm 0.2
Spectran (780nm) recoated	1	65.3	65.9 \pm 0.1	59.3 \pm 0.3
	2	100.8	101.2 \pm 0.2	99.4 \pm 0.2
	3	136.3	137.2 \pm 0.2	121.5 \pm 0.3
	4	100.8	100.5 \pm 0.2	92.4 \pm 0.2
	5	65.3	63.5 \pm 0.1	66.9 \pm 0.2
Fibrecore SM800 uncoated	1	65.3	66.2 \pm 0.1	73.4 \pm 0.3
	2	100.8	100.9 \pm 0.2	103.0 \pm 0.3
	3	136.3	138.8 \pm 0.2	134.8 \pm 0.3
	4	100.8	100.8 \pm 0.1	99.8 \pm 0.2
	5	65.3	64.9 \pm 0.1	62.5 \pm 0.3
Fibrecore SM800 recoated	1	65.3	66.1 \pm 0.1	62.4 \pm 0.3
	2	100.8	101.8 \pm 0.1	96.2 \pm 0.2
	3	136.3	140.5 \pm 0.2	129.4 \pm 0.2
	4	100.8	101.4 \pm 0.1	98.9 \pm 0.2
	5	65.3	64.4 \pm 0.1	60.7 \pm 0.2

Table 4.3. Comparison of the theoretical strain/deflection response, ϵ_s/D , to that measured by electrical strain gauges and IFBGs.

for SM800, $\overline{S_B}$ only has an error of $\pm 0.7\%$, whereas the error in $\overline{S_B}$ for the Spectran fibre could not be determined, for the reasons explained in section 4.2.2.

It has been assumed so far that the gratings are well bonded to the surrounding host material and that the fibre gratings remain fixed between the same ply layers throughout the cure process. However, it is possible that some movement could occur during this period. Bearing this in mind, it is interesting to note that the only uncoated fibre grating to yield a ϵ_s/D response significantly different from the predicted value was grating 1 of the uncoated SM800 fibre. This grating was one of the two IFBGs that yielded a lower than average residual strain value after embedding. A possible explanation for such a result, is that the optical fibre drifted from its original position during the cure process and consequently was not as well bonded to the surrounding host matrix as the other embedded fibres. The $+12.4\%$ difference in the ϵ_s/D value from the theoretical prediction, being in line with the $+12.5\%$ error that would be expected in this experiment if the optical fibre had migrated one ply layer towards the composite surface. However, the second anomalous residual strain value, grating 5 of the recoated SM800 fibre, did not appear to give a notably spurious ϵ_s/D result.

From the experimental results and the above discussion, it is apparent that for the applied strain range of $\pm 3400 \mu\text{strain}$ the majority of the gratings written into uncoated optical fibres yielded a strain response in-line with the theoretical prediction. Therefore, for the deflection range investigated, it would appear that the simple Butter and Hocker (1978) model – relating Bragg wavelength shifts to axial strain – allows a reasonably accurate determination of the axial strain experienced by optical fibres embedded into carbon fibre composite parallel to the adjacent ply directions. The lower ϵ_s/D response obtained from the recoated IFBGs indicated that the applied coating acted to slightly reduce the strain transferred to the fibre. However, the precise value for ϵ_s/D response is of secondary importance to the linearity and the repeatability of the strain measurements. In this work, the application of a fibre coating to the sensing region does not seem to adversely affect either of these two qualities. Since the majority of the gratings appeared reasonably well

bonded to the surrounding host matrix, no conclusion could be drawn about the affect of a coating on the stress concentration at the sensor host interface. Finally it should be noted, that overall, the results obtained from the IFBG sensors were still not as linear and repeatable as the electrical strain gauge measurements.

References

- Blagojevic, B., Tsaw, B., McEwan, K., and Measures, R.M., 'The influence of embedded optical fibers on the interlamina fracture toughness of composite materials' in *Proc. Review of Progress in Quantative NDE*, Brunswick, Maine (1989).
- Butter, C.D., and Hocker, G.P., 'Fiber optics strain gauge', *Appl. Opt.*, **17**, pp2867-2869 (1978).
- Dunphy, J.R., Meltz, G.F., Lamm, P., and Morey, W.W., 'Multi-function, distributed optical fiber sensor for composite cure and response monitoring', in *Proc. Fiber Optic Smart Structures and Skins III*, San José, pp116-118 (1990).
- Foote, P.D., 'Fibre Bragg grating strain sensors for aerospace smart structures', in *Proc. Second European Conference on Smart Structures and Materials*, Glasgow, pp290-293 (1994).
- Foote, P.D., and Read, I.J., 'Optical Sensors for aerospace structural monitoring', *IEE: Colloquium on Optical Techniques for Structural Monitoring*, Digest No: 1995/087, 28 April 1995.
- Kersey, A.D., Berkoff, T.A., and Morey, W.W., 'Multiplexed fiber Bragg grating strain sensors system with a fiber Fabry-Pérot wavelength filter', *Opt. Lett.*, **18**, pp1370-1372 (1993).
- Measures, R.M. (a), 'Smart composite structures with embedded sensors', *Composites Eng.*, **2**, pp597-618 (1992).
- Measures, R.M. (b), 'Advances toward fiber optic based smart structures', *Opt. Eng.*, **31**, pp34-47 (1992).

- Measures, R.M., 'Fiber optic sensing for composite smart structures', *Composites Eng.*, **3**, pp715-750 (1993).
- Melle, S.M., Alavie, A.T., Karr, S., Coroy, T., Liu, K., and Measures, R.M., 'A Bragg grating-tuned fiber laser strain sensor system', *IEEE Photon. Technol. Lett.*, **5**, pp263-266 (1993).
- Morey, W.W., Meltz, G., and Glenn, W.H., 'Fiber optic Bragg grating sensors', in *Proc. Fibre Optic and Laser Sensors VII*, Boston, pp98-107 (1989).
- Namihira, Y., 'Opto-elastic constant in single mode optical fibers', *J. Lightwave Technol.*, **5**, pp1078-1083 (1985).
- Read, I.J., 'High speed multiplexed interrogation of Bragg grating sensors using a Fabry-Pérot tunable filter' to published in *Smart. Mater. Struct.* (1997).
- Roberts, S.S.J., and Davidson, R., 'Short term fatigue behaviour of composite materials containing embedded fiber optic sensors and actuators', in *Proc. First European Conference on Smart Structures and Materials*, Glasgow, pp255-262 (1992).
- Sirkis, J.S., and Dasgupta, A., 'Optimal coatings for intelligent structure fiber optic sensors', in *Proc. Fiber Optic Smart Structures and Skins III*, San José, pp129-140 (1990).
- Sirkis, J.S., and Haslach, H.W. Jr., 'Full phase-strain relation for structurally embedded interferometric optical fiber sensors', in *Proc. Fiber Optic Smart Structures and Skins III*, San José, pp248-259 (1990).
- Takahashi, S., and Shibata, S., 'Thermal variation of attenuation for optical fibers', *J. Non-crys. Solids*, **30**, pp359-370 (1979).
- Waite, S.R., Tatam, R.P., and Jackson, A., 'Use of optical fibre for damage and strain detection in composite materials', *Composites*, **19**, pp435-442 (1988).

Chapter 5

Simultaneous strain and temperature measurement

5.1 Techniques for strain and temperature separation

It has been shown in section 4.1 that the temperature sensitivity of an IFBG, significantly limits its application to quasi-dc strain sensing. A number of sensing configurations have been reported to overcome this limitation. These schemes may be divided into those that allow only a temperature independent strain measurement to be made and those which allow simultaneous strain and temperature measurements.

A number of techniques may be used to measure strain independently of temperature, including the following methods. The simplest approach is to use an additional reference grating that is shielded from strain and therefore only measures temperature (Kersey *et al*, 1993). Cancellation of the thermal response of a grating has been reported using two IFBGs that are mounted on opposite sides of a bent surface, such that the gratings have equal, but opposite strains (Xu *et al*, 1994(a)). Yoffe *et al* (1995) have demonstrated a sensor package (50mm long by 5mm in diameter) that pre-strains a grating between two materials with different thermal expansion coefficients. Temperature compensation is achieved by applying an appropriate strain reduction. It has also be shown that the reflection bandwidth from a

chirped grating written into a tapered fibre is dependent upon applied strain, but independent of temperature (Xu *et al*, 1995). As the strain level is determined by monitoring the intensity of the reflected signal, serial sensor arrays can only be addressed by time-division multiplexing.

Four techniques for simultaneous strain and temperature measurement have been demonstrated. The dual wavelength technique demonstrated by Xu *et al* (1994(b)) involves writing two superimposed gratings with a large Bragg wavelength separation (850nm and 1300nm). The main disadvantages with this method are that the optical fibre will not be singlemode at one of the Bragg wavelengths and two broadband sources are required to address the sensor. A similar method has been proposed by Kalli *et al* (1995) which, instead of using two IFBGs, uses the first and second order diffraction from a single saturated grating. An alternative method, is to use another type of fibre optic sensor in conjunction with an IFBG. Kanellopoulos *et al* (1995) used a pair of polarisation-rocking filters, acting as a Mach-Zehnder interferometer, in combination with an IFBG. The sensor had a gauge length of 25cm, which is impractical for many applications. Recently Patrick *et al* (1996) combined the recently demonstrated long period grating (LPG) (Vengsarkar *et al*, 1996) with a pair of IFBGs wavelength spaced by $\sim 30\text{nm}$. The sensor measures the effect of the LPG wavelength shift on the relative intensities of the two IFBG reflections, in addition to monitoring the Bragg wavelength of one of the IFBGs directly. The technique appears promising, but it does not allow high density WDM and has the drawback that the sensor information is not purely spectrally encoded.

5.2 Simultaneous determination of strain and temperature

5.2.1 Inverse matrix solution of simultaneous linear equations

The simultaneous strain and temperature measurement techniques described above all assume that the effects of a temperature shift ΔT and an applied strain ϵ_x can

be linearly superimposed and that there is a negligible cross sensitivity term $\varepsilon_x \Delta T$ (Farahi *et al*, 1990). If this assumption is valid, temperature and strain may be recovered from a fibre sensor if two parameters can be measured that allow the solution of a pair of simultaneous equations. If parameters ϕ_1 are ϕ_2 are both functions of ε and ΔT then their relationship may be described by the following matrix formulation (Jin *et al*, 1996)

$$\begin{pmatrix} \phi_1 \\ \phi_2 \end{pmatrix} = \begin{pmatrix} K_{11} & K_{12} \\ K_{21} & K_{22} \end{pmatrix} \begin{pmatrix} \varepsilon \\ \Delta T \end{pmatrix} \quad (5.1)$$

or

$$\Phi = K\Omega \quad (5.2)$$

where K is the transfer matrix from Ω to Φ and is characteristic of the sensor scheme being investigated. If the elements of K are known ε and ΔT can be calculated from

$$\Omega = K^{-1}\Phi \quad (5.3)$$

where K^{-1} is the inverse of K . Equation 5.3 is valid as long as the determinant of K is non-zero, i.e.

$$K_{11}K_{22} - K_{21}K_{12} \neq 0 \quad (5.4)$$

In the case of schemes based purely on IFBGs, it has been demonstrated that $\varepsilon_x \Delta T$ is negligible for small perturbations (Morey *et al*, 1989). However, for larger measureands the inclusion of $\varepsilon_x \Delta T$ terms may be necessary. For strain measurements taken at temperatures above 400°C changes in the fibre physical properties become an issue (Morey *et al*, 1994). For example, Morey *et al* (1994) found a 5% decrease in the Bragg wavelength response with an applied stress at 650°C. This was due to a change in the Young's modulus of the fibre, but it was not as high as the 8% change expected. It was thought that this difference was due to a temperature induced change in the strain-optic coefficient. Also, when a high strain (0.3%) was applied for a prolonged period at 650°, a permanent shift in the Bragg wavelength was observed and it appeared that the fibre elastic limit had been exceeded.

5.2.2 Error sensitivity

It is obviously desirable to be able to compare the measurement accuracy of the techniques described in section 5.1 for simultaneous strain and temperature measurement. A direct comparison of the errors reported for each of the sensor configurations is not a good indicator of their relative merits. Firstly, the error analysis method is not consistent between schemes and secondly, the quoted errors are specific to a particular experimental arrangement.

A more appropriate method is to compare how sensitive the recovered measureands are to errors in the elements of \mathbf{K} and Φ . This can be done by assessing the ‘conditioning’ of the transfer matrix (Vengsarkar *et al*, 1994). If the transfer matrix is ill-conditioned even small errors in \mathbf{K} and Φ will lead to large errors in the recovered measureands. The condition number C_N (Dalquist, 1974) provides a quantitative measure of matrix conditioning. C_N can be determined from the ‘norms’ of \mathbf{K} and \mathbf{K}^{-1} which are denoted by $\|\mathbf{K}\|$ and $\|\mathbf{K}^{-1}\|$ respectively. Norms are scalar quantities that indicate the magnitude of a vector or matrix. From Dalquist (1974) C_N is simply given by

$$C_N = \|\mathbf{K}\| \|\mathbf{K}^{-1}\| \quad (5.5)$$

The value of C_N is always ≥ 1 and the less well-conditioned the matrix the larger C_N will be. The most ill-conditioned matrix being the singular matrix ($C_N = \infty$).

Later a comparison will be made between values of C_N calculated for the previously reported techniques and a new scheme that we have devised. For this comparison the ‘maximum norm’ (Dalquist, 1974) was preferred since it can easily be calculated. The maximum norm of \mathbf{K} and \mathbf{K}^{-1} being defined as

$$\begin{aligned} \|\mathbf{K}\|_{\infty} &= \max_{i=1,2} \sum_{j=1}^2 |K_{ij}| \\ \|\mathbf{K}^{-1}\|_{\infty} &= \max_{i=1,2} \sum_{j=1}^2 |K^{-1}_{ij}| \end{aligned} \quad (5.6)$$

5.3 Spliced grating pair technique

A novel method for separating the strain and temperature response of IFBG sensors has been demonstrated. The technique is based on the difference in strain response of two IFBGs written either side of a fusion splice between two fibres of different diameters. The work discussed in this section was carried out in collaboration with a colleague, Dr S.W. James.

5.3.1 Theory

The geometry of the grating pair is shown in figure 5.1. Using this arrangement it is possible to independently measure the total axial strain ϵ_x between the anchor points B and C, and a temperature shift ΔT .

For each IFBG the change in the Bragg wavelength $\Delta\lambda_i$ induced by a strain, ϵ_x , and a temperature shift, ΔT , is given by

$$\Delta\lambda_i = \kappa_{\epsilon i} \epsilon_i + \kappa_{T i} \Delta T \quad i = 1, 2 \quad (5.7)$$

where ϵ_i is the local strain experienced by a grating. Since equation 5.7 is really only a modified form of equation 4.11, the coefficients $\kappa_{\epsilon i}$ and $\kappa_{T i}$ are defined as

$$\begin{aligned} \kappa_{\epsilon i} &= S_{Bi} \lambda_{0i} \\ \kappa_{T i} &= T_{Bi} \lambda_{0i} \end{aligned} \quad i = 1, 2 \quad (5.8)$$

where S_{Bi} and T_{Bi} represent the strain and temperature gauge factors respectively of each fibre type, and λ_{0i} is the initial Bragg wavelength of an IFBG. For a given stress the strains experienced by the fibres will be related by

$$\frac{\epsilon_1}{\epsilon_2} = \frac{A_1}{A_2} \quad (5.9)$$

where A_i is the cross-sectional area of each fibre.

Now, in order to obtain a transfer matrix for this system, which when inverted can be used to calculate the total strain, ϵ_x , equation 5.7 needs to be modified so that ϵ_i is expressed in terms of ϵ_x . It is evident from figure 5.1 that

$$\epsilon_i = \frac{\Delta l_i}{l_i} \quad i = 1, 2 \quad (5.10)$$

and

$$\epsilon_x = \frac{\Delta l_1 + \Delta l_2}{l_1 + l_2} \quad (5.11)$$

where l_i represents the length of each fibre between the splice and the anchoring points, B and C , and Δl_i is the extension of each fibre. Substituting equations 5.9 and 5.10 into equation 5.11 and rearranging

$$\begin{aligned} \epsilon_1 &= \frac{l_1 + l_2}{l_1 \left(1 + \frac{A_1 l_2}{A_2 l_1} \right)} \epsilon_x \\ \epsilon_2 &= \frac{l_1 + l_2}{l_2 \left(1 + \frac{A_2 l_1}{A_1 l_2} \right)} \epsilon_x \end{aligned} \quad (5.12)$$

Thus equation 5.7 may now be written in the form of equation 5.1

$$\begin{pmatrix} \Delta \lambda_1 \\ \Delta \lambda_2 \end{pmatrix} = \begin{pmatrix} \kappa_{\epsilon 1} \frac{l_1 + l_2}{l_1 \left(1 + \frac{A_1 l_2}{A_2 l_1} \right)} & \kappa_{T1} \\ \kappa_{\epsilon 2} \frac{l_1 + l_2}{l_2 \left(1 + \frac{A_2 l_1}{A_1 l_2} \right)} & \kappa_{T2} \end{pmatrix} \begin{pmatrix} \epsilon_x \\ \Delta T \end{pmatrix} \quad (5.13)$$

and the temperature shift and the total strain can be calculated using the inverse of the matrix given in equation 5.13.

For fibres that have similar strain and temperature gauge factors, a temperature change will shift the Bragg wavelength of each grating by a similar amount, maintaining their wavelength spacing. In contrast, an applied strain results in a Bragg wavelength shift that is different for each grating. Thus the wavelength

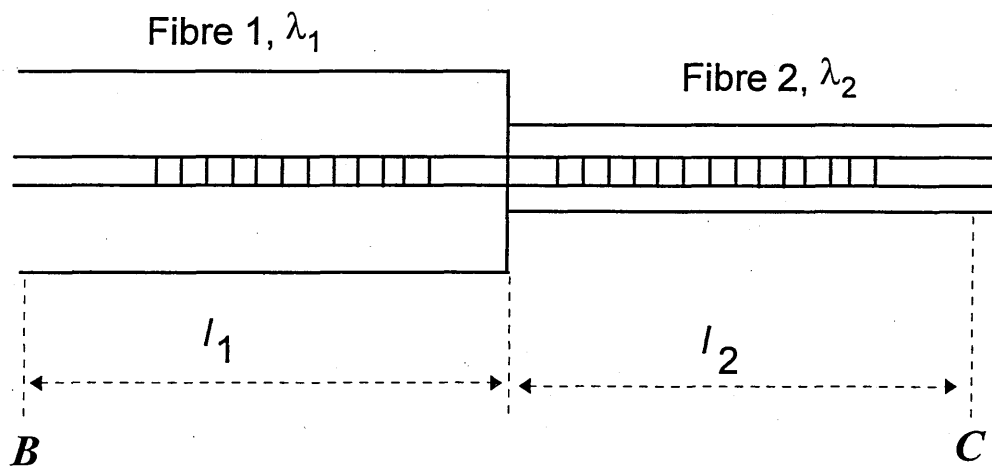


Figure 5.1 Geometry of the spliced IFBG pair. B and C are anchoring points across which a load was applied, l_1 and l_2 are the distances from the anchoring points to the splice.

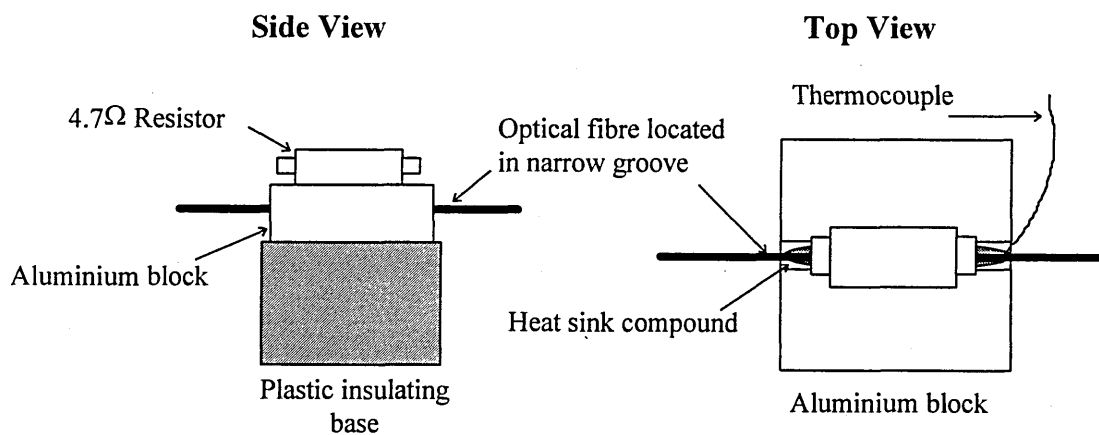


Figure 5.2 Experimental arrangement used to heat the optical fibres.

spacing provides a measurement of strain, while the absolute wavelength shifts include information on both strain and temperature.

The elements of the transfer matrix could in principle be calculated starting from the strain and temperature gauge factors. However, significant errors can arise in the calculation of the strain coefficients due to fibre diameter tolerances (usually between 2-4%) and errors in the measurement of length. In general, it is preferable to experimentally determine the matrix elements by monitoring the response of each IFBG to a given strain and temperature range.

5.3.2 Experimental determination of the transfer matrix

As a proof of principle, the transfer matrix was experimentally determined for a sensor scheme consisting of two IFBGs written either side of a fusion splice between a Spectran (780nm) and a Corning (820nm) Hi-Bi fibre. The cladding diameters for the Spectran and Corning fibres being $125\pm 2\mu\text{m}$ and $80\pm 3\mu\text{m}$ respectively.

The IFBGs were fabricated using the two-beam mirror interferometer technique (see section 3.2.4), both fibres having been hydrogen loaded prior to exposure. The gratings had initial Bragg wavelengths of 827.1nm (Spectran) and 834.7nm (Corning) and the peak reflectivities were estimated (from the minimum transmission) to be 60% and 75% respectively.

To determine the strain response of the IFBGs the experimental rig described in section 4.2.2 was used, and the Bragg wavelength shift of each grating was monitored using the automated scanning monochromator and ELED source (see section 4.2.1). The fusion splice was not optimised and from measurements of the ELED transmission it was estimated that the optical loss at the splice was $\sim 2\text{dB}$. The initial length of fibre between the fixing points was $60\pm 0.5\text{mm}$, which introduced a 0.8% systematic error. The splice was arbitrarily positioned in that the lengths l_1 and l_2 were not measured. Increasing strain was applied over the range $0\text{--}2833\mu\text{strain}$ in $167\pm 8\mu\text{strain}$ increments, and the zero strain condition could be located to an

accuracy of $85\mu\text{strain}$. Otherwise the experimental details were as described in section 4.2.2.

During the investigation of the sensor scheme's strain response, the splice failed at around $300\mu\text{strain}$. Unfortunately there was insufficient time to repeat the experiment, so in order to determine the temperature response of IFBGs written into Spectran and Corning fibre, a grating was written into a separate length of each fibre type. The initial Bragg wavelengths being 828.4nm (Spectran) and 831.74 (Corning) and the peak reflectivities were estimated to be 55% and 60% respectively. From equation 5.8 it can be seen that the temperature coefficient, κ_{Ti} , depends upon the initial Bragg wavelength. In this case, however, the relative difference between the initial Bragg wavelengths of IFBGs written into the same fibre type was $<0.4\%$ and so was not significant. The experimental arrangement used to heat the optical fibres is shown in figure 5.2. The fibre under test was located in a groove in an aluminium block that sat on an insulating plastic base. The IFBG lying approximately mid-way along the length of the groove. Heat sink compound was used to ensure a good thermal transfer between the aluminium and the optical fibre. To heat the assembly a large 25W , 4.7Ω resistor was bolted to the top of the aluminium block and connected to a dc power supply. The temperature of the fibre was controlled by varying the voltage across the resistor. Once set to a particular voltage the whole assembly was left for several minutes to reach an equilibrium condition. A thermocouple immersed in the heat sink compound close to the optical fibre monitored the temperature to an accuracy of $\pm 0.1^\circ\text{C}$. The temperature remained stable to this accuracy throughout the measurement period. The temperature was raised from room temperature to around 150°C with measurements being taken at approximately 10°C intervals. Again the automated scanning monochromator and ELED source were used to monitor the shifts in Bragg wavelength.

The change in the Bragg wavelengths with applied strain measured for IFBGs written into the spliced fibres are shown in figure 5.3(a). Measurements were made relative to a reference grating at 823.4nm . The gradients of straight line fits to the plotted data, represented by K_{ei}^{meas} , gave a measure of the strain response of each

IFBG and these are given in table 5.1. Similarly, the measured temperature responses of IFBGs written into separate lengths of Corning and Spectran fibre are shown in figure 5.3(b). In this case, measurements were made relative to reference gratings at 822.6nm (Spectran) and 823.5nm (Corning). The gradients of straight line fits to the plotted data are represented by K_{Ti}^{meas} and these are also given in table 5.1.

Now, it is apparent from the discussion in section 4.2.2 that the strain and temperature responses measured by the monochromator are prone to a large error that is a strong function of wavelength. Therefore, to be of any value, $K_{\epsilon i}^{meas}$ and K_{Ti}^{meas} require calibration to account for this effect. To this end a crude calibration was performed using the data plotted in figure 4.5. Firstly, the mean Bragg wavelengths of the IFBGs during the determination of $K_{\epsilon i}^{meas}$ and K_{Ti}^{meas} were obtained, and these are denoted by $\overline{\lambda_{\epsilon i}}$ and $\overline{\lambda_{Ti}}$ respectively. Then using the data plotted in figure 4.5, the value of the Spectran strain gauge factor at wavelengths $\overline{\lambda_{\epsilon i}}$ and $\overline{\lambda_{Ti}}$ were estimated, and these are denoted by $S_{\epsilon i}$ and $S_{\Delta Ti}$ respectively. The calibrated temperature and strain responses $K_{\epsilon i}^{cal}$ and K_{Ti}^{cal} were then calculated using the expressions

$$K_{\epsilon i}^{cal} = K_{\epsilon i}^{meas} \frac{\overline{S_B^{sp}}}{S_{\epsilon i}} \quad i = 1, 2 \quad (5.14)$$

and

$$K_{Ti}^{cal} = K_{Ti}^{meas} \frac{\overline{S_B^{sp}}}{S_{Ti}} \quad i = 1, 2 \quad (5.15)$$

where $\overline{S_B^{sp}}$ is the mean strain gauge factor for Spectran (780nm) fibre calculated from data plotted in figure 4.5, and has the value 0.76. The values of $\overline{\lambda_{\epsilon i}}$ and $\overline{\lambda_{Ti}}$, $S_{\epsilon i}$ and S_{Ti} , $K_{\epsilon i}^{cal}$ and K_{Ti}^{cal} are all given in table 5.1. The calculated values of $K_{\epsilon i}^{cal}$ and K_{Ti}^{cal} were used to form a transfer matrix for the system.

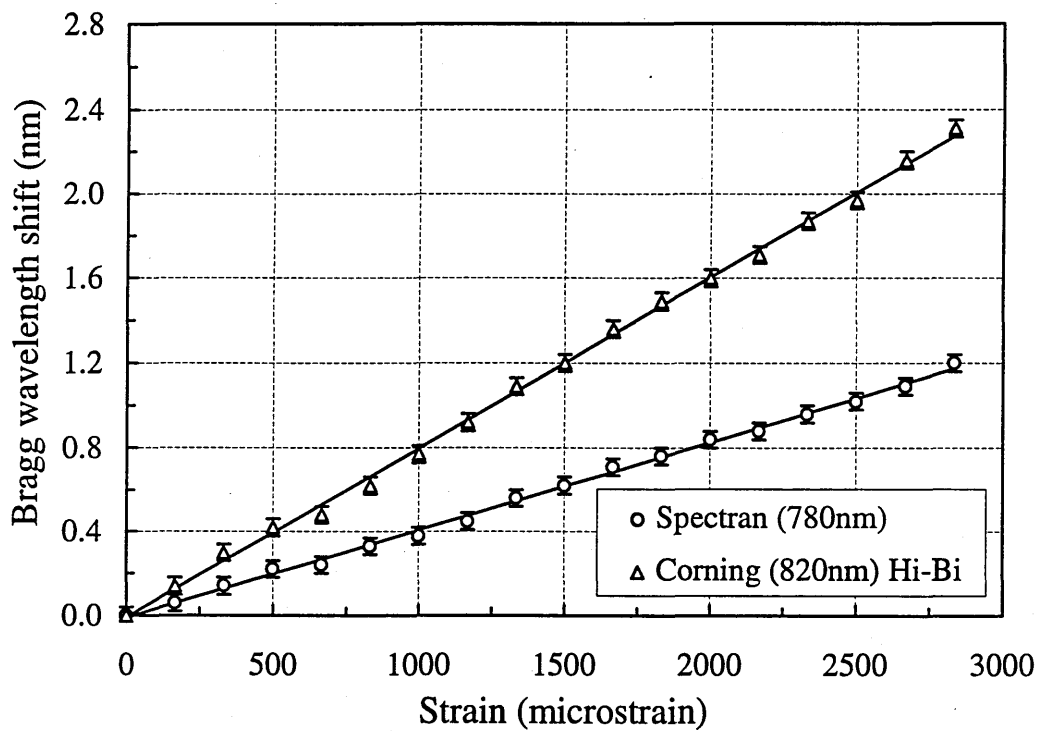


Figure 5.3(a) Measured strain response of the IFBG pair.

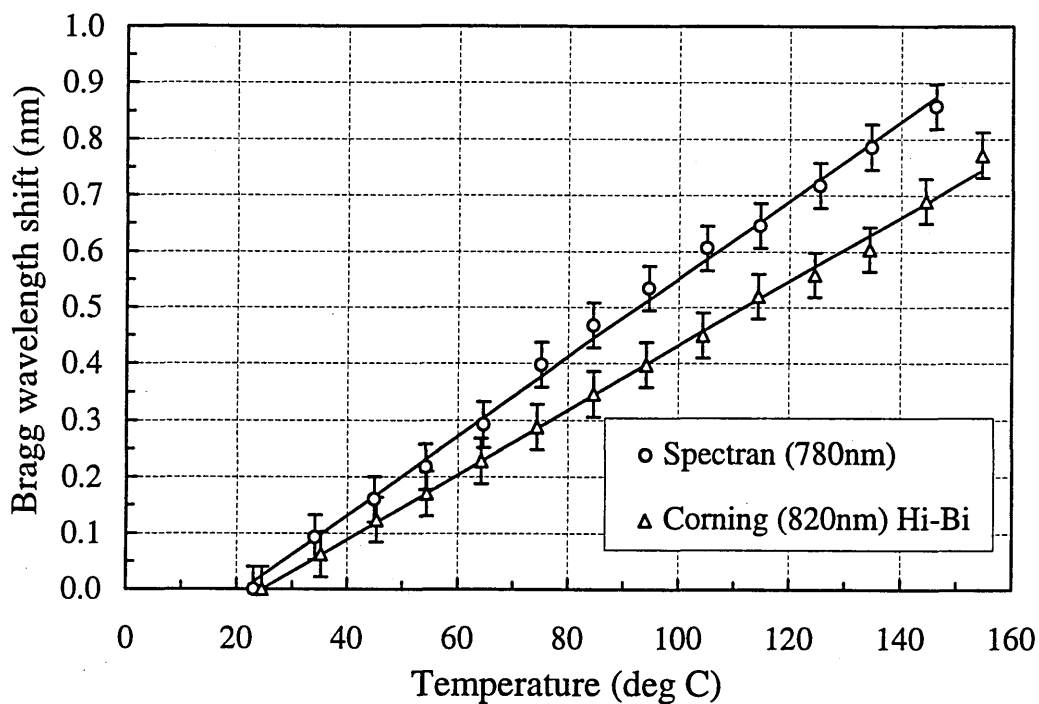


Figure 5.3(b) Measured temperature response of the IFBG pair.

Parameter	IFBGs in Corning (820nm) Hi-Bi	IFBGs in Spectran (780nm)
Measured strain response, $K_{\epsilon i}^{meas}$ (pm/ μ strain)	$0.806 \pm 8 \times 10^{-3}$	$0.418 \pm 5 \times 10^{-3}$
Strain calibration wavelength, $\bar{\lambda}_{\epsilon i}$ (nm)	835.9	827.7
Strain calibration factor, $\bar{S}_B^{sp} / S_{\epsilon i}$	(0.76/0.70) 1.086	(0.76/0.88) 0.8636
Calibrated strain response, $K_{\epsilon i}^{cal}$ (pm/ μ strain)	0.875	0.361
Measured temperature response, K_{Ti}^{meas} (pm/ $^{\circ}$ C)	5.73 ± 0.008	6.99 ± 0.12
Temperature calibration wavelength, $\bar{\lambda}_{Ti}$ (nm)	832.1	828.9
Temperature calibration factor, $\bar{S}_B^{sp} / S_{\Delta Ti}$	(0.76/0.81) 0.9383	(0.76/0.93) 0.8172
Calibrated temperature response, K_{Ti}^{cal} (pm/ $^{\circ}$ C)	5.38	5.71

Table 5.1 The measured and calibrated IFBG strain and temperature responses.

Sensor scheme	K matrix element				Cond No C_N
	K_{11} (pm/ μ strain)	K_{12} (pm/ $^{\circ}$ C)	K_{21} (pm/ μ strain)	K_{22} (pm/ $^{\circ}$ C)	
Dual wavelength IFBGs	0.96	8.72	0.59	6.30	161
First/second order IFBG reflection	1.155	13.9	0.585	6.39	407
Rocking filter/IFBG	0.670	7.37	-1.73	-204	351
LPG/IFBG	$-5 \times 10^{-2}*$	7*	1.03	8.7	20
Spliced IFBG pair	0.875	5.38	0.361	5.71	23

Table 5.2 Comparison of transfer matrix conditioning for the simultaneous strain and temperature measurement techniques.

* LPG strain and temperature elements have units of μ strain $^{-1}$ and $^{\circ}$ C $^{-1}$ respectively.

As the splice had failed whilst investigating the sensor scheme's strain response, it was not possible to experimentally determine how accurately a simultaneously applied strain and temperature shift could be recovered using equation 5.3. It was possible, however, to calculate the condition number for the transfer matrix using equations 5.5 and 5.6. and this was compared to the condition numbers determined for the other reported simultaneous strain and temperature measurement schemes. The transfer matrix elements and the condition numbers for all of these techniques are given in table 5.2. It can be seen that the spliced IFBG pair scheme compares favourably with the other reported methods. The spliced IFBG pair technique has the most well conditioned matrix of all the sensor configurations based purely on IFBGs. Another advantage it has over the dual wavelength techniques is that the Bragg wavelengths of the two gratings may differ by only a few nm, allowing grating pairs to be WDM and addressed by a single broadband source. The only configuration that has a similarly well-conditioned matrix is the LPG/IFBG technique. However, the spliced IFBG pair scheme allows denser WDM than the LPG/IFBG scheme and has the additional advantage that the sensor information is purely spectrally encoded.

The obvious drawback of using spliced IFBG pairs is the large number of fusion splices involved in creating a serial sensor array. Also, the spliced IFBG pair scheme is not suitable for applications where the sensor is bonded along its entire length to the host structure, as each grating will directly measure the strain field of its local environment and equation 5.9 will no longer apply. Therefore, the technique cannot be used to simultaneously monitor the temperature and strain of optical fibres embedded within composite structures, as described in section 4.3. The first of these limitations could be overcome, if instead of fabricating gratings in two separate fibres of different diameters, the grating pair was written into a single fibre and the fibre was locally etched to change its diameter at the location of one of the IFBGs. The strength of the fusion splice between fibres of different diameters (or indeed an etched sensor region) may also be an issue and requires investigation. Further the technique

assumes that the temperature is uniform across the IFBG pair, which may not necessarily be true in environments where there are steep temperature gradients.

It should be noted that the above discussion assumes that the transfer matrix elements for the spliced IFBG pair sensor have been reasonably accurately determined. For example, if there was an error of 20% in each of the matrix elements and these errors added in the worst possible way a condition number of 180 would be obtained. For this reason, and the fact that the demonstrated sensor was not optimised, further experimental work and analysis needs to be done to determine the optimum sensor configuration.

References

- Dalquist, G., 'Numerical Methods', Prentice-Hall, Inc., N.J., USA (1974).
- Farahi., F., Webb, D.J., Jones., J.D.C., and Jackson, D.A., 'Simultaneous measurement of temperature and strain: cross-sensitivity considerations', *J. Lightwave Technol.*, **8**, pp138-142 (1990).
- Jin, W., Michie, W.C., Thursby, G., Konstantaki, M., and Culshaw, B., 'Simultaneous strain and temperature recovery: error analysis', in *Proc. 11th Optical Fibers Sensors Conference, OFS-11*, Sapporo, Japan, pp116-119 (1996).
- Kalli, K., Brady, G., Webb, D.J., Jackson, D.A., Reekie, L., and Archambault, J.-L., 'Possible approach for the simultaneous measurement of temperature and strain via first and second order diffraction from Bragg grating sensors', *SPIE*, **2507**, pp190-198 (1995).
- Kanellopoulos, S.E., Handerek, V.A., and Rogers A.J., 'Simultaneous strain and temperature sensing with photogenerated in-fiber gratings', *Opt. Lett.*, **20**, pp333-335 (1995).
- Kersey, A.D., Berkoff, T.A., and Morey, W.W., 'Fibre optic Bragg grating strain sensor with drift compensated high resolution interferometric wavelength shift detection', *Opt.Lett.*, **18**, pp72-74 (1993).

- Morey, W.W., Meltz, G., and Glenn, W.H., 'Fiber optic Bragg grating sensors', in *Proc. Fiber Optic and Laser Sensors VII*, Boston, pp98-107 (1989).
- Morey, W.W., Meltz, G., and Weiss, J.M., 'High temperature capabilities and limitations of fiber grating sensors', in *Poc. 10th Optical Fibers Sensors Conference, OFS-10*, Glasgow, pp234-237 (1994).
- Patrick, H.J., Williams, G.M., Kersey, A.D., Pedrazzani, J.R., and Vengsarkar, A.M., 'Hybrid fiber Bragg grating/long period fiber grating sensor for strain/temperature discrimination', *IEEE Photon. Technol. Lett.*, **8**, pp1223-1225 (1996).
- Vengsarkar, A.M., Michie, W.C., Jankovic, L., Culshaw, B., and Claus, R.O., 'Fiber-optic dual-technique sensor for simultaneous measurement of strain and temperature', *J. Lightwave Technol.*, **12**, pp170-177 (1994).
- Vengsarkar, A.M., Lemaire P.J., Judkins, B.J., Bhatia, V., Erdogan, T., and Sipe, J.E., 'Long-period fiber gratings as band-rejection filters', *J. Lightwave Technol.*, **14**, pp58-65 (1996).
- Xu, M.G., Archambault, J.-L., Reekie, L., and Dakin, J.P. (a), 'Thermally-compensated bending guage using surface mounted fibre gratings', *Int. J. Optoelectron.*, **9**, pp281-283 (1994).
- Xu, M.G., Archambault, J.-L., Reekie, L., and Dakin, J.P. (b), 'Discrimination between strain and temperature effects using dual-wavelength fibre grating sensors', *Electron. Lett.*, **30**, pp1085-1087 (1994).
- Xu, M.G., Dong, L., Reekie, L., Tucknott, J.A., and Cruz, J.L., 'Temperature-independent strain sensor using a chirped Bragg grating in a tapered optical fibre', *Electron. Lett.*, **31**, pp823-825 (1995).
- Yoffe, G.W., Krug, P.A., Ouellette, F., and Thorncraft, D.A., 'Passive temperature-compensating package for optical fiber gratings', *Appl. Opt.*, **34**, pp6859-6861 (1995).

Chapter 6

Volume holographic demodulation of Bragg grating sensors

A novel method for parallel interrogation and demultiplexing of WDM grating arrays, using a volume holographic spectral filter bank has been demonstrated. This work was carried out in collaboration with a colleague, Dr S.W. James. Since Dr James was the principal investigator for this work, only a brief outline of the underlying principles and a summary of the experimental investigation are presented below.

6.1 Interrogation and demultiplexing techniques for WDM grating arrays

In order to make practical sensor schemes based on WDM gratings, a key requirement is the development of instrumentation that can accurately determine the relatively small Bragg wavelength shifts induced by a measureand. Clearly, the spectrometer systems described in previous sections would be inappropriate for a commercial system, due to their limited accuracy, size, and slow scan rates. However, the Fabry-Pérot tuneable filter system described in section 4.3.5 offers a more feasible solution. A number of other methods for monitoring the Bragg wavelength of gratings have been proposed, and are generally referred to as interrogation techniques. Some of these techniques may be extended to demultiplex WDM grating arrays. However,

this is an area of considerable research activity in itself, and since an investigation of IFBG interrogation schemes was not a primary aim of this work, a full review of such techniques is outside the scope of this thesis. A review of some of the most promising interrogation and demultiplexing schemes that have been investigated to date can be found in Kersey (1994).

To summarise, WDM grating arrays have been addressed serially, using a scanning Fabry-Pérot tuneable filter (Kersey *et al*, 1993); and in parallel, using an array of matched receiving gratings (Jackson *et al*, 1993), edge filters (Melle *et al*, 1992), and an acousto-optic tuneable filter (Xu *et al*, 1993). Interferometric interrogation schemes have also been demonstrated (e.g. Kersey *et al*, 1992; Kersey *et al*, 1994), however, these schemes can only be extended to serial IFBG arrays by using time division multiplexing. The serial technique suffers from a limited bandwidth for detecting dynamic measurands. Even using the improved signal processing scheme reported by Read (1997) (see section 4.3.5), the Fabry-Pérot technique has a potential bandwidth limit of only a few hundred Hz. The use of matched receiving gratings or filters produces a complicated fibre network which makes inefficient use of the available reflected signal.

6.2 Volume holographic demodulation scheme.

Volume holograms would appear to be attractive optical elements for demultiplexing WDM grating arrays. They may be used to form spectral filters, the bandwidth of the filter depending upon the recording geometry (Rakuliic and Leyva, 1993), and large arrays of such filters may be multiplexed within a single optical component. The concept of the technique is illustrated in figure 6.1. An array of volume holograms is written using a combination of wavelength and angular multiplexing (Campbell *et al*, 1994), as shown in figure 6.1(a). The reference beam direction for each of the holograms is identical, but a different angle of incidence is used for the object beams. The wavelength for each object beam is chosen to be related to the quiescent state of one of the gratings within the sensor array. The

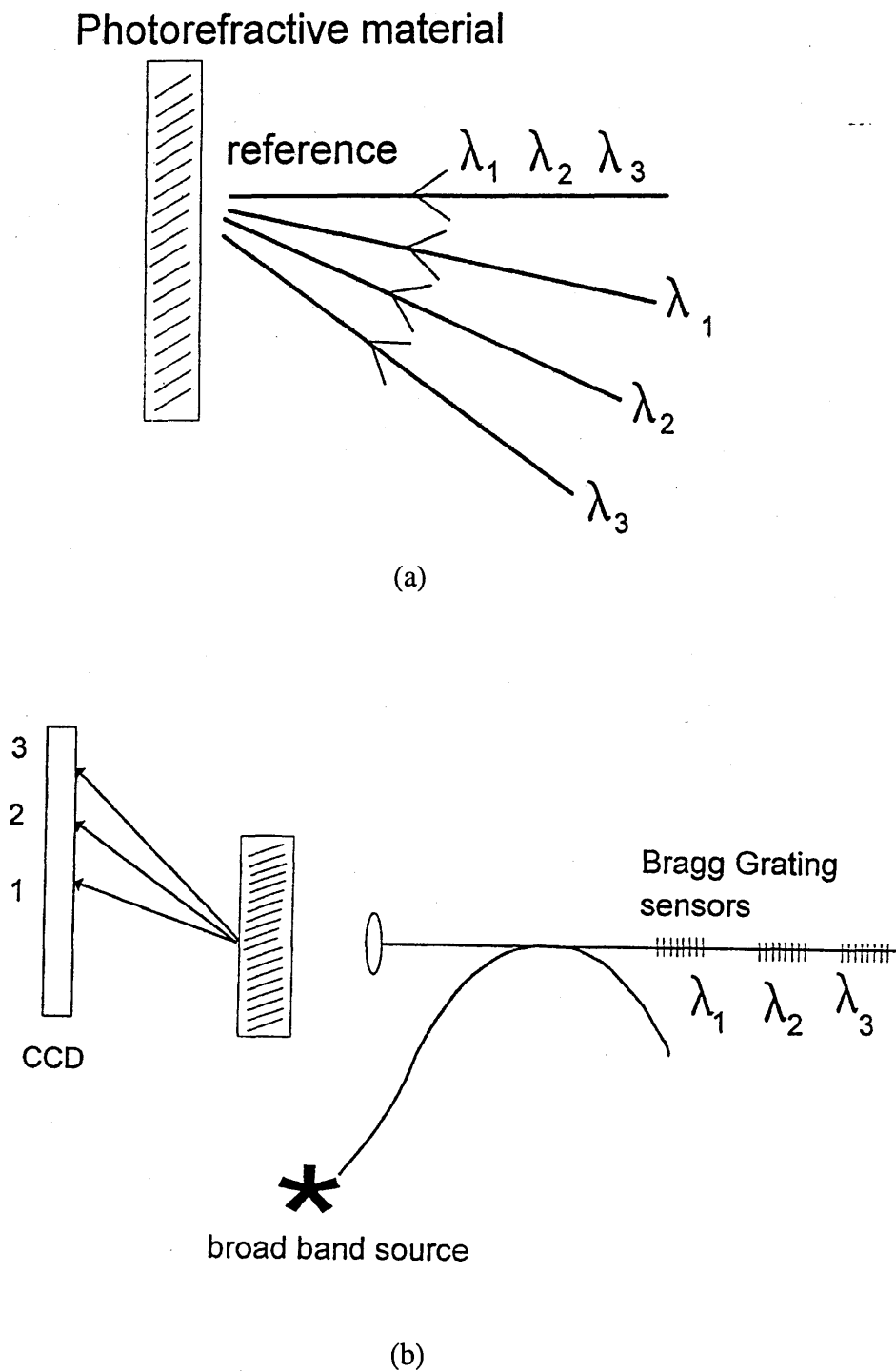


Figure 6.1 Concept of the proposed grating sensor demultiplexing scheme. (a) Recording the holographic filter bank using wavelength-angular multiplexing. (b) Illuminating the filter bank with the reflected grating signals angularly separates the signals. The diffracted power depends upon the Bragg wavelength shift.

holograms are written such that their bandwidth exceeds the range of the Bragg wavelength shift to be induced by the measurand. The holograms may be permanently fixed within the material, such that once the spectral filter bank has been recorded there is no further requirement for the writing source. A broadband source is used to address the IFBGs, and the reflected signals illuminate the volume hologram from the direction of the reference beam. The signal from each of the gratings is diffracted into a unique angle defined by angular-wavelength multiplexing of the holograms, with the diffraction efficiency being dependent upon the wavelength shift induced by the measurand. The grating's Bragg wavelength shift is thus transduced into a change in diffracted power by the transfer function of the volume hologram, while the holographic filter bank angularly separates the signals from each of the sensors.

Recently there has been renewed interest in the use of photorefractive materials for volume holographic data storage. Photorefractive materials offer the ability to form read/write volatile memory systems, or permanent memories by fixing the holograms (Gunter and Huignard, 1988). A number of multiplexing architectures have been proposed, including angular, spatial and wavelength, which use the high angular and wavelength selectivity of volume holograms to produce high density data storage systems.

Considering the arrangement shown in figure 6.1(b). Since the light is incident at or near the Bragg angle only diffraction into the outgoing signal beams needs to be taken into consideration. The other diffracted orders violate the Bragg condition strongly and are severely attenuated (Hariharan, 1984).

For a lossless phase grating the diffraction efficiency into each of the signal beams, η , can be determined from (Kogelnik, 1969)

$$\eta = \frac{\sin^2(\phi^2 + \chi^2)^{1/2}}{\left(1 + \frac{\chi^2}{\phi^2}\right)} \quad (6.1)$$

ϕ is known as the modulation parameter and is given by

$$\phi = \frac{\pi n_v l_v}{\lambda \cos \theta_v} \quad (6.2)$$

where n_v is the refractive index of the holographic material, l_v the length of the hologram, θ_v the half angle between the object and reference beams, and λ the wavelength. The parameter χ is a measure of the deviation from the Bragg condition and is related to a deviation in wavelength, $\Delta\lambda$, by the expression

$$\chi = \frac{-\Delta\lambda 2\pi \sin^2 \theta_v l_v}{\lambda^2 \cos \theta_v} \quad (6.3)$$

It can be seen from equation 6.1 that when $\chi=0$, for a given modulation parameter, the peak diffraction efficiency η_0 is

$$\eta_0 = \sin^2 \phi \quad (6.4)$$

The diffraction efficiency is maximised when $\phi=\pi/2$, at which point $\eta_0=1$ and all the energy is coupled into the diffracted beam.

Figure 6.2 shows a theoretical plot, calculated using equations 6.1 and 6.3, of the normalised diffraction efficiency (η/η_0) of a transmission volume hologram ($\lambda=840\text{nm}$, $l_v=12\text{mm}$, and $\theta_v=15^\circ$) as a function of the wavelength deviation from the Bragg condition. Curves were plotted for two different values of modulation parameter $\phi=\pi/2$ and $\phi=0.32$. These yield peak diffraction efficiencies of $\eta_0=1$ and $\eta_0=0.1$ respectively.

The angular and wavelength selectivity (the separation of the first zeros in the diffraction efficiency with respect to the Bragg angle and wavelength respectively), $\Delta\theta_v$ and $\Delta\Gamma$, are given by (Gunter, 1982)

$$\Delta\theta_v = \frac{n_v \lambda}{2l_v \sin \theta_v} \quad (6.5)$$

$$\Delta\Gamma = \frac{\lambda^2 \cos \theta_v}{2l_v \sin^2 \theta_v} \quad (6.6)$$

Thus for a hologram of length 1mm written in photorefractive BaTiO_3 , $n_v=2.424$, at a half-angle of 30° , and wavelength of 840nm, the angular selectivity is

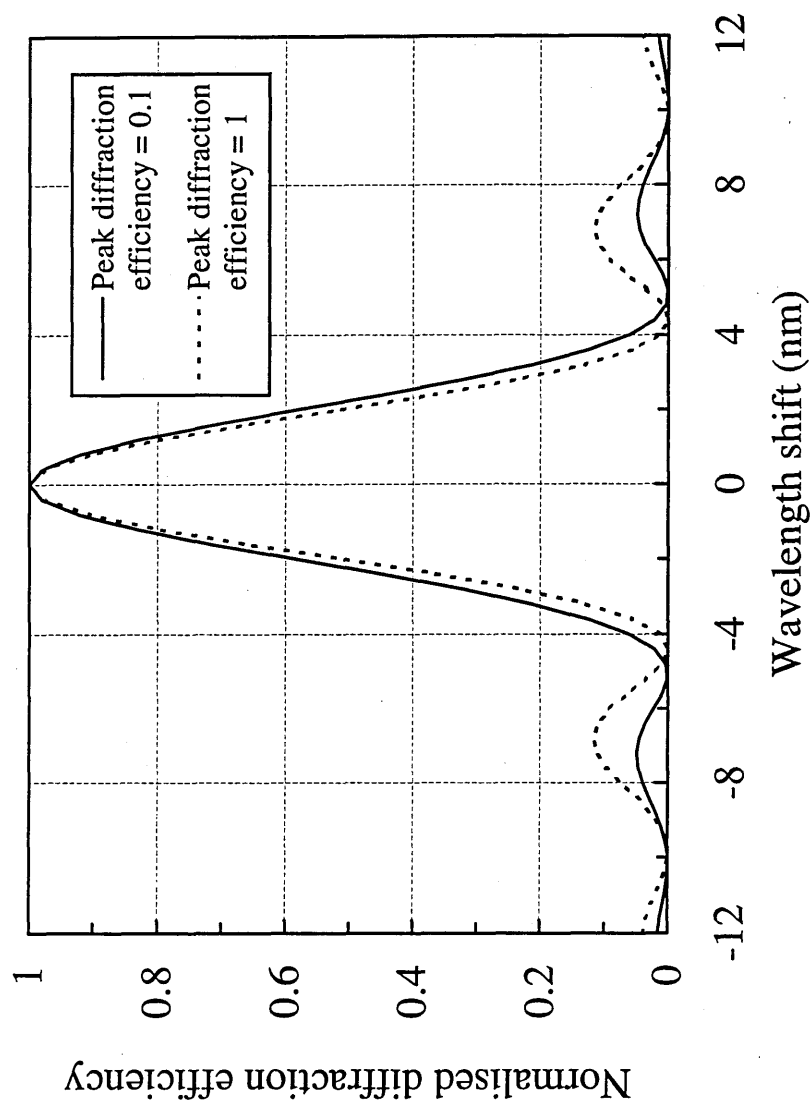


Figure 6.2 Volume transmission hologram wavelength sensitivity ($\lambda=840\text{nm}$, $L_p=1\text{mm}$, $\theta_p=15^\circ$). The normalised diffraction efficiency (η/η_0) is plotted as a function of the wavelength deviation from the Bragg condition for two different values of the modulation parameter, $\phi=\pi/2$ and $\phi=0.32$. These yield peak diffraction efficiencies of $\eta_0=1$ and $\eta_0=0.1$ respectively.

4mrad, and the wavelength selectivity is 5nm. The high angular selectivity of the holograms allows the construction of a compact detection system, possibly using a linear CCD array.

6.3 Interrogation of a Bragg grating using a volume hologram written into BaTiO₃.

An IFBG was fabricated in hydrogen loaded Spectran (780nm), using the two-beam mirror interferometer, with ~60% reflectivity at 840 nm, and 0.5 nm FWHM (monochromator resolution 0.35nm). The experimental configuration for writing the volume holographic database is shown in figure 6.3. The output from a Ti:sapphire laser was divided at a 3dB fibre coupler, with the outputs focused into a 5mm x 5mm x 5mm crystal of Rhodium doped BaTiO₃ such that they crossed at an angle of 30°. The Ti:sapphire was tuned to a wavelength chosen such that, in its quiescent state, the reflected signal from the grating would lie at the bottom of the positive slope of the hologram transfer function. The crystal was exposed for 30s at an intensity of 0.1Wcm⁻², producing holograms with 10% diffraction efficiency and 2nm FWHM. In this experiment the hologram was not fixed within the crystal, as the decay time of the hologram, when illuminated solely by the signal reflected from the IFBG, was in excess of 3 hours, sufficient to perform the measurements.

With the Ti:sapphire beams blocked, the IFBG was addressed using an ELED (as section 3.3.1) which was launched into the 3dB coupler, as illustrated in figure 6.3. The power incident upon the grating was 1μW, limited by the poor launch efficiency achieved from the highly divergent source. The signal reflected from the IFBG illuminated the hologram, and the diffracted light was observed on an appropriately positioned avalanche photodiode (APD). The experiment was carried out with a fixed polarisation state, which was determined by the in-line polarisation state controllers, and was set to give the maximum diffraction efficiency.

Lock in detection was used by square wave modulating the ELED injection current at 1 kHz. Figure 6.4 shows the variation of the diffracted power as a function

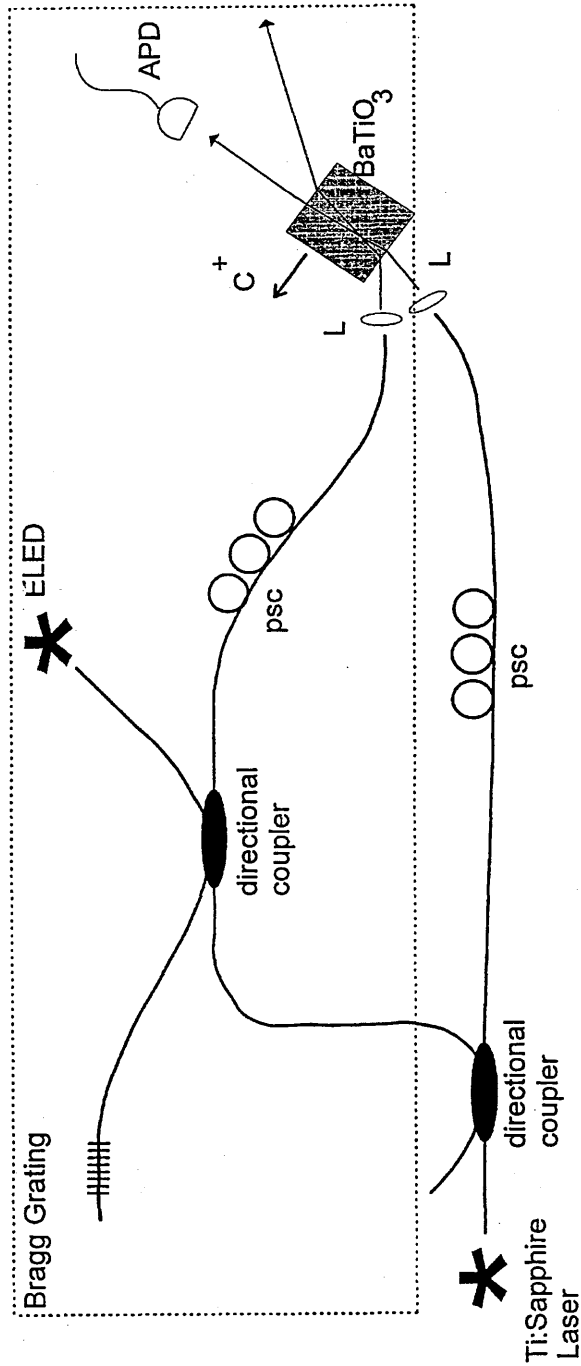


Figure 6.3 Experimental Configuration. psc, polarisation state controller; L, lens; APD, avalanche photodiode. ⁺ indicates the orientation of the optical axis of the BaTiO₃ crystal. The sensor system comprises only the components within the box. The Ti:sapphire laser source is required only during the recording of the hologram. In a practical system the hologram would be permanently fixed within the material, such that the tuneable laser would not be required in the field.

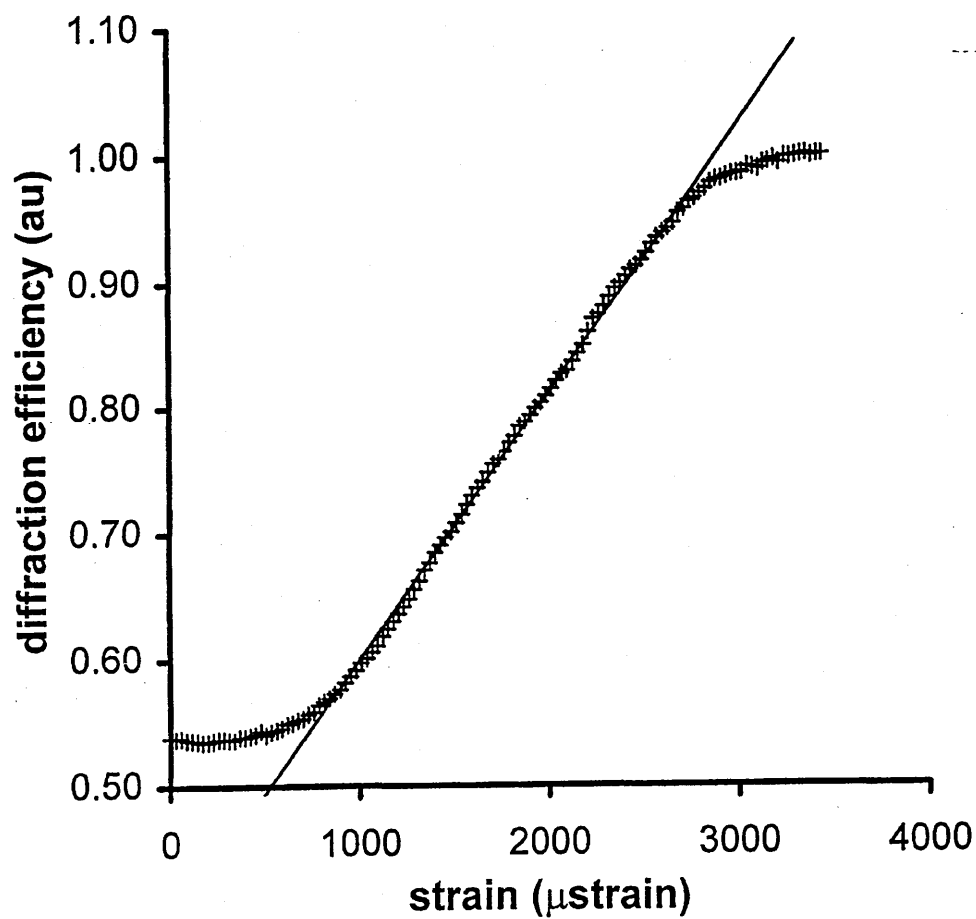
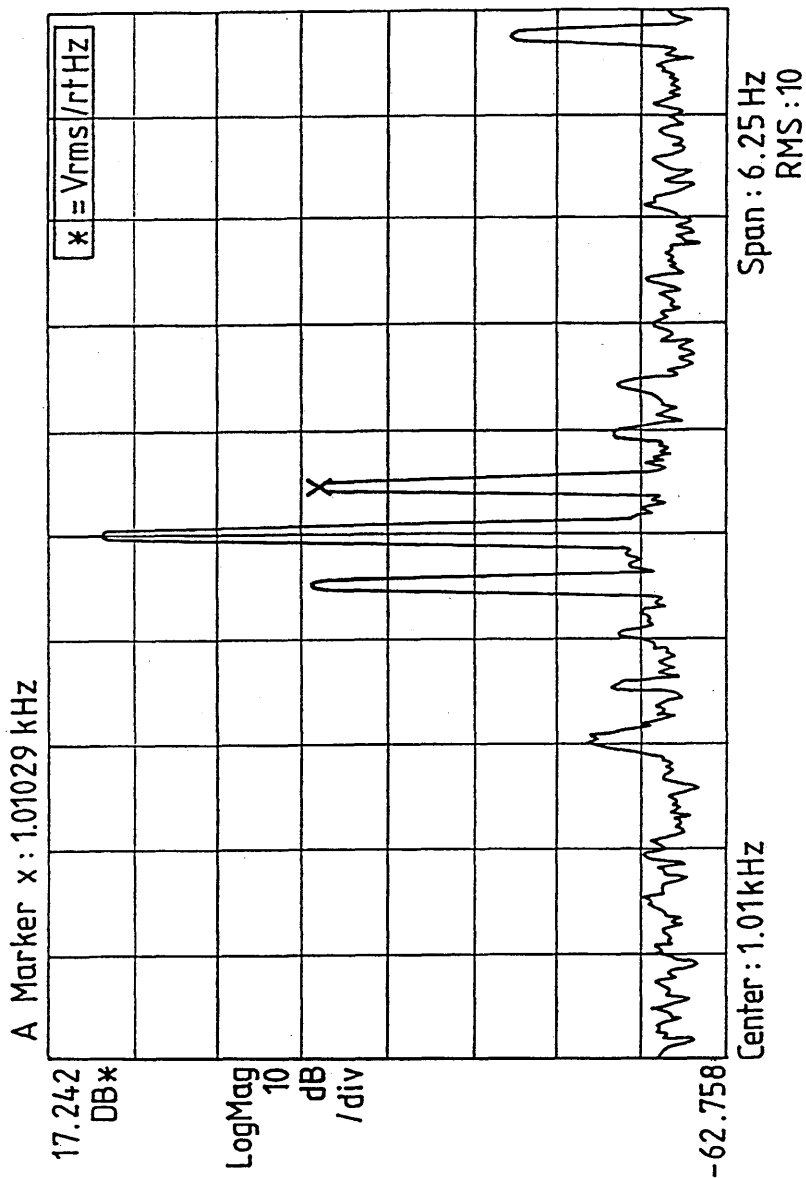


Figure 6.4 DC strain response of the demodulation scheme. The solid line is a fit to the linear portion of the transfer function. The measurement range is $2500\mu\text{strain}$, with $18\mu\text{strain}$ rms deviation.

of the strain applied to the fibre, illustrating a measurement range of 2500 μ strain with 18 μ strain rms deviation. The response of the system to dynamic strain was investigated by applying a sinusoidal signal to a piezo-electric stretcher, which was modulated at a frequency of 0.3Hz. Such a low modulation frequency was chosen because of the extremely limited frequency response of the piezo-electric stretcher. A typical spectrum analyser trace is shown in figure 6.5. The minimum detectable strain was determined from figure 6.5 by calculating the strain for that would give a signal:noise ratio of 1. The signal was measured at 13.6dBV/ $\sqrt{\text{Hz}}$ (dB=20log) for a strain of 371 μ strain and the adjacent noise floor was measured at 55dBV/ $\sqrt{\text{Hz}}$. From these values a minimum detectable strain of 4 μ strain/ $\sqrt{\text{Hz}}$ was calculated. The response of the system is determined by the characteristics of the volume hologram, which may be written to meet a specific requirement.

The use of volume holograms as spectral filters for demodulating IFBG sensors has a number of advantages over previously reported techniques. The properties of the hologram may be tailored to the application, allowing high sensitivity or large dynamic range. All of the filters required to demodulate an array of sensors may be stored within a single, passive, optical element. The IFBGs are interrogated in parallel, with negligible crosstalk. Any crosstalk being due to light scattered within the crystal. If photorefractive materials are used, the holograms may be fixed, or be updateable, and may also be tuned using electric fields. The use of photorefractive materials does present a number of issues. The diffraction efficiency is sensitive to the polarisation of the reflected signal, although no significant environmental perturbations of the polarisation state were observed in the laboratory. While, in this investigation, the hologram was not permanent, in a practical system the holographic spectral filter bank would be a array of permanent holograms, fixed within the material. Since diffraction efficiency of the photorefractive volume hologram is independent of the writing power (Tao *et al*, 1993), a low powered tuneable laser diode could be used in place of the Ti:sapphire laser. While, in many practical sensor systems, photorefractive materials may not be the optimum holographic medium, they are possibly the most flexible of holographic media, and



$xdB=20\log x$

Figure 6.5 Spectrum analyser trace illustrating the response to dynamic strain. The ELED was modulated at 1 kHz. A peak strain modulation of $370\mu\text{strain}$ at 0.3 Hz was applied to the grating. The minimum detectable signal is $4\mu\text{strain}/\sqrt{\text{Hz}}$.

have been used in this instance to demonstrate the potential of the use of volume holograms in demodulating IFBG sensors.

Intensity referencing may be used to remove ambiguities arising from changes in source intensity, down lead losses and polarisation, may be readily achieved using a second set of angular-wavelength multiplexed holograms written in the same crystal, such that the gratings' Bragg wavelengths sit on the negative slope of the holograms' transfer function. The signal from each sensor would then be diffracted in two directions, the ratio of the diffracted signals giving the measurand induced wavelength shift with double the sensitivity.

References

- Campbell, S., Yi, X., and Yeh, P., 'Hybrid-sparse wavelength angle multiplexed optical data storage system', *Opt. Lett.*, **19**, pp2161-2163 (1994).
- Gunter, P., 'Holography, coherent light amplification and optical phase conjugation', *Physics Reports*, **93**, pp199-299 (1982).
- Gunter, P., and Huignard J-P. (eds), 'Photorefractive materials and their applications I: fundamental phenomena', *Topics in Applied Physics*, vol **61**, Springer-Verlag, Berlin (1988).
- Hariharan, F., 'Optical Holography: Techniques and Applications', Cambridge University Press, Cambridge (1984).
- Jackson, D.A., Lobo Ribeiro, A.B., Reekie, L., and Archambault, J-L., 'Simple multiplexing scheme for a fibre optic grating sensor network', *Opt. Lett.*, **18**, pp1192-1194 (1993).
- Kersey, A.D., Berkoff, T.A., and Morey, W.W., 'High resolution fibre grating based strain sensor with interferometric wavelength shift detection' *Electron. Lett.*, **28**, pp236-238 (1992).
- Kersey, A.D., Berkoff, T.A., and Morey, W.W., 'Multiplexed fiber Bragg grating strain sensors system with a fibre Fabry-Perot wavelength filter', *Opt. Lett.*, **18**, pp1370-1372 (1993).

- Kersey, A.D., 'Interrogation and multiplexing techniques for fiber Bragg grating strain-sensors', *SPIE*, **2071**, pp30-48 (1994).
- Kogelnik, H., 'Coupled wave theory for thick hologram gratings', *Bell System Technical Journal*, **48**, pp2909-47 (1969).
- Measures, R.M., Melle S., and Liu, K., 'Wavelength demodulated Bragg grating fibre optic sensing systems for addressing smart structure critical issues', *Smart Mater. Struct.*, **1**, pp36-44 (1992).
- Rakuliic, G.A., and V. Leyva, "Volume holographic narrow band optical filter" *Opt. Lett.*, **18**, pp459-461 (1993).
- Read. I.J., 'High speed multiplexed interrogation of Bragg grating sensors using a Fabry-Pérot tunable filter' *to published in Smart. Mater. Struct.* (1997).
- Tao, S., Seviah, D.R., and Midwinter. J.E., 'Spatio-angular multiplexed storage of 750 holograms in Fe-LiNbO₃ crystal', *Opt. Lett.*, **18**, pp912-914 (1993).
- Xu, M.G., Geiger, H., Archambault, J-L., Reekie, L., and Dakin, J.P., 'Novel interrogating system for fibre Bragg grating sensors using an acousto-optic tunable filter', *Electron. Lett.*, **29**, pp1510-1511 (1993).

Chapter 7

Conclusions and future developments

7.1 Bragg grating fabrication schemes

The fabrication of IFBGs into hydrogen loaded fibres has been demonstrated using a near-field phase mask technique and two mirror interferometer schemes, in conjunction with a tuneable UV laser source: a frequency doubled, Nd:YAG pumped dye laser.

WDM grating arrays were written using the mirror interferometers by varying the UV source wavelength. A conventional mirror interferometer allowed a Bragg wavelength spectral coverage of 33nm with a potential laser limited Bragg wavelength accuracy of 0.07nm, for gratings written around 800nm. A modified version of the mirror interferometer that incorporated a phase mask beamsplitter enabled the usefulness of laser source tuning to be extended to situations where either greater spectral coverage or more precise control of the Bragg wavelength was required. Two configurations were demonstrated, one configuration allowing a 51nm spectral coverage and the other a laser limited Bragg wavelength accuracy of $\pm 0.03\text{nm}$ (for gratings written around 800nm). These values were specific to the phase mask and laser source used. By appropriate selection of the phase mask grating period, either improved Bragg wavelength accuracy or increased spectral coverage

can be achieved. The experimental results obtained using both the conventional and the modified interferometers agreed with theoretical predictions within the limits of experimental error.

In the future, the Bragg wavelengths of gratings within WDM arrays could be more precisely controlled by in-line monitoring during fabrication. Grating writing could be stopped when an IFBG's Bragg wavelength had shifted to the desired location and a CCD spectrometer system has recently been developed that could be used for this purpose. Also, prior to UV exposure, the regions of hydrogen loaded fibres where gratings are to be written could be thermally processed by, for example, a CO₂ laser source. The exposed regions would then have permanently enhanced photosensitivity and the fibre could be left for several weeks to allow the molecular hydrogen to completely diffuse out of the core. This would enable IFBGs to be written that did not experience any subsequent shift in their Bragg wavelengths as a result of hydrogen loading.

The range of writing conditions used for fabricating WDM grating arrays using the conventional mirror interferometer were established. It was estimated that the energy density per pulse at the optical fibre was in the range 70-145mJcm⁻². The photoinduced refractive index modulation, calculated using coupled-mode theory, for a typical IFBG (53% reflectivity, 2.8mm long) written into Spectran (780nm) fibre was 1.1×10^{-4} . This was in-line with previously reported values for hydrogen loaded germanosilicate fibres with low germania concentrations. IFBGs written using the interferometer had bandwidths of ~0.3nm FWHM when measured using a spectrum analyser with 0.1nm resolution. In comparison, coupled mode theory predicted a 0.1nm FWHM for uniform gratings with the otherwise identical parameters.

A short wavelength loss was often seen to accompany IFBGs and this was associated with the coupling of the fundamental LP₀₁ mode into back-reflected cladding and radiation modes. This loss was especially noticeable on highly reflective gratings. Such losses could limit the WDM density obtainable for strong IFBGs and therefore it would be advantageous to understand the dependence of the short wavelength loss on grating strength and tilt angle.

A shift in the Bragg wavelength of an IFBG (initially at 1225.7nm) written into a hydrogen loaded OF Deeside (1300nm) fibre was observed. A reduction in Bragg wavelength of 1.3nm was measured over a period of 37 days. The large shift in wavelength indicated that there was still a substantial amount of molecular hydrogen remaining in the fibre core after UV exposure. The Bragg wavelength was not measured during the first few hours following grating fabrication, and as significant shifts in the Bragg wavelength can occur during this period, it would be worthwhile using real-time monitoring to obtain a more detailed record of the Bragg wavelength shift over time. An absorption band at 1245nm with a 9.3nm FWHM was seen in the same fibre and this was associated with H₂ first overtone absorption. The initial absorption was estimated at 1420dBkm⁻¹, but after a period of 37 days this had reduced to such an extent that it could not be measured in a 0.8m length of fibre. The H₂ absorption band could, in future, be use to estimate the level of molecular hydrogen within the core of an optical fibre and thereby give an indication of its photosensitivity.

7.2 Embedded Bragg grating strain sensors in carbon fibre composite

The axial strain sensitivity of a Spectran (780nm) fibre was investigated. The monochromator based spectrometer used to measure the Bragg wavelength proved to be insufficiently accurate (absolute accuracy $\pm 0.2\text{nm}$) and a periodic systematic error was introduced into the strain sensitivity measurements. An attempt was made to calibrate out this systematic error and the strain gauge factor for Spectran fibre, which relates the fractional Bragg wavelength shift to the applied strain, was calculated to be 0.76. No experimental error can be quoted because the magnitude of the systematic error was not determined; though the experimental value was within 3% of a theoretically calculated value for silica glass fibres of 0.78. Clearly a more satisfactory system for monitoring the Bragg wavelength shift is required. To that

end, a tuneable Fabry-Pérot filter has subsequently been obtained, which will allow a far more accurate determination of optical fibre strain gauge factors.

WDM grating arrays have been embedded into an aerospace carbon fibre composite material for the purpose of quantitative dc strain measurement. Four optical fibres were embedded parallel to the adjacent ply directions, with an array of five gratings on each fibre. Two arrays were fabricated into Spectran (780nm) and two into Fibrecore SM800. One fibre of each type had an acrylate coating applied to the small sections of stripped fibre where the IFBGs had been written.

Measurements of the IFBGs' Bragg wavelengths were made prior to and immediately following embedding. Gratings within the same fibre type experienced a fairly consistent shift in Bragg wavelength on embedding, regardless of whether they were written into uncoated or recoated fibres. A residual tensile strain in the range 2100-2350 μ strain was determined from the Bragg wavelength shifts of IFBGs written into SM800 fibre. Two anomalous, low residual strain values of -413 μ strain and 518 μ strain indicated the possibility of poor sensor-host bonding at these locations. Residual strain could not be calculated using the Spectran fibres as hydrogen present in the fibre core prior to embedding would have affected the results. Compressive strain measurements rather than tensile residual strain measurements were expected and this difference requires further investigation.

Using a three-point bend test, the theoretical surface strain applied to a carbon fibre test beam was compared to strain measurements made by five surface mounted electrical strain gauges and the embedded fibre grating arrays. The theoretical surface strain applied to the test beam mid-point was in the range $\pm 3400\mu$ strain. Within this range all but one of the uncoated IFBGs had a measured strain response within experimental error, with the IFBG strain responses deviating from the theoretical values by $\leq 4.3\%$. The exception had a strain response 12.4% greater than the theoretical value, and this was the same grating that had an anomalous residual strain measurement of 518 μ strain. For the anomalous measurement, the deviation from theory was in-line with the error that would have arisen if the fibre had migrated one ply layer toward the composite surface (12.5%). This could be confirmed by taking a

cross-section of the beam at the IFBG location. On average the uncoated grating arrays had a strain response $\sim 4\%$ less than the coated arrays, indicating that the applied coating acted to slightly reduce the strain response. However, the coatings did not appear to affect the linearity or the repeatability of the strain measurements, with the standard error in the measurements from both uncoated and recoated fibres being no greater than 0.5%.

Thus in summary, it would appear that, for the deflection range investigated, the simple model used to calculate the applied strain from the Bragg wavelength shifts allows a reasonably accurate determination of the axial strain for optical fibres embedded into carbon fibre composites parallel to the adjacent ply directions. The results from the IFBG sensors, however, were not as linear or repeatable as the electrical strain gauge measurements, which had standard errors of no greater than 0.2% and a fit to theory of $\leq 3.1\%$.

The three-point bend test only provided a preliminary appraisal of the suitability of IFBGs for embedded strain sensing within composite materials. A more useful assessment of the sensor-host bonding could be achieved by measuring the strain response over many load cycles. Destructive testing of specimens would allow the degradation of material strength, due to the embedded fibres, and the failure point of IFBG sensors to be determined. Finally, a comparison between the IFBG strain response under transverse and axial loading would enable a more quantitative evaluation of the accuracy of the simple (axial) strain model.

7.3 Simultaneous strain and temperature measurement

A novel method for separating the strain and temperature response of IFBG sensors has been demonstrated. This was based on the difference in response of two IFBGs written either side of a fusion splice between fibres of different diameters. A transfer matrix relating the temperature and strain measurements to the induced Bragg wavelength shifts was experimentally determined. The measured matrix elements were calibrated to take into account the systematic error introduced by the

monochromator based spectrometer. A condition number of 23 was calculated for the transfer matrix, which compared favourably with the condition numbers calculated for the other reported simultaneous strain and temperature measurement techniques. The spliced IFBG pair scheme had the most well conditioned transfer matrix of all the techniques based purely on IFBGs.

An advantage of the spliced IFBG pair technique is that the Bragg wavelengths of the gratings may be closely separated and thus high density WDM can be achieved. The technique is not suitable for use in embedded composite materials and large sensor arrays require a great number of fusion splices.. The latter limitation could be removed, if in a modified version of the scheme, a pair of IFBGs were written into a single fibre and the fibre was etched at the location of one of the gratings to change its diameter. The strength of the fusion splice between fibres of different diameters (or indeed an etched sensor region) may also be an issue and requires investigation. It should also be noted that the technique assumes that the temperature is uniform across the IFBG pair, which may not necessarily be true in environments where there are steep temperature gradients.

Further theoretical analysis is required to determine the optimum configuration for the sensor scheme. A much more accurate determination of the transfer matrix elements could be obtained using an interrogation system based on the recently acquired Fabry-Pérot tuneable filter. This would also allow a more meaningful experimental assessment of the scheme.

7.4 Volume holographic demodulation scheme

A novel IFBG sensor demodulation scheme using a photorefractive hologram has been demonstrated. A strain measurement range of $2500\mu\text{strain}$ was achieved with a resolution of $4\mu\text{strain}/\sqrt{\text{Hz}}$. The resolution and measurement range may be tailored to the application by appropriated choice of hologram characteristics.

The technique may be extended to allow demultiplexing of WDM grating arrays by using a single optical component, consisting of angular-wavelength

multiplexed volume holograms. Also, intensity referencing may be used to remove ambiguities arising from changes in source intensity.

Appendix A

Laser beam calculations performed using the Spiricon LBA-100A

The results obtained by the LBA-100A were highly sensitive to beam presentation. Therefore, to obtain the best possible accuracy, a reference frame was subtracted from the captured beam profile, to null the background energy, before the calculation of beam parameters. Also, either a circular or elliptical software aperture (depending on the beam shape) was placed around the beam profile and all calculations were restricted to the data contained within this aperture. This prevented noise in the rest of the frame degrading the results. Finally the ambient lighting was kept as low as possible, to reduce the risk of background fluctuations upsetting the calibration. The system was calibrated prior to use by capturing a beam profile of a known energy.

The expressions given below are taken, either directly or in a modified form, from the LBA-100A operators manual. The x and y pixel co-ordinates being along the CCD array horizontal and vertical axes respectively.

Beam width calculation

Beam widths are computed using algorithms which simulate knife-edge techniques. The calculated beam width is set to correspond to the $1/e^2$ diameter for a Gaussian TEM_{00} beam. The LBA uses a 10% and 90% of energy approach with a 1.561 multiplier as recommended by Siegman *et al* (1991). The simulated knife-edges

cut along the x and y directions. Therefore an elliptical beam's symmetric axes should be aligned with the x and y axes of the display.

Gaussian fit and correlation of fit

For a whole beam fit, the LBA performs a least squares bivariate normal equation (Gaussian equation) fit using all the data in the aperture. The least squares method minimises the sum of the squares of the differences between the data and the fitted surfaces, A_{\min} , so that

$$A_{\min} = \sum_x \sum_y (Z_{xy} - S_{xy})^2 \quad \text{A.1}$$

where Z_{xy} is the amplitude of the pixel data at (x,y) and S_{xy} is amplitude of the fitted surface at (x,y) . The definition of the bivariate normal equation being

$$S_{xy} = S_0 e^{-\left[\left(\frac{x-\bar{x}}{w_x} \right)^2 + \left(\frac{y-\bar{y}}{w_y} \right)^2 \right]} \quad \text{A.2}$$

where S_0 is amplitude at the Gaussian centre, w_x is the horizontal radius at $1/e^2$ of energy, and w_y is the vertical radius at $1/e^2$ of energy.

The correlation of the data with the Gaussian surface G_c is determined from

$$G_c = 1 - \frac{\sum |Z - S|}{\sum Z} \quad \text{A.3}$$

where Z is the pixel amplitude data and S is the Gaussian surface data. The allowed range of G_c is minus infinity to one. However, the practical range for most real beam profiles is from zero to one, a value of one equating to a perfect Gaussian surface. If the correlation does yield a negative value then the beam profile is certainly not Gaussian.

Reference:

Siegman, Sasnett and Johnston, 'Choice of clip levels for beam width measurements using knife edge techniques', *IEEE J. Quant. Electron.*, **27** (1991).

Appendix B

Optical fibre parameters

Text label	OF Deeside (1300nm)
Fibre type	Optical Fibres of Deeside 1300nm
Hi-Bi/singlemode	Singlemode
Nominal operating wavelength	1300nm
Cut-off wavelength	1204nm
Numerical aperture	0.11
Attenuation (at 1300nm)	2.5dB/km
Core diameter	8-9µm
Cladding (inner) diameter	125µm
Coating diameter	250µm
Core composition	Silica/Ge doped (wt % unknown)
Cladding composition	Silica
Coating composition	Dual layer acrylate

Text label	Spectran (780nm)
Fibre type	Spectran FS SMC-AO780B
Hi-Bi/singlemode	Singlemode
Nominal operating wavelength	780nm
Cut-off wavelength	730±40nm
Numerical aperture	0.11
Attenuation (at 780nm)	4dB/km
Core diameter	5µm
Cladding (inner) diameter	125±2µm
Coating diameter	245±15µm
Core composition	Silica/5% wt Ge conc
Cladding composition	Silica
Coating composition	Dual layer acrylate

Text label

Andrew Corp. E-series (820nm)

Fibre type

Andrew Corp. 48280-820S-1, E-series

Hi-Bi/singlemode

Hi-Bi elliptical core

Nominal operating wavelength

820nm

Birefringence

1.5×10^{-4}

Cut-off wavelength

$700 \pm 50 \text{nm}$

Numerical aperture

0.34

Attenuation (at 820nm)

7-9dB/km

Core diameter

$1 \times 2 \mu\text{m}$

Cladding (inner) diameter

$125 \pm 3 \mu\text{m}$

Coating diameter

$225 \pm 5 \mu\text{m}$

Core composition

Silica/18% wt Ge conc

Cladding composition

Flourine doped silica

Coating composition

Dual layer acrylate

Text label

Andrew Corp. D-series (1550nm)

Fibre type

Andrew Corp. 205170-1550S-2, D-

series

Hi-Bi/singlemode

Hi-Bi elliptical core

Nominal operating wavelength

1550nm

Birefringence

1.5×10^{-4}

Cut-off wavelength

$1290 \pm 70 \text{nm}$

Numerical aperture

0.31

Attenuation (at 1550nm)

2-3dB/km

Core diameter

$2 \times 4 \mu\text{m}$

Cladding (inner) diameter

$125 \pm 3 \mu\text{m}$

Coating diameter

$225 \pm \mu\text{m}$

Core composition

Silica/18% wt Ge conc

Cladding composition

Flourine doped silica

Coating composition

Single layer acrylate coating

Text label

Fibre type
Hi-Bi/singlemode
Nominal operating wavelength
Cut-off wavelength
Numerical aperture
Attenuation (at 830nm)
Core diameter
Cladding (inner) diameter
Coating diameter
Core composition
Cladding composition
Coating composition

SM800

Fibrecore SM800
Singlemode
830nm
722nm
0.11
2.7dB/km
5µm
125µm
240µm
Silica/5% wt Ge conc
Phosphorous/flourine doped silica
Single layer acrylate, Desoto 131

Text label

Fibre type
Hi-Bi/singlemode
Nominal operating wavelength
Birefringence
Cut-off wavelength
Numerical aperture
Attenuation (at 820nm)
Core diameter
Cladding (inner) diameter
Coating diameter
Core composition
Cladding composition
Coating composition

Corning (780nm)

Corning PMF-38
Hi-Bi elliptical core
780-850nm
 5.4×10^{-4}
 710 ± 50 nm
0.3
10dB/km
-
 $80 \mu\text{m} \pm 3 \mu\text{m}$
 $185 \mu\text{m} \pm 15 \mu\text{m}$
-
-
Dual layer acrylate

Appendix C

Two-beam mirror interferometer with a phase mask beamsplitter: sensitivity of the out-of-plane geometry to writing wavelength

For the two-beam mirror interferometer with phase mask beamsplitter geometry (section 3.2.5) shown in figure 3.12(b). The sensitivity of the Bragg wavelength to changes in writing wavelength for an out-of-plane mirror tilt angle γ_m is shown overleaf.

The expression was symbolically derived from equation 3.8 using MathSoft, Inc., Mathcad V3.1, where

λ_b = Bragg wavelength

λ_w = Writing wavelength

θ_m = In-plane mirror tilt angle

γ_m = Out-of-plane mirror tilt angle

Λ_{pm} = Phase mask period

n_{eff} = Effective mode index

$$\frac{d\lambda_b}{d\lambda_w} = \frac{in_{eff} \sin \left(\sin^{-1} \left(\frac{\lambda_w}{\Lambda_{pm}} \right) + 2\theta_m \right) \cdot \cos^2 \left(\frac{\pi}{2} - \gamma_m \right) \cdot \cos \left(\sin^{-1} \left(\frac{\lambda_w}{\Lambda_{pm}} \right) + 2\theta_m \right)^2}{\left(\cos \left(\sin^{-1} \left(\frac{\lambda_w}{\Lambda_{pm}} \right) + 2\theta_m \right) - 1 \right)^2 \cdot \left(\sin \left(\frac{\pi}{2} - \gamma_m \right) \cdot \sqrt{\cos^2 \left(\frac{\pi}{2} - \gamma_m \right) \cdot \cos \left(\sin^{-1} \left(\frac{\lambda_w}{\Lambda_{pm}} \right) + 2\theta_m \right)^2} - 1 \right)^2}$$

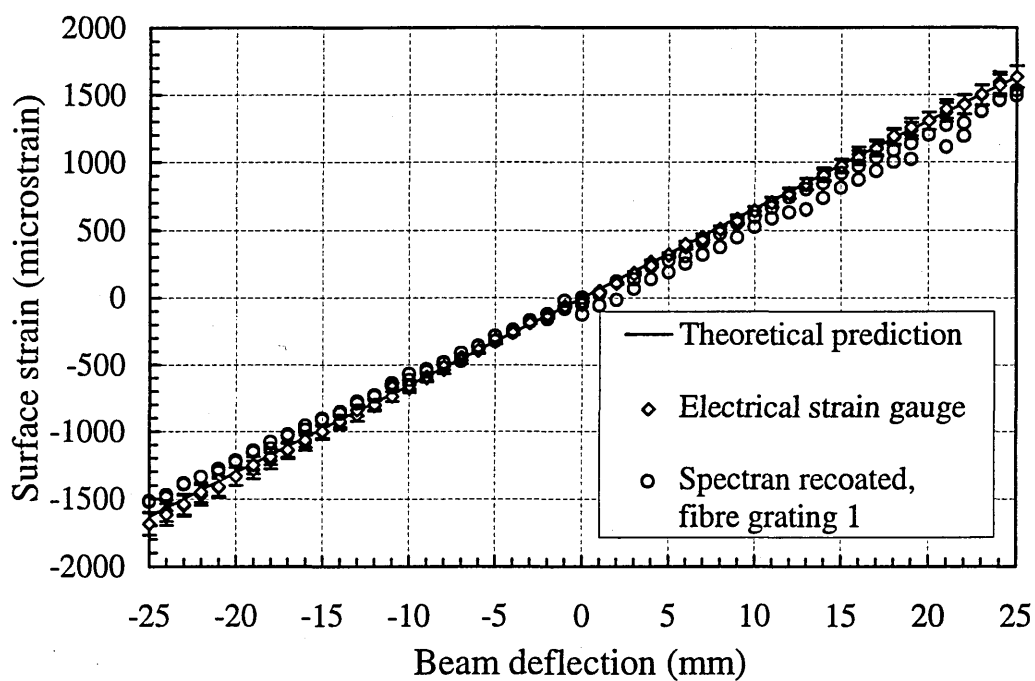
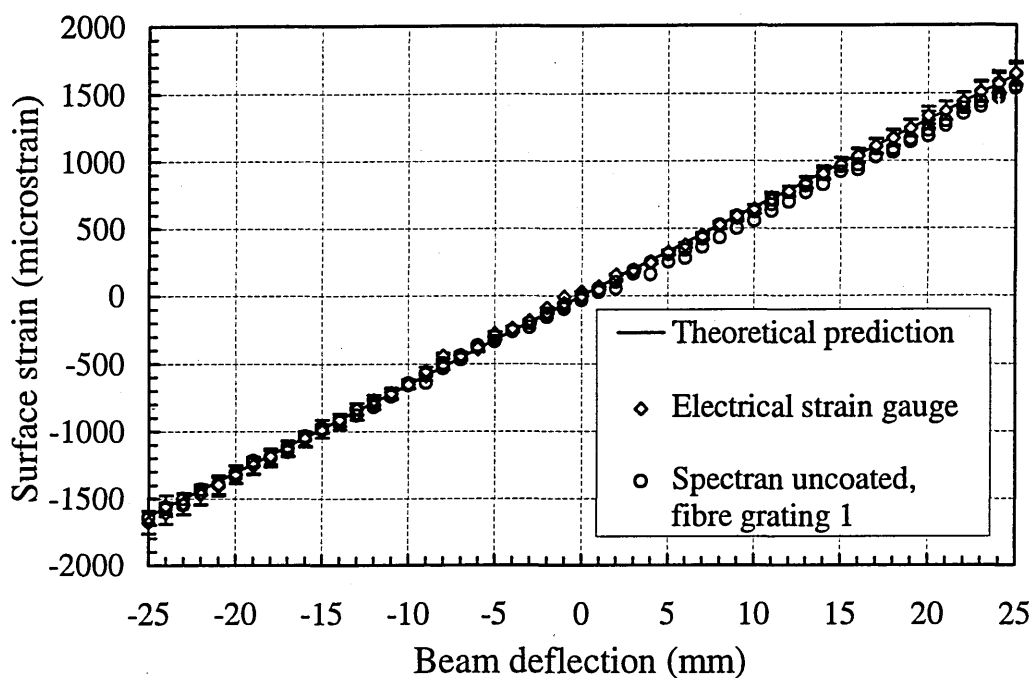
193

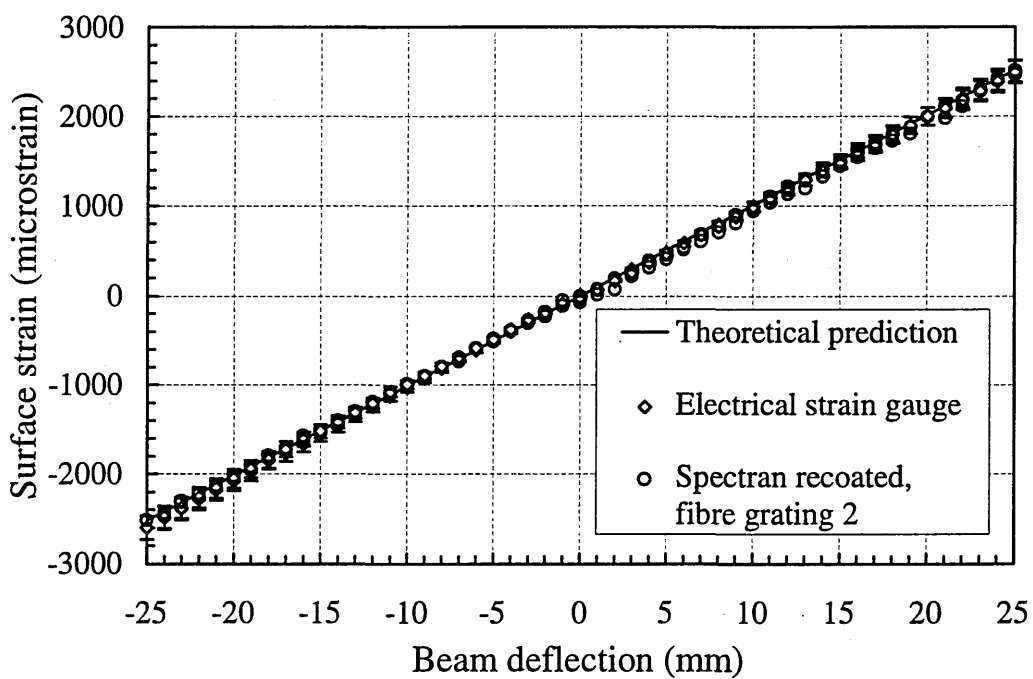
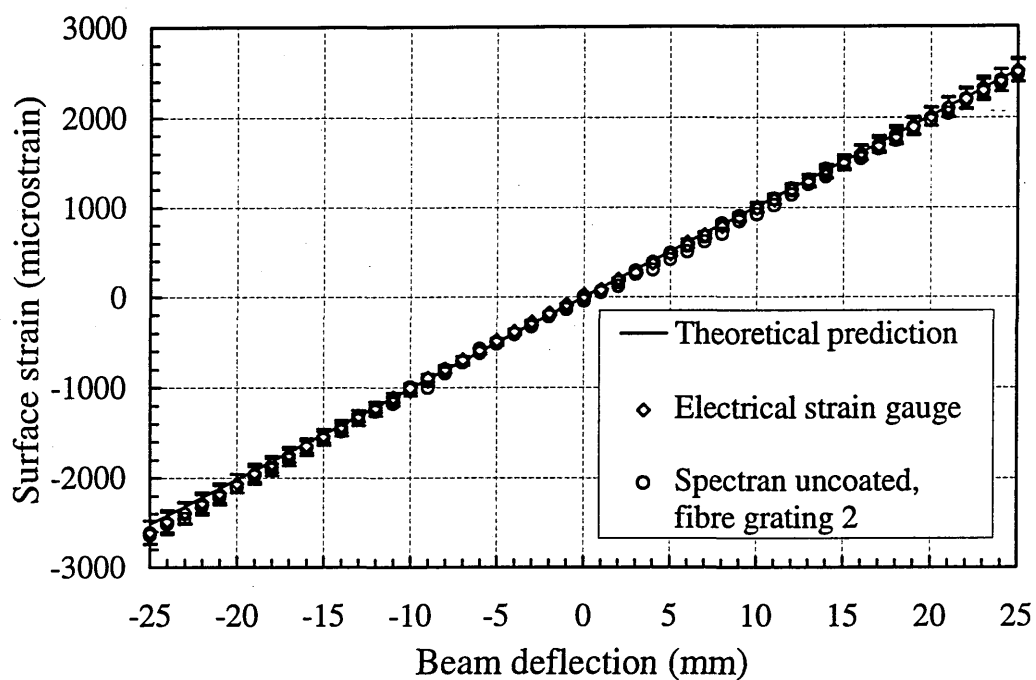
$$\frac{n_{eff} \left(i \sin \left(\sin^{-1} \left(\frac{\lambda_w}{\Lambda_{pm}} \right) + 2\theta_m \right) \cdot \sqrt{\lambda_w^2 - \Lambda_{pm}^2} - \lambda_w \cos \left(\sin^{-1} \left(\frac{\lambda_w}{\Lambda_{pm}} \right) + 2\theta_m \right) + \lambda_w \cos^2 \left(\frac{\pi}{2} - \gamma_m \right) \cdot \cos \left(\sin^{-1} \left(\frac{\lambda_w}{\Lambda_{pm}} \right) + 2\theta_m \right) \right)}{\left(\cos \left(\sin^{-1} \left(\frac{\lambda_w}{\Lambda_{pm}} \right) + 2\theta_m \right) - 1 \right)^2 \cdot \left(\sin \left(\frac{\pi}{2} - \gamma_m \right) \left(\sqrt{\lambda_w^2 - \Lambda_{pm}^2} \right) \cdot \sqrt{\cos^2 \left(\frac{\pi}{2} - \gamma_m \right) \cdot \cos \left(\sin^{-1} \left(\frac{\lambda_w}{\Lambda_{pm}} \right) + 2\theta_m \right)^2} - 1 \right)^2} \quad C.1$$

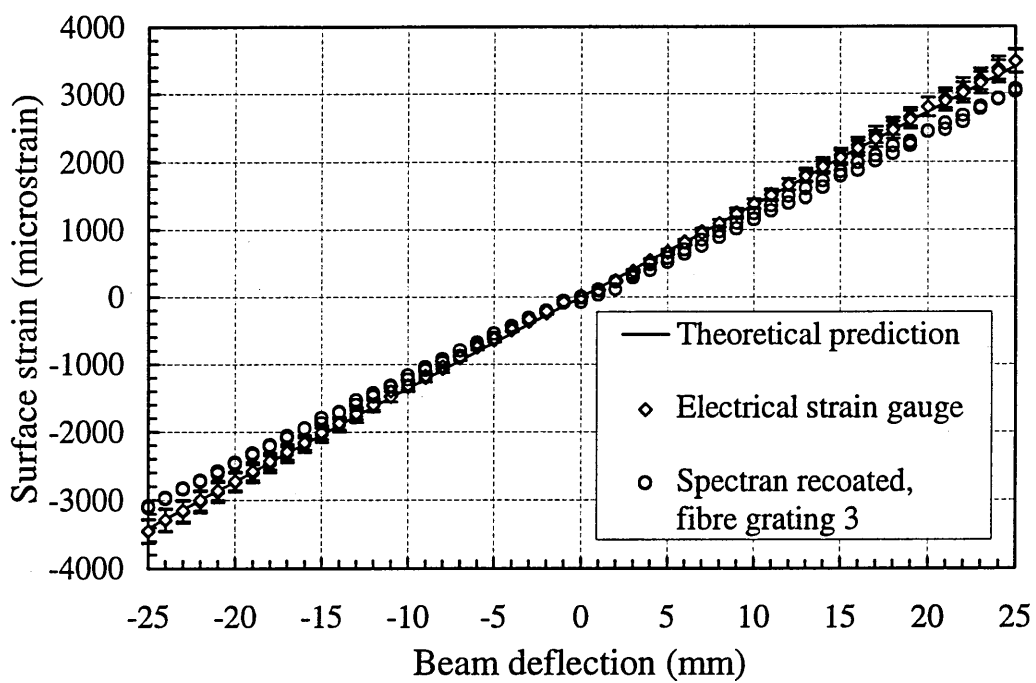
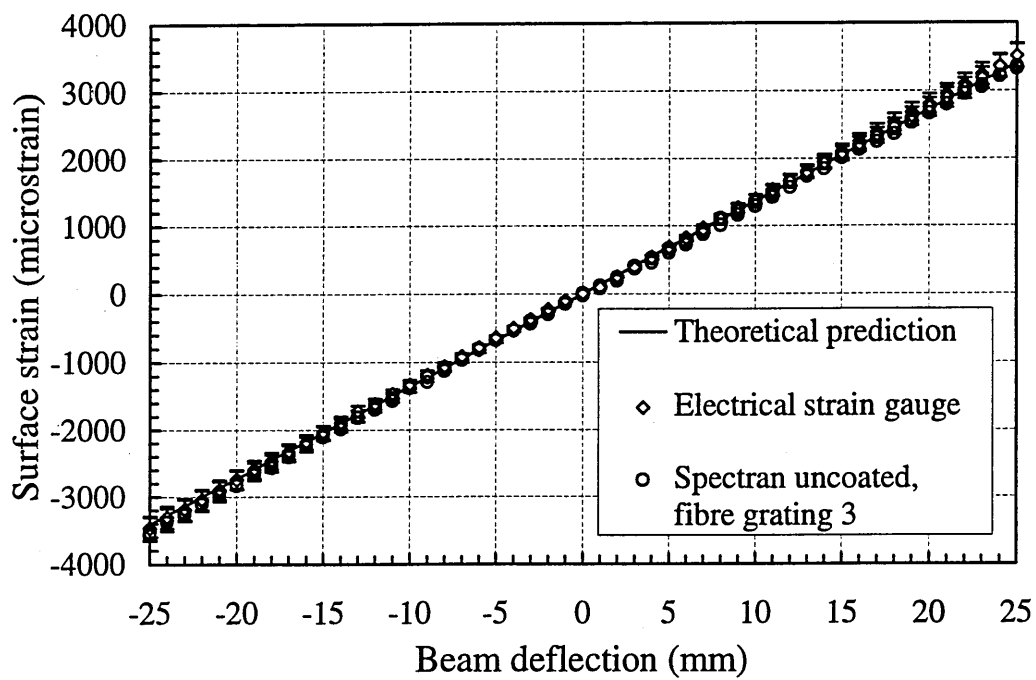
Appendix D

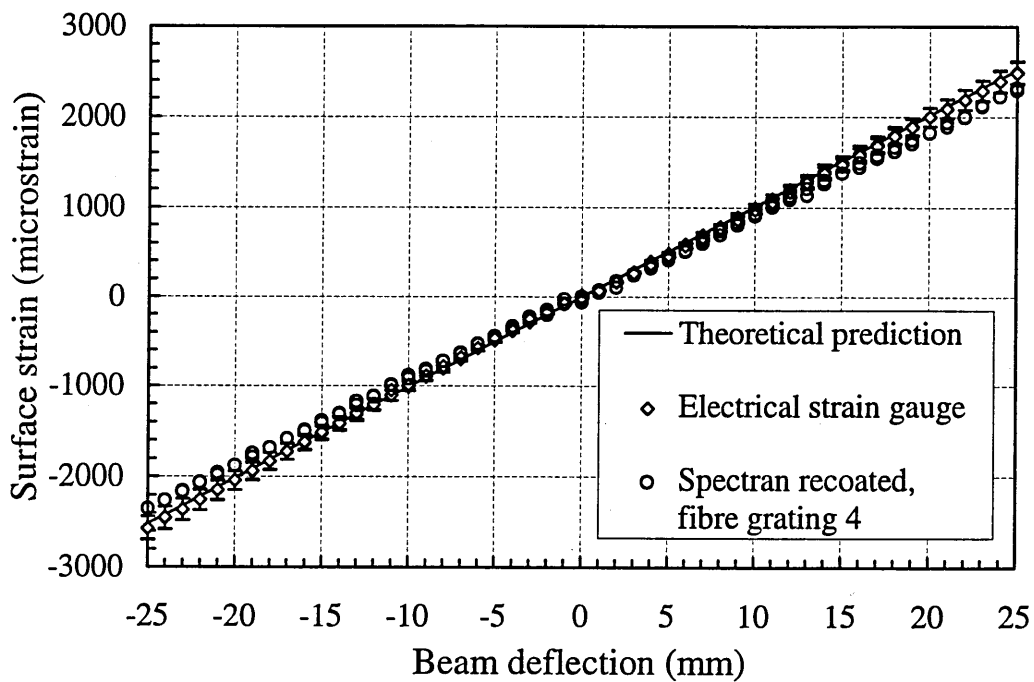
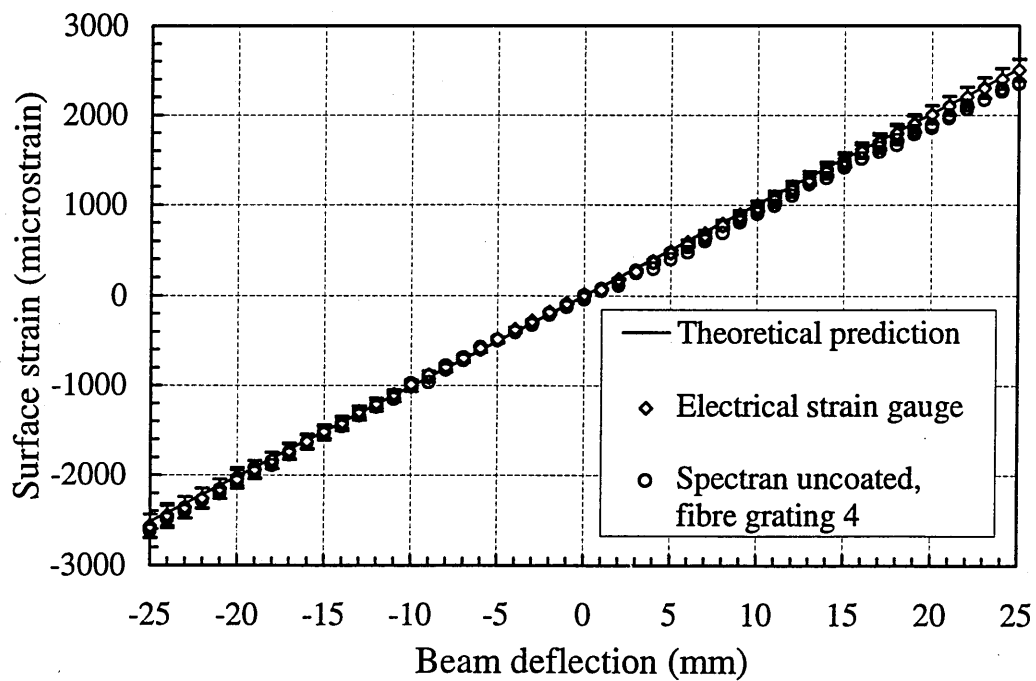
Carbon fibre composite test beam experimental data.

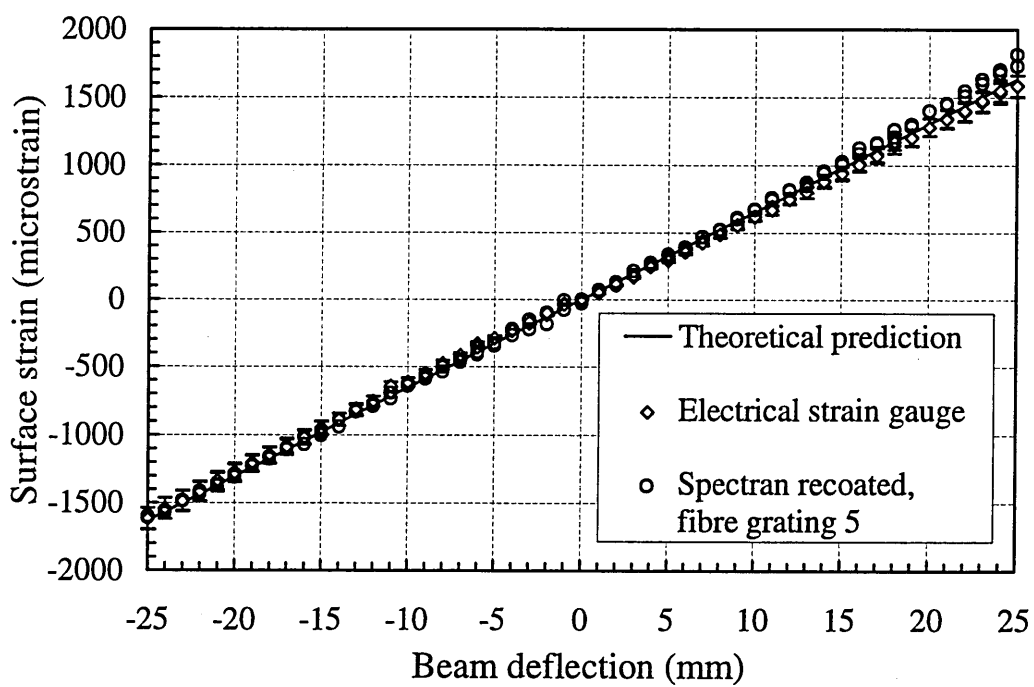
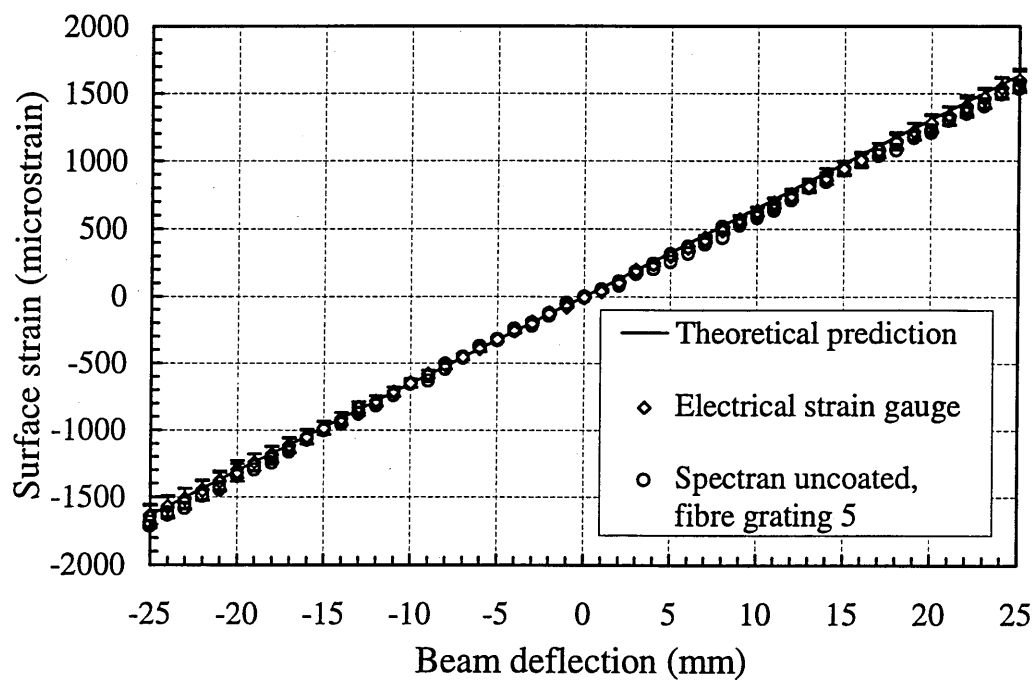
Graphs comparing the theoretical strain applied to the carbon fibre test beam with the measurements made by surface mounted electrical strain gauges, and embedded IFBG arrays.

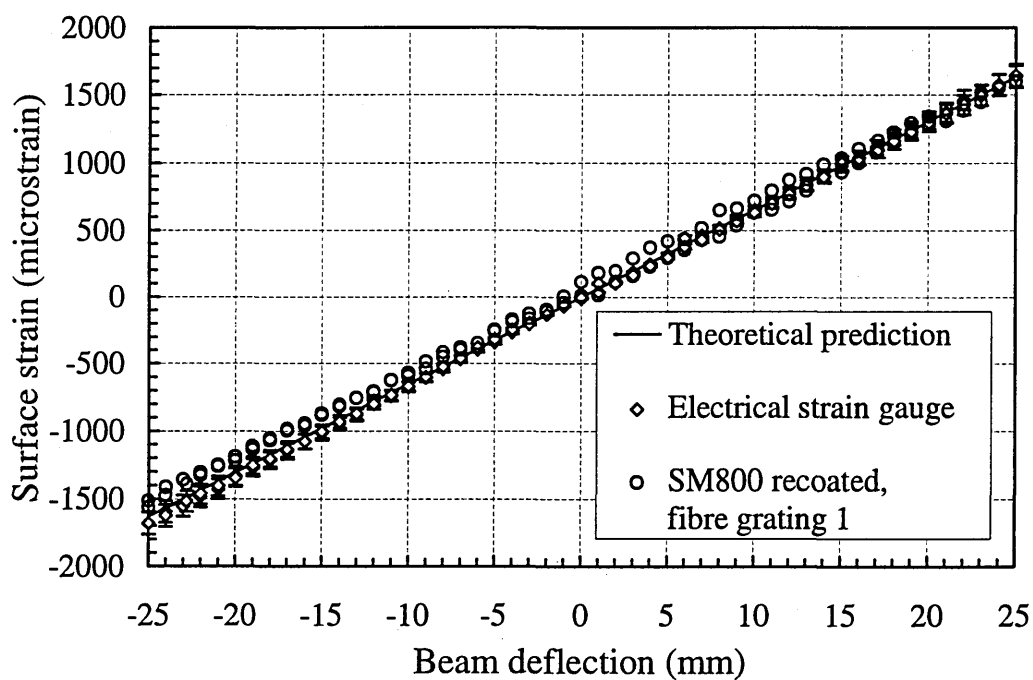
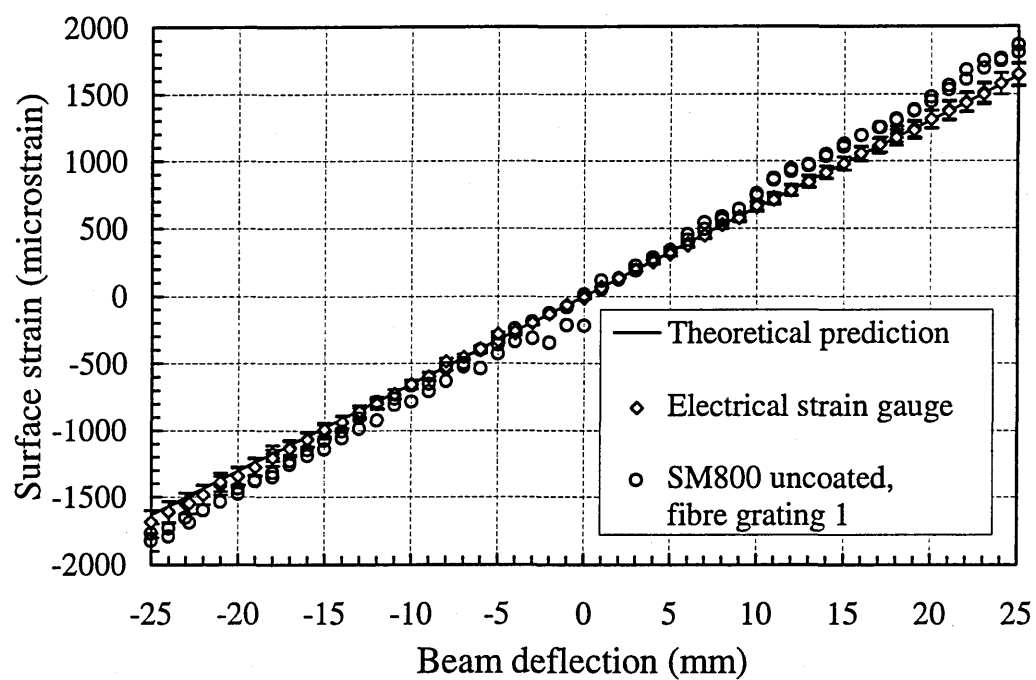


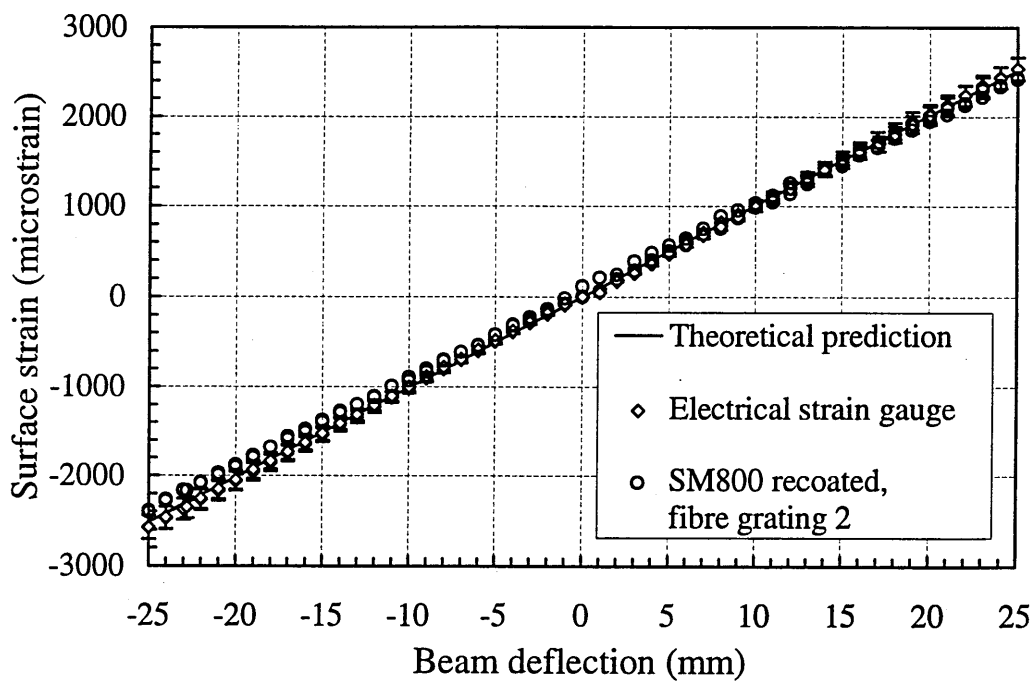
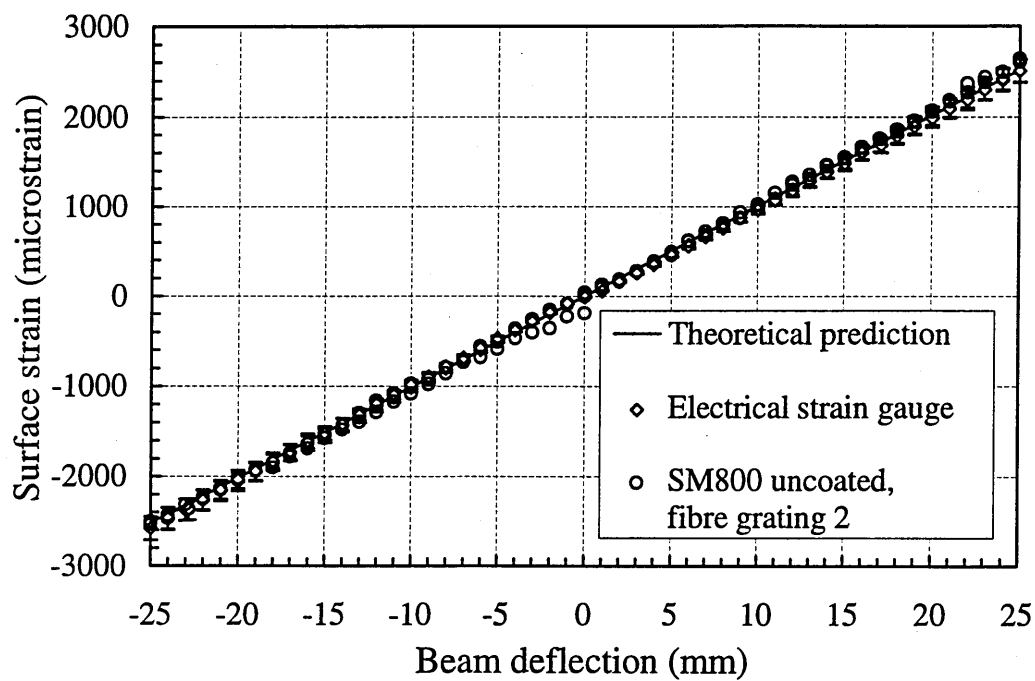


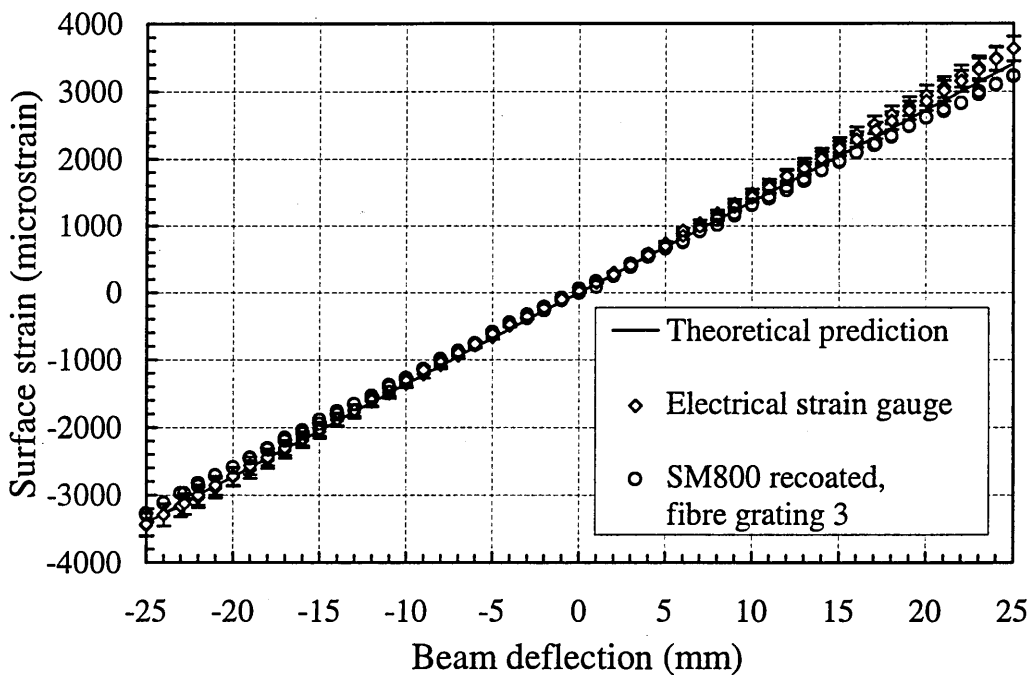
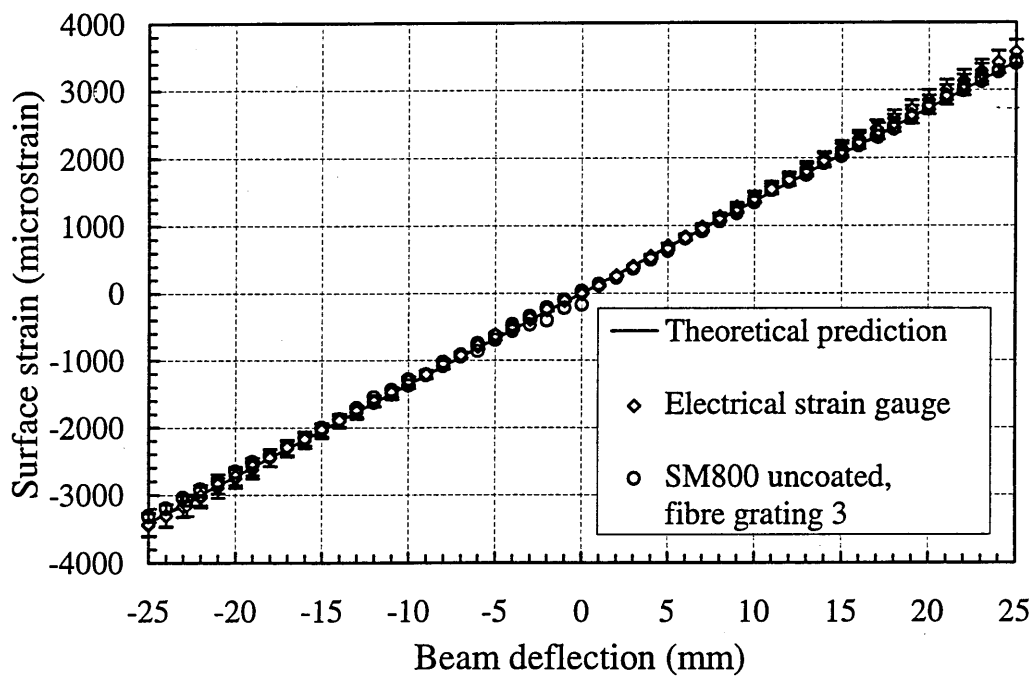


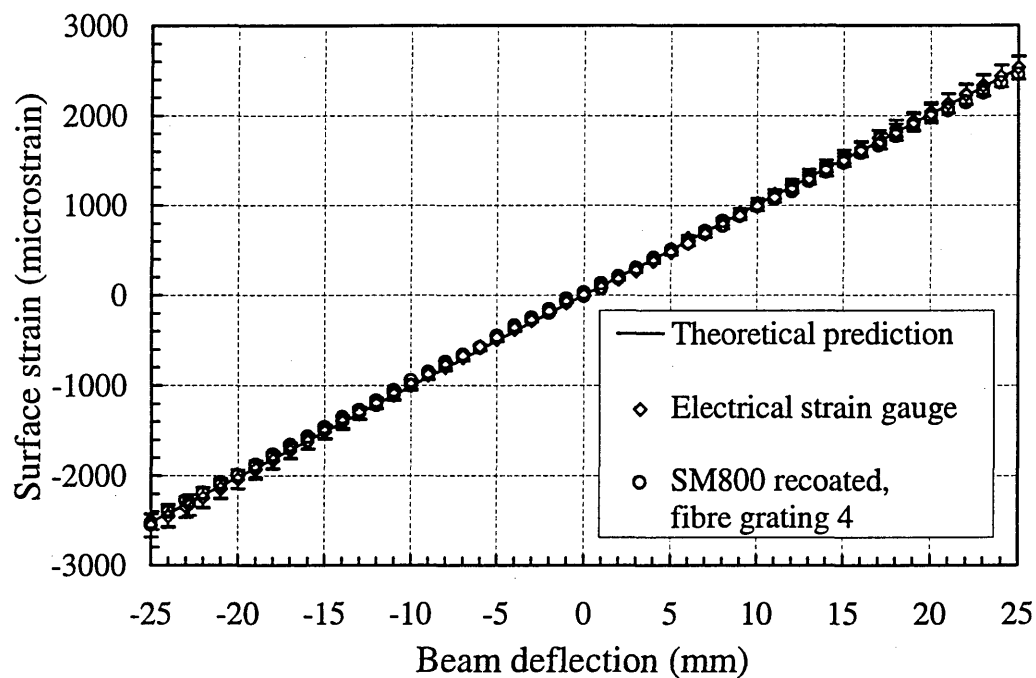
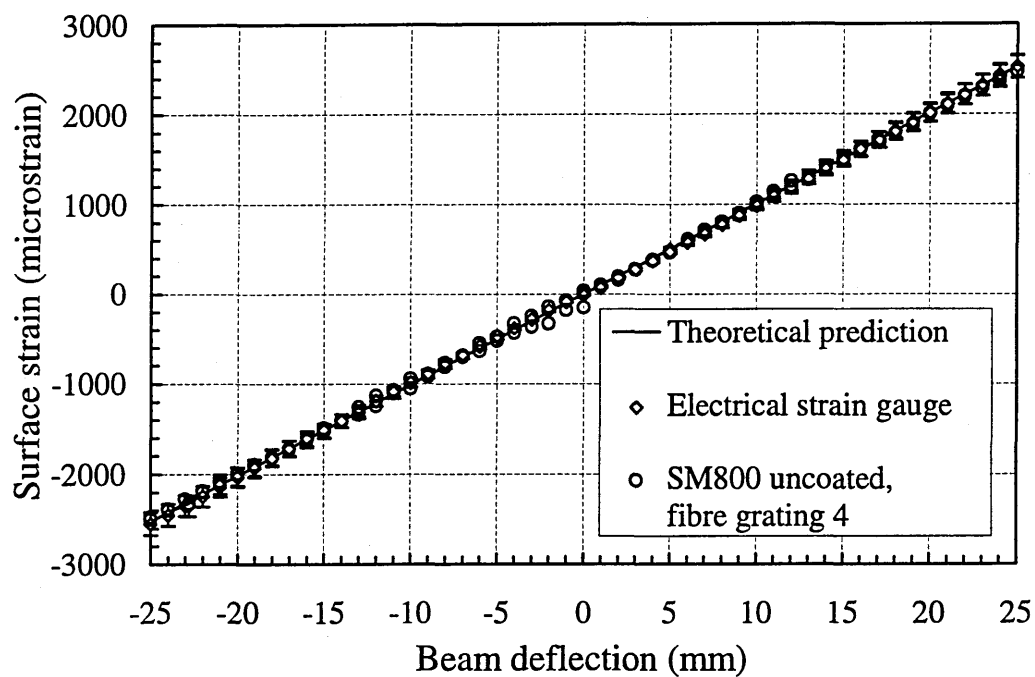


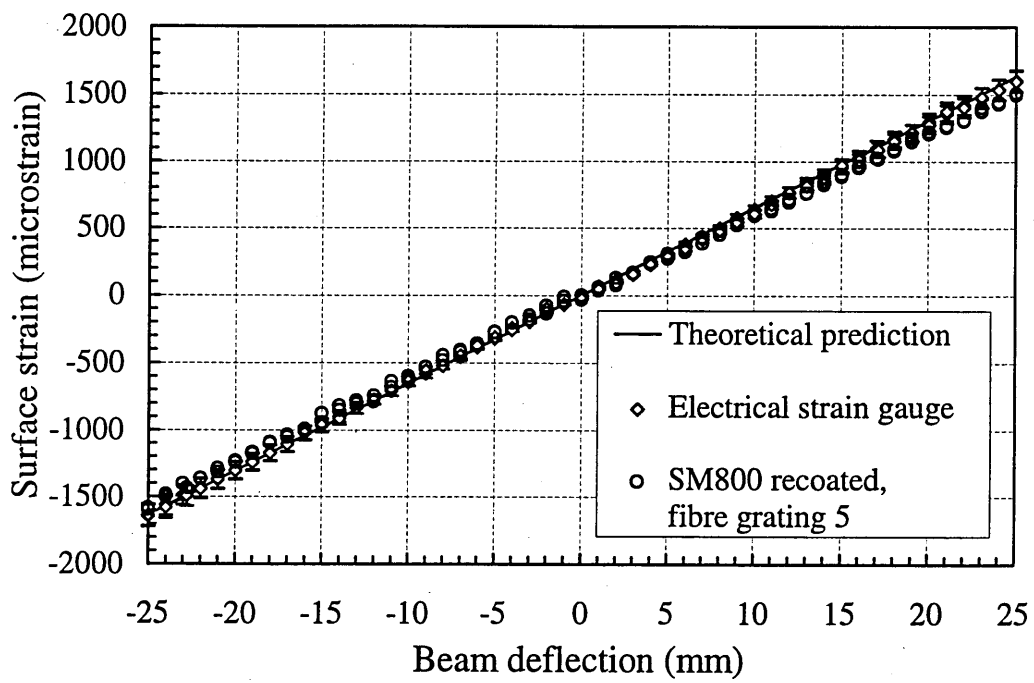
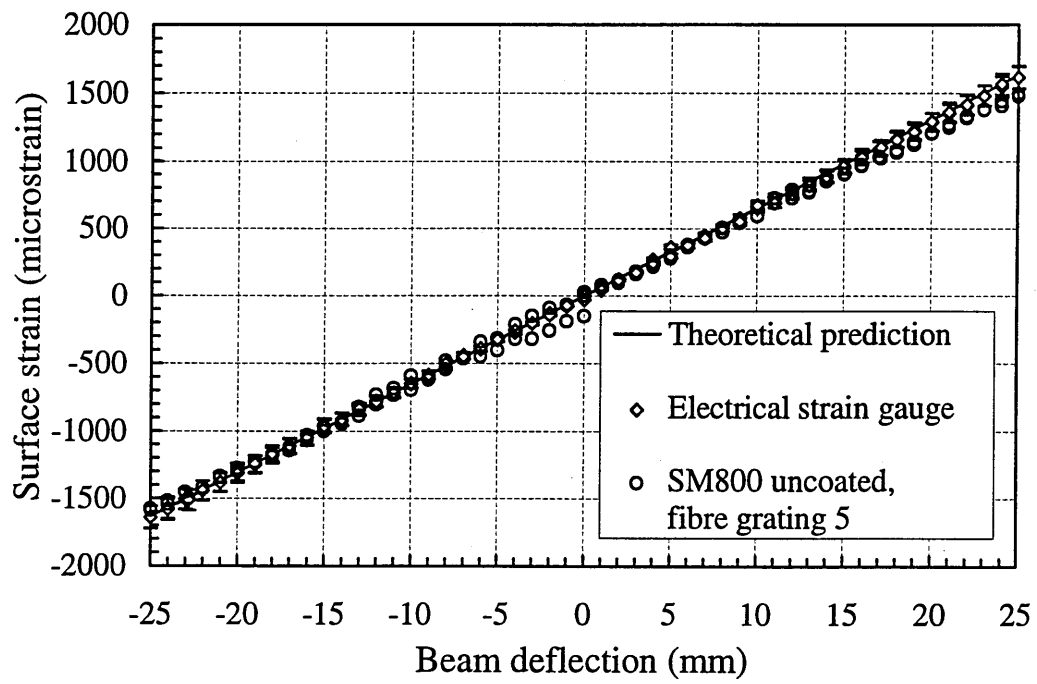












Publications arising from this study

1. M.L. Dockney, S.W. James and R.P. Tatam, 'Fibre Bragg gratings fabricated using a phase mask based interferometer and tuneable UV source', *Measurement, Science and Technology Rapid Communications*, **7**, pp445-458 (1996).
2. M.L. Dockney, I.J. Read, P.D. Foote and R.P. Tatam, 'Embedded optical fibre Bragg gratings for aerospace monitoring', *presented at the IEE Colloquium on Optical Techniques for Smart Structures and Structural monitoring*, Digest No. 1997/033, 17 February 1997.
3. M.L. Dockney, I.J. Read, P.D. Foote and R.P. Tatam, 'Embedded in-fibre Bragg grating sensors for quantitative dc strain measurement in aerospace carbon fibre composite material ' *to be published*.
4. M.L. Dockney, S.W. James and R.P. Tatam, 'In-fibre Bragg gratings fabricated using a wavelength tuneable source and a phase mask based interferometer', *presented at a one day meeting of the Institute of Physics Optical Group*, 24 May 1995.
5. S.W. James, M.L. Dockney and R.P. Tatam, 'Photorefractive volume holographic demodulation of in fibre Bragg grating sensors', *IEEE Photon. Technol. Lett.*, **8**, pp664-666 (1996).
6. S.W. James, M.L. Dockney and R.P. Tatam, 'Simultaneous, independent measurement of temperature and strain using in-fibre Bragg grating sensors', *Electron. Lett.*, **32**, pp1133-1134 (1996).

7. S.W. James, M.L. Dockney and R.P. Tatam, 'Volume holographic demodulation of in fibre Bragg grating sensors', *presented at the 11th International Conference on Optical Fiber Sensors, OFS-11*, Sapporo, Japan, May 1996.
8. S.W. James, M.L. Dockney and R.P. Tatam, 'Independent measurement of temperature and strain using in-fibre Bragg grating sensors', Post-deadline paper, *presented at the 11th International Conference on Optical Fiber Sensors, OFS-11*, Sapporo, Japan, May 1996.
9. S.W. James, M.L. Dockney and R.P. Tatam, 'Demodulation of in fibre Bragg grating sensors using volume holograms', *presented at Distributed and Multiplexed Fibre Optic Sensors IV, SPIE symposium on Optical science, engineering and instrumentation, PROC SPIE 2838*, Denver, August 1996.